

Ultrafast Visible and Ultraviolet Fluorescence Studies of Molecular and Biological Systems in Solution

THÈSE N° 5148 (2011)

PRÉSENTÉE LE 22 SEPTEMBRE 2011
À LA FACULTÉ SCIENCES DE BASE
LABORATOIRE DE SPECTROSCOPIE ULTRARAPIDE
PROGRAMME DOCTORAL EN PHYSIQUE

ÉCOLE POLYTECHNIQUE FÉDÉRALE DE LAUSANNE

POUR L'OBTENTION DU GRADE DE DOCTEUR ÈS SCIENCES

PAR

Olivier Christian BRÄM

acceptée sur proposition du jury:

Prof. G. Meylan, président du jury
Prof. M. Chergui, Dr A. Cannizzo, directeurs de thèse
Prof. T. Gustavsson, rapporteur
Prof. J.-E. Moser, rapporteur
Prof. J.-P. Wolf, rapporteur



ÉCOLE POLYTECHNIQUE
FÉDÉRALE DE LAUSANNE

Suisse
2011

Table of Content

Abstract	vii
Résumé	ix
1 Basic concepts	1
1.1 Optical spectroscopy	3
1.1.1 <i>Einstein coefficients</i>	3
1.1.2 <i>Transition dipole moment</i>	4
1.1.3 <i>Absorption</i>	5
1.1.4 <i>Lifetime and Quantum Yield</i>	6
1.1.5 <i>Absorption, Emission spectra and Stokes Shift</i>	7
1.2 Molecular Dynamics	12
1.2.1 <i>Vibrational Relaxation</i>	12
1.2.2 <i>Electronic solvation dynamics</i>	17
2 Chemical systems	25
2.1 UV dye molecules	26
2.1.1 <i>2,5-diphenyloxazole</i>	26
2.1.2 <i>Para-terphenyl</i>	28
2.2 Tryptophan	31
2.2.1 <i>Stokes shift</i>	33
2.2.2 <i>Anisotropy</i>	34
2.3 Metal and free base porphyrins	35
2.3.1 <i>General photophysics</i>	35
2.3.1 <i>Absorption and emission of TPP and OEP</i>	40
2.4 Haemoproteins	45
2.4.1 <i>Cytochrome c</i>	45
2.4.2 <i>Myoglobin</i>	47
2.5 Metal-polypyridine complexes	49
2.5.1 <i>[Ru(bpy)₃]²⁺ and [Fe(bpy)₃]²⁺</i>	49
2.5.2 <i>RuN719 and DSSCs</i>	52
3 Experimental	55
3.1 Introduction	56
3.2 Sum frequency generation	59
3.3 The set-up	61
3.3.1 <i>Femtosecond laser system</i>	61
3.3.2 <i>Excitation and gate Beam</i>	62

3.3.3	<i>Sample flow</i>	64
3.3.4	<i>Emission collection and time-gating</i>	64
3.4	Data treatment	66
3.5	Set-up characterization	67
3.5.1	<i>GVD</i>	67
3.5.2	<i>Spectral Response</i>	68
3.5.3	<i>Temporal Resolution</i>	69
3.5.4	<i>Polarization</i>	71
4	Vibrational relaxation of UV chromophores	73
4.1	Time-wavelength resolved fluorescence	74
4.1.1	<i>Static fluorescence spectra</i>	74
4.1.2	<i>Time-resolved data analysis</i>	76
4.1.3	<i>Sub-ps dynamics</i>	81
4.2	Tracking the intramolecular temperature	85
4.3	Summary	89
5	Relaxation dynamics of aqueous Tryptophan	91
5.1	Fluorescence up-conversion data	92
5.1.1	<i>Anisotropy</i>	93
5.1.2	<i>Solvation and intramolecular dynamics</i>	96
5.2	Non-equilibrium Molecular Dynamics Simulations	99
5.3	Conclusions	107
6	Relaxation dynamics of Porphyrins	109
6.1	Free base porphyrins	111
6.1.1	<i>Non-sequential electronic relaxation</i>	111
6.1.2	<i>S₂→S₁ internal conversion of H₂TPP</i>	114
6.1.3	<i>Vibrational relaxation</i>	114
6.1.4	<i>Wavepacket dynamics</i>	115
6.1.5	<i>Nonradiative channel</i>	118
6.1.6	<i>Summary</i>	120
6.2	Zn (TP and OE) porphyrins	122
6.2.1	<i>Ultrafast dynamics of Zn porpyrins</i>	122
6.2.2	<i>Sequential electronic relaxation</i>	123
6.2.3	<i>Summary</i>	127
6.3	Transition metal (TP and OE) porphyrins	129
6.3.1	<i>Ultrafast emission</i>	129
6.3.2	<i>Parameters affecting the relaxation processes</i>	132
6.4	Conclusion	134
7	Protein dynamics	135
7.1	Cytochrome c	136

7.1.1	<i>Introduction</i>	136
7.1.2	<i>Time-resolved fluorescence</i>	136
7.1.3	<i>Transient Absorption</i>	139
7.1.4	<i>Discussion</i>	141
7.1.5	<i>Conclusion</i>	148
7.2	Myoglobin	149
7.2.1	<i>Dual UV fluorescence</i>	149
7.2.2	<i>Local Trp7 dynamics</i>	153
7.2.3	<i>Haem electronic relaxation</i>	156
7.2.4	<i>Summary</i>	158
8	Metal-polypyridine complexes and Dye Sensitized Solar Cells	159
8.1	Solution phase studies	161
8.1.1	<i>Time zero Stokes shift</i>	161
8.1.2	<i>Excitation dependence of $[M(bpy)_3]^{2+}$</i>	162
8.1.3	<i>Ultrafast IVR mechanism</i>	164
8.1.4	<i>Solvent effect</i>	165
8.1.5	<i>Solar cell sensitizer: RuN719</i>	167
8.2	RuN719 adsorbed on semiconductor thin films	171
8.2.1	<i>RuN719 adsorbed on injecting and non injecting substrates</i>	171
8.2.2	<i>Electron injection process</i>	173
8.3	Conclusion	175
9	Conclusion and outlooks	177
	Appendix	181
A	Time-resolved spectral analysis	181
B	Fluorescence and vibrations calculation of UV dyes	186
C	Time-resolved anisotropy of Trp	190
D	Fluorescence and Molecular Dynamics calculations of Trp in water	196
E	Transient fluorescence of Transition metal porphyrins	198
F	Transient fluorescence and absorption of Cyt c	200
G	Metal-polypyridine complexes	203
	Abbreviations	209
	Bibliography	211
	Curriculum Vitae	227
	Remerciements	235

Abstract

A wide variety of physical and chemical processes at the molecular level, as charge or energy transfer, solvation, electronic as well as vibrational relaxation, is at the origin of the biological functionality of proteins. The work reported in this thesis is devoted to the study of these molecular dynamics in different chromophore systems. More specifically, this study is focused on the role of these dynamics in the ultrafast photophysics and photochemistry of haemoproteins. This important class of proteins has been widely studied through various spectroscopic techniques, in order to understand their functionality. These proteins contain several chromophore moieties, among which one aminoacid residue, Tryptophan, and the haem prosthetic group, which are of particular interest in this work. While Tryptophan is used as a probe of the local environment via intermolecular relaxation dynamics, we investigated the role of haem intramolecular dynamics on the protein functionality.

While different kind of ultrafast spectroscopic techniques are indicated to tackle these issues, like pump probe or photon-echo peak shift experiments, we choose a different approach to probe directly the energetic relaxation, which consists in following the ultrafast changes in the photoluminescence spectrum. The dynamics are then extracted from the spectral evolution of the emission. With this purpose, we implemented a fluorescence up-conversion set-up, which allows us resolving temporally and spectrally the photoluminescence of the sample under investigation, excited with an ultrashort light pulse, and with a temporal resolution on the femtosecond timescale.

The thesis is structured in 9 chapters. Chapter 1 resumes the theoretical background required for the interpretation of the experimental results. Chapter 2 describes the photophysical properties of the different systems investigated. Chapter 3 presents the experimental technique of fluorescence up-conversion, used to achieve broadband femtosecond detection of photoluminescence.

In Chapter 4, we present a study on the role of ultrafast vibrational and structural dynamics on the time-resolved fluorescence spectra from two UV dyes. The measurements allow us exploring the capabilities of the set-up in revealing subtle relaxation dynamics with an unequaled accuracy.

In Chapter 5, we move on to the study of the relaxation dynamics of Tryptophan (Trp) in water. This aminoacid served as an *in vivo* probe of solvation dynamics, owing to its high dipolar moment in its excited state. Our study focuses on water reorganization around the chromophore and on the distinction of this important process from the electronic internal conversion occurring on a similar timescale.

In the framework of the study of protein dynamics, Chapter 6 reports the investigation of a family of molecules extensively found in nature, namely porphyrins. In these molecular systems, a quite complex pattern of intramolecular relaxation mechanisms occurs, which needed to be clarified. A systematic study on the free base and on a wide series of metallo-porphyrins definitely clarified the picture of their electronic relaxation pathways. We

finally elaborate a comprehensive scheme of this relaxation, including substituent's influence. The mechanisms observed are intrinsically related to the photophysical properties used by nature, as will be illustrated in the next Chapter.

Trp and metallo-porphyrin constitute the key natural chromophore molecules for the non-invasive spectroscopic investigation of complex biological systems as haemoproteins. In Chapter 7, we follow relaxation dynamics of photo-excited Tryptophan and Haem (Fe-porphyrin) in ferro- and ferricytochrome c and in Myoglobin in its met form. In the former protein, an ultrafast energy transfer from Tryptophan to Heme is evidenced, the efficiency of which is found to depend on the oxidation state. The energetic relaxation pathway of the haem, also dependent on the oxidation state, is characterized by a porphyrin to metal charge transfer that triggers the ligand dissociation. In metMyoglobin, the fluorescence contribution of the two Tryptophans (W14 and W7), also quenched by resonant energy transfer to the haem, are temporally and spectrally separated, and the solvation dynamics of W7, located in the water-protein interface, is followed. The haem of metMb, which is in the ferric form, shows an electronic relaxation similar to that of ferricytochrome c.

In parallel to the biology oriented investigations presented above, we extended our study to the metal-polypyridine complexes. Due to their specific photophysics, mainly characterized by a photo-induced Metal-to-Ligand Charge Transfer (MLCT), they are extensively used in photochemical applications involving charge transfer dynamics. In particular, they are used as sensitizer in the Dye-Sensitized-Solar-Cells (DSSCs). In Chapter 8, we present studies of these dyes, both in solution and adsorbed on a substrate, in order to understand the role of intra- and intermolecular dynamics on the electron injection process occurring upon absorption of light. Finally, Chapter 9 summarizes the conclusions of the investigations of the various systems studied.

Keywords: ultrafast optical spectroscopy, femtosecond laser pulse, fluorescence up-conversion, solvation dynamics, IVR, cooling dynamics, protein dynamics, energy transfer, 2,5-diphenyloxazole, para-terphenyl, Tryptophan, Cytochrome c, Myoglobin, [Ru(bpy)₃]²⁺, RuN719.

Résumé

Une grande variété de processus physico-chimique au niveau moléculaire, comme la solvatation, le transfert d'énergie ou de charge ou encore les relaxations électronique et vibrationnelle est à l'origine du fonctionnement des protéines. Le travail présenté dans cette thèse est dédié à l'étude de ces dynamiques moléculaires dans différents chromophores. Plus spécifiquement, cette étude tend à faire le lien entre ces dynamiques et les photophysique et photochimie ultrarapide des hémoprotéines. Cette classe importante de protéines est au cœur de nombreuses études, menées à l'aide de diverses techniques spectroscopiques, afin de mieux comprendre leur fonctionnement. En outre, ces protéines contiennent plusieurs chromophores, dont un acide aminé en particulier, le Tryptophane ainsi que le groupement prosthétique qu'est l'hème. Ces deux molécules nous sont d'un intérêt particulier pour ce travail : alors que le Tryptophane est utilisé en tant que sonde de l'environnement local dans la protéine, à travers les dynamiques de relaxation intermoléculaires (solvatation), nous avons étudié comment les dynamiques intramoléculaires de l'hème s'intègrent dans le fonctionnement de la protéine.

Alors que diverses techniques de spectroscopie ultrarapide sont indiquées pour ce genre d'études, comme les expériences de pompe-sonde ou d'écho de photon, nous avons choisi une approche différente, permettant de suivre directement la relaxation énergétique d'un chromophore. Cette approche consiste à observer les changements ultrarapides du spectre de photoluminescence. Les dynamiques sont alors déduites de l'évolution spectrale de l'émission. Dans ce but, nous avons réalisé une expérience de conversion de fluorescence permettant de résoudre en temps et en fréquence la photoluminescence d'un échantillon, avec une résolution atteignant l'échelle de la femtoseconde.

Cette thèse se structure en 9 chapitres. Dans le premier chapitre, nous résumons la théorie nécessaire pour l'interprétation des résultats présentés. Dans le deuxième chapitre, nous décrivons la photophysique des divers systèmes chimiques étudiés. Dans le troisième chapitre, nous présentons le principe de fonctionnement d'une expérience de conversion de fluorescence, ainsi que les caractéristiques particulières du montage expérimental utilisé lors de ce travail.

Dans le quatrième chapitre, nous présentons l'étude de deux colorants UV, menée en vue de tester les capacités de notre montage ainsi que de nous familiariser avec certains concepts importants dans l'étude de la fluorescence à des temps ultrarapides, comme l'effet des dynamiques vibrationnelle et structurelle ou de la température sur le spectre de fluorescence aux temps courts. Ces mesures ont révélé un enchevêtrement subtil de plusieurs processus de relaxation et démontrent l'acuité nécessaire à l'étude envisagée dans ce travail.

Le cinquième chapitre porte sur les dynamiques de relaxation du Tryptophane dans l'eau. Cet acide aminé, grâce à son fort moment dipolaire à l'état excité, sert de sonde de la dynamique de solvatation de l'eau. Notre étude, basée sur des résultats expérimentaux ainsi qu'une simulation de dynamique moléculaire, se focalise sur la réorganisation des

molécules d'eau autour du chromophore et la distinction entre ce processus important et la relaxation électronique intramoléculaire, qui se déroule sur une même échelle de temps.

Dans le cadre de l'étude des dynamiques des protéines, le chapitre 6 rapporte l'étude des porphyrines, une famille de molécules fréquemment rencontrées dans la nature. Dans ces systèmes moléculaires, un scénario complexe de relaxations intramoléculaires prend place. Afin de clarifier ce dernier, une étude systématique des formes protonée et métallique de la porphyrine a été menée. Nous avons pu finalement élaborer un descriptif de ces relaxations, incluant l'influence de métal et des substituants. Ces mécanismes de relaxation constituent les principales propriétés photophysiques de l'hème, utilisées par la nature, comme le sera illustré dans le prochain chapitre.

Le Tryptophane et les porphyrines métalliques constituent les chromophores clés dans l'étude spectroscopique non-invasive de systèmes biologiques plus larges et plus complexes que sont les hémoprotéines. Dans le septième chapitre, nous présentons les dynamiques de relaxations du Tryptophane et de l'hème du Cytochrome c dans l'état ferreux et ferrique, ainsi que de la myoglobine dans sa forme oxydée. Dans la première protéine, un transfert d'énergie ultrarapide entre le Tryptophane et l'hème est mis à jour, l'efficacité duquel dépend de l'état d'oxydation. La relaxation énergétique de l'hème, dépendant aussi de l'état d'oxydation, est caractérisée par un transfert d'électron de l'anneau de la porphyrin au métal, déclenchant la dissociation du ligand. Dans le cas de la metmyoglobine, les contributions des deux Tryptophane (W7 et W14) à la fluorescence, inhibée par transfert d'énergie à l'hème, est séparée en fréquence et en temps. La dynamique de solvation du Tryptophane W7, localisé sur l'interface protéine-eau, est observée. L'hème de la metmyoglobine, qui est à l'état oxydé, montre une relaxation électronique similaire à celle du cytochrome c dans le même état d'oxydation.

En parallèle à cette étude dédiée aux systèmes biologiques, nous avons étendu notre champ d'investigation aux complexes métallo-polypyridiniques. Grâce à leur photophysique particulière, principalement caractérisée par un transfert de charge photo-induit, ces composés sont fréquemment utilisés pour des applications impliquant des dynamiques de transfert de charge. En particulier ils sont utilisés comme sensibilisateur dans les cellules solaires à colorant. Dans le huitième chapitre, nous présentons des études en solution et sur substrat de ces colorants, dans le but de comprendre le rôle des dynamiques intra- et intermoléculaires dans le processus d'injection d'électron prenant place lors d'absorption de lumière. Finalement, le chapitre 9 résume les conclusions des études menées lors de ce travail et présente les diverses perspectives.

Mots clés: *spéctroscopie optique ultrarapide, pulse laser femtoseconde, conversion de fluorescence, dynamique de solvation, redistribution vibrationnelle interne, dynamique de refroidissement, dynamique des protéines, transfert d'énergie, 2,5-diphenyloxazole, paraterphenyl, Tryptophane, Cytochrome c, Myoglobine, [Ru(bpy)₃]²⁺, RuN719.*

Chapter 1

Basic Concepts

1.1 Optical spectroscopy

1.1.1 Einstein coefficients

1.1.2 Transition dipole moment

1.1.3 Absorption

1.1.4 Lifetime and Quantum Yield

1.1.5 Absorption, Emission spectra and Stokes Shift

1.2 Molecular Dynamics

1.2.1 Vibrational Relaxation

1.2.2 Electronic solvation dynamics

Absorption of light can induce a great variety of phenomena such as light emission, thermal heating, free charge generation and structural modification. Focusing to the microscopic level, these phenomena correspond to different ways how a photo-excited molecule can relax to its energetically lowest state. Figure 1.1 summarizes these processes in a so-called Jablonski diagram. Beside the radiative transitions (fluorescence and phosphorescence), the isoenergetic interstate transitions of internal conversion (IC) and intersystem crossing (ISC) are followed by vibrational relaxation (VR), during which energy is converted into heat. These different intramolecular relaxation mechanisms and their dynamics are dramatically affected by interactions of the chromophore with its environment. This chapter is aimed at reviewing the basic concepts of molecule photophysics, and in particular those phenomena of significant relevance for this work, i.e. ultrafast intra- and intermolecular dynamics.

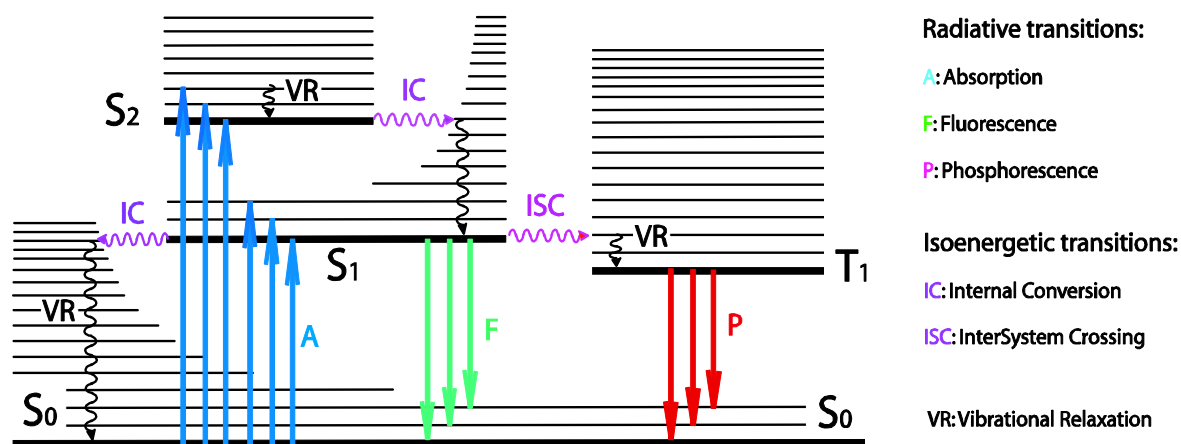


Figure 1.1 : Jablonski diagram resuming the possible intramolecular processes (electronic and vibrational relaxation) following light absorption. The different processes are divided into horizontal (isoenergetic) and vertical (with energy exchange) transitions. Despite non explicitly shown, each of these process are usually accompanied by configurational changes of the molecule.

1.1 Optical spectroscopy

1.1.1 Einstein coefficients

In the following we describe how a two-level -atom like- system interacts with an electromagnetic field. This is the simplest system, where no nuclear motion is included. These degrees of freedom will be included in the next paragraph. The two-level system is formed by S_0 , the ground and S_1 the excited electronic states of energy E_0 and E_1 , respectively. A strong interaction occurs when the frequency of an incident oscillating electromagnetic field (light radiation) is in resonance with the energy gap ΔE between these two states. In 1900, laying the foundation of quantum mechanics, Max Planck introduced the constant h to relate frequency ν and energy:

$$\Delta E = E_1 - E_0 = h\nu \quad (1.1)$$

The interaction of this system with the electromagnetic perturbation can lead to three different processes: absorption, stimulated and spontaneous emission. The phenomenological treatment of such processes was proposed by Einstein, describing the probability W of absorption and emission by introduction of the corresponding Einstein coefficient:

$$\begin{aligned} W_{1\leftarrow 0} &= B_{01}\rho(\nu) \\ W_{1\rightarrow 0} &= B_{10}\rho(\nu) \\ W_{1\rightarrow 0}^{spont} &= A_{10} \end{aligned} \quad (1.2)$$

B_{01} , B_{10} and A_{10} are respectively the absorption, stimulated and spontaneous emission Einstein coefficients, and $\rho(\nu)$ is the energy density of incident radiation, at the transition frequency. The electromagnetic interaction coupling the two-level system and the light radiation is expressed by the following hamiltonian:

$$H = -\hat{\boldsymbol{\mu}} \cdot \boldsymbol{E} \quad (1.3)$$

where \boldsymbol{E} is the electric field and $\hat{\boldsymbol{\mu}}$ is the electric dipole operator. From a time independent perturbation treatment we can express the Einstein coefficients in terms of off-diagonal elements of this operator:²

$$B_{01} = B_{10} = \frac{|\mu_{10}|^2}{6\varepsilon_0\hbar^2} \quad \text{and} \quad A_{10} = \frac{8\pi h\nu_{10}^3}{c^3} B_{10} \quad (1.4)$$

where ε_0 is the vacuum permittivity, \hbar is the reduced Planck constant and $\boldsymbol{\mu}_{10}$ is the transition dipole moment:

$$\boldsymbol{\mu}_{10} = \int \psi_1^* \boldsymbol{\mu} \psi_0 \quad (1.5)$$

where ψ_0 and ψ_1 are the electronic wavefunctions of S_0 and S_1 respectively. This is at the base of the optical selection rules described in the next §.

1.1.2 Transition dipole moment

Due to the great difference in their masses, the motion of electrons is typically a few order of magnitude faster than the nuclei motion. Assuming the configuration corresponding to the instantaneous position of the nuclei, neglecting any terms related to the nuclei speed (adiabatic approximation), the total eigenfunction $\psi(\mathbf{r}, \mathbf{R})$ of a molecular system, which depends on the electronic (\mathbf{r}) and nuclear (\mathbf{R}) coordinates, can be factorized into electronic $\varphi_{es}(\mathbf{r}, \mathbf{R})$ and vibrational $\varphi_v(\mathbf{R})$ wave functions (Born-Oppenheimer approximation):

$$|i\rangle = \psi^i(\mathbf{r}, \mathbf{R}) = \varphi_{es}^i(\mathbf{r}, \mathbf{R}) \varphi_v^i(\mathbf{R}) \quad (1.6)$$

$$|f\rangle = \psi^f(\mathbf{r}, \mathbf{R}) = \varphi_{es}^f(\mathbf{r}, \mathbf{R}) \varphi_v^f(\mathbf{R}) \quad (1.7)$$

where φ_{es} , which describe also the spin states, is parameterized with the instantaneous position of the nuclei. Now we can, at least formally, calculate the transition dipole moment $\boldsymbol{\mu}_{fi}$ and disentangle the contributions of electronic and vibrational terms to the probability of a transition between an initial $|i\rangle$ and a final $|f\rangle$ state:

$$\boldsymbol{\mu}_{fi} = \langle i | \hat{\boldsymbol{\mu}} | f \rangle \quad (1.8)$$

where $\boldsymbol{\mu} = -\sum_i e \cdot \mathbf{r}_i + \sum_j Ze \cdot \mathbf{R}_j$ is the electric dipole moment operator, with e the elementary charge, Z the atomic number and \mathbf{r}_i and \mathbf{R}_j being the position of the i th electron and j th nucleus, respectively. This transition dipole moment can be regarded as a transient dipole resulting from the rearrangement of charge distribution in the molecule occurring during the transition.

We are dealing with an electronic excitation, which occur on the timescale of electron motion (attosecond). With the same arguments of adiabatic approximation, we can consider that nuclei positions immediately before and after the excitation are the same. Since electrons are 1000 times lighter than nuclei, any velocity change of the former will not

affect the velocity of the latter. The assumption of identical nuclear position and velocity is the essence of the Franck-Condon (FC) principle, and the electronic transition is said to be “vertical”. Accordingly, the transition dipole moment (**Error! Reference source not found.** and **Error! Reference source not found.**) can be developed in a product of three terms:

$$\boldsymbol{\mu}_{fi} = \int \psi^{f*} \hat{\boldsymbol{\mu}} \psi^i d\tau, \quad d\tau = drd\mathbf{R} \quad (1.9)$$

$$\begin{aligned} \boldsymbol{\mu}_{fi} &= \int \varphi_{es}^{f*} \varphi_v^{f*} (\hat{\boldsymbol{\mu}}_n + \hat{\boldsymbol{\mu}}_e) \varphi_{es}^i \varphi_v^i d\tau = \int \varphi_{es}^{f*} \varphi_v^{f*} \hat{\boldsymbol{\mu}}_n \varphi_{es}^i \varphi_v^i d\tau + \int \varphi_{es}^{f*} \varphi_v^{f*} \hat{\boldsymbol{\mu}}_e \varphi_{es}^i \varphi_v^i d\tau \\ \boldsymbol{\mu}_{fi} &= \underbrace{\int \varphi_{es}^{f*} \varphi_{es}^i dr}_{=0} \cdot \int \varphi_v^{f*} \hat{\boldsymbol{\mu}}_n \varphi_v^i d\mathbf{R} + \int \varphi_v^{f*} \varphi_v^i d\mathbf{R} \cdot \int \varphi_{es}^{f*} \hat{\boldsymbol{\mu}}_e \varphi_{es}^i dr \\ \boldsymbol{\mu}_{fi} &= \int \varphi_v^{f*} \varphi_v^i d\mathbf{R} \cdot \int \varphi_e^{f*} \hat{\boldsymbol{\mu}}_e \varphi_e^i dr \cdot \int \varphi_s^{f*} \varphi_s^i d\tau_s \end{aligned} \quad (1.10)$$

The first term is the Franck-Condon integral, the second is the molecular orbital overlap and the third reflects the spin contribution. These terms lead to the selection rules of a vibrational-electronic transition.³ The orbital and vibrations symmetry and spin multiplicity are thus the fundamental aspects one has to consider to know if a transition is allowed or forbidden.

1.1.3 Absorption

The absorption of light by a medium at a given wavelength λ is experimentally characterized by the absorbance $A(\lambda)$ (transmittance $T(\lambda)$) defined as follows:^{4,5}

$$A(\lambda) = \log\left(\frac{I_\lambda^0}{I_\lambda}\right) = -\log T(\lambda) \quad \left(T(\lambda) = \frac{I_\lambda}{I_\lambda^0}\right) \quad (1.11)$$

where I_λ^0 and I_λ are respectively the incident and transmitted beam intensities. In the weak field approximation, the absorbance is proportional to the photon flux I_λ and the Beer's law expresses the proportionality of the absorbance to the concentration:

$$A(\lambda) = \varepsilon(\lambda) \ell c \quad (1.12)$$

where $\varepsilon(\lambda)$ is the molar extinction coefficient [$\text{M}^{-1}\text{cm}^{-1}$], c the concentration [M] of solute and ℓ the absorbing medium thickness [cm]. The molar extinction coefficient $\varepsilon(\lambda)$ is a direct measurement of the light absorbing efficiency of the solute in a specific solvent and gives direct access to the oscillator strength and the spontaneous emission coefficient:

$$f = \left(\frac{4\pi m_e \nu_{fi}}{3e^2 \hbar}\right) |\boldsymbol{\mu}_{fi}|^2 = \left(\frac{4m_e c \varepsilon_0}{N_A e^2}\right) \int \varepsilon(\nu) d\nu = \left(\frac{m_e \varepsilon_0 c^3}{\pi e^2 \nu_{fi}^2}\right) A_{fi} \quad (1.13)$$

where m_e is the electron mass, c the speed of light, N_A Avogadro number, μ_{fi} and ν_{fi} the transition dipole moment and corresponding frequency. The spontaneous emission coefficient A_{fi} corresponds to the rate of radiative deactivation of the excited state k_r^S also expressed as the natural lifetime of emission $\tau_r = (k_r^S)^{-1}$. This lifetime is intrinsically related to the homogenous contribution of the spectral bandwidth of the transition.

1.1.4 Lifetime and Quantum Yield

While the process of photon emission through the $S_1 \rightarrow S_0$ transition is as fast as the absorption one, i.e. < 1 fs, the probability of this radiative transition to occur is typically 10^8 - 10^9 s⁻¹ (in the case of an allowed transition). On such a long timescale, other non-radiative relaxation processes can affect the lifetime of excited molecules. A population of fluorescing molecule M^* of concentration $[M^*]$, impulsively excited (excitation simulated by a Dirac function $\delta(t)$) to the S_1 state, undergoes radiative and/or non-radiative relaxation to the fundamental electronic state S_0 . A basic kinetic reasoning leads to the following differential equation and its solution:^{5,6}

$$-\frac{d[M^*]}{dt} = (k_r^S + k_{nr}^S)[M^*] \quad [M^*](t) = [M^*]_0 e^{-t/\tau_s} \quad \text{with } \tau_s = \frac{1}{k_r^S + k_{nr}^S} \quad (1.14)$$

where k_r^S and k_{nr}^S are the radiative and non-radiative $S_1 \rightarrow S_0$ de-excitation rate constants, i.e. $k_{nr}^S = k_{IC}^S + k_{ISC}^S$, the rates of IC and ISC, $[M^*]_0$ is the initial concentration of excited molecules and τ_s is the total lifetime of the S_1 state. As a consequence, the fluorescence intensity $I_F(t)$, directly proportional to the population of excited molecule at time t , decays exponentially:

$$I_F(t) = k_r^S \times [M^*](t) = k_r^S [M^*]_0 e^{-t/\tau_s} \quad (1.15)$$

In time-resolved linear spectroscopic techniques and more specifically in the case of time-gated fluorescence, almost all kinetics observed are characterized by exponential decay behavior since we are dealing with temporal evolution of populations obeying to first order rate equations.

The emission quantum yield (QY) Φ is defined as the fraction of excited molecules which relaxes radiatively to the ground electronic state. The fluorescence QY is expressed as a function of the rate constants, or lifetimes as follows:

$$\Phi_F = \frac{k_r^S}{k_r^S + k_{nr}^S} = k_r^S \tau_S = \frac{\tau_S}{\tau_r} \quad (1.16)$$

In continuous wave (c.w.) measurements, the quantum yield is easily accessible since it corresponds to the ratio between the total number of emitted photons, i.e. the intensity integrated over time, to the number of molecules initially in the emitting state $[M^*]_0$, as can be easily found by time integration of eq. (1.15):

$$\Phi_F = \frac{I_{cw}(\nu)}{[M^*]_0} = \frac{1}{[M^*]_0} \int_0^\infty I(\nu, t) dt \quad (1.17)$$

This emission QY is a direct indicator of emission quenching mechanisms, due to opening of new de-excitation channels. Conversely, time-resolved measurements give access to the spontaneous emission coefficient by spectrally integrating the intensity at $t = 0$:

$$A_{fi} = k_r^S = \frac{1}{[M^*]_0} \int I(\nu, 0) d\nu \quad (1.18)$$

1.1.5 Absorption, Emission spectra and Stokes Shift

The electronic absorption and emission spectra contain contributions from vibrational and rotational transitions. However, the rotational fine structure of polyatomic molecules in condensed phases cannot be resolved and it is ignored here. In the solution phase, even low frequency vibrational mode are smeared out by inhomogenous broadening and only high frequency modes may show up in electronic spectra.

In the harmonic approximation (small nuclear motion around a local minimum), it is possible to find a set of normal coordinates \mathbf{Q} related to the Cartesian coordinates \mathbf{R} of the n nuclei, which factorizes the vibrational wave function (eqs (1.6) and (1.7)) as a product of $3n-6$ harmonic oscillator eigenfunctions, n being the number of atoms constituting the molecule. It is then possible to project the multidimensional electronic potential surface on a particular normal coordinate \mathbf{Q} among the $3n-6$ vibrations. The shape of the corresponding potential well strongly depends on the nature of the vibration. An electronic transition is represented as a jump between two such potential wells. The shape and position of the excited electronic potential may be different from the ground state one. The case of a similar curvature (linear coupling approximation) but different equilibrium nuclear position is shown on Figure 1.2. The structure of the spectrum is directly given by the Franck-Condon factor

$$\mathcal{M}_{if} = \int \varphi_v^{f*}(\mathbf{Q}) \varphi_v^i(\mathbf{Q}) d\mathbf{Q} \quad (1.19)$$

corresponding to the first factor in eq. (1.9). In the ideal case of parabolic potential energy curves, which is a first order approximation of a more realistic Morse potential, the vibrational wave function are the solutions of the quantum harmonic oscillator φ_v , associated to the eigenvalue E_v

$$\varphi_v = N_v H_v(Q) e^{-Q^2/2} \quad (1.20)$$

$$E_v = h\nu \left(v + \frac{1}{2} \right) \quad (1.21)$$

where N_v is a normalization factor, H_v is the v th Hermite polynomial. The vibrational energy levels are represented by horizontal lines over the potential well in Figure 1.2. For $0 \rightarrow v$ transitions, the overlap integral and thus the transition probability become

$$\mathcal{M}_{0v} = N_0 N_v \int_{-\infty}^{+\infty} H_0(q) H_v(q + \xi) e^{-q^2/2} e^{-(q+\xi)^2/2} dq \quad \text{and} \quad \mathcal{M}_{0v}^2 = e^{-\xi^2/2} \left(\frac{\xi^2}{2} \right)^v \frac{1}{v!} \quad (1.22)$$

where ξ is the displacement between the two potential curves. As eq. (1.22) shows, the absorption and emission spectra are characterized by a Poisson distribution. Figure 1.2 illustrates the link between the overlap of the initial and final wavefunctions and the electronic spectrum. In this picture, the 0-0 transition (zero-phonon-line), corresponds to the axis of the mirror image symmetry between absorption and emission spectra, observed when the curvatures of both potential energy curves are similar. The energy spacing between the vibronic transitions corresponds to the vibration frequency. An inhomogenous broadening of the individual bands is simulated by convolution of the resulting spectrum with a Gaussian. In principle, more than one vibrational mode may be coupled with the electronic transition and the resulting spectrum is a product of the Franck-Condon factors associated with each FC-active vibrational normal mode:

$$\varphi_v(\mathbf{Q}) = \prod_{i=1}^N \varphi_v^i(\mathbf{Q}_i) \quad (1.23)$$

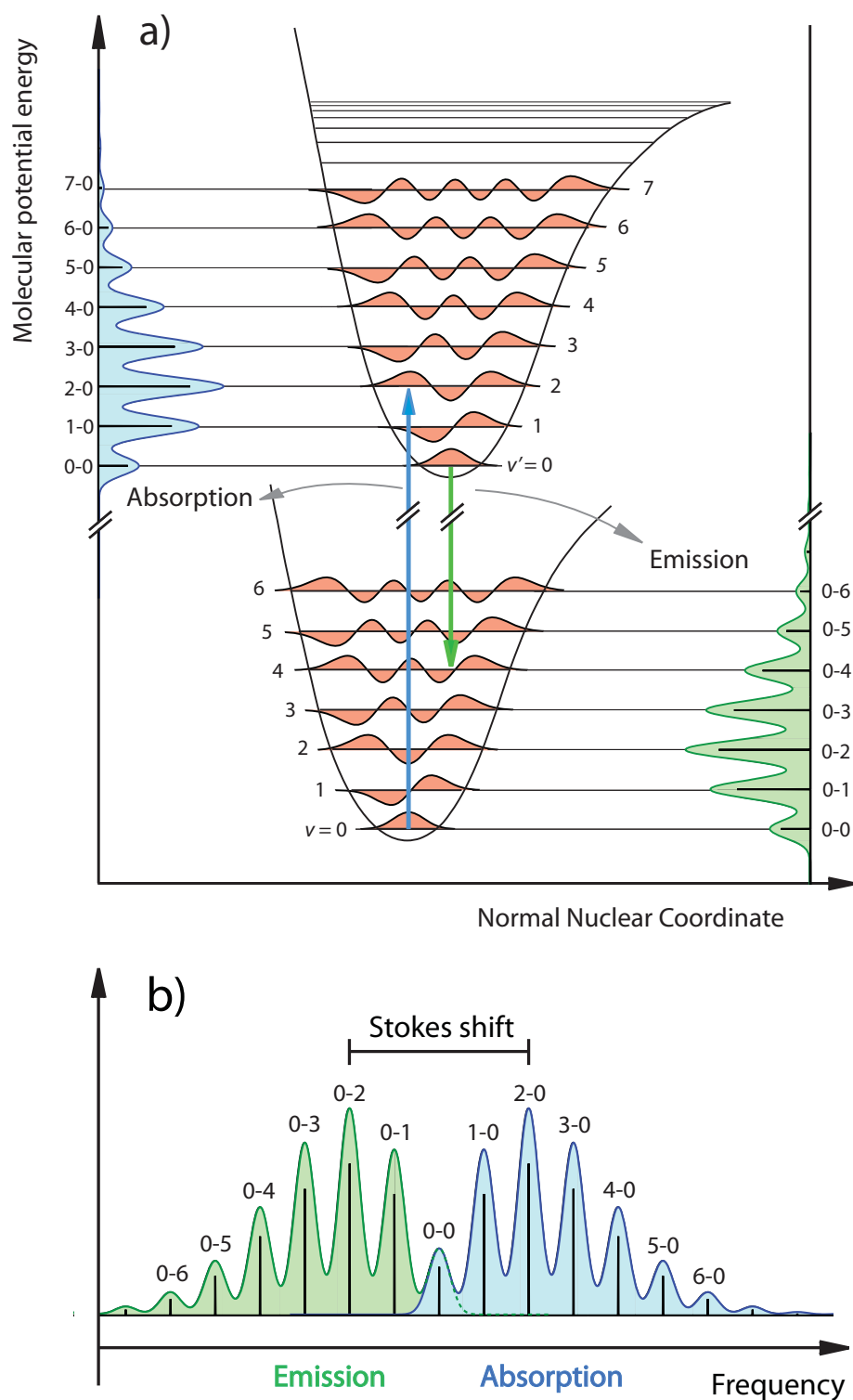


Figure 1.2: A) Schematic illustration of an electronic transition, showing vibronic transitions probability (FC factor) to higher energy than the pure electronic 0-0 line. The vertical arrows shows the Franck-Condon transition with maximum probability in absorption (blue) and emission (green). B) Corresponding graph of absorption and emission as a function of energy (frequency). The distance between the two maxima represent the total intramolecular Stokes shift.

Kasha's rule states that "the emitting level of a given multiplicity is the lowest level of that multiplicity."^{7,8} In fact, even if in some cases the IC rate is low enough to observe emission from a higher excited electronic state in static measurements, the vibrational relaxation is far too fast to measure "hot" emission, i.e. emission stemming from higher vibrational levels than $\nu' = 0$. Nevertheless, such emission may occur in the femtosecond/picosecond timescale (§1.2.1). According to the Franck-Condon principle, this emission has a spectrum different from the Poisson distribution (eq. (1.22)). Nevertheless, it can be easily calculated in the linear coupling approximation with eq. (1.19).

Stokes shift

The Stokes shift (SS) ΔE_∞ is defined as the energy difference between the maxima of the absorption (ν_{max}^{abs}) and emission (ν_{max}^{em}) bands:^{5,6}

$$\Delta E_\infty = \nu_{max}^{abs} - \nu_{max}^{em} \quad (1.24)$$

In the gas phase, the Stokes shift corresponds to the loss of vibrational energy, occurring before emission (Figure 1.2B), i.e. the difference between the blue and green arrows of Figure 1.2A. In the liquid phase, the presence of the solvent also contributes to the SS through electrostatic (polar) and at a minor extend sterical (nonpolar) solute-solvent interactions. The origin of this contribution lies in a different solute-solvent interaction and thus stabilization of the ground and excited states, implying a change in the transition energy. On the contrary of the intramolecular SS, it modulates the energy gap (0-0 line) by inducing a vertical shift of the ground and excited potential energy surface. The solvent-related contribution to the Stokes shift can be determined by the energy difference between the 0-0 line of absorption and emission bands. In practice, it is very difficult to estimate it since the related broadening does usually not allow a clear distinction of the 0-0 lines. Finally, the total Stokes shift ΔE_∞ is the sum of the purely vibrational ΔE_∞^V and solvation ΔE_∞^S shifts:

$$\Delta E_\infty = \Delta E_\infty^V + \Delta E_\infty^S \quad (1.25)$$

While the stationary measurement of ΔE_∞ brings important information about the solute and solvent physical properties,⁶ time-resolving the Stokes shift allows us to separate the two contribution bringing further information on intra- and intermolecular dynamics.

Solvatochromism

In liquid phase, the proximity of the solvent molecule with the solute implies a strong electrostatic and to a lower extent, steric interactions. These interactions strongly depend on the geometric and electronic properties of solvent and solute molecules.⁹ The major solute-solvent interactions are the permanent dipole-dipole and dipole-induced-dipole interactions. When a chromophore exhibits a different permanent dipole in the ground (μ_g) and excited (μ_e) states, the different stabilization energy with the surrounding solvent molecules induces a change in the energy gap. Solvatochromism characterizes the solvent-dependent shift observed in static absorption and emission spectra. Since Onsager,¹⁰ several continuum electrostatic descriptions of this effect have been developed, as a function of the dielectric constant (nuclear relaxation) and refractive index (electronic relaxation) of the solvent.^{11,12} In the frame of the reaction field theory of Onsager and for a solute geometry simulated by an effective spherical cavity of radius a ,¹⁰ the magnitude of the solvent contribution to the Stokes shift is given by:

$$\Delta E_{\infty}^S = \left(\frac{2}{hca^3} \right) |\mu_e - \mu_g|^2 \left(\frac{\varepsilon - 1}{2\varepsilon + 1} - \frac{n^2 - 1}{2n^2 + 1} \right) \quad (1.26)$$

where ε is the dielectric constant of the solvent and n its refractive index. This quantity has been extensively used to estimate the permanent dipole moment of the excited state of various chromophores molecules.¹³ However, one should be aware that the ability of the solute to form hydrogen bonding will further affect its solvatochromic property.¹⁴ In parallel, the statistical distribution of different solvent environments (fluctuating among different configurations) induces a spread of the transition frequency. Assuming harmonic potential curves of identical curvature in the ground and excited states, one can also derive the solvent-dependent contribution to the spectral width, described by a gaussian of variance σ^2 .^{15,16}

$$\sigma^2 = \left(\frac{k_B T}{hc} \right) \Delta E_{\infty}^S \quad (1.27)$$

1.2 Molecular dynamics

1.2.1 Vibrational Relaxation

Upon vibronic excitation, a large excess of vibrational energy ΔE_{∞}^V is deposited in the molecule. This section aims at explaining how and where this energy is dissipated. In the liquid phase, the vibrational energy dissipation proceeds as a sequence of two mechanisms. The first step is intramolecular: molecule undergoes Internal Vibrational Redistribution (IVR), followed by the second, intermolecular process of vibrational energy transfer (VET) to the solvent.¹⁷ The vibrational relaxation constitutes the first contribution to the Stokes shift and understanding its characteristic timescales is important to distinguish it from the solvation contribution.

Intramolecular vibrational Redistribution

In the classical mechanical view of a molecular structure, one can picture a molecule as a set of balls (atoms) linked together by springs (chemical bonds). If one particular spring is displaced from its equilibrium by stretching or compressing it (or even bending it), the following induced vibration will not stay localized on the bond, but will rather spread over the whole ball and spring network. While this intuitive picture is often used to illustrate the mechanism of IVR, the full description of the latter is more subtle and needs the introduction of the concept of anharmonicity.¹⁸⁻²⁰

In the quantum description of a molecule, vibrations are described by an orthonormal basis of eigenstates $\{\psi_i\}$, solutions of a first approximation molecular Hamiltonian (harmonic oscillator). However, this is only an approximation and in reality the existence of anharmonic terms in the expression of the potential energy makes different normal modes to be coupled (off diagonal terms in the matrix potential). The mixing of an initially excited vibrational mode with other normal modes by anharmonic interaction constitutes the relaxation channels of IVR. When a high frequency mode is excited, it will rapidly split into few quanta of a lower frequency mode. The probability of this transition decreases with the number of quanta required for a given low frequency mode. However, the probability to leave the initial bright excited state increases with the density of lower frequency mode available. Moreover, the coupling strength increases as we go higher in vibrational energy, since anharmonicity will be more pronounced.

Two extreme situations can be distinguished, depending on the density of background states to which the initial bright state is coupled. If this density is very low, the system oscillates between few states and undergoes a reversible IVR.²⁰⁻²³ In this case, the population of the initially excited state can be partially recovered, after a defined revival time, forming a coherent wavepacket. On the other hand, if this density of states is high and forms a continuum uniformly coupled with the excited bright state, the excited energy quickly spread over a large ensemble of states. The system is said to undergo an irreversible, statistical IVR. In this situation, the population of the initially prepared bright state decays exponentially with the following rate, given by the Fermi Golden Rule expression:

$$\Gamma = 2\pi \langle V^2 \rangle \rho \quad (1.28)$$

where $\langle V^2 \rangle$ is the root mean square coupling element and ρ is the average density of states. Between these two situations, lies the irreversible non-statistical IVR, for which one or more sub-group of states (often called doorway states) are more coupled to the initially excited state than others. In this case, one speaks of a hierarchical IVR mechanism, during which the vibrational energy is sequentially redistributed from one tier to the other, as illustrated in Figure 1.4. The IVR mechanism is usually described by such an intermediate behavior, being closer to one or the other extreme situation depending on the molecular structure. As a consequence, different coupling strengths between each class of vibrational modes leads to multimodal decay of the autocorrelation function, spanning a large temporal range (from few picoseconds to 100s of nanosecond in the gas phase).

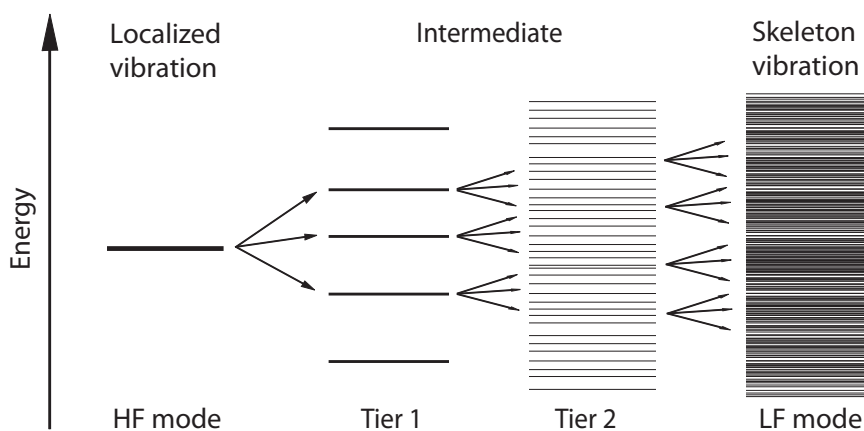


Figure 1.4: Schematic illustration of IVR mechanism: the intermediate dark states are sorted into tiers by their coupling strength with the initial bright state (high frequency (HF) mode).

Considering one particular molecule, the IVR rate is often seen to increase with increasing vibrational excitation energy.^{20,24} This effect is due to the increase of density of states going towards the high vibrational energy region and to the stronger influence of anharmonicity in this region. Such studies have strengthened the idea that increasing the available density of states will make the IVR to behave more statistically. However, probing different molecules with similar density of states does not confirm this rule, and several contradicting examples hold.^{19,25,26} Several alternative models involving van der Waals interactions, mode specificity, presence of heavy atoms and molecular flexibility were developed in a way to rationalize the trends observed in the various experimental works.¹⁸ The inability to provide a global description of IVR has restricted these studies to case by case considerations. For instance, a study on three basic aromatic molecules (benzene, pyrrole and triazine) has shown different behaviors despite similar sizes and densities of states.²⁷

The experimental study of IVR has mainly been performed in the frequency-domain, using high resolution IR spectroscopy to extract information from the spectral line shape.²⁸ As a consequence, most of the reported works have been achieved with a molecular beam to remove the Doppler, collision and temperature effects on the bandwidth. The extension of these numerous gas phase studies to the liquid phase only started the last two decades with the use of time-domain spectroscopic techniques. Most of these studies were performed by pump-probe experiments, where a near IR laser pulse deposits a certain amount of energy in a specific bright mode of the ground electronic state while a subsequent UV probe pulse monitor the transient changes in the electronic absorption. This technique applied to small molecules in the gas and liquid phases has revealed an enhancement of the IVR relaxation in solution, but was not able to clearly highlight the origin of the solvent effect.²⁹⁻³³ However, the IVR mechanisms are believed to be unchanged by the presence of surrounding solvent molecules.³⁴ The use of supercritical fluids as density-monitored environment brought new insights into the role of solvent on IVR.^{35,36} In particular the work of von Bente *et al.*³⁷ on the benchmark molecule of benzene and some derivatives, shed light on the role of a dense environment. The IVR enhancement was shown to have its origin in the collisions with the bath of solvent molecules, but in a different manner than is the VET (see next §). Indeed, von Bente *et al.* excluded that strong collisions with back and forth energy exchange are at the origin of the IVR acceleration in the liquid phase. The

latter being rather due to the fact that “collision induced broadening of vibrational state energy levels reduces the energy gaps and enhances existing couplings between tiers.”³⁷ Therefore, if the amount of energy ΔE exchanged in a collision affects the VET rate, it seems that it does not play a crucial role for IVR. Conversely, the frequency of weak collisions between the solute and solvent molecule seems to influence the IVR efficiency.

The intramolecular vibrational energy relaxation of large dye molecules in solution has most often been seen to occur on a sub-picosecond timescale.³⁸⁻⁴⁵ In some recurrent cases, this relaxation can even not be followed, because of time resolution limits, i.e. it occurs on timescales < 100 fs.⁴⁶⁻⁵³ On the contrary, other chromophore molecules show entangled intra- and intermolecular vibrational energy redistribution ranging from hundreds of femtoseconds to a few picoseconds, as is the case of perylene.⁵⁴⁻⁵⁶

In summary, after excitation of a vibronic transition of a chromophore, the vibrational energy ΔE_{∞}^V stored in the Franck-Condon active modes is redistributed through anharmonic coupling among the bath of other (dark or bright) vibrational modes. The excited state population finally forms a canonical ensemble, allowing us to define a molecular temperature (Boltzmann distribution of the low frequency vibrational levels). It is usually assumed that during this step the internal energy of the molecule is conserved, i.e. no energy transfer to the surrounding occurs. As a consequence, once IVR has occurred, we can define a molecular temperature which is different from that of the solvent.

Vibrational Energy Transfer

After IVR, the “hot” molecule will undergo thermal equilibration with its environment. The intermolecular vibrational energy transfer to the closest solvent molecules can be thought in a similar way as IVR mechanism, where solvent molecules constitute a new bath of vibrational degree of freedom. Therefore, an important factor influencing the VET mechanism is the density of states of the surrounding solvent.⁴¹ Another more classical approach consists in considering the frequency of collisions with neighboring molecules, as well as the average amount of energy transferred per collision as the main factor monitoring the VET rate.³⁷ After this first transfer of energy at the solute-solvent “interface”, a successive energy transport towards the bulk takes place between solvent molecules. This last step is usually described by considering the solvent molecules as a continuum, with the use of classical heat conduction model, involving transport properties

of the solvent as the thermal diffusivity k .^{57,58} The local heat flux \bar{Q} follows a diffusion-type equation:

$$\frac{\partial \bar{Q}}{\partial t} = k \nabla^2 T \quad (1.29)$$

As a consequence the cooling rate is dependent on the temperature gradient, itself time dependent, such that this process is highly nonexponential. Moreover, this rate also depends on the initial temperature, i.e. on the internal energy of the molecule which is given by the excess vibrational energy provided to the molecule during the excitation. The typical time constants observed for the cooling dynamics span the picosecond to hundred picoseconds timescale, depending on the nature of the environments. Consecutive of the IVR mechanism, which has for consequence a broadening of the fluorescence bands through the population of low frequency modes, the VET to the solvent will have the reverse effect, i.e. to reduce the broadening, through depopulation of these low frequency modes.

1.2.2 *Electronic solvation dynamics*

Most of the chemical and biological processes occur in liquids. The dense and dynamic natures of the liquid phase provide a favourable environment for energy exchange and thus for chemical reactions. During electronic solvation, the redistribution of charges in a photo-excited solute changes the field of forces between solute and solvent molecules, such that the latter rearrange in a new equilibrium configuration. As does IVR, this process plays a crucial role in the rates and outcomes of chemical reactions (charge/proton transfer, isomerisation, etc...). Furthermore, in the last decade the study of solvation dynamics was extended to complex systems, as micelles, nanocavities, protein layer and DNA among others, in order to understand the role of solvent on motions of longer time and spatial scales.⁵⁹⁻⁶¹ Solvation dynamics illustrates how insights into molecular dynamics at very short timescales are crucial for the understanding of slower processes.

Polar solvation dynamics

At the molecular scale, the process of polar solvation experienced by a solute chromophore can be described by a rather simple picture. The specific charge distribution of the chromophore (solute) in its ground electronic state corresponds to a given permanent dipole moment. Within thermal fluctuations, the dipoles of the surrounding solvent molecules are in an equilibrium configuration (position and orientation) with respect to the electric field generated by the solute. According to the Franck-Condon principle, upon absorption of a photon the electronic redistribution occurs in the chromophore, while the positions of the solute and solvent nuclei remain unchanged. This redistribution eventually modifies the dipole moment amplitude and orientation leading to a Franck-Condon excited state in non-equilibrium with the environment. The solvent molecules start then to relax through reorientation and rearrangement around the solute to a new equilibrium minimizing the free energy. This photocycle is depicted on Figure 1.5.

During relaxation, the amplitudes of solvent motion are assumed to be small, the rearrangement sketched in Figure 4 is exaggerated for sake of clarity. The external perturbation (solute dipole change) on the solvent is often considered small, allowing to assume a linear response of the latter which simplifies its theoretical description. While this assumption is considered valid for many perturbed solute-solvent configurations,⁶²⁻⁶⁴ it is disapproved in some cases.⁶⁵⁻⁶⁷

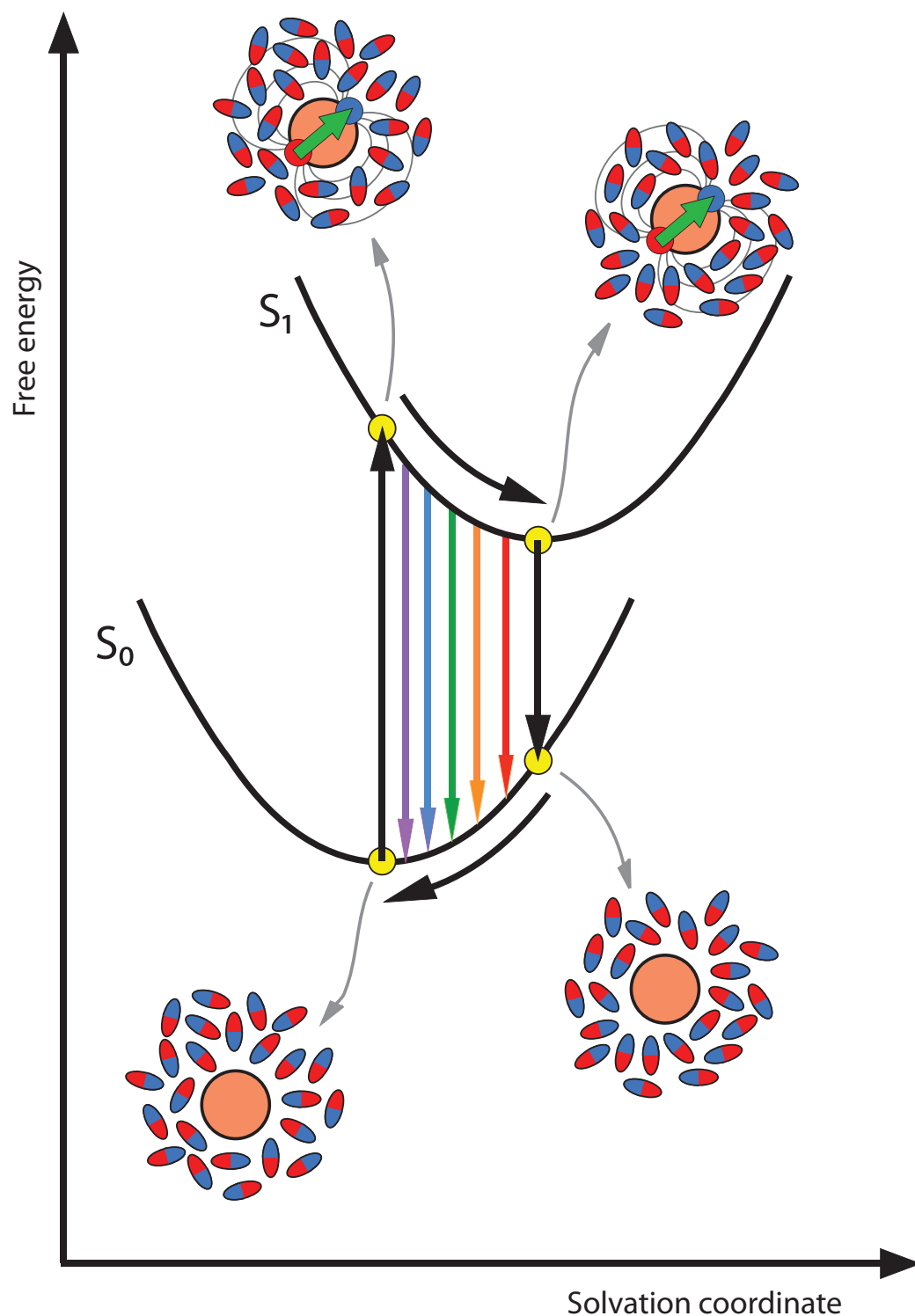


Figure 1.5: Schematic representation of polar solvation dynamics through a simplified view of the potential energy surface as a function of solvation coordinate (polar solvent reorientational motion). For simplicity, the ground state dipole moment μ_{GS} has been chosen to be null. A more general picture should consider $\Delta\mu$. After a Franck-Condon transition (yellow points), an instantaneously appearing dipole moment (green arrow) induced by a change in solute's charge distribution, changes the surrounding electric field and puts the system in a non-equilibrated position. The relaxation towards the new equilibrium implies a reduction of the energy gap between excited and ground electronic state of the chromophore, corresponding to a change in the averaged emission wavelength (colored arrows).

The solvent relaxation is described in the frame of the fluctuation-dissipation theorem,^{68,69} involving the influence of Brownian motion on the stochastic process of equilibration.^{70,71} The temporal evolution of the solvation energy $E_S(t)$ is driven by the fluctuations $\delta E_S(t)$ of the solvent, and described by the time correlation function $C_S(t)$:⁷²

$$C_S(t) = \frac{\langle \delta E_S(0) \cdot \delta E_S(t) \rangle}{\langle \delta E_S^2 \rangle} = \frac{\langle E_S(t) \rangle - \langle E_S(\infty) \rangle}{\langle E_S(0) \rangle - \langle E_S(\infty) \rangle} \quad (1.30)$$

Experimentally, the time evolution of this process can be accessed through different time-resolved spectroscopic techniques.⁷³ While the Optical Kerr Effect allows investigation of bulk liquids relaxation dynamics,⁷⁴⁻⁷⁶ The solute-solvent interactions can be studied with the Photon Echo (PE) technique.⁷⁷⁻⁷⁹ Another approach consists in following the temporal evolution of the fluorescence emission, which is the one adopted in this thesis. This simpler approach allows additionally to extract information about intramolecular dynamics occurring in the excited state. Within the linear response approximation, the expression **Error! Reference source not found.** can be identified as the normalized, time-dependent average emission wavelength $\nu(t)$, also called the solvation correlation function $S(t)$:

$$C_S(t) = S(t) = \frac{\nu(t) - \nu(\infty)}{\nu(0) - \nu(\infty)} \quad (1.31)$$

In order to keep the information on the amplitude of the shift, only the non-normalized solvent contribution to the shift will be considered in the analysis of the results:

$$\Delta E_\infty^S = \langle E_S(t) \rangle - \langle E_S(\infty) \rangle = \nu(t) - \nu(\infty) \quad (1.32)$$

Continuum dielectric models

To understand this time evolution, a continuum model was first proposed, based on the equilibrium solvation models of Born⁸⁰ and Onsager,¹⁰ extended to the time-dependent regime.⁸¹ In this model, the solute is simulated by a cavity with a simple shape and the solvent by a homogenous dielectric continuum. In the case of a spherical cavity, this considerations lead to a mono-exponentially decaying correlation function, with a time constant τ_L , corresponding to the longitudinal polarization relaxation time of the solvent, related to its Debye relaxation time τ_D :

$$\tau_L = \left(\frac{2\varepsilon_\infty + \varepsilon_c}{2\varepsilon_0 + \varepsilon_c} \right) \tau_D \quad (1.33)$$

where ε_0 , ε_∞ are respectively the static and infinite dielectric constant of the solvent and ε_c the one of the molecular cavity. As soon as we depart from this spherical approximation, the decay becomes multi-exponential. This raw model does not account for the specific interactions of the solvent molecules in the immediate proximity of the solute, which have different polar responses than those of the bulk.

As a consequence, inhomogeneous dielectric models were developed in which the response from the solvent molecules depends on the solvent-solute distance. In these new models,⁸²⁻⁸⁶ different solvent shells are considered, each with a particular and independent dynamical response. This intuitive, phenomenological approach greatly improves the agreement with experiment since it takes into account the strong solvent-solute interactions.

Microscopic theories

The first time-resolved studies of polar solvation dynamics, in the 1980's, were limited to the picosecond regime. The solvation times observed were found to be more sensitive to the solvent properties than the chromophore size.⁸⁷⁻⁹¹ Moreover, multi-exponential solvent relaxations were observed, often with an unresolved ultrafast component. In the 1990's, the discovery of sub-100 fs solvation dynamics pushed the development of microscopic molecular theories of non-equilibrium solvation,⁹²⁻¹⁰³ recently reviewed by Bagchi *et al.*^{72,81} The theoretical analysis is performed via a molecular hydrodynamic approach based on energy and density conservation laws. The basic idea lies in the fact that the time-dependent solvent polarization $\mathbf{P}(\mathbf{r},t)$ is related to the position \mathbf{r} and orientation θ dependent density $\rho(\mathbf{r},\theta,t)$:

$$\mathbf{P}(\mathbf{r},t) = \mu_s \int d\theta \hat{\alpha}(\theta) \rho(\mathbf{r},\theta,t) \quad (1.34)$$

μ_s being the amplitude of the solvent dipole moment and $\hat{\alpha}(\theta)$ a unit vector with orientation θ . Once the polarization is characterized, the time-dependent solvation energy is obtained via the following expression:

$$E_s(t) = -\frac{1}{2} \int d\mathbf{r} \mathbf{D}(\mathbf{r}) \cdot \mathbf{P}(\mathbf{r},t) \quad (1.35)$$

with $\mathbf{D}(\mathbf{r})$ the electric displacement field induced by the presence of the solute. The important factor is therefore the orientation dependent density $\rho(\mathbf{r},\theta,t)$. The kinetic equation for $\rho(\mathbf{r},\theta,t)$ is provided by molecular hydrodynamics laws, leading to the generalized

Smoluchowski-Vlasov equation (GSVE).¹⁰⁴⁻¹¹¹ The resulting temporal evolution of the solvation energy joins the continuum model description at long length scales, but is different at a molecular scale since it takes into account intermolecular correlation. In addition, it demonstrates the relative importance of the translational modes in the polarization relaxation.^{81,112-114} The mechanisms of rotational and translational relaxation are illustrated in Figure 1.6, in the mean spherical approximation. While rotational motion is fast for large distances, the translational one becomes important at small distances of the solute, since here the rotational motion is slowed down due to strong interaction with the solute.¹⁰⁷ Therefore, the role of translational diffusion is crucial in the dynamics of proximal solvent molecules, unresolved by continuum models.

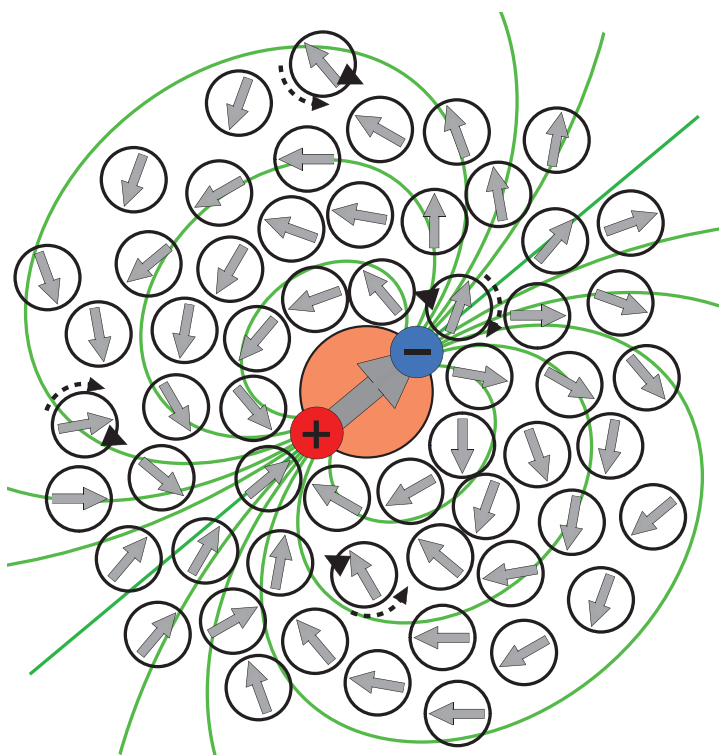


Figure 1.6: Schematic description of the translational and rotational diffusion in solvation dynamics of a dipolar solute. The four example solvent molecules can align their dipole on the field lines either by rotational (dashed arrows) or translational (small arrows) motion.

The application of this theory to computer simulation studies has made great advances in the comprehension of solvation dynamics at the molecular scale, as illustrates the pioneering computational and experimental work of Maroncelli and Flemming, for a wide variety of solvents.^{95,98,115,116} As a general behavior, the solvation correlation function of

different solvents, probed with a dipolar solute chromophore, was shown to have triphasic decay. The typical correlation functions of several solvents are shown in Figure 1.7, illustrating these three solvent relaxation mechanisms. The initial relaxation is ultrafast (0-300 fs, sometimes fitted with a gaussian component) and is due to hindered motion of the bulk solvent molecules, also called frictionless librational motion. The slower bi-exponential relaxation is due to collective rotational and translational diffusion of proximal solvent molecule. The translational motion is predominant in the close shell because of a strong intermolecular correlation (1-10 ps), whereas rotational contribution increases in the intermediate shell (300 fs – 1 ps).

Bulk hydration dynamics

Despite the description above is general, water is a particular solvent molecule due to its specific physical and chemical molecular properties, among which small size (2.8 Å), relatively large permanent dipole (1.85 D) and ability to form hydrogen bonding. Among polar solvents, it seems to be one of the fastest solvents studied.^{117,118} The solvation dynamics observed in aqueous chromophores has been shown to occur on three different timescales, well described by 3 exponential decays of ~1 ps, 150 fs and < 50 fs time constants,⁹⁸ with this last ultrafast response accounting for not less than half of the total solvation energy (Figure 1.8). This behavior was confirmed by photon echo peak shift measurements on eosin dye¹¹⁹ and by pump-probe spectroscopy of hydrated electron.¹²⁰ From computer simulations, this dominant initial response takes place in a few tens of femtosecond and is due to hindered rotation (also named libration) and intermolecular vibration/libration due to the extensive hydrogen bonding. On such a timescale, the heavy oxygen atoms of water molecules are stuck in their initial position, whereas the hydrogen atoms immediately react to the new electric field, through rotations and vibrations (high-frequency intermolecular modes of water molecules). This inertial motion is of small amplitude and is uncoupled with the other water molecules, but contributes to the major part of the solvent relaxation. For instance, as we will see later in the case of aqueous indole, Callis et al. obtained from molecular dynamics (MD) simulations that the first half of the shift occurs in 20 fs, with significant contribution from 20 water molecules.^{121,122}

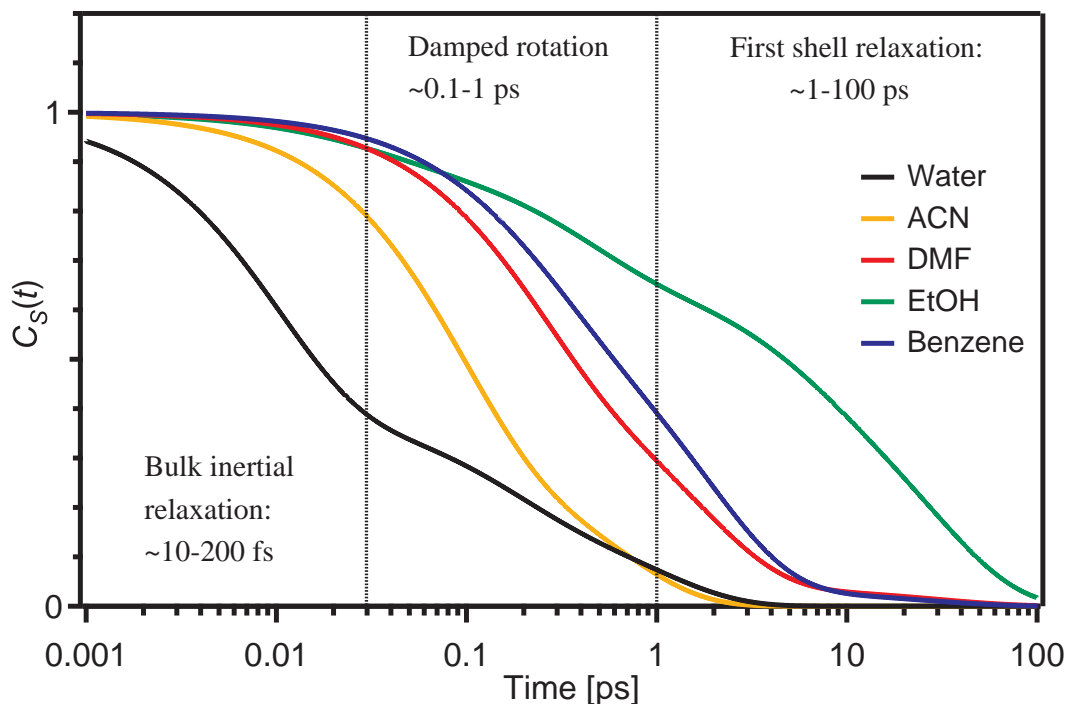


Figure 1.7: Solvation correlation function $C_S(t)$ for water, acetonitrile (ACN), dimethylformamide (DMF), ethanol (EtOH) and benzene, simulated by the multiexponential fit parameters obtained by Maroncelli *et al.*^{95,98}

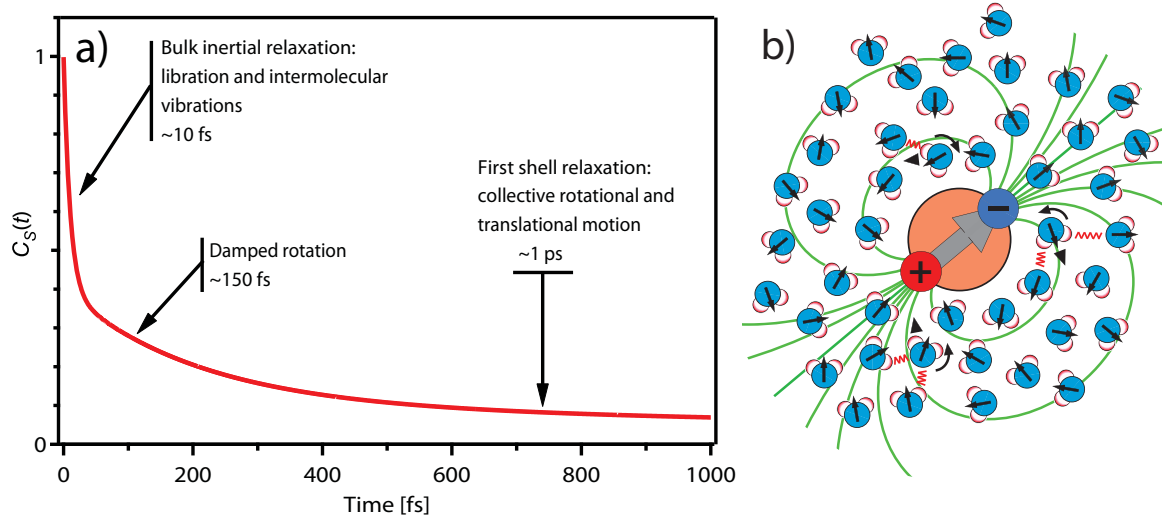


Figure 1.8: A) A typical solvation correlation function $C_S(t)$ for water, simulated by three exponential decay of 10 fs (60%), 150 fs (20%) and 1 ps (20%). B) Schematic picture of the molecular motion responsible for the dynamic water relaxation. The red springs represent hydrogen bonding between water molecules.

The intermediate 150 fs corresponds to remaining contributions from the moderately damped rotational motions of water molecules. During this time, the interactions between all water molecules start to affect the general motion. Therefore, the slowest contribution arises from collective and larger amplitude rotational and translational motions of the nearest neighbor molecules, in the first solvation shell. Indeed, the 1 ps time constant is in agreement with a description in terms of rotational and translational diffusion coefficients, taking into account an orientational correlation among the water molecules.¹²³

Non-polar solvation

In non-polar solvation, the rearrangement of solvent molecules near an excited solute chromophore has a totally different origin. In this case, the solvent molecules are apolar, and/or the solute chromophore does not show any difference in its ground/excited state dipole moment. As a consequence, rather than dipole-dipole interactions, a change in size and shape of the solute is responsible for the solvent rearrangement. The pressure inside the solute cavity is modified upon excitation, and the solvation energy relaxes as the cavity volume is re-equilibrating with the solvent shell. In this case, the relative orientation of the solvent molecules has a minor contribution compared to the predominant role of motion of their center of mass. The corresponding solvation response function has been shown to decay on mainly two different timescales.¹²⁴⁻¹²⁹ This biphasic decay originates from a fast inertial contribution and a slower, viscosity-dependent diffusive contribution.

Chapter 2

Chemical systems

- 2.1 UV dye molecules
 - 2.1.1 *2,5-diphenyloxazole*
 - 2.1.2 *Para-terphenyl*
- 2.2 Tryptophan
 - 2.2.1 *Stokes shift*
 - 2.2.2 *Anisotropy*
- 2.3 Metal and free base porphyrins
 - 2.3.1 *General photophysics*
 - 2.3.2 *Absorption and emission of TPP and OEP*
- 2.4 Haemoproteins
 - 2.4.1 *Cytochrome c*
 - 2.4.2 *Myoglobin*
- 2.5 Metal-polypyridine complexes
 - 2.5.1 *[Ru(bpy)₃]²⁺ and [Fe(bpy)₃]²⁺*
 - 2.5.2 *RuN719 and DSSCs*

This thesis reports the femtosecond fluorescence study of very different molecular systems: 2,5-diphenyloxazole, para-terphenyl, Tryptophan, free base and metallo-porphyrins, Cytochrome c, Myoglobin and metal polypyridine complexes. In order to lighten the presentation and discussion of the results, this chapter aims at describing the photophysical properties of each system.

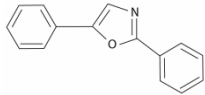
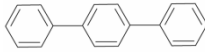
2.1 UV dye molecules

We started this work with the investigation of two UV chromophores, 2,5-diphenyloxazole (PPO), composed of two phenyl and one oxazole aromatic rings, and para-terphenyl (pTP) composed of three phenyl rings. The choice of these dyes was guided by their strong and structured emission in the UV range. In addition, their peculiar photophysics discussed below indicate some important conformational change in their excited states. Accordingly, they represent ideal systems to study the influence of such processes on the femtosecond fluorescence spectrum. In addition, these systems are excited with significant excess of vibrational energy, allowing investigation of the energy dissipation mechanisms. Their photophysical properties are summarized in table 2.1, and their absorption and emission spectra are plotted on Figure 2.1.

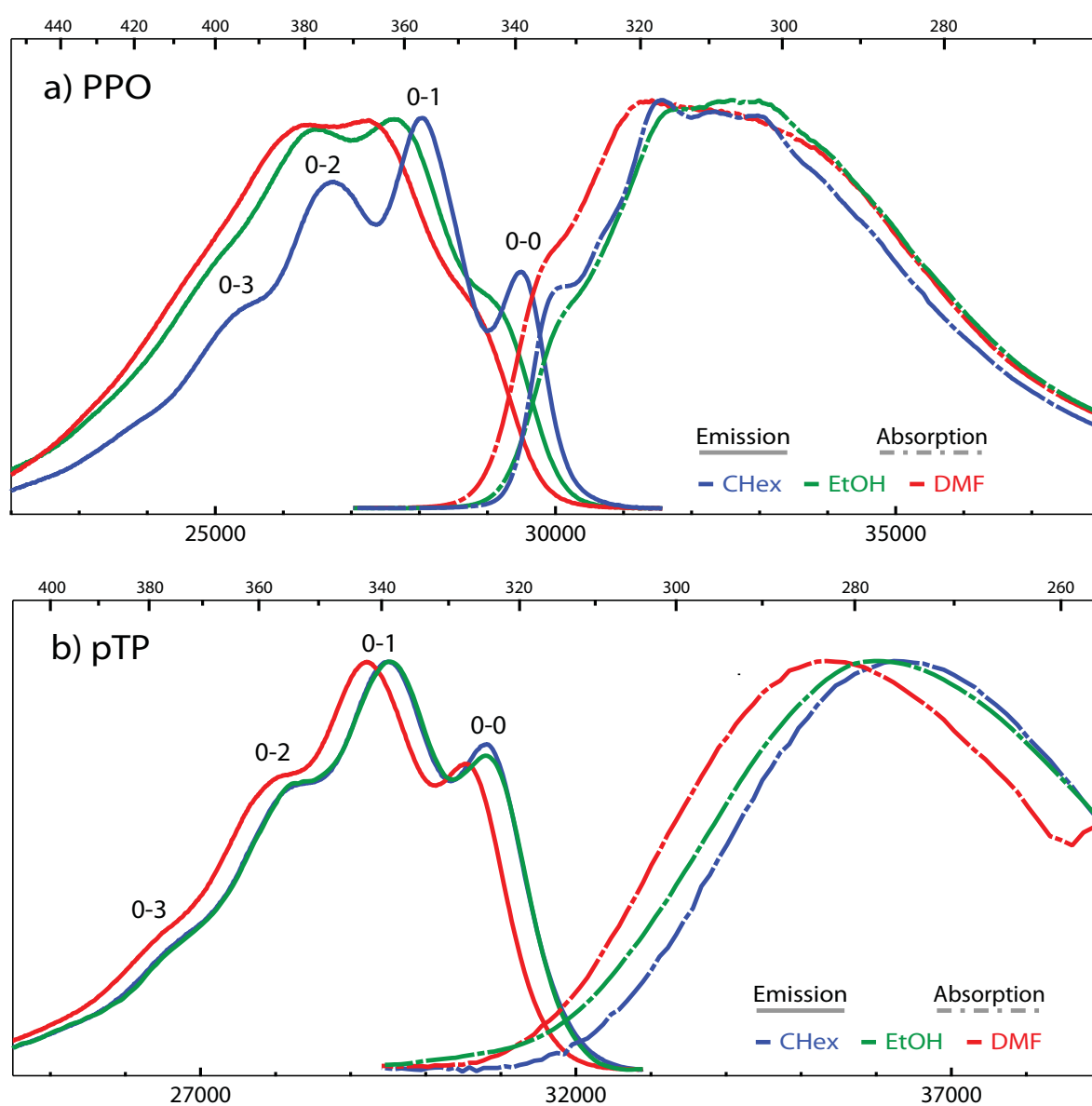
2.1.1 2,5-diphenyloxazole

The high photostability, emission quantum yield and its important Stokes shift (SS) made PPO dye molecule to be extensively used as wavelength shifter in liquid scintillators and as a laser dye.¹³⁰⁻¹³⁵ The emission properties of this UV dye are determined by the extension of the π -electronic system on all three rings. The corresponding absorption band around 310 nm, assigned to the $S_1 \leftarrow S_0$ transition, shows a vibronic structure in non-polar solvents, which is blurred in polar ones (Figure 2.1). At higher energy (not shown here), the absorption stems from the individual absorptions of the different chromophore moieties.^{136,137} The fluorescence exhibits a large Stokes shift of $\sim 4500 \text{ cm}^{-1}$, and a well resolved vibrational structure with apparent average spacing of 1370 cm^{-1} ,¹³⁸ arising from the coupling with two modes of 1544 cm^{-1} and 980 cm^{-1} assigned to oxazole ring C=N + C=C stretching and deformation mode.¹³⁹⁻¹⁴¹ In cyclohexane, the absorption and fluorescence spectra deviate from the mirror image symmetry, suggesting a structural change in the excited state. Despite of single bonds joining the three π -systems, both absorption and emission spectra are structured, speaking for a weak molecular flexibility. Moreover, the more pronounced vibronic progression of the fluorescence denotes a more rigid structure in the S_1 state compared to S_0 . An important influence of solvent polarity is observed on the fluorescence, both in terms of position and width, washing out the vibrational structure. The frontier molecular orbital (MO) of PPO were obtained by semi-empirical calculations.¹³⁸

Table 2.1: Photophysical properties of three studied UV dyes in methanol and cyclohexane.

<i>Compound</i>	τ_{fluo} ^a [142]	λ_{abs} ^b [nm]	λ_{em} ^c [nm]	<i>Q.Y.</i> ^d	Radiative transition	Ground state dipole	Excited state dipole	Molecular Structure
2,5-diphenyloxazole (methanol)	1.65 ns	303	362	0.5 ¹³⁸	S ₁ →S ₀	1.59 ¹⁴³	2.10 ¹⁴³	
(cyclohexane)	1.36 ns	303	357	0.85 ¹³⁸				
para-terphenyl (methanol)	1.17 ns	274	339		S ₁ →S ₀	-	-	
(cyclohexane)	0.98 ns	276	339	0.93 ¹⁴⁴				

^a total lifetime of fluorescence, ^b wavelength of the maximum of the absorption spectrum, ^c wavelength of the maximum of the fluorescence spectrum, ^d fluorescence quantum yield

**Figure 2.1:** Steady state absorption (discontinuous line) and emission (continuous line) spectra of a) 2,5-diphenyloxazole (PPO), b) para-terphenyl (pTP) and c) 1,2-diphenylacetylene (DPA) in cyclohexane (CHex, blue), ethanol (EtOH, green) and dimethylformamide (DMF, red).

The electronic ground state has a planar geometry and the HOMO is mainly localized on the oxazole ring, with an asymmetric character with respect to an axis passing through the oxygen atom and the middle of the nitrogen-carbon bond.¹³⁸ Conversely, the LUMO is symmetric with respect to this axis and mainly localized in the region of the oxazole-phenyl bonds, confirming a more rigid structure in the first excited state. The permanent dipole moment is increased in the S_1 state (Table 2.1),¹⁴³ explaining the solvent polarity influence on the fluorescence spectrum.

One peculiarity of this dye molecule is its anomalous amplified spontaneous emission (ASE).¹⁴⁵ Indeed, the ASE efficiency is higher for the 0-2 vibronic transition and not the F-C maximum 0-1 transition (Figure 2.1a). An electromer model was developed to explain the behavior of this particular class of compounds: a solitonic transfer of vibrational distortion (IVR) occurring between two normal mode segments of the electronic system.¹⁴⁶ However, this model supposes an overlap of two electronic transitions characterizing the lowest absorption band, which appeared to be erroneous.^{138,143} The extension of the ASE behavior study to conformationally restricted PPO derivatives demonstrated the failure of this model.¹⁴⁷ As alternative explanations, a weak transient ESA that could lead to lowering of the 0-1 ASE intensity and saturation of the 0-1 prior to 0-2 transition because of different population lifetimes of the 1st and 2nd ground state vibronic levels (IVR), have been proposed.

2.1.2 Para-terphenyl

pTP molecules have been extensively used as crystalline environment for single molecule spectroscopy measurements,¹⁴⁸⁻¹⁵⁰ and were studied in the field of π -conjugated material for a prospective use in optoelectronic applications.^{151,152} As in the case of PPO, the HOMO and LUMO are characterized by π -electronic state covering all three phenyl rings. Due to its high symmetry, it does not show any permanent dipole moment either in the ground or the excited state and is thus an apolar dye molecule. Accordingly, pTP steady state absorption and emission spectra do not show important changes in the different solvent, apart from a small shift in DMF. Nevertheless, the mirror image symmetry rule is clearly violated, the absorption being broad and featureless compared to the structured emission. This reflects an important conformational change occurring upon excitation.¹⁵³ In the ground state, the weak single C-C bonds joining the phenyl rings imply the presence of low frequency librational modes. The related potential is characterized by an anharmonic

W-shaped well, with minima at an angle of $\sim 30^\circ$ with the planar configuration (Figure 2.2). In the excited state, the phenyl-phenyl bonds are strengthened and the molecule becomes planar with near harmonic (U-shaped) potential. The absorption is smeared out by the wide vibronic progression from the torsional motion, which is a Poisson distribution with most important accepting level having quantum number equal to 14. Conversely, the strong anharmonicity in the ground state potential results in a large deviation of the vibronic progression of the torsional mode from the Poisson distribution. Indeed, the structured emission spectrum suggests that the libration does not couple to the optical transition. In fact the shape of the wave functions associated to the accepting levels in the ground state (with maximum just above the potential barrier) are reminiscent of that of wave functions from a harmonic oscillator, with small quantum numbers ($\nu = 0, 1, 2, \dots$). Consequently, while the most important accepting level has quantum number $\nu = 9$, the overlap of the ground and excited librational wave functions results in a very narrow progression, as if it was almost not coupled to the transition. This behavior is illustrated in Figure 2.2 with the potential energy curves associated to the phenyl rings torsion in the ground and excited states.¹⁵³

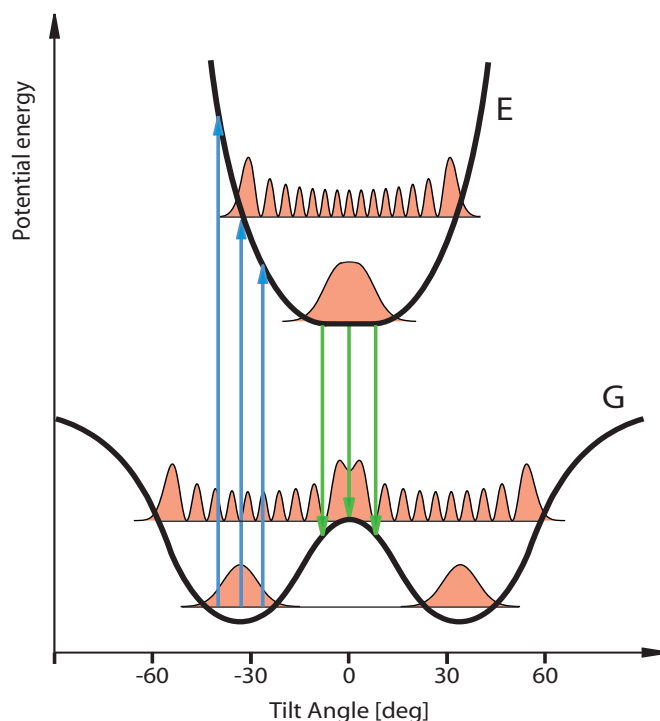


Figure 2.2: Potential energy curves of the ground (G) and excited (E) state of pTP projected on the libration mode coordinate (tilt angle) of the phenyl rings, from ref. ¹⁵³. The blue and green arrows represent the FC absorption and emission, respectively.

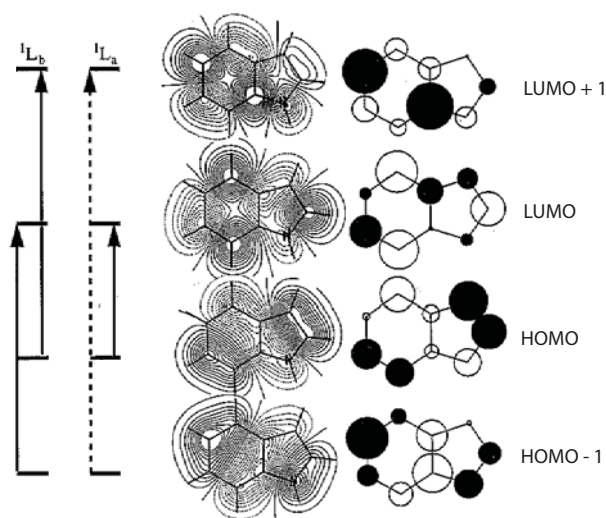
The vibronic structure of the fluorescence spectrum of pTP has been resolved by measurements in the crystalline phase at 4.2 K.^{154,155} The progression is dominated by two high frequency modes of 1614 and 1286 cm^{-1} and one low frequency mode of 228 cm^{-1} . The individual vibronic lines were seen to be broad ($\sim 120 \text{ cm}^{-1}$) and asymmetric. This feature is thought to be due to the torsional mode of the phenyl rings at the calculated frequency of 55 cm^{-1} .

2.2 Tryptophan

Tryptophan (Trp) is the most common aromatic amino acid residue in biological systems. Its absorption and emission bands are well separated from the spectral bands of other amino acids and peptides,⁶ and are very sensitive to the local environment, making it an ideal probe of structural changes in the course of protein functions, folding-unfolding processes, etc.^{121,156} Indeed, several of its fluorescence features such as band maximum and width,¹⁵⁷ quantum yield,¹⁵⁸ lifetimes,¹⁵⁹ energy transfer,¹⁶⁰ and time-resolved anisotropy¹⁶¹ have been extensively exploited to this aim. Fluorescence up-conversion studies on Trp were carried out to probe the solvation dynamics at the surface of^{61,123,162-164} or within¹⁶⁵ proteins. More recently, ultrafast UV transient absorption spectroscopy was used to probe the Trp response to a light triggered biological function in bacteriorhodopsin,^{166,167} and in hemoproteins.^{168,169} The Trp residue is the ideal local probe of protein dynamics, and in a non-invasive way, i.e. without the need of binding an extra chromophore molecule which could influence the protein functionality.

The photophysics of Trp is rather complex. Figure 2.3 shows the calculated molecular orbital (MO) for indole in vacuum. The 280 nm absorption band of Trp shown in Figure 2.4, contains the overlap of two transitions, namely 1L_a and 1L_b .¹⁷⁰ The 1L_a transition corresponds to a direct excitation from the HOMO to the LUMO, with a small contribution from of the HOMO - 1 to LUMO + 1 transition. On the other hand, the 1L_b transition is an equal superposition of HOMO - 1 \rightarrow LUMO and HOMO \rightarrow LUMO + 1 excitations. In the literature, the excited state resulting from the 1L_a and 1L_b transitions are usually directly referred to as 1L_a and 1L_b . In the following we will use the same nomenclature for these states.

Whereas 1L_b has its permanent dipole moment close to the ground state one, both in value and direction (~ 2 D), the 1L_a state has a significantly larger permanent dipolar moment almost perpendicular to that of the ground state. The latter transition is characterized by a sizeable charge transfer from the indole to the benzene ring, leading to a 6 D large dipole moment.¹²¹ As already emphasized, this is the main property of the Trp residue, responsible for its high sensitivity to solvent.

**Figure 2.3:**

Molecular orbitals for indole in vacuum from the INDO/S-CI method¹⁷¹ compared with those from an ab initio method.¹⁷² The main configurations composing the 1L_a and 1L_b transition are also shown. This Figure is taken from ref. ¹²¹.

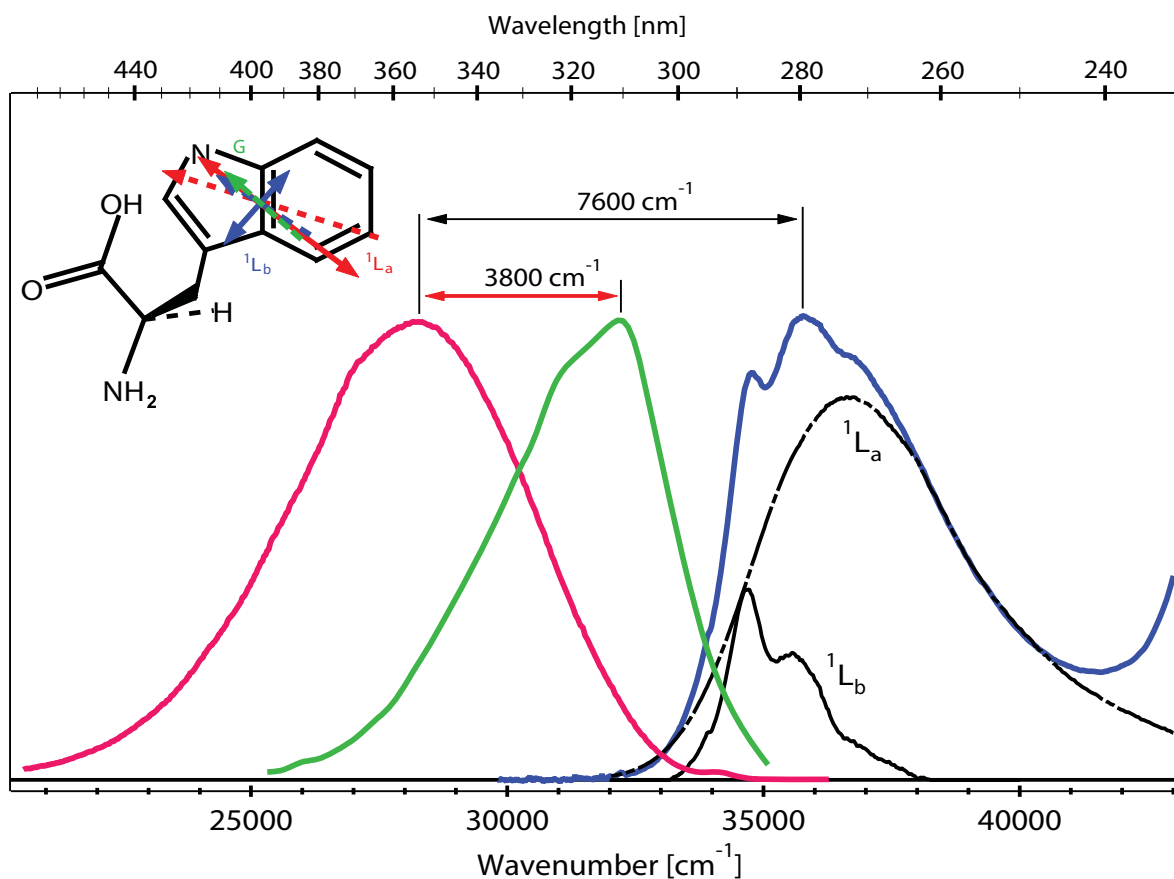


Figure 2.4: Steady state absorption (blue) and emission (red) spectra of Trp in water at room temperature. The absorption is decomposed into the 1L_a (dashed-dotted black line) and 1L_b (solid black line) contributions.^{121,173-176} The fluorescence emission of Trp in a cryosolvent is also reported (green line),¹⁷⁷ in order to distinguish the pure solvent contribution to the Stokes shift. The molecular structure of Trp with the transition (solid arrows) and permanent (dashed arrows) dipole moments of 1L_a (red) and 1L_b (blue) and of the ground state (green) are shown in inset.

Figure 2.4 shows the absorption and emission spectra of aqueous Trp, along with the decomposition of the absorption in 1L_a and 1L_b contribution. A broad band, with the maximum far from the origin characterizes the 1L_a transition in which many vibrations are Franck-Condon active.¹²¹ Moreover, the strong inhomogeneous broadening is due to the high sensitivity of the dipolar moment to the local environment. Concerning 1L_b , its absorption spectrum is structured and characterized by less Franck-Condon active modes. In vacuum, 1L_a lies $\sim 500\text{ cm}^{-1}$ above 1L_b .¹⁷⁸⁻¹⁸⁰ However, due to its larger dipole moment, the 1L_a state is more stabilized by polar solvent molecules than the 1L_b state, such that the former becomes the lowest in energy. Accordingly, it is considered to be the emitting state in most polar environments. The emission spectrum is broad and featureless in a polar solvent such as water, with a particularly large Stokes shift. In non-polar solvents, the emission is expected to stem from the 1L_b state and to be narrow, structured and with a relatively small Stokes shift. Until now, no measurements have clearly evidenced the fluorescence emission stemming from the 1L_b state. In indole and Trp, 1L_a is lower than 1L_b in energy, but this is not always the case. For 3-methylindole, a compound close to Trp, the 1L_a origin has been indeed distinctly identified at least 260 cm^{-1} above the 1L_b (jet cooled and solid argon experiments, see Ref ¹⁸¹ and ¹⁷⁸). Hence, for Trp embedded in a specific protein site with a local electric field causing a sufficient blue shift of the 1L_a state, one can expect to see emission from the 1L_b state.

In bulk water, the presence of different rotamers due to the different relative orientations of amino- and carboxylic groups, results in two different radiative time constants (quenching through electron or proton transfer): a main 3 ns component with a smaller and faster component of 0.5 ns, the latter having a slightly different spectrum centered at 335 nm.¹⁸² In the 0-100 ps temporal window, only $^1L_b \rightarrow ^1L_a$ internal conversion (IC) and solvation dynamics occur together with rotational diffusion.¹⁸³

2.2.1 Stokes shift

Ultrafast Time-Resolved Stokes Shift (TRSS) measurements on tryptophan were carried out to extract the local solvation dynamics by characterizing the solvation correlation function. Shen and Knutson,¹⁶¹ Zewail and coworkers^{60,123,162-165,184} and Zhong and co-workers^{61,185} measured single-wavelength fluorescence traces across the spectrum of aqueous Trp. Zhong *et al.* established a procedure to reconstruct the whole emission spectrum, and found a total Stokes shift, up to the longest time delay (830 ps) of 2186 cm^{-1} ,

including a 200 cm^{-1} shift in the nanosecond time domain, attributed to rotamers dynamics. They fitted their correlation function with a gaussian-type component and an exponential decay, and obtained two decay times of 340 fs and 1.6 ps, in agreement with the water solvation time constants.^{97,98} Interestingly a simple analysis of steady state absorption and emission spectra of aqueous Trp would give a total expected Stokes shift of $\sim 3800\text{ cm}^{-1}$: A mirror image of the Trp absorption band yields an emission spectrum centered at $\sim 32\,000\text{ cm}^{-1}$, in agreement with measurement of Trp emission spectrum in glassy matrices at cryogenic temperature (Figure 2.4).¹⁷⁷ Indeed, this would correspond to the exact spectrum of Trp surrounded by an unrelaxed solvent. Compared to the steady-state emission centered at $28\,200\text{ cm}^{-1}$ (355 nm), this gives a total expected Stokes shift of $\sim 3800\text{ cm}^{-1}$ implying that a shift of $\sim 1600\text{-}1700\text{ cm}^{-1}$ occurs on a timescale shorter than their temporal resolution (~ 400 fs). A similar effect was predicted by Callis *et al.* who, on the basis of molecular dynamics simulations, found that 2000 cm^{-1} of the shift would occur within 20 fs, with significant contribution from 20 water molecules within 6 \AA of the indole ring center.¹⁷⁰ The occurrence of a Stokes shift in 10's of fs has been recently confirmed by experimental studies on metal complexes, where upon optical excitation "instantaneous" Stokes shifts as large as 6000 cm^{-1} are observed between excitation and emission.^{52,186-188} However, as will be seen in chapter 8, an internal vibrational redistribution (IVR) mechanism likely seems the origin of the effect in these cases. Furthermore the occurrence of sub-10 fs IVR in large molecules was proposed¹⁸⁹ on the basis of QM/MM (Quantum Mechanical/Molecular Mechanics) methods.

2.2.2 Anisotropy

Since the 1L_a and 1L_b states are characterized by transition dipole moments with almost perpendicular orientations, time-resolved anisotropy measurements were used,^{161,185,190,191} concluding that the internal conversion (IC) time τ_{ic} is < 100 fs. These studies were carried out with a typical temporal resolution of ≥ 300 fs, using a monochromatic detection (i.e., single wavelength detected fluorescence kinetics). The use of a polychromatic detection in the UV^{192,193} is important to separate the spectral evolution due to the IC process from other mechanisms, such as cooling and solvation dynamics. Furthermore, this detection makes the correction for group velocity dispersion (GVD) more reliable, since it can easily be estimated with independent measurements on dye laser emission¹⁹³ or with a continuum.¹⁸⁷

2.4 Metal and free base porphyrins

The family of porphyrin molecules plays an important role in biology. Indeed, its photophysical and photochemical properties make it a very functional prosthetic group, extensively used by proteins as active center in haemoproteins or in an assembly of several units in the light harvesting complex. In parallel, the development of biomimetics science promoted their use in photo-activated applications such as dye sensitized solar photovoltaic cells,¹⁹⁴⁻¹⁹⁶ photodynamic therapy,^{2,197-199} oxygen sensor²⁰⁰⁻²⁰² and molecular electronics.²⁰³⁻²⁰⁵ In the framework of the ultrafast protein dynamics study of haemoproteins, porphyrins represent model systems to study haem relaxation dynamics.

2.3.1 General photophysics

The porphyrin is a highly symmetric molecule –with D_{4h} symmetry- constituted of four pyrrole rings linked together by methine bridges (Figure 2.5), forming an extended π -electronic system. The absorption spectrum stems from $\pi \rightarrow \pi$ transitions and is characterized by a strong and narrow band around 400 nm (Soret or B band) and much weaker bands in the 500-600 nm region (Q band) (see for instance the spectrum of free base porphyrin in Figure 2.5a). Certain Q bands have been assigned to vibrational replica on the basis of their recurring energy separation with the 0-0 peak and their relatively constant intensity, although sometimes no clear Franck-Condon progression could be identified. The transitions underlying the general absorption profile of porphyrin systems are well described in the framework of Martin Gouterman's Four-Orbital Model.²⁰⁶ To decipher the origin of these bands, one has to look at the frontier orbital. The top filled (HOMO) and lowest empty (LUMO) orbital can be found by simple MO calculation (Figure 2.5b).²⁰⁷ As in the case of Trp, while the nomenclature used here (Q and B) should refer only to transitions, for sake of simplicity we will use the same label for the corresponding excited state.

a) electronic transitions

The two LUMO are of e_g symmetry and hence are completely degenerate. These states are responsible for the two orthogonally polarized transition dipole moments, labeled x and y in the following. The HOMOs have respectively the symmetry a_{1u} and a_{2u} with very close energies. This accidental degeneracy makes the porphyrins to behave as the cyclic polyenes.²⁰⁸

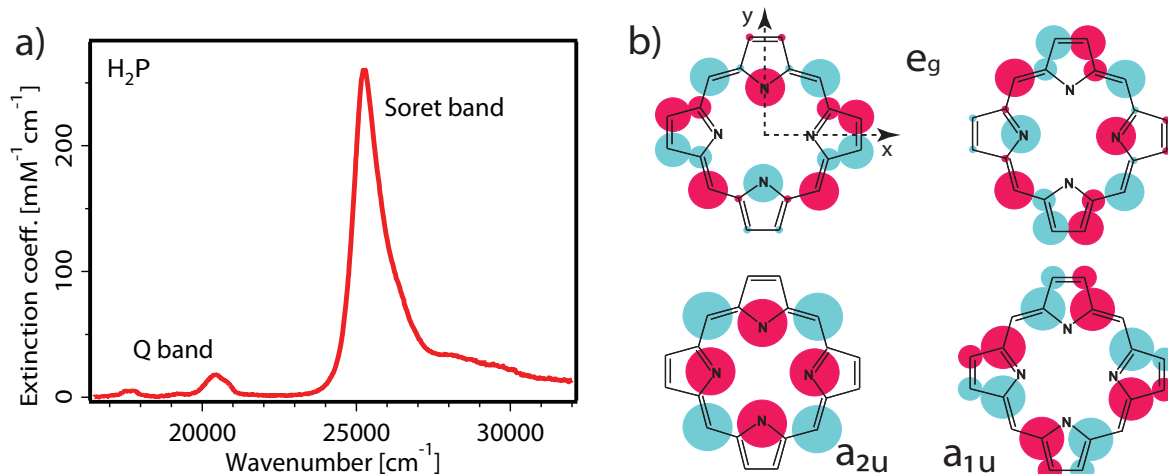


Figure 2.5: a) Extinction coefficient of free base porphyrin (H_2P) in toluene. b) Porphyrin frontier orbitals, the HOMOs (bottom) are of a_{1u} and a_{2u} symmetry whereas the LUMOs are of e_g symmetry, from ref²⁰⁹.

In these systems, 4 excited configurations are strongly mixed by electronic interactions, giving rise to 2 pairs of degenerate states (E_u symmetry).²¹⁰⁻²¹⁴ The wave function (ab), corresponding to the single electronic configuration of one hole in orbital a and one electron in orbital b solves the problem

$$\mathbf{H}_{eff}(ab) = E(ab) \quad (2.1)$$

and the full Hamiltonian is

$$\mathbf{H} = \mathbf{H}_{eff} + \mathbf{H}' \quad (2.2)$$

where H' corresponds to electron repulsion terms, corresponding to the interactions between the different electronic configurations. On the basis of symmetry considerations, Gouterman restricted the configuration mixing to the $(a_{2u}e_g)$ and $(a_{1u}e_g)$ states. He then formulated the problem for the y polarized states -the x polarized states behaving identically- by defining the following quantities:²⁰⁹

$$\begin{aligned} A_{1g}' &\equiv \frac{1}{2} [E(a_{1u}e_{gx}) + E(a_{2u}e_{gy})] \\ A_{1g} &\equiv \frac{1}{2} [-E(a_{1u}e_{gx}) + E(a_{2u}e_{gy})] \\ A_{1g}'' &\equiv \int (a_{2u}e_{gx})H(a_{1u}e_{gy})d\tau \end{aligned} \quad (2.3)$$

The use of these particular symbols, which are standard group theoretical notations,³ is introduced to simplify the symmetry consideration of further treatment of the effect of substituent on the porphyrin. The last term is the configuration interaction term.

In the case of a 50-50 mixture, the resulting states are named B_y^0 and Q_y^0 :

$$\begin{aligned} B_y^0 &\equiv \frac{1}{\sqrt{2}} \left[(a_{2u} e_{gy}) + (a_{1u} e_{gx}) \right] \\ Q_y^0 &\equiv \frac{1}{\sqrt{2}} \left[(a_{2u} e_{gy}) - (a_{1u} e_{gx}) \right] \end{aligned} \quad (2.4)$$

The associated transition dipole moments μ_B and μ_Q are derived from the single configurations ones, i.e. μ_1 for $(a_{1u} e_{gx})$, and μ_2 for $(a_{2u} e_{gy})$:

$$\begin{aligned} \mu_B &= 2^{-1/2} (\mu_1 + \mu_2) \\ \mu_Q &= 2^{-1/2} (\mu_2 - \mu_1) \end{aligned} \quad (2.5)$$

The B and Q states arise from the rigorously diagonalized Hamiltonian

$$\begin{aligned} B_y &\equiv \cos \nu B_y^0 + \sin \nu Q_y^0 \\ Q_y &\equiv -\sin \nu B_y^0 + \cos \nu Q_y^0 \end{aligned} \quad \text{with } \tan 2\nu \equiv A_{1g} / A_{1g}'' \quad (2.6)$$

The strength of the mixing is then monitored by the energy difference between the two initial configuration (A_{1g}) and the configuration interaction term (A_{1g}''). If $A_{1g} / A_{1g}'' \ll 1$, then $\nu \ll 1$ and the B and Q states are now described as

$$\begin{aligned} B_y &= B_y^0 + \nu Q_y^0 \\ Q_y &= Q_y^0 - \nu B_y^0 \end{aligned} \quad (2.7)$$

In this case, the transition dipole of Q transitions is $\nu \cdot \mu_B - \mu_Q$, i.e. of weak amplitude. The Q bands gain intensity through the departure from the totally degenerate case. The energy splitting corresponds to the configuration interaction term of eq.(2.3):

$$E_B - E_Q = 2A_{1g}'' (1 + 2\nu^2) \approx 2A_{1g}'' \quad (2.8)$$

The deviation from the totally degenerate case is possible through changes in the energy of one of the HOMOs, through a completely symmetric perturbation (A_{1g}) like adding substituent on the meso or beta position of the porphyrin ring, or by changing the electronegativity of the central metal atom in the case of metalloporphyrins. A strong non symmetric perturbation (for instance the protonation of two nitrogen atoms, i.e. the free base porphyrin) acts mainly on the LUMO by lifting their degeneracy, splitting the two

orthogonally polarized transitions and giving rise to the B_x , B_y , Q_x and Q_y bands. The B band splitting is much smaller than that of the Q bands and usually not observed at room temperature. The reason lies in the B_{1g}'' symmetry of the perturbation, acting only on the Q states.²⁰⁸ We can notice here that for metalloporphyrins in an isotropic medium no x or y polarization is favoured. In other words, the symmetry is preserved and no splitting is observed. In protein environment, a metalloporphyrin (for instance a haem group) may experience some anisotropic constraints changing the energy of the e_{gx} and e_{gy} states. Nevertheless, the induced Q band splitting is far smaller than that of the corresponding free base porphyrin.²¹⁵

a) vibronic structure of the Q band

The strong Soret band has its maximum in the 0-0 FC transition (zero-phonon-line), with a weak intensity in higher vibronic levels. This property is weakly dependent on the substituent or on the central nitrogen protonation. Conversely, the Q band shape is strongly modulated by the substituent. Moreover, the mirror image symmetry is often broken. Figure 2.5 represents the absorption and emission spectra in the Q band region of Zn 5, 10, 15, 20-tetraphenylporphyrin ($Zn^{II}TPP$) in cyclohexane, one of the compound of the present study. The intensity ratio between the zero-phonon-line and the first vibronic level is different in absorption and emission. However, both have maxima in the vibronic replica and strongly deviate from a Poisson distribution.

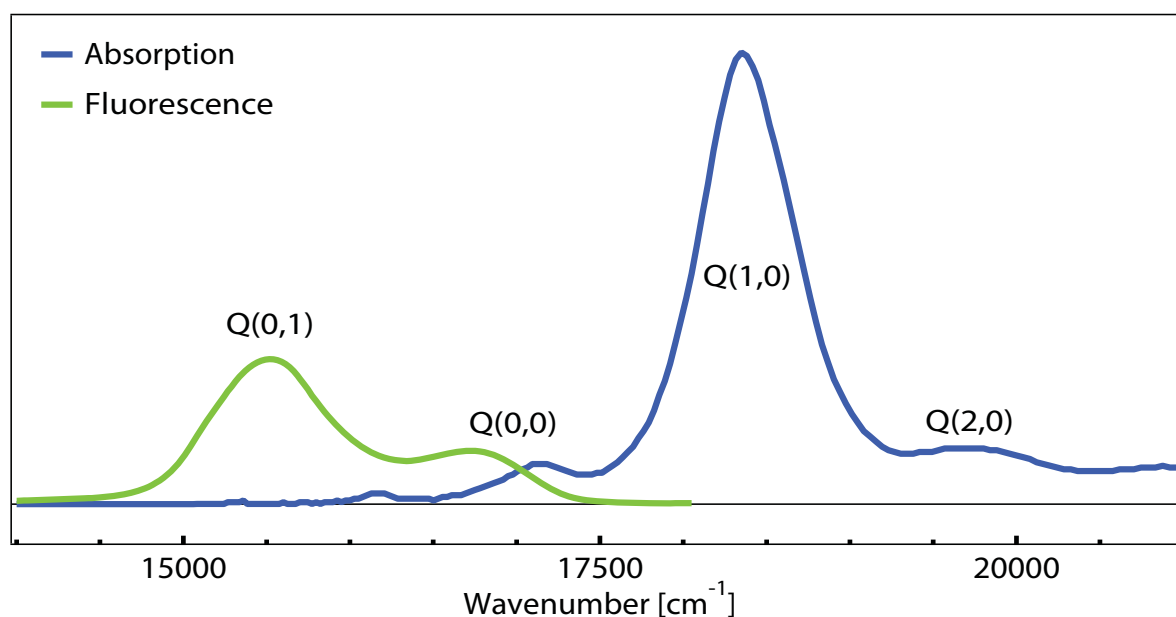


Figure 2.5: Steady state absorption (blue trace) and emission (green trace) of Zn(II)TPP in cyclohexane.

The vibronic transitions underlying the Q band are inherent to its forbidden character. Indeed, this electronic transition becomes allowed thanks to strong vibronic effects. In this case the Condon approximation breaks down, i.e. the transition dipole moment between the ground and excited electronic states μ_{fi} cannot be anymore considered independent on the nuclear coordinates \mathbf{Q} , but can be expanded as

$$\hat{\mu} = \mu_0 + \sum_k \mu_k Q_k + \sum_{k,l} \mu_{k,l} Q_k Q_l + \dots \quad (2.9)$$

A strongly allowed transition as the Soret band, is dominated by the zero-order term μ_0 corresponding to the FC spectrum. For weakly allowed or forbidden transitions one has to consider also the first order term (Herzberg-Teller (HT) approximation):²¹⁶

$$\mu_{fi} = \mu_0 + \sum_k \mu_k Q_k \quad (2.10)$$

In addition, to account for non negligible changes in the nuclear coordinates in the excited state \mathbf{Q}' , one has to go beyond the linear coupling approximation by using the following linear transformation:

$$\mathbf{Q}' = \mathbf{D}\mathbf{Q} + \Delta\mathbf{Q} \quad (2.11)$$

where $\Delta\mathbf{Q}$ is the displacement between the equilibrium geometries in the ground and excited states (expressed in the basis of \mathbf{Q}) and \mathbf{D} is the Duschinsky matrix.²¹⁷ As a consequence, the probability of the $|i\rangle \rightarrow |f\rangle$ transition is given by:

$$\mu_{fi} = \langle i | \hat{\mu} | f \rangle = \underbrace{\langle i | \mu_0 | f \rangle}_{FC \text{ term}} + \underbrace{\langle i | \sum_k \mu_k Q_k | f \rangle}_{HT \text{ term}} \quad (2.12)$$

Finally the intensity, proportional to the square of μ_{fi} , contains three terms: the pure FC and HT terms and a third FC/HT interference term. This formalism has been applied to porphyrin system with success.^{215,218,219} In particular, Santoro *et al.* compared the calculated FC spectrum of the free base porphin with the one taking into account HT terms.²¹⁸ The FC spectrum appeared to be of similar shape than that of the Soret band, i.e. a strong 0-0 line with weak intensity in the higher vibrational levels, i.e. reflecting a weak vibronic coupling. The full treatment, i.e. with the HT terms, shows conversely a weak 0-0 line but a bunch of lines shifted by $\sim 1300 \text{ cm}^{-1}$ from the zero-phonon-line, all corresponding to the excitation of a single quantum of various modes. The normal modes

involved in the spectra are of a_{1g} and b_{1g} symmetry. While the totally symmetric modes give rise to both FC and HT contributions polarized along x , b_{1g} modes are only involved in the HT contributions polarized along y . Symmetry considerations indicate that the x and y polarized HT terms reflect intensity borrowing from the B_x and B_y Soret bands respectively. Since the FC spectrum is confined to the 0-0 line, the interference term does not dramatically influence the final spectrum. The main transitions in both absorption and emission spectra therefore correspond to the 0→1 transition of a couple of modes. This observation was explained by a small coordinate displacement and frequency shift together with a moderated Duschinsky mixing. Moreover, both Duschinsky and HT effects can account for absorption/emission asymmetry.

2.3.2 Absorption and emission of TPP and OEP

With the aim at understanding the ultrafast processes characterizing the electronic relaxation of porphyrins, required for the extension of the study to haem groups in proteins, we decided to start an extensive study on 12 different porphyrin derivatives. The structural effects on the relaxation mechanisms are examined through the use of two different substituents on the porphyrin macrocycle: four phenyl groups bound on the meso positions (5, 10, 15, 20-tetraphenylporphyrin or TPP) and eight ethyl group on the β positions (2, 3, 7, 8, 12, 13, 17, 18-octaethylporphyrin or OEP), both shown in Figure 2.6. For each type of porphyrin, we investigated the free base molecule (H_2TPP and H_2OEP) as well as a completely filled d shell metalloporphyrin ($Zn^{II}TPP$ and $Zn^{II}OEP$) and some transition metal porphyrin (Ru, Cu, Ni, Co).

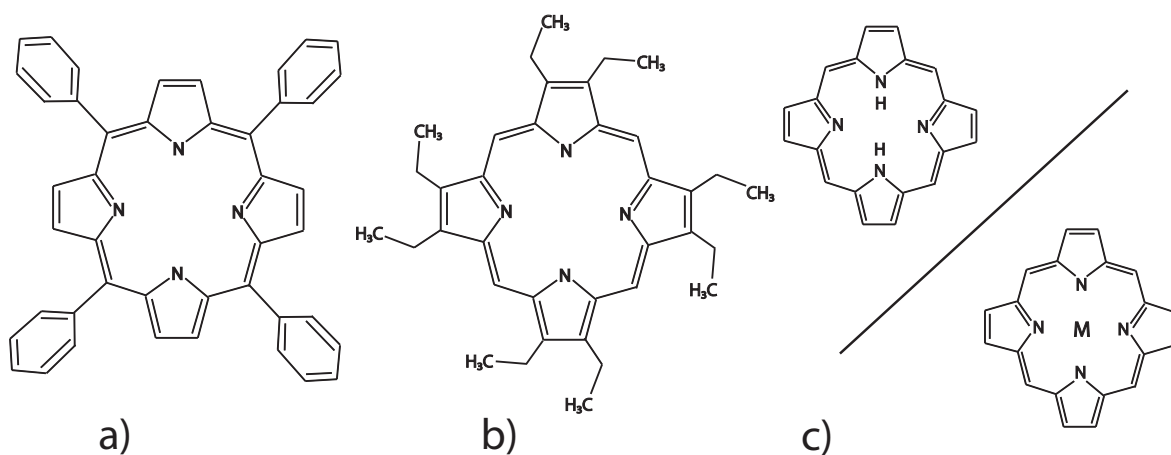


Figure 2.6: Chemical structures of a) 5, 10, 15, 20-tetraphenylporphyrin, b) 2, 3, 7, 8, 12, 13, 17, 18-octaethylporphyrin and c) free base and metallo-porphyrin.

We carried out a femtosecond fluorescence study of these compounds in cyclohexane. The choice of this solvent comes from three main reasons: i) all these complexes dissolve well in it, ii) it is non-polar, meaning that no polar solvation dynamics will interfere with the overall relaxation dynamics, and iii) it is one of the least coordinating solvent.²²⁰ Only the Zn^{II}OEP compound was measured in dimethylformamide, since its solubility limit prevents the use of cyclohexane.

a) Free base TPP and OEP

Figure 2.7 shows the steady state absorption and fluorescence spectra of H₂TPP and H₂OEP in cyclohexane. In the absorption spectrum, the Soret or *B* band of H₂TPP at 416 nm (410'000 cm⁻¹M⁻¹) is narrow and has shoulder at 400 nm, whereas the Soret band of H₂OEP is blue-shifted to 399 nm (shoulder at 375 nm), and is substantially broader and lower in intensity (160'000 cm⁻¹M⁻¹). Because of lowering of symmetry from *D*_{4h} to *D*_{2h} due to the protonation of the nitrogen of two facing pyrrole rings, the *Q* band splits into *Q*_x and *Q*_y electronic transitions. The *Q*_x transition is the lowest in energy, the *x* axis corresponding to the H H axis.²⁰⁶ Contrary to the Soret band, the *Q* bands of H₂OEP are narrower than those of H₂TPP. If the fluorescence shows the same vibronic progression for both compounds (but slightly broader for H₂TPP), the absorption shows a different behavior. Indeed the ratio between 0-0 and 1-0 vibronic bands of *Q*_x and *Q*_y transitions are smaller for H₂OEP than for H₂TPP. Apart from the dominant features of the *Q*_x(0,0) and *Q*_x(0,1) fluorescence, one can notice a shoulder centered at ~610 nm with amplitude ~0.8% of the *Q*_x(0,0) peak (see Figure 6.1e and 6.1f). The main channel for *Q*_x relaxation is intersystem crossing in ~10 ns to a lower triplet state T₁, which decays on the millisecond timescale. The fluorescence quantum yield of these two compounds has been reported to be around 0.1.^{1,221} The very small Stokes shift of both molecules is evidence of negligible structural rearrangement and solvation.

The frequency spacing between 0-0 and 0-1 lines of ~1600 cm⁻¹ corresponds to C=C stretching in the pyrrole rings. However, as seen in the previous §, the spectrum is highly non-Condon and the 0-1 band is in fact a bunch of about 10 different modes.²¹⁸ The main effects of substituent are an important decrease in the intensity (H₂OEP maximum three times lower than H₂TPP) and a blue shift of all bands of H₂OEP compared to H₂TPP. The energy splitting *E*_B-*E*_Q is weakly affected by the peripheral group.

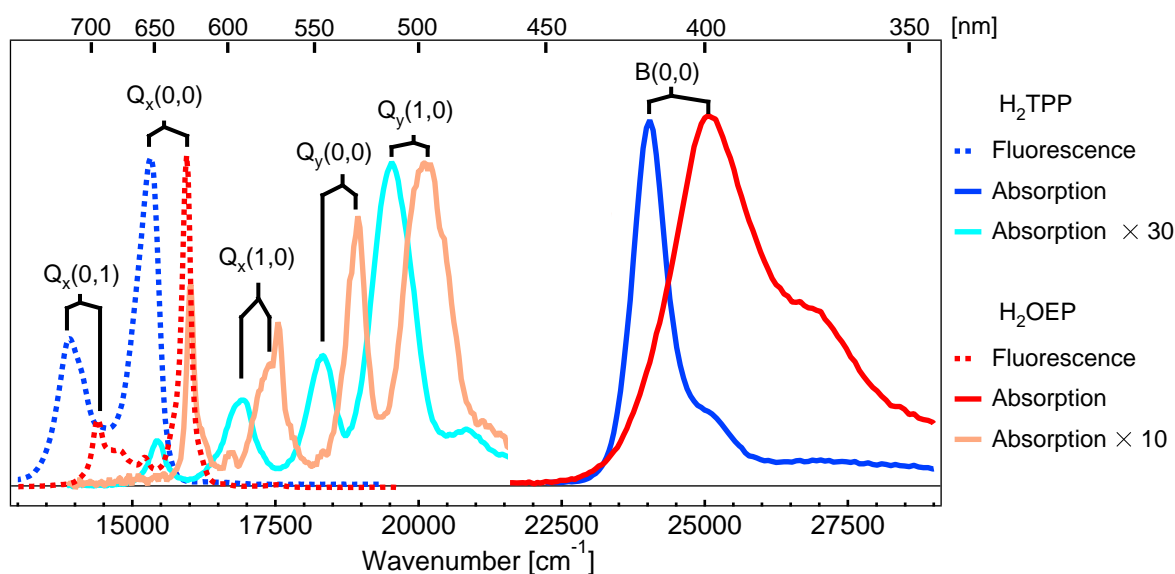


Figure 2.7: Steady state absorption (continuous lines) and emission (dashed lines) of H_2TPP (blue lines) and H_2OEP (red lines) in cyclohexane.

b) Metal TPP and OEP

Figure 2.8a shows the absorption and emission spectra of ZnTPP and ZnOEP in cyclohexane. The presence of the metal in the center of the porphyrin ring leads to the full D_{4h} symmetry. In this case, the Q band is not split but shows a pronounced influence of the substituent. The Soret or B band of ZnTPP at 415 nm is narrow and has shoulder around 395 nm, whereas the Soret band of ZnOEP is blue-shifted to 408 nm with the shoulder at 388 nm (respectively 400 nm and 380 nm in DMF), and is slightly broader. In contrast to the Soret band, the Q bands of ZnOEP are narrower than those of ZnTPP and both show a different vibronic progression. ZnTPP show a strong 1-0 vibronic band at 545 nm, with weak 0-0 and 0-2 bands, whereas the 0-0 band of ZnOEP is much stronger than the vibronic bands (in both cyclohexane and DMF solvents).

The conjugated effect of a central metal atom and a peripheral group is hard to explain. However, one reason could be that the 8 ethyl groups on the pyrrole rings constitute a stronger perturbation of the HOMO than the phenyl groups on the meso positions.²⁰⁸ Indeed, the Q band of ZnOEP is about 2.5 times more intense with respect with their B band than that of ZnTPP , and is thus more allowed. As a consequence, the weight of FC contribution to the spectrum, i.e. the 0-0 band increases at the expense of the HT contribution, i.e. the 0-1 band. Ohno et al. suggested that the intensity ratio of the 0-0 to the 0-1 transition is indicative of the energy difference between ($a_{2u}e_g$) and ($a_{1u}e_g$) states. In

parallel, the coordinating property of the solvent is known to influence the static absorption in a similar way for TPP.²²⁰ However, this effect is reversed for OEP. Indeed, Figure 2.8a reports also the absorption and emission spectra of ZnOEP in dimethylformamide, a strongly coordinating solvent. This influence, related to the electron-donating properties of the solvent molecule, is in agreement with the fact that ligand coordination and substituent on the meso positions are affecting the same orbital, i.e. the a_{2u} HOMO (Figure 2.4).

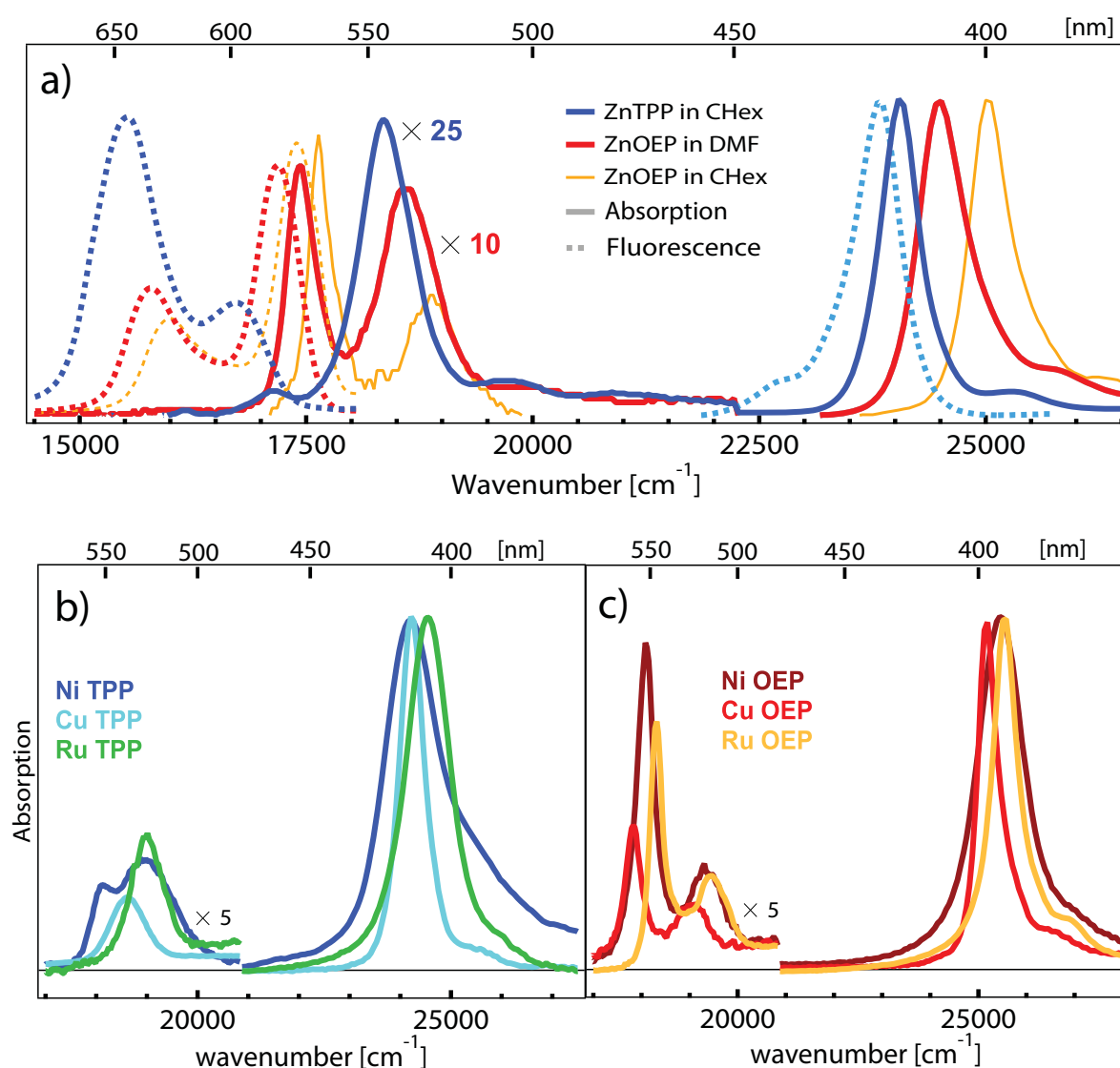


Figure 2.8: a) Steady state absorption (continuous lines) and emission (dashed lines) of ZnTPP in cyclohexane (blue lines) and ZnOEP in dimethylformamide (red lines). Absorption and emission spectra of ZnOEP in cyclohexane is also shown (thin orange lines). b) Steady state absorption spectra of Ni, Cu and Ru TPP. c) Steady state absorption spectra of Ni, Cu and Ru OEP. In all panels, the Q band region is amplified by a factor indicated close to the spectrum.

Both Zn porphyrins show emission from the *Q* band with QY of 0.03 for ZnTPP and 0.04 for ZnOEP,^{221,222} decaying on the ns timescale to a triplet state by ISC. In addition, ZnTPP shows fluorescence from the Soret band, reflecting a very inefficient $S_2 \rightarrow S_1$ IC. Indeed, this IC has been followed by fluorescence up-conversion and a timescale of 1-2 ps was observed.²²³⁻²²⁶ The absorption spectra of transition metal porphyrins are similar to the Zn ones. Figure 2.8b and c show the absorption of Cu, Ni and Ru TPP and OEP respectively. The major difference of these compounds compared to the Zn ones is their lack of fluorescence emission. This is due to an efficient quenching of the excited porphyrin ring through charge transfer to the empty d orbitals, provided by the transition metals. Until now, no time-resolved *Q* band emission measurements of these compounds have been reported.

2.4 Haemoproteins

The next step of the present work consists in extending the bulk solvent investigation of Trp and Haem-like systems to the protein environment, and more specifically to the wild type haemoproteins. It has been shown that in such biological systems, it is possible to artificially trigger a biological function by the use of impulsive photoexcitation. The mechanism of ligand releasing after ligand-haem bond photodissociation has been extensively studied in haemoglobin and myoglobin through time-resolved spectroscopic experiment.²²⁷⁻²³⁵ However, the electronic relaxation dynamics responsible for the photodissociation are still not elucidated. In particular, from which electronic excited state does the bond breaking occur, and how fast the system reaches this states are still unanswered questions. In addition, the extension of the fluorescence up-conversion technique to the UV allows following the dynamics of the photoexcited Trp residue in different protein environments. The 3D structure of the haemoproteins investigated here are presented in Figure 2.9.

The visible part of the electronic absorption spectrum of haemoproteins is dominated by the haem absorption features, the main characteristic of which are corresponding to those of porphyrin (B and Q bands), just described above. The absorption of Trp residue dominates the near UV region (250-300 nm), whereas more in the UV ($\lambda < 270$ nm) contributions from other aminoacids as tyrosine have to be considered. The characteristic features of absorption of cytochrome c and myoglobine are now discussed.

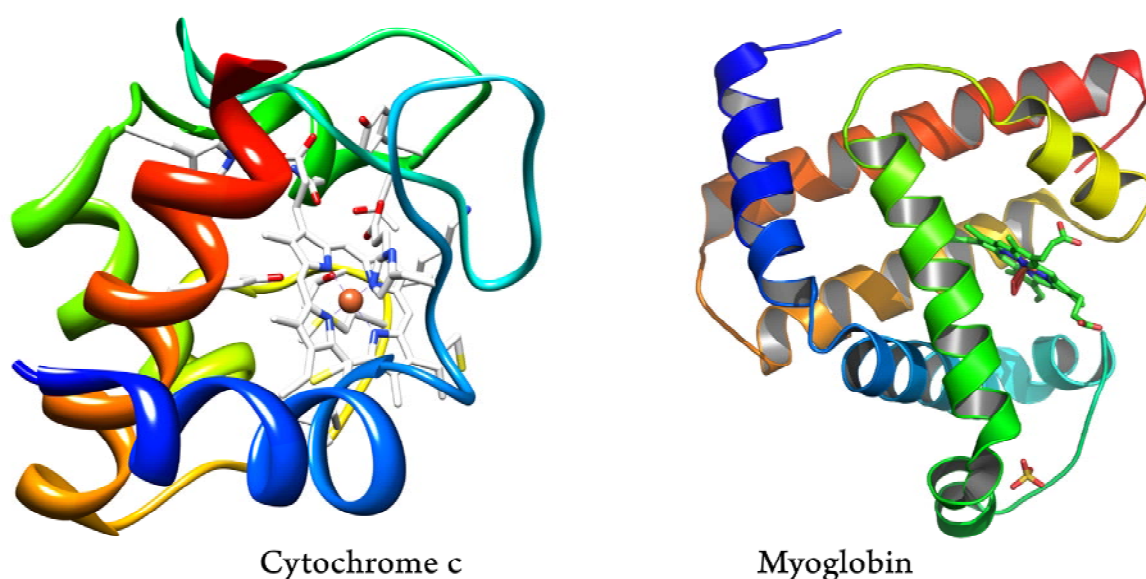


Figure 2.9: 3D structures of Cytochrome c and Myoglobin haemoproteins

2.4.1 Cytochrome c

Cytochrome c is a relatively small and highly soluble haemoprotein. It is loosely associated with the inner membrane and is involved in the electron transport chain of mitochondria.^{236,237} The Cyt c active site consists of a 6-coordinated iron porphyrin capable of undergoing oxidation and reduction. Histidine (H18) and methionine (Met80) residues constitute the biaxially ligated side chains of the haem and are of particular relevance to its stability and functionality.²³⁸ Moreover, both ferric and ferrous redox states play important physiological roles. The Met80 axial ligand is known to undergo photodissociation upon Visible excitation, and to recombine in ~ 6 ps.^{239,240} This peculiarity makes Cyt c a useful system to study the geminate ligand photodissociation-recombination cycle. Moreover, in hemoproteins, the photo-excited Trp residue is known to undergo Förster-Dexter resonance energy transfer to the haem group, whose efficiency depends on the distance and relative orientation of the Trp-haem pair.^{241,242} For this reason, it has been extensively used to study protein folding through emission QY measurements.^{243,244} Cyt c contains only one tryptophan residue, very close to the haem group (~ 9 Å), and known to undergo very efficient energy transfer to it.²⁴⁵

Figure 2.10 shows the UV-Vis steady-state absorption spectra of ferrous and ferric Cyt c. The haem group is responsible for the main features of these spectra with bands at 500-550 nm (Q band), 410-415 nm (B or Soret band) and 250-290 nm,^{206,209,246} all due to porphyrin transitions. The 250-300 nm region contains the absorption band of Trp and slightly more to the blue that of the four tyrosine residues. At the excitation wavelength of 286 nm, we estimate that $\sim 25\%$ of the absorption is due to the tryptophan, 65 % to the haem prosthetic group (namely the δ band²⁴⁶), and less than 10% to the four Tyrosine residues.

The UV fluorescence emission of Cyt c stems mainly from Trp.^{238,247,248} A bimodal fluorescence was however observed at low pH and investigated by Löwenich *et al.*²⁴⁹ through excitation-wavelength-dependent fluorescence spectroscopy. They claimed that upon excitation at 280 nm and at pH 7, the porphyrin system contributes about 80 % and tryptophan about 20 % to the total fluorescence. They fitted the stationary emission spectrum of Cyt c with two broad Gaussians, respectively centered at 355 nm for the Trp contribution and 370 nm for the haem contribution.

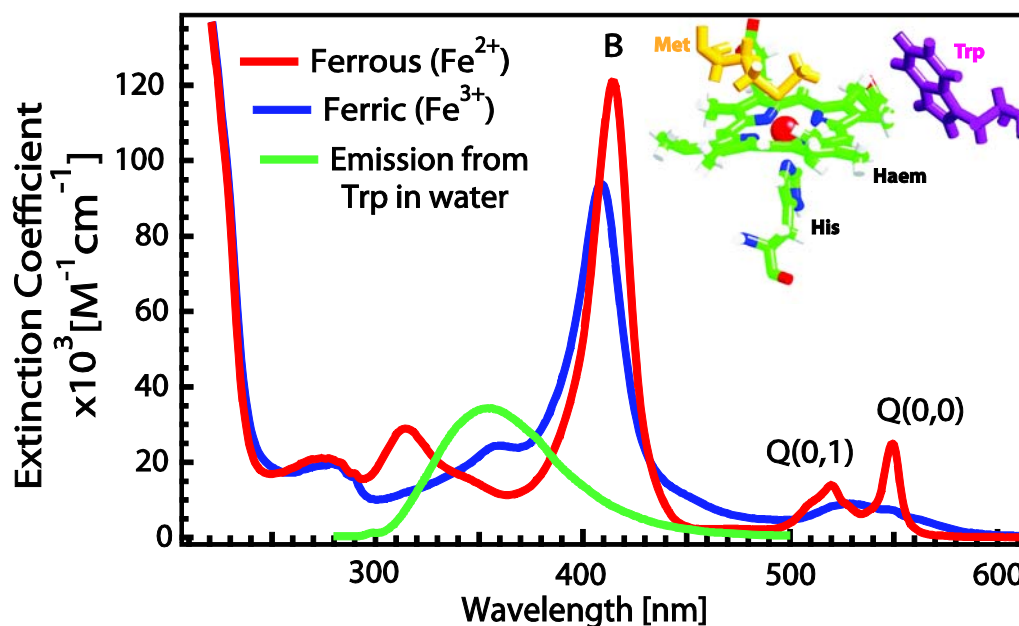


Figure 2.10: Absorption spectra of ferrous (red) and ferric (blue) Cyt c at pH 7. The excitation wavelengths are marked by arrows and the range of detection in the fluorescence and transient absorption experiment are highlighted in green and yellow, respectively.

The primary photoprocesses of ferrous Cyt c, after photodissociation, have already been investigated through femtosecond transient absorption exciting the cofactor within the so-called Soret or Q bands (400-420 nm and 500-560 nm, respectively) and probing in the Visible range.^{239,240} The derived picture is the photolysis of the Met axial ligand in 10's of femtosecond followed by its geminate recombination, accompanied by Internal Vibrational Redistribution (IVR) and Cooling dynamics. In the last decade, several works have strongly suggested that the impulsive photodissociation occurs via a Ligand-to-Metal-Charge-Transfer (LMCT), where "Ligand" stands for the porphyrin macrocycle:^{234,250-252} after photoexcitation, an electron is transferred from the porphyrin ring to a metal axial d orbital which corresponds to an anti-bonding state.^{227,234} The subsequent ligand-cleavage brings the haem from a 6 to a 5 coordinated high-spin state, accompanied by a doming of the porphyrin plane.^{239,240}

2.4.2 Myoglobin

Myoglobin is the protein responsible for the oxygen transport and storage in the muscle tissues. Relatively small like Cytochrome c (153 residues), it has been thoroughly studied since it represents the model haemoprotein with ligand-regulated biological activity. Its active site, a haem prosthetic group, consists of a 5-coordinated iron porphyrin capable of undergoing oxidation and reduction. A histidine (H93) residue constitute the proximal

axially ligated side chains on the haem iron, whereas a di- or triatomic molecule (O_2 , H_2O , CO , CN , etc...) may bind the iron atom on the opposite (“distal”) side of the haem. The latter diatomic ligands are known to undergo light-induced dissociation.²⁵³ This ligand photodissociation has been extensively studied by various time-resolved spectroscopic techniques,²⁵⁴⁻²⁵⁶ in order to investigate the related conformational transformations, and to study more generally the structures, dynamics and thus the functions of the protein. Myoglobin contains two tryptophan residues, with different orientation and distance with respect to the haem group, undergoing resonant energy transfer to it with distinct timescales.²⁴¹ As far as we are concerned, in this system we are mainly interested in the Trps fluorescence spectral evolution at early times, in a way to extract information about local protein dynamics as well as in the haem fluorescence, giving information about its electronic relaxation. We decided to study the wild type Myoglobin in its met form in buffer solution ($pH = 7$). This form, in which a water molecule is bound to the iron in the ferric state,²⁵⁷ is the most stable but the less studied, since the water ligand is believed to not photodissociate.²³⁵

The static absorption spectrum of aqueous metMb at $pH 7$ is reported in Figure 2.11. The main contribution to the spectrum stems from the haem group, through the Q, Soret, N and L bands at respectively 505, 409, 357 and < 290 nm. The latter is overlapped with the contribution from 2 Trp, absorbing at 289 nm. At this wavelength, corresponding to our excitation wavelength, the respective contribution amounts to 57% for the haem, 41% for the two Trp and 2% for two tyrosine residues.

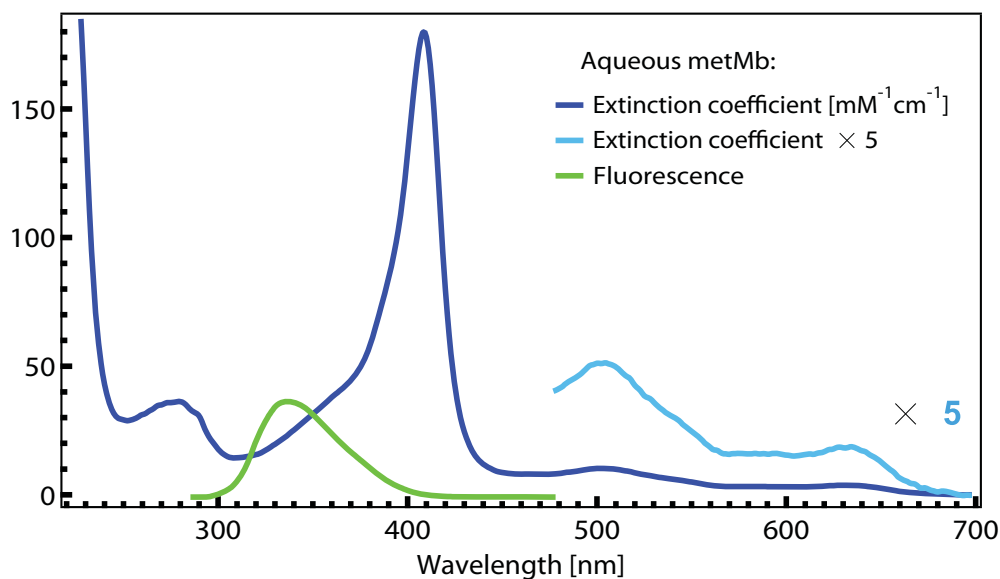


Figure 2.11: Absorption and emission spectra of metMb at $pH 7$. The emission spectrum was acquired under 290 nm excitation.

2.5 Metal-polypyridine complexes

The transition metal complexes²⁵⁸ constitute an important class of coordination chemistry compounds. Their chemistry is determined by the presence of unpaired d electrons involved in the molecular bonding with the coordinating ligands.²⁵⁹ The resulting basic physical properties are described in the frame of the Ligand Field theory,²⁶⁰ which consider the ligand as an external electrostatic perturbation term in the molecular Hamiltonian. The photophysics of such compounds strongly depends on the electronic configuration of the transition metal. Owing to their excitation energies generally lower than for most organic molecules, the visible excitation can trigger photochemical reactions in transition metal complexes. Such excitation usually corresponds to mixed metal and ligand excited states of low energy, with charge transfer character.²⁶¹ These are conventionally named Metal-to-ligand-charge-transfer (MLCT) states. Our group has recently characterized two aqueous metal-tris-bipyridine complexes (namely the Ru- and Fe- one) with both X-ray and optical time-resolved spectroscopy.²⁶² While in $[\text{Ru}(\text{bpy})_3]^{2+}$ the photoexcitation leads to long-lived MLCT excited states, in $[\text{Fe}(\text{bpy})_3]^{2+}$ the MLCT excited states are extremely short-lived due to efficient ISC to lower-lying metal centered (MC) states corresponding to an ultrafast back electron transfer.²⁶³ However in both systems, the fluorescence emission observed is instantaneously Stokes shifted and quenched in < 30 fs by ISC to lower lying triplet states (ISC rate estimated to 15 ± 10 fs).^{52,186}

In the view to extend this investigation to the application of these dyes in dye-sensitized-solar-cells (DSSCs), we decided to study in more details the early intra- and intermolecular dynamics occurring in these compounds in solution, and to focus on another dye commonly used in such solar cells, the RuN719 complex in solutions well as adsorbed onto a semiconductor substrate.

2.5.1 $[\text{Ru}(\text{bpy})_3]^{2+}$ and $[\text{Fe}(\text{bpy})_3]^{2+}$

The ruthenium(II)-(tris-bipyridine) metal complex, $[\text{Ru}(\text{bpy})_3]^{2+}$ is one of the most widely studied coordination chemistry compounds since the 1950's.²⁶⁴⁻²⁶⁷ It serves as model molecule for intramolecular electron transfer reactions and more specifically it is a paradigm molecule for transition metal-based devices for solar energy conversion.²⁶⁸ The ferrous-(tris-bipyridine) complex, $[\text{Fe}(\text{bpy})_3]^{2+}$ is also extensively studied, but for its prospective applications in magnetic data storage.²⁶⁹ In particular, the main interest in this

compound is focused on the phenomenon of spin crossover, that can be induced by light excitation.²⁷⁰

Static absorption spectra

Figure 2.12 shows the static absorption spectrum of these complexes. The band assignment are reported in table 2.2. The UV range ($33'000\text{-}50'000\text{ cm}^{-1}$) is dominated by intra-ligand ($\pi \rightarrow \pi^*$) and ligand-to-metal charge transfer transitions. In addition, the $[\text{Ru}(\text{bpy})_3]^{2+}$ complex contains metal-centered transition the near UV region ($28'000\text{-}33'000\text{ cm}^{-1}$). However, the lowest energy transition (HOMO \rightarrow LUMO) is a broad band centered at $22'200\text{ cm}^{-1}$ and $19'200\text{ cm}^{-1}$ in $[\text{Ru}(\text{bpy})_3]^{2+}$ and $[\text{Fe}(\text{bpy})_3]^{2+}$, respectively. The excited state is a metal-to-ligand charge transfer state, corresponding to promotion of an electron from the d orbitals of Ru^{2+} to the π^* orbital of the bipyridine (bpy) ligand. This $^1\text{MLCT}$ absorption band is dominated by a progression of the skeletal C=C mode at 1607 cm^{-1} of the bpy with a Huang–Rhys factor of 0.74.²⁷¹

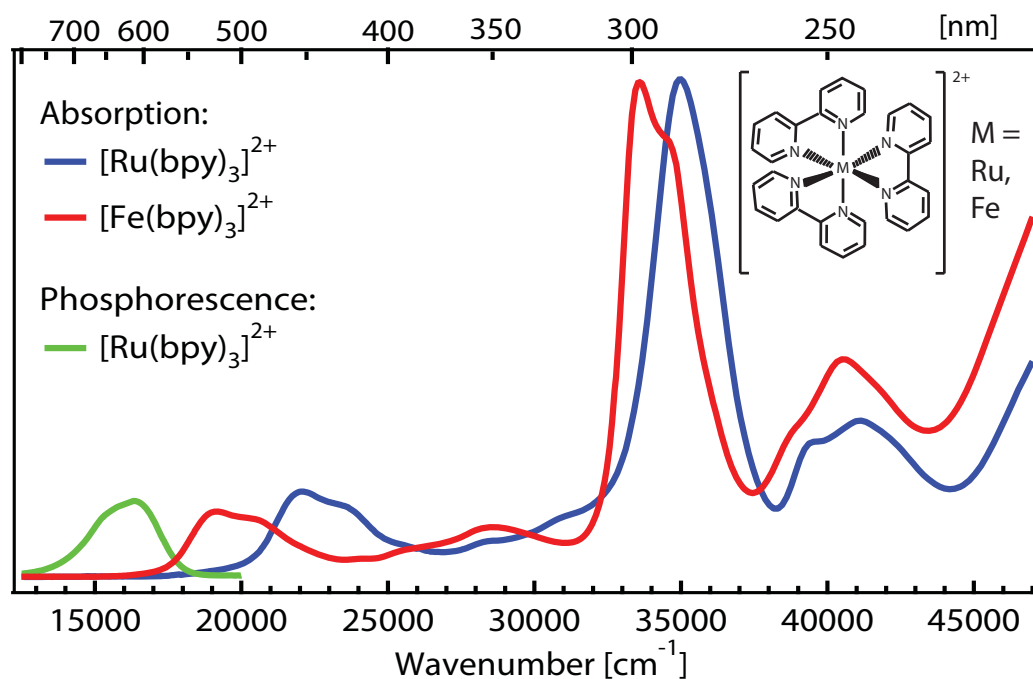


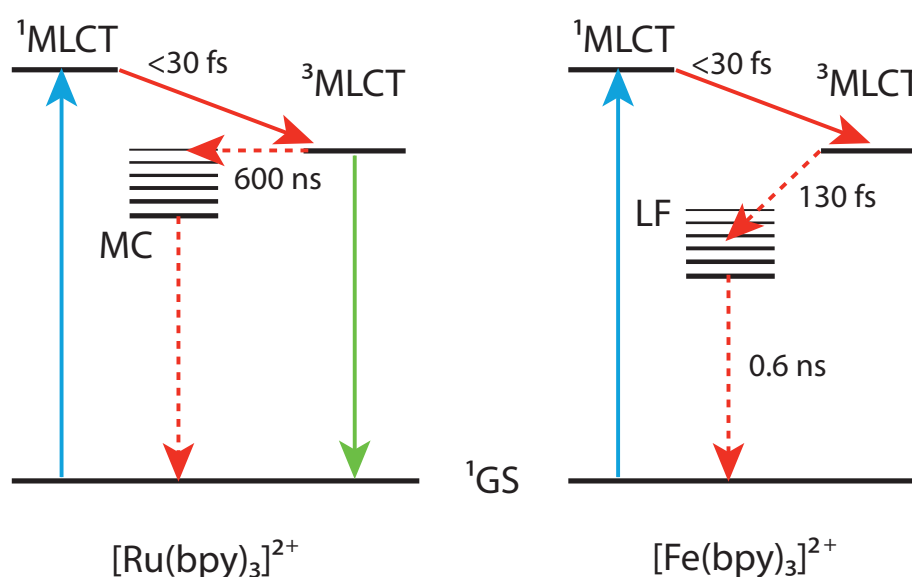
Figure 2.12: Absorption spectra of aqueous $[\text{Ru}(\text{bpy})_3]^{2+}$ (blue) and $[\text{Fe}(\text{bpy})_3]^{2+}$ (red) normalized to the maximum (extinction coefficient values are reported in table 2.2), along with the phosphorescence spectrum of $[\text{Ru}(\text{bpy})_3]^{2+}$ (green).

Table 2.2: Assignment of the absorption bands of $[\text{Ru}(\text{bpy})_3]^{2+}$ and $[\text{Fe}(\text{bpy})_3]^{2+}$ complexes in water.²⁶²

Complex	Wavelength [nm]	Wavenumber $\cdot 10^3 [\text{cm}^{-1}]$	Assignment	Extinction coefficient $\cdot 10^3 [M^{-1} \text{cm}^{-1}]$
$[\text{Ru}(\text{bpy})_3]^{2+}$ Ref. ^{265,272}	200-300	33-50	Ligand-centered	50-80
	220-260	38-45	Ligand-to-metal-charge-transfer	15-26
	300-360	28-33	Metal-centered	6-20
	380-520	19-26	Metal-to-ligand-charge-transfer	5-15
	620	16	Metal-to-ligand-charge-transfer	-
$[\text{Fe}(\text{bpy})_3]^{2+}$ Ref. ^{273,274}	200-320	31-50	Ligand-centered	50-80
	320-400	25-31	Metal-to-ligand-charge-transfer	60-70
	450-590	17-22	Metal-to-ligand-charge-transfer	30-80

Photochemical cycle

The scheme of the relaxation pathway of $[\text{Ru}(\text{bpy})_3]^{2+}$ and $[\text{Fe}(\text{bpy})_3]^{2+}$ photoexcited at 400 nm are depicted in Figure 2.13. In both complexes, the excited $^1\text{MLCT}$ state undergoes an ultrafast (< 30 fs) ISC to a triplet $^3\text{MLCT}$ state, still localized on the ligand.²⁶² In $[\text{Ru}(\text{bpy})_3]^{2+}$, the triplet state is long-lived (see the phosphorescence spectrum in Figure 2.11), nevertheless quenched on a 600 ns timescale by efficient nonradiative deactivation through the high vibrational levels of the metal-centered and ground states. Conversely, in $[\text{Fe}(\text{bpy})_3]^{2+}$ the decrease in ligand-field strength results in the presence of a minifold of lower lying states of high spin configuration, allowing fast (130 fs) deactivation of the $^3\text{MLCT}$ state by spin cross over transition.²⁶³

**Figure 2.13:** Energy level schemes of $[\text{Ru}(\text{bpy})_3]^{2+}$ (right) and $[\text{Fe}(\text{bpy})_3]^{2+}$ (left).

2.5.1 RuN719 and Dye Sensitized Solar Cells

The semiconductor used in DSSCs is titanium dioxide (TiO_2). Its high refractive index, chemical stability and its low production cost make it the best candidate for this application. On the other hand, the bandgap of TiO_2 is 3.2 eV and consequently does not absorb light of wavelength above 400 nm. This semiconductor has to be sensitized to longer wavelengths to obtain an efficient solar light energy conversion. The best sensitization is achieved with the use of anchored dye molecule.^{275,276} The excited state of the latter, accessed by visible light absorption, has an oxidation potential allowing electron injection into the conduction band of TiO_2 . This photocycle is depicted in Figure 2.14.^{268,277} The subsequent regeneration of the dye ground state is ensured by a redox mediator in the electrolyte solution, usually iodide (I^-/I_3^-).

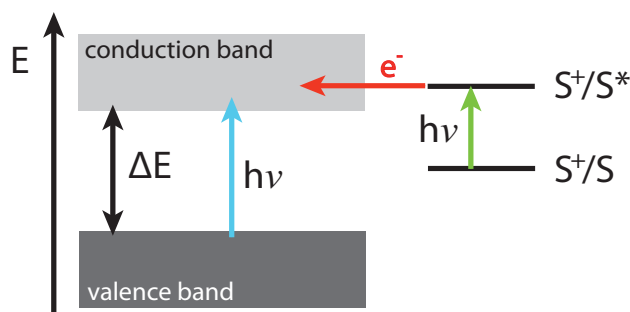


Figure 2.14: Simplified scheme illustrating the mechanism of dye sensitization. Light with energy lower than the bandgap promotes electron in the conduction band through the excited state of the dye sensitizer (S).

However, the light harvesting ability of single layers of dye molecules adsorbed onto a planar semiconductor surface is low. The use of mesoporous nanocrystalline films increases the available surface by three orders of magnitude,^{278,279} significantly improving the efficient of the DSSCs up to ~12%.²⁸⁰

The photophysics of the Ru complex described in the previous section, in particular the long-lived metal-to-ligand charge transfer excited state, make it an efficient sensitizer. However, the extinction coefficient in the visible significantly drops above 500 nm. This drawback has been overcome by substitution of one bipyridine ligand with two isothiocyanate (S-C-N) groups, which are displacing the HOMO towards themselves inducing a shift of the absorption spectrum to the red. Moreover, two carboxylic (COOH) groups were added to the two remaining bpy ligands in order to efficiently anchor the dye onto a semiconductor surface.²⁸¹ The final molecular structure and the absorption spectrum

of RuN3 ($[\text{Ru}(\text{dcbpyH}_2)_2(\text{NCS})_2]^{2+}$) and RuN719 ($(\text{Bu}_4\text{N})_2[\text{Ru}(\text{dcbpyH})_2(\text{NCS})_2]^{2+}$) are shown in Figure 2.15. The two lowest energy bands at $18\,900$ and $26\,300\text{ cm}^{-1}$ (380 and 530 nm) are assigned to $d \rightarrow \pi^*$ $^1\text{MLCT}$ transitions as in the case of $[\text{Ru}(\text{bpy})_3]^{2+}$. RuN719 is the deprotonated form of RuN3, obtained by addition of tert-butylammonium (*t*-BA) groups to set the net charge of the compound to zero. The deprotonation acts on the spectrum by slightly shifting the bands to the blue. The triplet $^3\text{MLCT}$ state is weakly luminescent and decays with a lifetime of $\sim 10\text{ ns}$. As we will see in chapter 8, the substitutions affect only weakly the photochemical cycle and the description of the relaxation pathway of $[\text{Ru}(\text{bpy})_3]^{2+}$ is still valid for these compounds.²⁷⁵ However, such changes (addition of substituents) are monitoring the redox potential of the dye, thus changing the electron injection efficiency. This is not the purpose of the present study and no consideration of the influence of this parameter is pursued here.

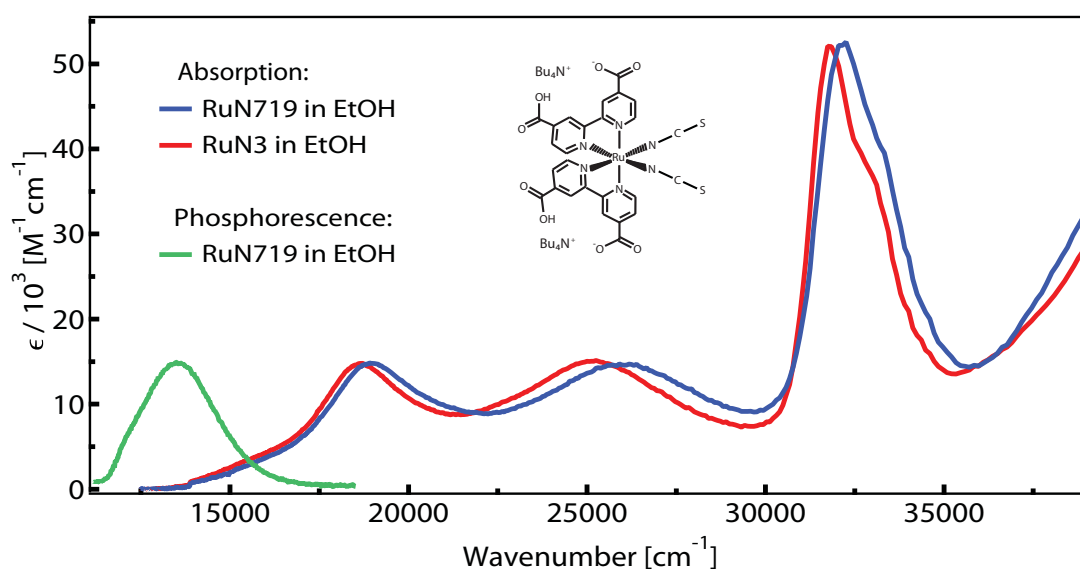


Figure 2.15: Extinction coefficient of RuN3 (red) and RuN719 (blue) in ethanol, along with the phosphorescence spectrum of RuN719 (green) in ethanol.

Electron injection mechanism

A central issue for the optimization of the efficiency of dye-sensitized solar cells is the detailed understanding of the mechanism of electron injection. Much effort has been devoted to the optimization of the sensitizer of DSSCs in the past 15 years, mainly using nanosecond and femtosecond transient absorption spectroscopy in the visible, near-IR, and mid-IR spectral regions.²⁸²⁻²⁹² Overall these studies concluded that at least part of the photoinduced electron transfer in the RuN3-TiO₂ films occurs in $< 100\text{ fs}$. This was also

one of the reasons to believe that the electron injection may occur from non-thermalized vibrationally excited states prior to internal energy relaxation in the sensitizer. Sundström and co-workers addressed this question in a systematic way by transient absorption spectroscopy of RuN3 on TiO₂ in the 400-1100 nm range with a time resolution of ~30 fs.²⁹¹ In particular, at the shortest time delays, which deal with injection from the ¹MLCT state, they probed the stimulated emission at 600 nm, observing an instantaneous rise of the signal and a fast recovery with a time constant of ~30 fs to a level, caused by the overlapping ground state bleach, that remains constant for several picoseconds. This was supported by a measurement of the ³MLCT state formation, which was probed at 1050 nm, a region where its absorption is supposed to be broad and featureless, and therefore insensitive to cooling processes. However, the probed region also contains a non negligible absorption by the conduction band electrons. By measuring the rise time of the ³MLCT of RuN3 in solution they independently estimated an intersystem crossing (ISC) of ~70 fs. From this value and the total relaxation rate of (30 fs)⁻¹, they concluded that the injection occurs at a rate of (50 fs)⁻¹ and proceeds from a non-thermalized singlet state.

Bhasikkuttan and Okada reported the first femtosecond fluorescence measurements at single emission wavelengths of the RuN3 dye in ethanol with a resolution of 130 fs.²⁹³ They deduced an ultrafast decay of the Franck-Condon state of ~40 fs at 600 nm, which they attributed to intersystem crossing and internal conversion. They also noted a lengthening of the decay time towards longer emission wavelengths. As pointed out by them, the limited data available under such conditions did not allow getting a full picture of the ultrafast relaxation kinetics. In addition, their laser source ran at a repetition rate of 82 MHz (period 12 ns), while the ³MLCT lifetime of RuN3 in ethanol is 59 ns,²⁹⁴ which may cause build-up problems due to re-excitation of the excited state by subsequent pulses.

In chapter 8, we show a clarified picture of the early intramolecular relaxation of this family of compound, and we show the relevance of such dynamics on the electron injection mechanisms in Dye Sensitized Solar Cells.

Chapter 3

Experimental

- 3.1 Introduction
- 3.2 Sum frequency generation
- 3.3 The set-up
 - 3.3.1 Femtosecond laser system*
 - 3.3.2 Excitation and gate Beam*
 - 3.3.3 Sample flow*
 - 3.3.4 Emission collection and time-gating*
- 3.4 Data treatment
- 3.5 Set-up characterization
 - 3.5.1 GVD*
 - 3.5.2 Spectral Response*
 - 3.5.3 Temporal Resolution*
 - 3.5.4 Polarization*

3.1 Introduction

Time-resolved luminescence spectroscopy is beyond all doubts a powerful tool to investigate early dynamical behavior of many physical systems in condensed phase. An intense research activity in the past decades have shown that most of non-radiative intramolecular processes (IC, IVR) as well as most of early intermolecular dynamics occur on the femtosecond to 10s of picosecond timescale.^{19,72,295} Since the first experiments with flash lamps (George Porter Nobel prize, 1967), the time resolution has been pushed more and more to these timescales: Nowadays, the most advanced electronic-based detection systems (e.g. fast photomultiplier, time-correlated photon counting, streak camera) reach the picosecond time domain. The subsequent step to fs resolution has been possible only with the advancement of femtosecond pulsed laser technology. This brought a new approach of time-resolved spectroscopy, allowing the development of new techniques based on non-linear optical phenomena, as e.g. sum frequency, four-wave mixing, etc... The far more popular technique is the pump-probe one,²⁹⁶ which consists in probing the changes in absorption after excitation of the sample with a femtosecond pulse. Thanks to a relatively simple implementation it provides both femtosecond resolution and broad-band detection, and gives direct access to ground and excited state dynamics. Indeed, the transient absorption (TA) signal contains contribution from ground state bleaching (GSB), excited state absorption (ESA), and stimulated emission (SE). The overlap of these multiple contributions often makes the interpretation of TA ambiguous, in particular at the earliest times. In this respect, time-gated emission provides a more straightforward signal since it reports only on the emissive, populated excited states. Following the temporal evolution of the emission is therefore the best approach to extract information about excited states relaxation.

The concept of femtosecond resolution emission, illustrated in Figure 3.1, requires the use of two synchronized pulses, of which the second can be deliberately delayed with the required fs precision. The first pulse is used to impulsively excite the sample molecules. The time-dependent emission is then focused onto a non-linear medium. The second gate pulse will mix with the emission, generating a third pulse proportional to the emission intensity. The emission profile is recovered as time slices, with temporal window corresponding to the laser pulse width. Therefore, varying the delay between the excitation and gate pulse allows full reconstruction of the temporal evolution of the emitting state(s).

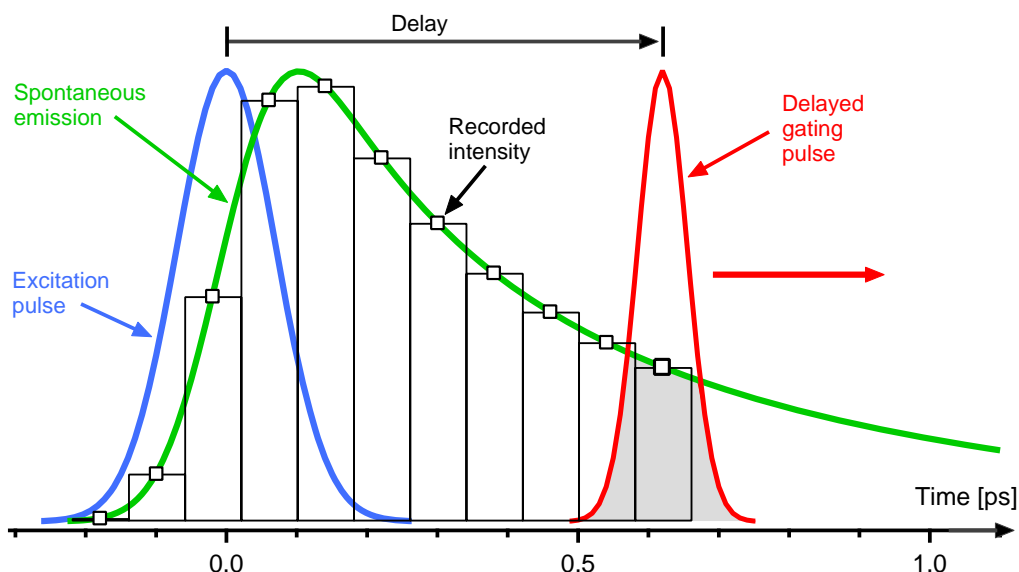


Figure 3.1: Basic principle of time-gated fluorescence techniques. The emitted photons are sliced by the gating pulses in the non-linear medium. The detected signal (squares) directly reflects the time-dependent intensity profile of the spontaneous emission.

Only few techniques allow time-gating of the emission with femtosecond resolution. One is based on the optical Kerr effect:²⁹⁷ an optical shutter is simulated by two crossed polarizers with an isotropic Kerr medium in between. The emission light is transmitted only when this shutter is activated by a gate pulse that induces optical anisotropy in the Kerr medium. This technique allows both broad-band detection and femtosecond resolution. However, it is not suitable for our requirements, since the detection window does not cover the UV range and the emission polarization is not easily monitored. Another approach, based on non-collinear optical parametric amplification (NOPA),²⁹⁸ is also not suitable because of a large background contribution and a too narrow spectral detection range. Finally, the last possibility is the fluorescence up-conversion,²⁹⁹ based on the nonlinear phenomenon of sum frequency (SF) generation. In this technique, the emission is mixed with a delayed gate pulse to generate the SF radiation (Figure 3.2).

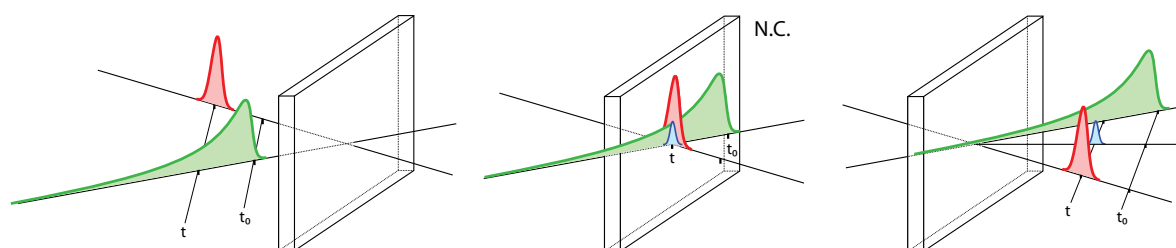


Figure 3.2: Schematic cartoon of the fluorescence up-conversion technique: The sum-frequency signal (blue) is generated only when fluorescence (green) and gate (red) photons are simultaneously present in the non-linear crystal (N.C.).

Owing to the birefringent nature of the non-linear crystal, only a specific emission frequency can be efficiently mixed with the gate frequency for a given crystal angle (phase matching condition, §3.2). The achievable acceptance bandwidth is inversely proportional to the crystal thickness and playing with this parameter allows to overcome the spectral range limitation. For instance, Schanz *et al.*³⁰⁰⁻³⁰² used a specific non-linear crystal (KDP), thin enough to achieve a large bandwidth. However, this method does not satisfy our requirements. Indeed the sum frequency efficiency of KDP is not high enough in the UV. Moreover, the generated signal intensity would be low since it is proportional to the square of the crystal thickness. We rather employed another method to achieve a broadband detection, which needs the automation of the non-linear crystal phase-matching position. The tilt angle of the crystal was continuously varied during the acquisition at a given delay time, in a way to satisfy the phase-matching condition of all wavelengths of the broad emission spectrum.

The measurements reported in this thesis have been performed with a broadband (300-700 nm) up-conversion detection set-up, with tunable excitation in the UV-Vis (250-640 nm).

3.2 Sum frequency generation

Nonlinear optics concerns the nonlinear dielectric response of matter to an applied electric field \vec{E} . These non-linear contributions to the polarization are described by higher order terms of susceptibility χ :³⁰³

$$\vec{P} = \varepsilon_0 \left(\chi^{(1)} \vec{E} + \chi^{(2)} \vec{E}^2 + \chi^{(3)} \vec{E}^3 + \dots \right) \quad (3.1)$$

where $\chi^{(n)}$ is the n th order susceptibility. If the electric field is intense enough, nonlinear terms of the polarization \vec{P} are considered. In our set-up, we are using the second order term for the second harmonic generation (SHG), the optical parametric amplification (OPA) and the sum frequency generation (SFG). We are only interested in the sum frequency generation here, at the core of the up-conversion technique. The incident electric fields, corresponding to the fluorescence and gate photons of energy $\hbar\omega_F$ and $\hbar\omega_G$ respectively, are mixed together to produce the up-converted signal of energy $\hbar\omega_S$. Beside the energy conservation law

$$\omega_S = \omega_F + \omega_G \quad (3.2)$$

the momentum conservation law

$$\vec{k}_S = \vec{k}_F + \vec{k}_G \quad (3.3)$$

where \vec{k}_S , \vec{k}_G and \vec{k}_F are the wave vector of the signal, fluorescence and gate beams, constitutes the phasematching condition.^{302,304} At this point we need to introduce the phase mismatch parameter $\Delta\vec{k}$, which has to be set to zero to maximize the sum frequency mixing process:²⁹⁹

$$\left| \Delta\vec{k} \right| = \left| \vec{k}_S - \vec{k}_F - \vec{k}_G \right| = \frac{n(\omega_S)}{\lambda_S} - \frac{n(\omega_F)}{\lambda_F} - \frac{n(\omega_G)}{\lambda_G} \quad (3.4)$$

where $n(\omega)$ is the index of refraction at the frequency ω . We can, thanks to the birefringent property of the nonlinear crystal used in our set-up, reduce this parameter by tuning the effective refractive index through rotation of the crystal. This condition depends on the polarization of the three beams. We are using the type I phase-matching condition, i.e. with fluorescence and gate electric fields polarized horizontally, implying a vertical polarization of the sum frequency signal.

Another geometrical consideration affects the phase mismatch parameter: the collinearity of the three wave vectors. If the maximum of efficiency is achieved in a perfect collinear configuration (Figure 3.3), we intentionally choose to deviate from this condition, in order to realize a better signal filtering through spatial selection of the up-converted photons.

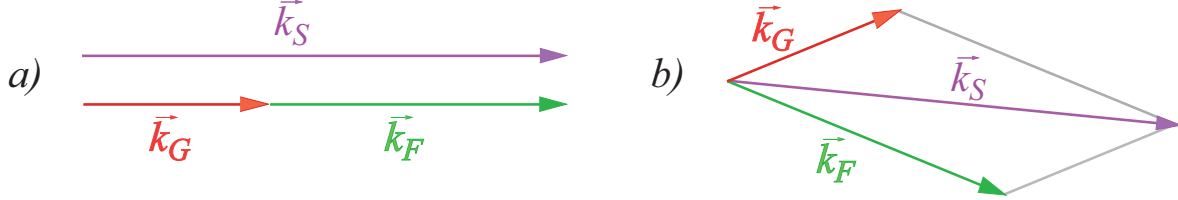


Figure 3.3: a) collinear and b) noncollinear configuration for sum frequency mixing.

Finally, in the low depletion regime, the efficiency of the up-conversion process η is the ratio between the generated and incident numbers of photons, given by the following expression.^{299,304,305}

$$\eta = \frac{N_S}{N_F} = \frac{2\pi^2 d_{eff}^2 L^2 P_G}{c\epsilon_0^3 \lambda_F \lambda_S n(\lambda_F) n(\lambda_G) n(\lambda_S) A} \cdot \frac{\sin^2(|\Delta\vec{k}|L/2)}{(|\Delta\vec{k}|L/2)^2} \quad (3.5)$$

where d_{eff} is the effective nonlinear susceptibility of the crystal, L its thickness, P_G is the power of the gate beam and A is the overlap area of the mixed beams. The sinc factor in the last equation reflects the effect of a deviation from a perfect phase matching condition, i.e. if $\Delta\vec{k} = 0$. It gives access to the acceptance spectral bandwidth $\Delta\lambda$. In our experiment, with the use of a 250 μm thick BBO crystal, this value is smaller than 1000 cm^{-1} (~ 25 and $\sim 10 \text{ nm}$ respectively in the Vis and UV), i.e. far too small to cover the entire spectral window we are interested in. As previously mentioned, this limitation is overcome by continuously rotating the crystal during the acquisition, in order to cover a large spectral window.

3.3 The set-up

The 800 nm femtosecond pulses used in our experimental set-up was provided by a Ti:Sapphire laser system. The set-up allows two different configurations depending on the excitation wavelength required for the experiment. In both configurations, the main 800 nm beam was splitted in two branches, one for the pump and the remaining for the gate beam. The excitation pulses were obtained either by generating the SHG of the fundamental (400 nm), either by pumping an OPA to generate visible light (500-600 nm) used as it is or frequency doubled (SHG, 250-300 nm). The scheme of the time-gated up-conversion set-up is presented in Figure 3.4.

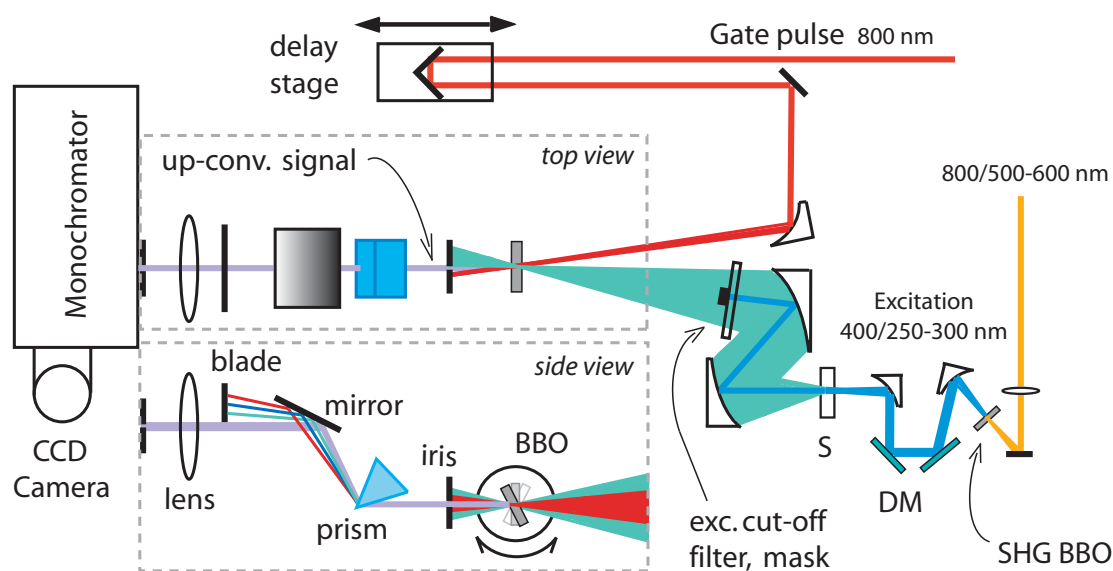


Figure 3.4: Scheme of the time-gated up-conversion experimental set-up. The SFG process and the signal filtering parts are shown both from top and side view.

After excitation of the sample (S), the spontaneous emission is collected and focused with reflective optics onto a 250 μm thick sum-frequency (SF) crystal. The broad emission spectrum is then time-gated by the delayed 800 nm pulses, throughout the continuous rotation of the SF crystal. After spatial filtering of scattered light, the up-converted signal is dispersed by a grating monochromator and finally detected by a liquid nitrogen cooled, UV-enhanced³⁰⁶ CCD-camera.

3.3.1 Femtosecond laser system

The ultrafast laser system consists of a set of Coherent[©] oscillator plus amplifier laser. Two Verdi solid-state single frequency Nd:Vanadate laser (diode-pumped) at 532 nm (CW) are

pumping the oscillator at 3W (V5) and the amplifier at 10W (V10). The oscillator is a Kerr Lens modelocked Mira-SEED Ti:Sapphire laser that produces wide-bandwidth, femtosecond pulses at 800 nm: Horizontally polarized 3 nJ pulses, created at a repetition rate of 82 MHz, have a temporal length of 40 fs and a bandwidth of 40 nm. A grating-based stretcher stage broadens the pulses duration to hundreds of ps before seeding the Ti:Sapphire Regenerative Amplifier RegA which selects one pulse at a tunable repetition rate between 10 and 250 kHz. After around 24 round trips in the cavity, each pulse is amplified to 4 μ J (average power of 1.3 W at 250 kHz). The ejected pulses are compressed by a grating-based compressor to 50 fs pulses. These steps are resumed in the Figure 3.5. As a compromise between energy per pulse and average power, we decided to set the repetition rate of the laser system to 150 kHz.

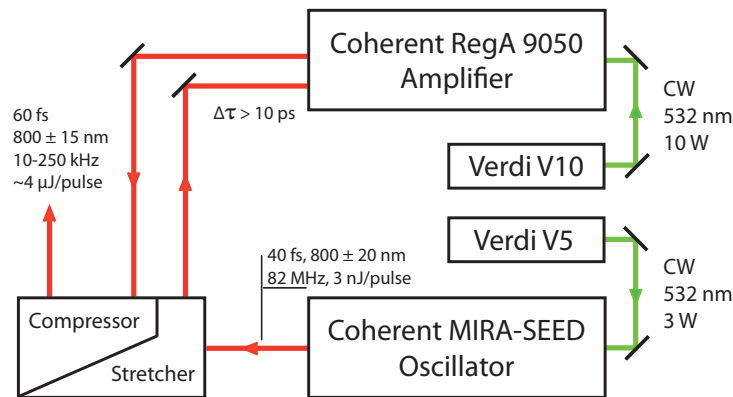


Figure 3.5: Scheme of the Ti:Sapphire oscillator-amplifier femtosecond laser system.

3.3.2 Excitation and gate Beams

In the first configuration, the 800 nm pulses leaving the compressor of the main laser system is split in two branches by a 30%/70% beamsplitter. The weaker (reflected) fraction is focused by a $f = 200$ mm lens on a 0.5 mm thick BBO crystal (Beta Barium Borate³⁰⁷), cleaved at 29° with respect to its optical axis, in order to obtain the 400 nm SHG signal. An efficiency of $\sim 20\%$ was achieved, providing 60 mW at a repetition rate of 250 kHz, corresponding to 240 nJ pulses.

In the second configuration, a 10%/90% pellicle beamsplitter is used to separate gate and excitation branches. The major (transmitted) fraction is used to pump an OPA system, able to deliver 500-600 nm pulses with a bandwidth of 15 nm. At 150 kHz and on average over the wavelength range, the OPA delivers 400 nJ pulses which were compressed to the

optimal value of 50 fs by a set of two SF11 prisms. This beam is then either attenuated by a variable neutral density filter to be directly used for visible excitation of the sample, either focused by a $f = 100$ mm lens on a 0.15 mm thick BBO crystal (cleaved at 43.3°), in order to obtain the 250-300 nm SHG signal, with 10% efficiency.

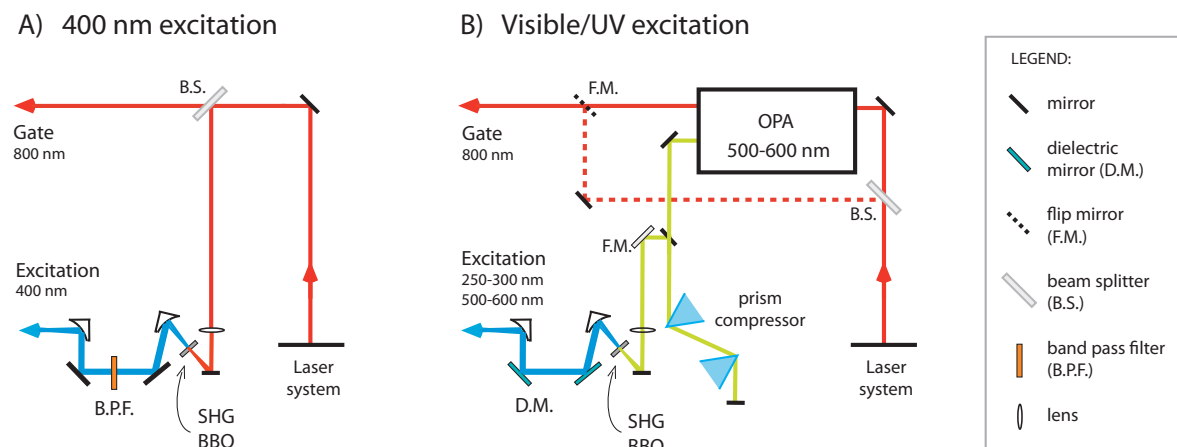


Figure 3.6: Scheme of the excitation and gate beams configurations: A) 400 nm excitation provided by the SHG of the 800 nm laser beam, B) Tunable excitation in the UV and visible region, provided by an OPA. In configuration B), two possible gate pathways are possible, chosen depending on beam quality/intensity requirements (see text).

In both configurations, a 45° off-axis $f = 50$ mm parabolic mirror collimated the generated second harmonic and the remaining fundamental was filtered out by a 2 mm thick BG 39 filter in the case of 400 nm excitation or by two dielectric mirrors in the case of UV excitation. The excitation beam is then focused on the sample by a 90° off-axis $f = 50$ mm parabolic mirror, with a spot diameter at focal point estimated to $30\text{-}40\ \mu\text{m}$. A variable neutral density filter is used before the SHG stage in a way to tune the excitation power. In the case of polarization dependent measurements, an appropriate lambda half wave plate is used before the focalization (see last § of this chapter).

The gate beam is sent in a time delay stage, consisting of a cubic retroreflector mounted on a motorized translation stage, with a feedback position reader.³⁰⁴ The spatial resolution of $0.1\ \mu\text{m}$ allows a time delay step of less than 1 fs. The beam was then focused on the SF crystal with a 30° off-axis $f = 300$ mm parabolic mirror, to reach a spot diameter of $200\ \mu\text{m}$. All the mirrors of the gate branch –including retroreflector and focusing parabolic mirror– are gold coated to improve the reflectivity at 800 nm. In the configuration for 400 nm excitation, the gate power is reduced to ~ 300 mW with a neutral density filter to

avoid thermal damages of the SF crystal and minimize undesired non-linear signal. In the other configuration, the gate power was 40 mW at the position of the SF crystal. In the case of very low up-converted signal intensity, the OPA is pumped with the full power from the laser system, and we use the remaining 800 nm beam of the SHG from the OPA system as the gate, at the cost of worse spatial and temporal profile quality. Indeed the pulse width is increased to 80-90 fs and the spatial mode is elliptically distorted, owing to the SHG stage in the OPA. However, in this condition the gate intensity is tripled and the OPA output is increased of 20%, implying an increase of more than 40% of the UV excitation beam.

3.3.3 Sample flow

The high energy per pulse concentrated on a small sample volume (30-40 μm spot diameter) may generate photoproducts, even on very photostable molecules, and prevent us to use a static cell for the experiment. As a consequence, the sample is flowed through a quartz quality flow cell (48/Q/I Starna), with a minimum speed depending on the sample robustness, excited state lifetime and repetition rate. The different speed requirements are achieved by the use of a peristaltic pump which can reach a speed of 2.4 m/s in the cell, corresponding only to 40% of refreshed sample between two pulses (2.5 shots per sample spot), or a gear pump reaching 7.4 m/s, corresponding to 100% of refreshed sample between two pulses (1 shot maximum per spot), at 150 kHz with a 0.5 mm thick flowcell.

In some occasion, photo-aggregation was observed on the inner window of the flow cell, dramatically influencing the measurements, as a result of the decrease of the transmitted emission signal and increase in the scattering light from excitation. This problem is solved by mounting the sample holder on horizontal and vertical motorized translational stages, changing the spot position on the flow cell during acquisition.

3.3.4 Emission collection and time-gating

Emission is collected by a large solid angle parabolic mirror (45° off-axis $f=50$ mm, 50 mm diameter), and focused on the SF crystal with a similar parabolic mirror but with a $f=250$ mm focal length (see Figure 3.4). 100 mm before the crystal, a long-pass filter (LPF) suited for the excitation wavelength in use, is used to remove the major remaining pump beam intensity. The telescope formed by the two successive parabolic mirrors magnified the excitation spot size by a factor of five, producing an image of the spot of 150-200 μm on the SF crystal. This magnification ratio results from the facts that a large

collection angle is needed and that the refocusing is limited by the acceptance angle of the SF crystal. On the other hand, the emission spot size at the SF crystal needs to be slightly smaller than that of the gate, and both spots have to be minimized in order to reduce effects worsening the time resolution as the the non-collinear geometry (see §3.3.5). As a consequence, the magnification ratio is chosen as a compromise between the optimized sum frequency efficiency and temporal response.

Mainly two SF BBO crystal (250 μm thick) were used in the experiment, with cleavage angle depending on the wavelength detection range investigated: 36° for visible detection (central wavelength of 550 nm) and 50.3° for UV detection (central wavelength of 340 nm). In the particular case of the measurement of Trp in water, we used a 100 μm thick BBO cut at 52.4° (central wavelength of 320 nm) to improve the temporal resolution, at the expense of the signal intensity which was decreased by a factor of 6. The SF crystal is mounted on a motorized rotational stage allowing a rotation amplitude of 40° with respect to the vertical position, corresponding to the phase-matching of a wide wavelength range. The angle is rotated of 20° to cover the 400-700 nm range, whereas it is rotated of 40° to cover the 300-500 nm range. One scan (one rotation) takes 20 seconds.

The non-collinear geometry configuration of the SFG allows an efficient spatial filtering of the main part of emission, gate and residual excitation beams with a diaphragm, positioned after the SF crystal (Figure 3.4). With a fine tuning of its position and aperture size we can select the up-converted signal solely. The signal is vertically dispersed through a quartz prism in order to block with a blade the still remaining scattered light at unwanted wavelengths (Figure 3.4). The up-converted beam is finally focused on the entrance slit of the monochromator (SpectraPro 500i, Acton Research) by a UV coated $f=150$ mm lens. As a compromise between signal intensity, background level due to scattered light and spectral resolution, the slit of the spectrometer is set to between 0.25 and 1 mm. A 600 grooves/mm grating blazed for 300 nm is used to spectrally resolved the up-converted signal, which is detected by liquid nitrogen cooled, Metachrome II charge-coupled device (CCD) camera (SDS 9000, Photometrics). On the CCD, the signal is again spatially selected by integrating only the photons acquired in a diagonal strip array of pixels (horizontal dispersion due to the monochromator and vertical dispersion due to the prism).

3.4 Data treatment

The data file created by the software monitoring the broadband up-conversion set-up is a matrix, with one dimension corresponding to the CCD pixel array (256 pixels with 4×4 binning each), i.e. the wavelength scale, and the other dimension corresponding to the time delay steps. The software delivers also the wavelengths vector (monochromator calibrated with a low pressure mercury lamp (Oriel)) in the up-converted wavelength range. In order to cover the largest time window possible with the smallest number of time steps, specific time files with non-constant step were used.

The raw data matrix is distorted by several effects:

- ▶ The high sensitivity of the CCD camera has the disadvantage to also measure cosmic rays, which appear as strong peaks usually localized on one unique pixel but spread over the CCD randomly. These artifacts are removed by replacing the pixel value with the averaged intensity of the neighboring pixel.
- ▶ In addition to the electronic background signal from the each pixel, residual scattered light could lead to a wavelength dependent (but time-independent) background. In the time file, several points well before the time zero are acquired, in order to make an averaged spectrum of the background which will be removed to the whole matrix.
- ▶ The wavelength file delivered by the software has to be “down-converted”, to obtain the wavelength of the emission before up-conversion. This is done through the formula:

$$\lambda_F = (\lambda_S^{-1} - \lambda_G^{-1})^{-1} \quad (3.6)$$

- ▶ The presence of dispersive media between the sample and the SF BBO (excitation cut-off filter and flow cell window) induces a wavelength dependent time delay in the emission, due to group velocity dispersion (GVD). This effect is corrected using an independently measured GVD curve (§ 2.5.1).^{304,305}

The data are then corrected for the spectral instrumental response function (*irf*), and time zero is determined –when possible– on the instantaneous response of the solvent Raman band.

3.5 Set-up characterization

3.5.1 GVD

As previously mentioned, dispersive media between the excitation and time-gating processes introduce a delay between wavelengths of the collected emission due to group velocity dispersion. Indeed, the phase and group velocity v_p and v_g depend both on the refractive index, itself wavelength dependent:

$$v_g = v_p \left(1 + \frac{\lambda}{n(\lambda)} \frac{\partial n(\lambda)}{\partial \lambda} \right) \quad \text{and} \quad v_p = c \cdot n(\lambda)^{-1} \quad (3.7)$$

The refraction index usually decreases towards the longer wavelengths, as well as its first derivative, leading to a higher group velocity. This difference in group velocity between blue and red light corresponds to a wavelength dependent time delay, increasing as the emission passes through the flow cell, the excitation cut-off filter and in the SF crystal. Photon emitted at the same time will reach the SF crystal at different moments. In the 400 nm configuration, this delay is about 600 fs over the detection window, while in the UV it can reach 1.5 ps (Figure 3.7). It results in a strong distortion of the final data matrix, since the time zero is not equivalent for all wavelengths. An accurate correction of this effect is needed to avoid misinterpretation during data analysis.

The full characterization of the GVD in the 400 nm excitation configuration was performed through white light (WL) generation in water.³⁰⁴ This instantaneously generated signal, mainly due to self phase modulation in the solvent, constitutes a time zero reference for a broad spectral region.

In the Visible/UV excitation configuration, the energy per pulse available is not enough to generate a WL continuum. Moreover, the tunability of the excitation wavelength implies the use of filters with different cut-off wavelengths, which have different GVD responses (changes in the refractive index wavelength dependence). Consequently, another method is used to determine the wavelength dependence delay caused by GVD. We use the up-converted signal from a dye strongly emitting in the region of interest. We then make a selection of kinetic traces from the acquired data matrix. One possibility to extract the delay is to make a global fitting of this selection of traces. But this analysis might be biased by dynamics inherent to the dye molecule, as IVR and solvation. We rather choose to normalize all the kinetic traces from the selection, in order to establish the delay by looking

at the moment when the signal starts to rise up at each wavelength. This method is analysis independent, but the signal to noise ratio constitute a limiting factor for its accuracy. Figure 3.7 shows the delay induces by GVD as a function of wavelength for the different filters used in this work.

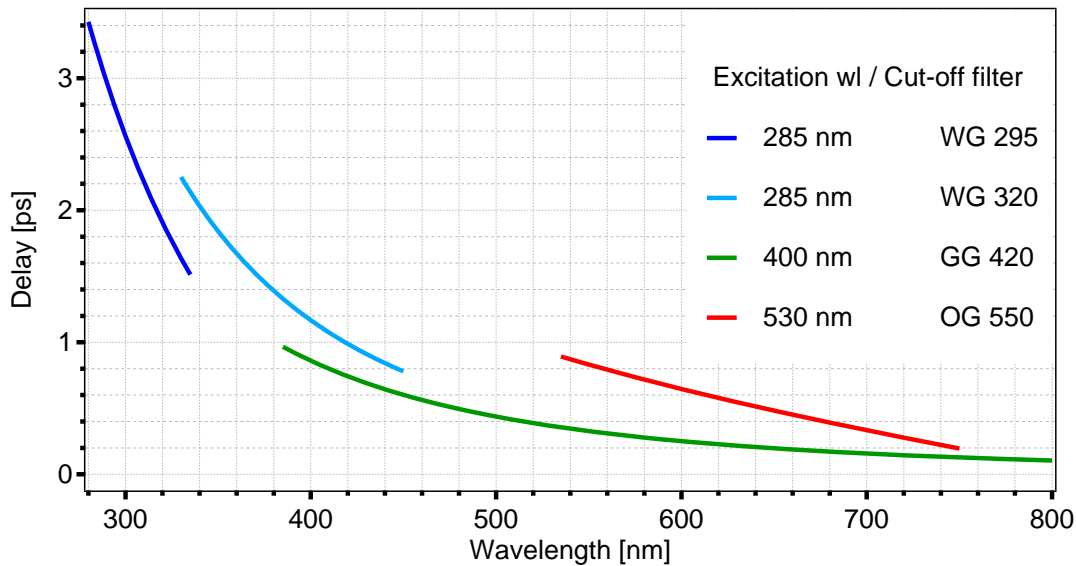


Figure 3.7: GVD correction curves for the different excitation cut-off filter used in this work.

3.5.2 Spectral Response

Besides the monochromator and CCD which have relatively flat spectral response, there are three main sources of spectral response deterioration. Firstly, the lens collecting the up-converted signal has an intrinsic chromatic aberration. Since it has to focalize a spectrally broad signal (210-310 nm in the UV, 270-370 nm in the Visible), the spot size on the CCD camera is broadened moving towards blue-most and red-most wavelengths. This effect is partly compensated by choosing a sufficiently large pixel strip on the CCD and slit width of the monochromator, but can still reduce the spectral response in the blue and red edges. Secondly, the presence of the prism induces a vertical dispersion which vertically broadens the up-converted beam size. Negligible in the visible region, this effect is important in the UV (210-310 nm) and can increase the effect of chromatic aberration of the lens. Moreover, the dispersed signal might be slightly cut by optics in the spectrometer, decreasing the spectral response. Finally, the angles of the SF crystal far from the vertical position, i.e. for wavelengths far from the central phasematching angle (SF crystal cleavage

angle), are positions of slightly reduced SF efficiency, due to the increase in the reflectivity of the incident beams.

For these reasons, the data need to be corrected for the spectral *irf*. This correction is performed by normalizing the time-integrated or the longest time spectrum to the steady state one. If the steady state spectrum is not available due to low emission QY preventing any static measurement, or if the spectrum is expected to change during the time window inaccessible with our up-conversion experiment (300 ps to ms), then the up-converted emission from a dye is used to establish the *irf*.

If a good spectral resolution is not required to follow dynamics that are characterized by spectral shift or simple decay, it is an advantage when the emission spectrum is structured and that more sophisticated spectral evolution occurs at early times, as in the case of cooling dynamics. Our spectral resolution is limited by the spectrum width of the gating beam. In the UV, we can estimate it with the width of the up-converted Raman band of water, shown on Figure 3.8. After the subtraction of its intrinsic width (400 cm^{-1})³⁰⁸ we obtain an absolute upper limit of 570 cm^{-1} , corresponding to a resolution of 6 nm in the UV region and 15 nm in the Visible one.

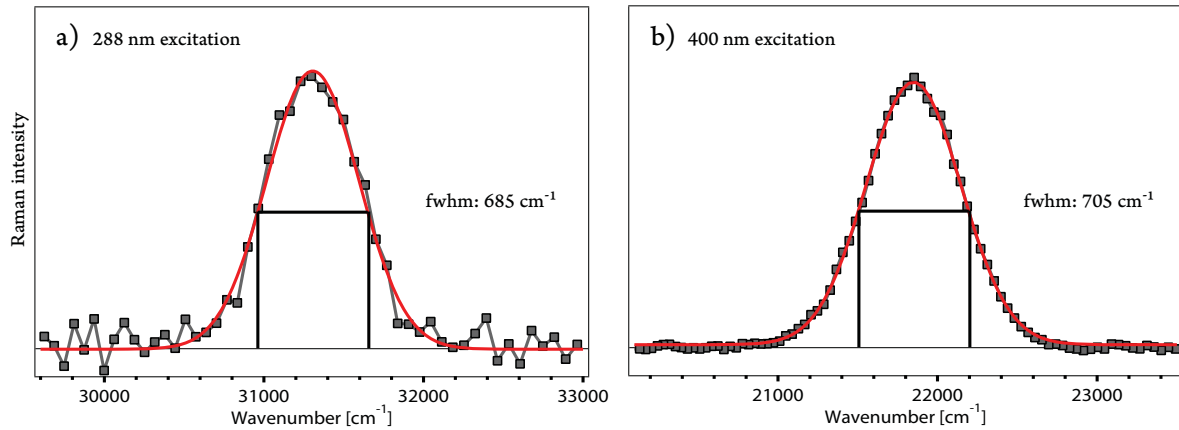


Figure 3.8: Up-converted Raman band of water excited at a) 288 nm and b) 400 nm. After subtraction of the intrinsic width of 400 cm^{-1} , the spectral resolution is 570 cm^{-1} .

3.5.3 Temporal Resolution

The time (*irf*) is inherently related to the excitation and gate pulses duration and is given by the convolution of their time profiles $E(t)$ and $G(t)$, well approximated by gaussians:

$$irf(\tau) = \int_{-\infty}^{+\infty} E(t) \cdot G(t - \tau) dt \quad (3.8)$$

The pulse durations of the laser beams give us the lowest limit of the temporal resolution. The spectral chirp of the fundamental 800 nm beam is compensated by grating compressor (Figure 3.5), while the excitation pulses in the UV/Vis configuration are pre-compressed by a set of 2 prisms, before the SHG. No compression of the UV pulses was necessary.

However, two additional effects are contributing to a time elongation of the *irf*. The first most important contribution stems from the non-collinear geometry adopted to spatially filter out the unwanted excitation and gate beams, resulting in a wave front tilt in the SF crystal. This pulse front tilt increases the spatial overlap of the two beams when scanning the time delays, deteriorating the temporal resolution. The angle between fluorescence and gate beams is set to 5° , as a compromise between signal intensity, filtering and time resolution optimization. Another factor, particularly important in the UV, is the group velocity mismatch (GVM). Due to GVD in the dispersive medium, two interacting pulses with different wavelength do not travel with the same speed (eq.(3.7)). It is the case of the excitation and emission in the sample and the emission and gate beams in the SF crystal. The sample does not contribute much to the GVM effect, because of a quite small wavelength discrepancy between excitation and emission. On the contrary, the SF crystal contributes much more to the GVM since the wavelength of the emission is far from the gate one, in particular for UV detection.¹⁹³ The GVM effect can be reduced by the choice of a sufficiently thin SF crystal. For instance, in the UV, the *irf* can be improved from 370 fs down to 180 fs by reducing the thickness of the BBO from 500 to 250 μm .¹⁹³

The *irf* is fully described by the up-converted Raman band of a solvent. Figure 3.9 shows the kinetic trace of the Raman's peak of water in the three different configurations, i.e. under 290, 400 and 530 nm excitation.

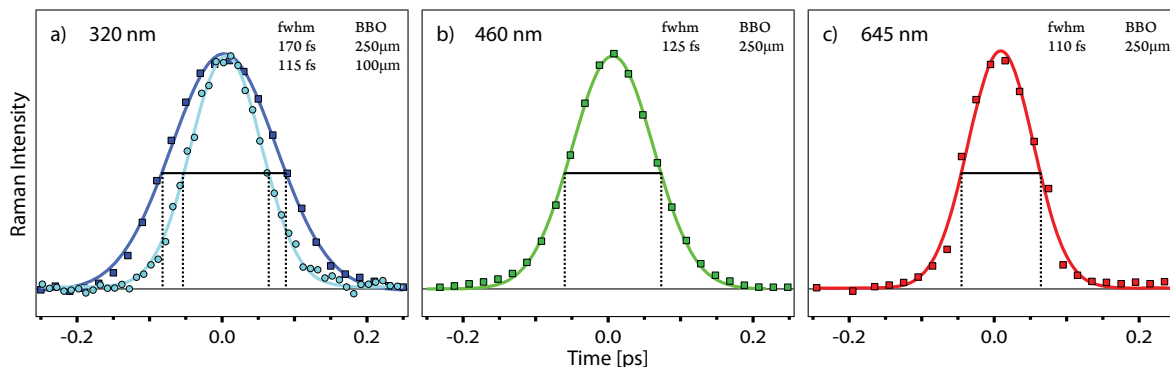


Figure 3.9: Kinetic traces of the up-converted Raman band of water excited at a) 288 nm b) 400 nm and c) 530 nm. Under UV excitation, a thinner BBO of 100 μm was used to improve the *irf*.

3.5.4 Polarization

The time-gated up-conversion technique is intrinsically polarization sensitive. Indeed, the type I phasematching condition used in our set-up allows only conversion of photon with parallel polarization with respect to the gate beam. Since the detection is already polarized, it is enough to add a lambda half wave plate before excitation of the sample, in order to tune the polarization of the excitation beam.

The configuration of the collecting and focalizing parabolic mirrors after the sample forms a Z shape. This kind of configuration induces a partial depolarization of the emission, due to reflections in two different planes. To estimate the depolarization ratio, we recorded water Raman signal with horizontal and vertical polarizations and calculate the instantaneous anisotropy value. The obtained value of 0.55 is very close to the expected value of 0.63. Since this depolarization is small, an approximate correction of the experimental anisotropy was applied by scaling it by a factor of 1.15 ($0.63/0.55$).

Chapter 4

Vibrational relaxation of UV Chromophores

4.1 Time-wavelength resolved fluorescence

4.1.1 Static fluorescence spectra

4.1.2 Time-resolved spectra

4.1.3 Sub-ps dynamics

4.2 Tracking the intramolecular temperature

4.2.1 Static fluorescence as a function of temperature

4.2.2 Estimation of the molecular temperature

4.3 Summary

Before starting the measurements on the organic and metal complexes relevant for the global work of this thesis, we decided to face several concepts dealing with the spectral properties of time-resolved fluorescence, which are: excess of vibrational energy, photoinduced structural changes or temperature. To tackle these issues, and in parallel, to test the ability of the experimental set-up to follow fine and complex dynamics, we have measured the time- and wavelength-resolved fluorescence of two UV-emitting dyes, namely 2,5-diphenyloxazole (PPO) and para-terphenyl (pTP). The spectral evolution, followed within the first 100 ps after excitation, reveals a subtle entanglement of vibrational relaxation mechanisms.

4.1 Time-wavelength resolved fluorescence

4.1.1 Static fluorescence spectra

In order to extract information from the femtosecond transient fluorescence spectra of PPO and pTP, we need to understand the origin of the vibronic structure modulating the static spectra. As previously seen in chapter 2, the fluorescence of these dyes stems only from the first excited singlet state. The static fluorescence spectra (Figure 2.1 and 4.1), are characterized by a major vibronic progression, with an individual width increasing towards lower energies. This peculiarity suggests that more than one vibrational mode is coupled to the transition. Indeed, as mentioned in chapter 2, jet and low temperature spectroscopy have shown the Franck-Condon (FC) activity of three modes in the fluorescence of PPO¹⁴¹ and pTP.¹⁵⁴ Figure 4.1 shows their static fluorescence spectra in cyclohexane at 300 K, fitted with a FC progression. While only the two modes of frequency $\nu_1 = 1544 \text{ cm}^{-1}$ and $\nu_2 = 980 \text{ cm}^{-1}$ were enough to satisfactorily fit the spectrum of PPO, the three modes of frequency $\nu_1 = 1614 \text{ cm}^{-1}$, $\nu_2 = 1286 \text{ cm}^{-1}$ and $\nu_3 = 228 \text{ cm}^{-1}$ were necessary to fit that of pTP:

$$\begin{cases} I^{PPO}(\nu) = \frac{e^{-(S_1+S_2)}}{\sigma} \sum_{n,m=0} \frac{S_1^n \cdot S_2^m}{n!m!} \cdot e^{-\left(\frac{\nu-\nu_{0-0}+n\cdot\nu_1+m\cdot\nu_2}{\sigma}\right)^2} \\ I^{pTP}(\nu) = \frac{e^{-(S_1+S_2+S_3)}}{\sigma} \sum_{n,m,l=0} \frac{S_1^n \cdot S_2^m \cdot S_3^l}{n!m!l!} \cdot e^{-\left(\frac{\nu-\nu_0+n\cdot\nu_1+m\cdot\nu_2+l\cdot\nu_3}{\sigma}\right)^2} \end{cases} \quad (4.1)$$

where ν_{0-0} is the zero-phono-line, ν_i are the frequencies of the vibrational modes, S_i are the related coupling (Huang-Rhys) constants, σ is the individual bandwidth and n , m and l are the population numbers of ν_1 , ν_2 and ν_3 , respectively. During the fit, the vibration frequencies were kept fixed to the values reported in the literature, all the other parameters being freely adjusted. Table 4.1 resumes the obtained fitting parameters.

Table 4.1: Parameters of the FC fit showed in Figure 4.1, with eqs (4.1). All frequencies are in [cm^{-1}].

Compound	ν_{0-0}	ν_1	S_1	ν_2	S_2	ν_3	S_3	Σ
PPO	29'460 ± 2	1544 ¹⁴¹ (fixed)	1.214 ± 0.003	980 ¹⁴¹ (fixed)	0.857 ± 0.004	-	-	497 ± 2
pTP	31'050 ± 45	1614 ¹⁵⁴ (fixed)	0.42 ± 0.01	1286 ¹⁵⁴ (fixed)	0.93 ± 0.01	228 ¹⁵⁴ (fixed)	0.95 ± 0.3	688 ± 22

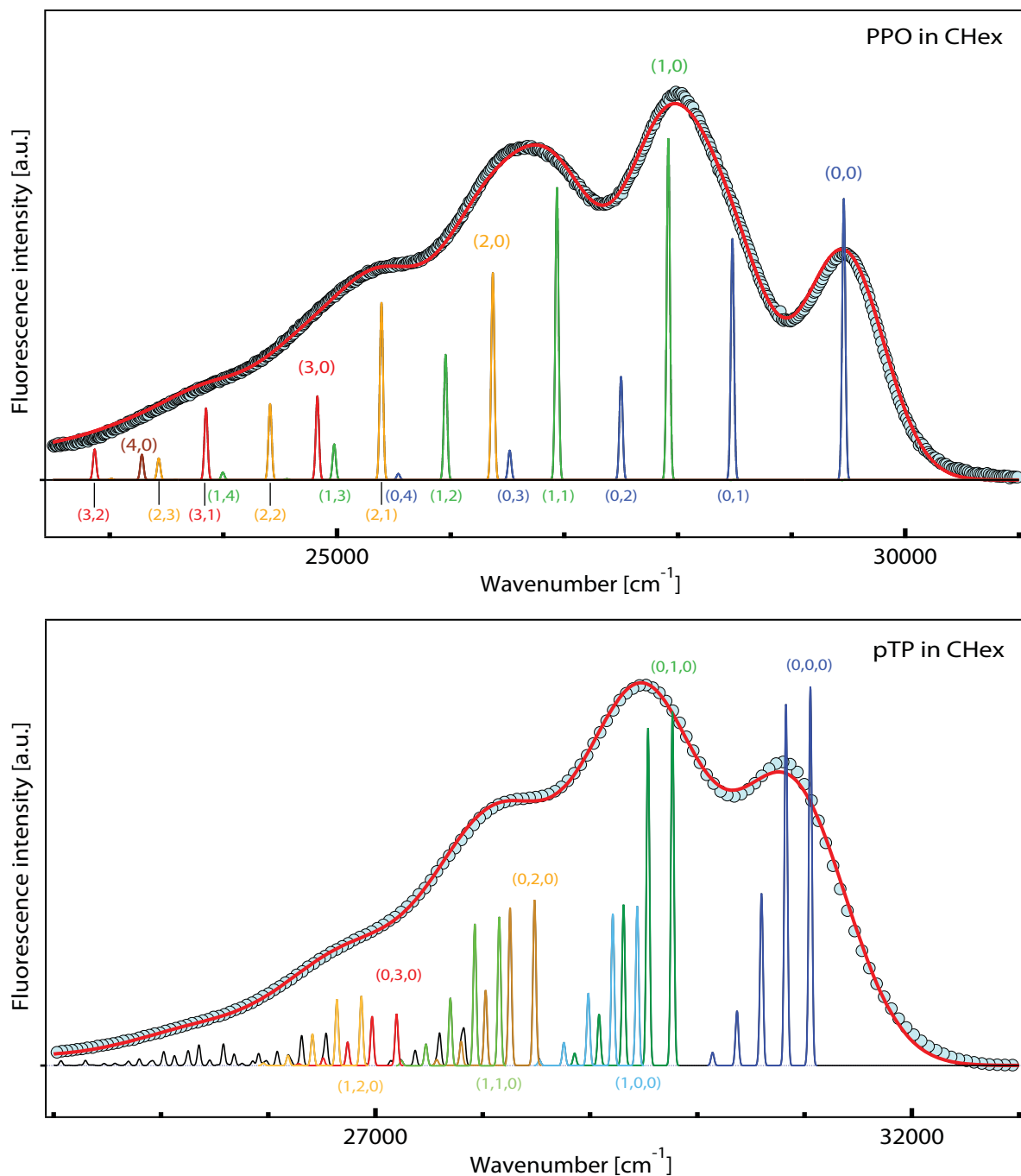


Figure 4.1: Steady state emission spectra (circles) of 2,5-diphenyloxazole (PPO, top) and para-terphenyl (pTP, bottom) in cyclohexane at 300 K, along with their fit (red trace) involving 2 and 3 coupled vibrational modes for PPO and pTP, respectively. The colored traces are plots of the fit function with the individual bandwidth (σ) set to 20 cm⁻¹. The blue, green, orange and red lines correspond to the decomposition in progressions of the lowest frequency mode, with high frequency mode accepting level 0, 1, 2 and 3, respectively. The peaks leading to the major progression are labeled with the quantum number of the accepting vibrational level. The latter are ordered in the parenthesis as decreasing frequency (ν_1, ν_2, ν_3).

4.1.2 Time-resolved spectra

The time-wavelength fluorescence of PPO and pTP in cyclohexane, ethanol and dimethylformamide are reported in Figure C.1. Figure 4.2a and 4.2b shows a selection of transient spectra at various time delays. In all solvents, the fluorescence spectra of PPO and pTP at time zero are broad and already centered close to the maximum of the steady state fluorescence band, without any clear further spectral evolution. Most of the total Stokes shift ($\sim 5000 \text{ cm}^{-1}$) occurs in less than 60 fs (our time resolution) in all three solvents. The emission bands at early times are featureless on the contrary of the respective static spectra. From the end of the excitation pulse (orange trace, $t = 200 \text{ fs}$) to the last spectrum acquired (dark blue trace, $t = 100 \text{ ps}$) the intensity still increases, and the spectrum becomes progressively narrower to finally match the steady state fluorescence before 100 ps. For PPO, this narrowing is best noticeable in cyclohexane where the structured spectrum at 100 ps dramatically differs from that at time zero.

Figure 4.2c and 4.2d show the corresponding integrated band area $M_0(t)$. 70% of the signal appears within the *irf*. The fluorescence was detected with orthogonal polarization, such that 10% of the total intensity increases exponentially with a time constant $\tau_{rot} \sim 60 \text{ ps}$, due to rotational diffusion of the dye.^{309,310} The remaining 20% is recovered within $\sim 5 \text{ ps}$ for cyclohexane and ethanol solvents, whereas no such rise is seen in dimethylformamide. The reason is that the time-resolved spectra are cut on the blue side by the cut-off filter at 310 nm, used to remove the scattered light from the excitation pulse. As the band narrows down, part of the decaying signal on the blue edge lacks and the corresponding rise in the center of the band is no longer compensated in the integrated signal. In DMF, the fluorescence is the most red shifted and thus the least affected.

Transient spectra were fitted with the corresponding steady state FC progressions (eq.(4.1)) (Fit plotted in Figure 4.2a and 4.2b). The aim of this FC analysis is to extract the zero-phonon-line ($\nu_{0,0}$) and the width (σ) of individual bands at every time delay, so as to reconstruct their time evolution. The only assumption required to perform such an analysis is that the emission stems uniquely from one excited state, vibrationally cold with respect to the high frequency FC modes, i.e. IVR already occurred. The width describes the broadening induced by population of the bath of optically silent lower frequency modes. Only the origin of the transition ($\nu_{0,0}$) and the individual bandwidth (σ) were free during the fit, all other parameters being set to the values reported in Table 4.1.

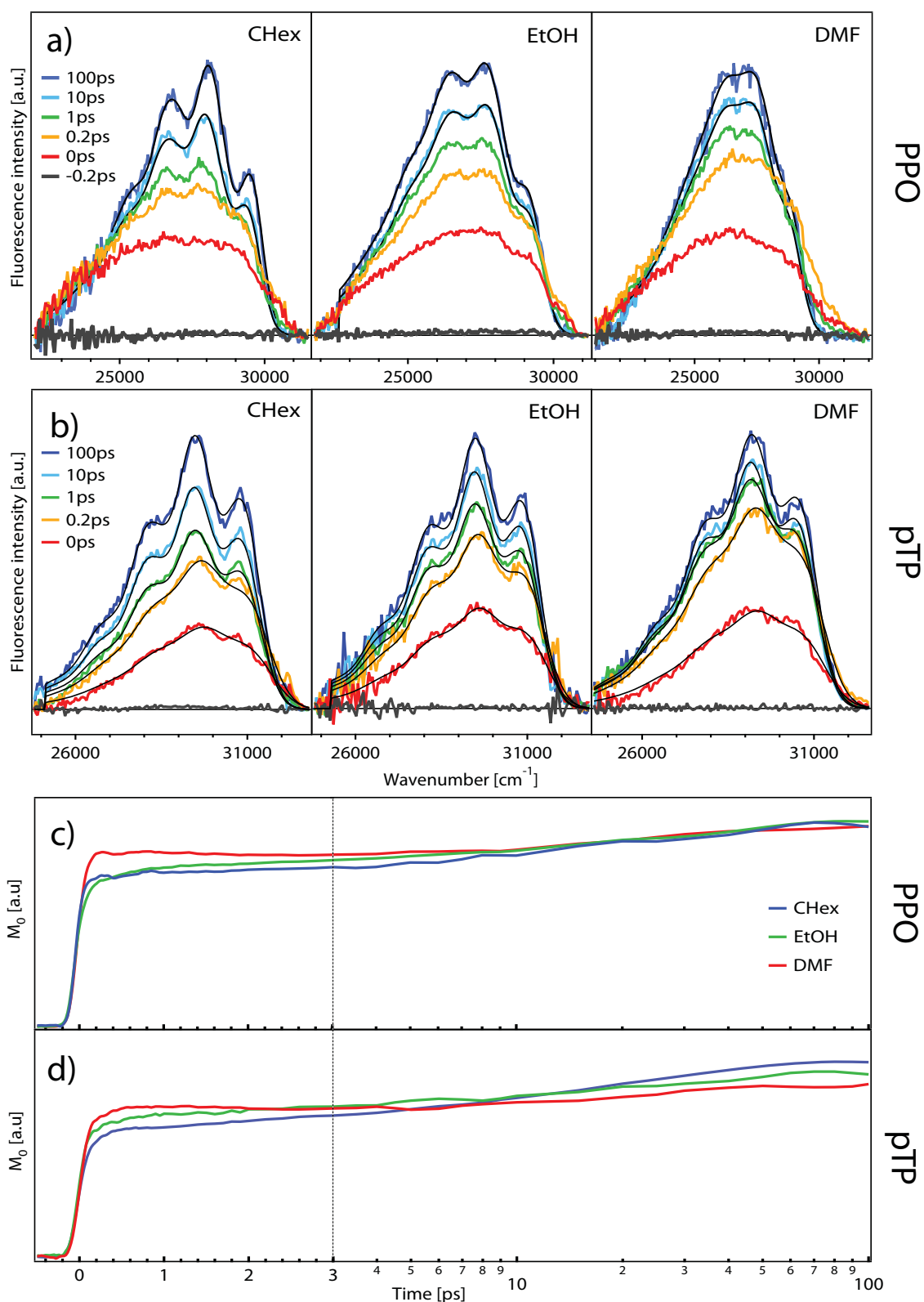


Figure 4.2: Representative Selection of fluorescence spectra from a) PPO and b) pTP in cyclohexane (left), ethanol (middle) and dimethylformamide (right) at different time delays, upon 290 nm excitation, along with their fit, when satisfactory. The lower panels show the integrated spectral area ($M_0(t)$) for PPO (c) and pTP (d), in the three solvents.

In order to analyze the spectral evolution in more details, we calculated the first spectral moments $M_1(t)$ and $M_2(t)$ corresponding respectively to the average position and spectral variance (see appendix A). The obtained time evolution of the moments for both dyes in all solvents is plotted in Figure 4.3. The zero-phonon-line obtained from the fit is shown in the same plot as $M_1(t)$.

In the case of PPO, the first 500 fs are marked in all solvents by an initial blue shift of the band followed by a red shift. The amplitude of these blue and red shifts is $\sim 150 \text{ cm}^{-1}$ in CHex and EtOH, and $\sim 250 \text{ cm}^{-1}$ in DMF. The first three transient spectra normalized in Figure 4.4a, give a hint to the explanation of the early blue and red shifts: in the first 200 fs, the intensity on the red side decays faster than the blue side (red and green traces), whereas after 200 fs, this behavior is reversed (green and blue traces). This is clearly observed in the kinetic traces taken on the blue and red side of the spectra (Figure 4.4b), which are modulated by a counter phase oscillating pattern. Accordingly a clear oscillation is present around 400 fs in the first moment for all solvents. As described in the next paragraph, the presence of such a damped spectral oscillation definitely speaks for a vibrational wavepacket generated (directly or indirectly) by the excitation of a low frequency FC active mode. Its period of ~ 350 fs, measured as the delay between the first and second bump, corresponds to a frequency of $\sim 95 \text{ cm}^{-1}$. After 1 ps, the band has reached its static position in ethanol and dimethylformamide, whereas a multimodal 300 cm^{-1} blue shift still occurs in cyclohexane. This shift is also appreciable on the normalized spectra in Figure 4.3c. The band narrowing, reflected as a decay in $M_2(t)$, occurs mainly within 3 ps, followed by a small decay in few ps for the polar solvent and in 10s of ps for CHex. The values of M_2 at time zero are large and the related spectra strongly deviate from the static spectra.

Concerning pTP, a small ($\sim 300 \text{ cm}^{-1}$) red shift of the band occurs in the first ps, with similar amplitude and timescales in all solvents. Normalized spectra at 0 ps, 0.2 ps and 1 ps presented in Figure 4.3c and 4.4b give the origin of the initial red shift: the maximum of the band does not shift but the intensity on the blue (red) edge decreases (increases) relatively to the maximum. The latter is already relaxed at time zero, implying that the emission stems from a cold level, as far as high frequency modes are concerned. It also rules out any contribution from solvation dynamics to the red shift observed. A monoexponential fit of the traces of $M_1(t)$ with the function A.13 gives the time constants reported in Table 4.2.

Table 4.2: Time constants obtained from exponential fits of $M_I(t)$ for pTP, according to function A.13.

	CHex	EtOH	DMF
τ	500 ± 20 (340)	360 ± 40 (250)	260 ± 10 (370)

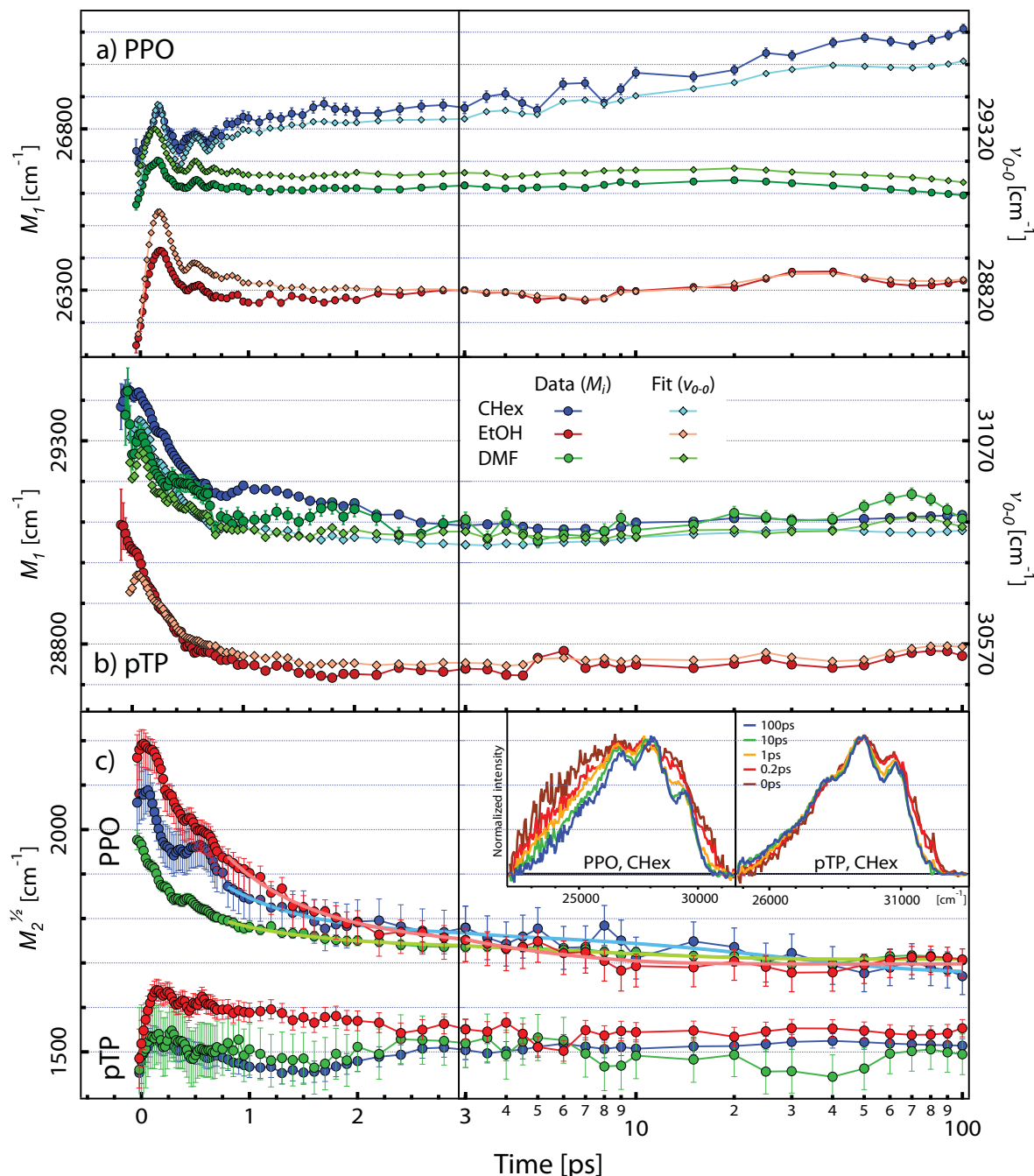


Figure 4.3: Average fluorescence spectral position $M_I(t)$ of a) PPO and b) pTP in CHex, EtOH and DMF. c) Square root of the fluorescence spectral variance $M_2(t)^{1/2}$ of PPO and pTP. The error bars $\Delta M_I(t)$ and $\Delta M_2(t)$ are calculated via formula A.7 and A.8 respectively, with the value of 3σ as the average uncertainty on the pixel intensity $\langle \Delta I \rangle$. In all panels, the first 3 ps are in a linear scale, whereas from 3 to 100 ps the time is in a logarithmic scale. Inset of bottom panel: emission spectra at different time delays (colored lines) from PPO and pTP in cyclohexane, normalized to the maximum.

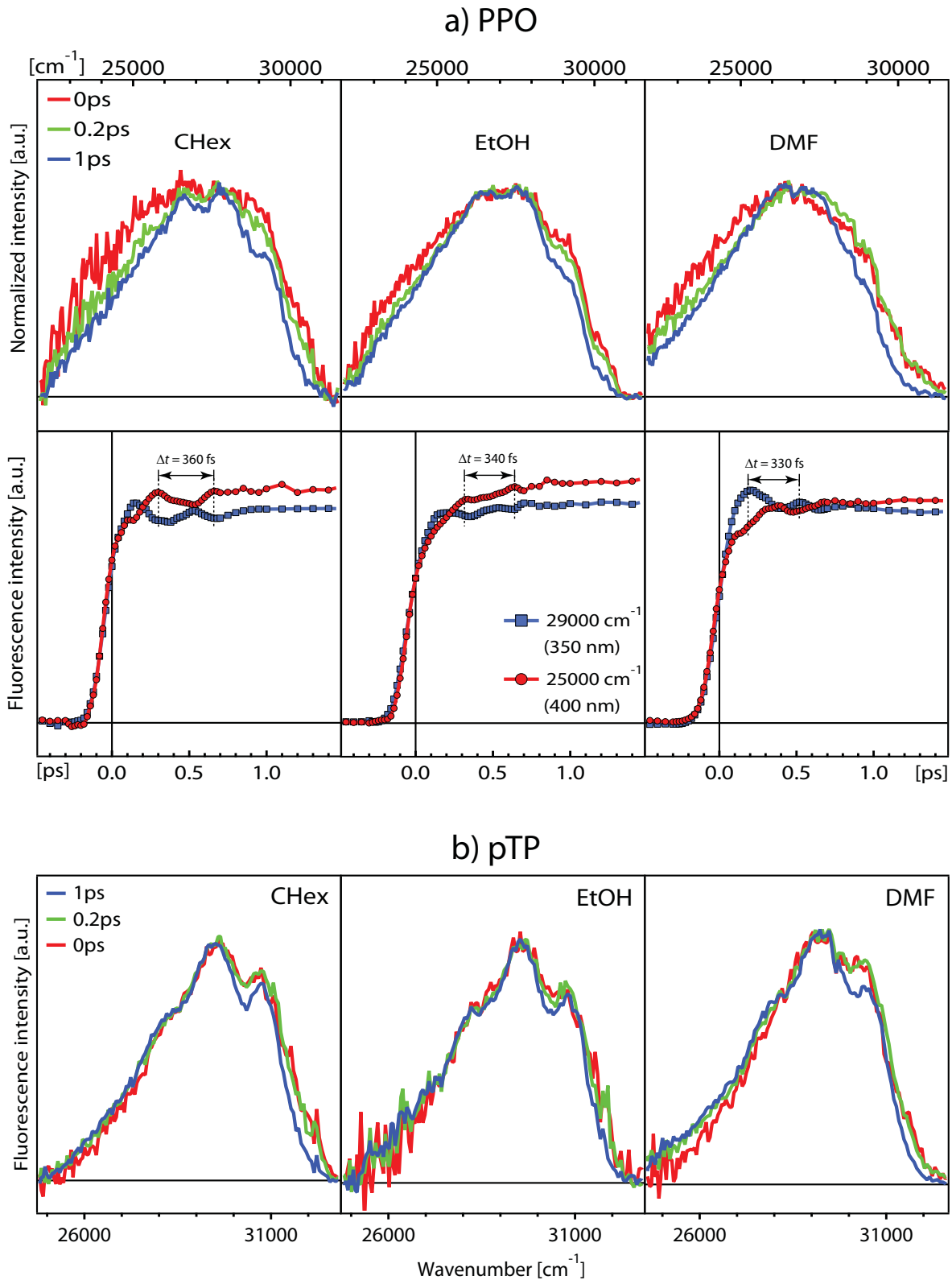


Figure 4.4: a) Normalized fluorescence spectra at 0 ps, 0.2 ps and 1 ps from PPO in cyclohexane (left), ethanol (middle) and dimethylformamide (right) upon 290 nm excitation (top panels). Corresponding kinetic traces at 350 nm and 400 nm (bottom panels). b) Normalized fluorescence spectra at 0 ps, 0.2 ps and 1 ps from pTP in cyclohexane (left), ethanol (middle) and dimethylformamide (right) upon 290 nm excitation

4.1.3 Sub-ps dynamics

The FC analysis of the time-resolved spectra requires two hypothesis. First, we should be able to define the temperature of the molecule. This assumption is achieved only if the population of each vibrational mode is given by a Boltzmann distribution. It is the case once the IVR mechanisms are finished, i.e. once the excess vibrational energy is completely (statistically) redistributed among all vibrational modes. Second, no important structural changes occur, ensuring the validity of the FC approximation. We have evidences that one or both of these hypothesis do not hold in the sub-ps domain:

- 1) As mentioned above, the spectra of PPO before ~ 1 ps cannot be satisfactorily fitted with the Franck-Condon progression of the static spectrum (eq.(4.1), Figure 4.1).
- 2) The normalized spectra on Figure 4.3c and 4.4 show a change in relative peak height of the 0-0, 0-1 and 0-2 Franck-Condon bands, which is not described with the former treatment. This observation and the presence of a wavepacket dynamics in the case of PPO, speak for non-thermalized systems.
- 3) The breakdown of the mirror image symmetry in the static absorption/emission spectra (Figure 2.1) suggests important structural changes in the excited state. These changes must occur on a given timescale ranging from the fs to the ps timescale.

For this reason, in this paragraph we will focus on the relaxation occurring in the first ps. The deviation of the absorption/emission spectra from the mirror image symmetry is particularly evident in pTP, due to an important structural change in the excited state (see chapter 2).¹⁵³ It is tempting to assume that the early dynamics observed in the first moment of pTP and PPO are triggered by this structural change.

In the case of PPO, the time zero spectrum resembles the mirror image of the absorption, suggesting that the structural change has still not occurred. If the coordinate describing the conformational change involves one (few) vibrational mode(s) slow enough, we could have generation of a wavepacket, which would slow down the structure-related effects on the spectra in this transient regime. While the maximum of the band is immediately there, the wavepacket dynamics appears as a successive broadening of the red and blue wings, giving rise to the oscillations seen in $M_I(t)$ and in the kinetic traces on the blue and red edges (Figure 4.4a), with a period of ~ 350 fs and a damping constant of ~ 700 fs. The Fourier analysis of the oscillating pattern, shown in Figure 4.5, shows a peak at 100 ± 30 cm^{-1} for all the solvents ($\tau = 330 \pm 90$ fs), and an additional peak at ~ 260 cm^{-1} in CHex.

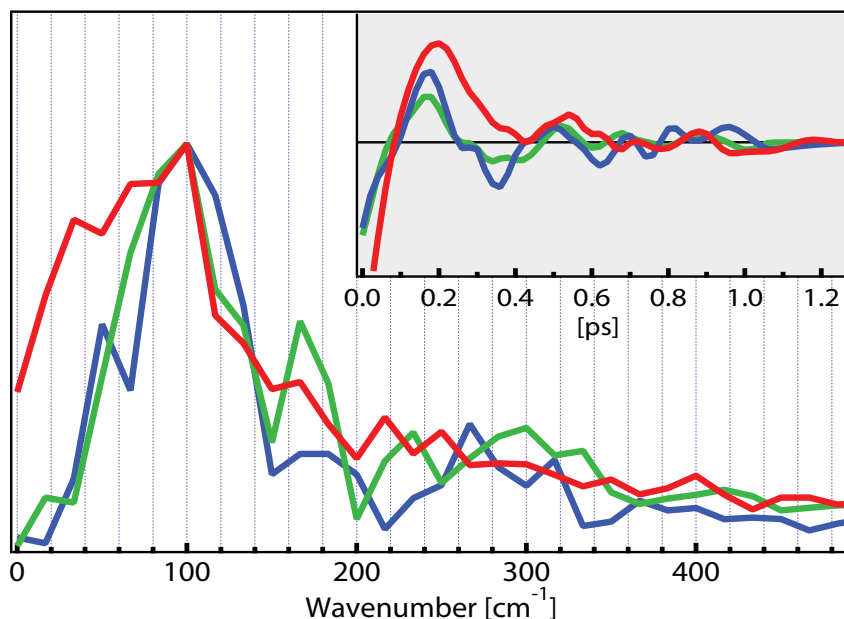


Figure 4.5: Fourier Transform spectra of the oscillations pattern (inset) of $M_i(t)$ from the fluorescence of PPO in CHex, EtOH and DMF.

In collaboration with Dr. Thomas Penfold, the vibrational frequencies of PPO and pTP were calculated using the Gaussian program (reported in table B.1). The first 8 low frequency modes calculated are plotted in Figure B.3. *Ionescu et al.*¹³⁸ reported the optimized geometries of a derivative compound of PPO, showing an increase of the phenyl-oxazole bond order and a decrease in that of the C=N and C=C bonds inside the oxazole ring, in the excited state. These changes speak for an in-plane phenyl-oxazole-phenyl bending contraction. The third calculated vibration of frequency 67 cm^{-1} , shown in Figure B.3, corresponds to such a vibrational deformation and might be involved in the wavepacket. The next vibrational mode has a frequency of 89 cm^{-1} and is a combination of out-of-plane torsional and waving motion. This mode, better matching the observed oscillation frequency, cannot be excluded from the contribution to the wavepacket. In addition, the 260 cm^{-1} observed in CHex can be assigned to the calculated mode of frequency 258 cm^{-1} , corresponding to the phenyl-oxazole-phenyl bending motion (Figure B.3). This mode has also been observed in jet spectroscopy at a frequency of 256 cm^{-1} .¹⁴¹ The time dependent spectral shift probably originates from oscillation of the system at the bottom of the excited state potential well, along the coordinate of the main low frequency mode involved. Accordingly, the long transient regime of 1 ps is not the time to reach the excited state configuration but the time of oscillation damping, during which the vibrational energy, stored in the mode responsible for the wavepacket, is still redistributed.

In the case of pTP, no oscillation is observed, but the same consideration applies: the maximum is already relaxed at time zero, whereas the zero-phonon-line decreases and narrows concomitantly with an increase of the red wing, resulting in the red shift in $M_I(t)$. As mentioned before, the structural rearrangement is assigned in this case to a planarization mainly involving the torsional motion of the phenyl rings.¹⁵³ To show the effect of a hot low frequency mode on the emission spectrum of pTP, we calculated the emission spectra from different “hot” vibrational levels of the third mode (228 cm^{-1}) of the excited state of pTP in CHex and compared them to the transient spectra in Figure 4.6.

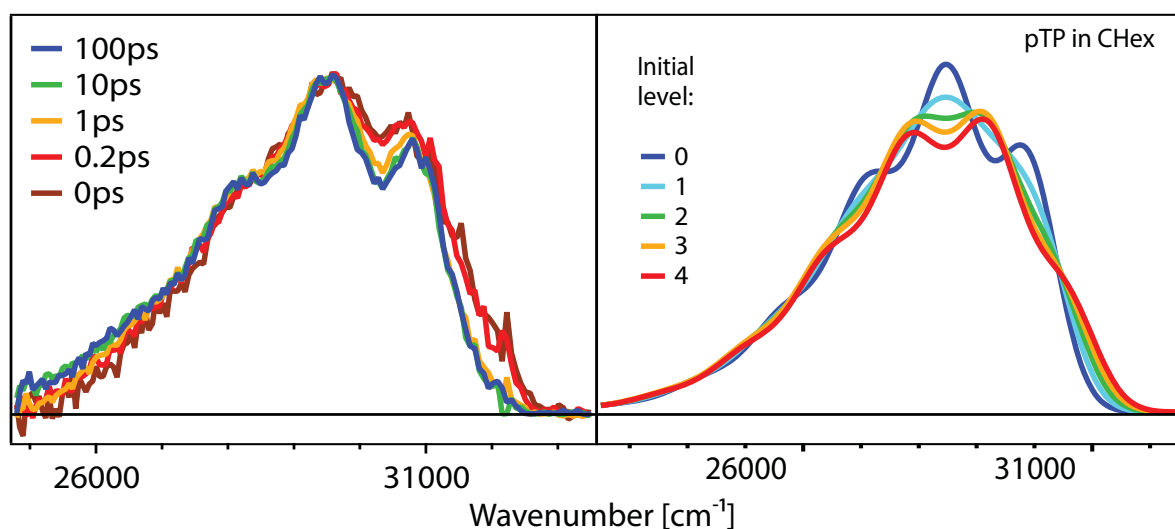


Figure 4.6: Normalized fluorescence spectra at various time delays (left) and calculated Franck-Condon spectra of fluorescence from hot levels of the 228 cm^{-1} frequency mode (see Figure 4.1).

The mode used here might not be the one involved in the dynamics observed, however, any hot low frequency mode would have the same effects on the spectrum, i.e. a strong broadening and a small blue shift of the band. The contribution of emission from hot levels of an optically active low frequency mode is thus consistent with the distortion of the early transient spectra of pTP. Consideration of the ground and excited state potential configuration shown in Figure 2.2 indicates that emission from high torsional levels lead to a similar behaviour: broader and blue shifted emission. The observed early dynamics are likely due to torsional relaxation towards the planar configuration.

In summary, the sub-ps dynamics of PPO and pTP observed in the first moment reflect some structural changes induced by the photoexcitation. While the symptoms are different, i.e. damping of a wavepacket in PPO and red shift in pTP, they are both signature of a

similar process, related to structural changes in the excited state. The faster relaxation process in pTP agrees with the fact that while for PPO, the time zero spectrum compares with the mirror image of the absorption, such a comparison cannot be done for pTP since the FC progression still reasonably fit the early spectra. The following spectral change, namely the band narrowing, corresponds to the evacuation of the excess of vibrational energy, i.e. cooling of the molecule. The next section aims at characterizing the internal temperature evolution of PPO and pTP.

4.2 Tracking the intramolecular temperature

The broadening of optical transition due to the temperature is described by considering the different low frequency modes as a single mode of average frequency $\langle \nu \rangle$, degeneracy N and average linear coupling constant S (Einstein approximation). The temperature contribution to the broadening is expressed through the following formula:³¹¹

$$\sigma^2(T) = N \cdot S \cdot \langle \nu \rangle^2 \coth\left(\frac{h\langle \nu \rangle}{2k_B T}\right) \quad (4.2)$$

For temperature higher than the low average frequency ($k_B T \gg h\langle \nu \rangle$), this relation becomes linear:

$$\sigma^2(T) \simeq \frac{N \cdot S \cdot \langle \nu \rangle 2k_B T}{h} \quad (4.3)$$

The PPO (pTP) molecule contains 28 (32) atoms and hence 78 (90) vibrational modes. The computed vibrational frequencies of PPO and pTP are reported in table B.1. The excess vibrational energy deposited in each molecule after excitation at 290 nm can be estimated by subtracting the absorption zero-phonon-line energy to the excitation energy ($\sim 34\,500 \text{ cm}^{-1}$), which gives $\sim 4500 \text{ cm}^{-1}$ for PPO. In the case of pTP, it is more difficult to estimate, due to the lack of a clear vibronic structure in the absorption spectrum. However, as reported in Ref¹⁵³, we can estimate the position of the zero-phonon-line at the intersection between absorption and emission spectra, giving an excess energy of $\sim 2500 \text{ cm}^{-1}$. As already mentioned, to assign a temperature to any system, the population of each vibrational mode has to be given by a Boltzmann distribution. Accordingly, the temperature corresponding to a given vibrational energy, in the case of an isolated and thermalized molecule, is given by:³¹²

$$\langle E_{vib} \rangle(T) = \sum_i^{3N-6} \frac{h\nu_i}{e^{h\nu_i/k_B T} - 1} \quad (4.4)$$

where ν_i is the frequency of the i th mode. The frequencies used here are the one determined in the ground electronic state, as the calculation of the first singlet excited state is much more demanding. However, only a small shift in the frequency energy is expected, without dramatic influence on the obtained temperature. The latter is found to be $\sim 510 \text{ K}$ and $\sim 420 \text{ K}$ for PPO and pTP, respectively. Remarkably, while at infinite time molecule and solvent have the same temperature, this could not be the case at early times.

In parallel to this analysis, the static fluorescence spectra of both dyes were acquired for different temperature ranging from 280 to 360 K in CHex and from 260 to 370 K in EtOH. The same FC fit was performed on all spectra, in order to see the influence of temperature on the bandwidth of the vibronic structure. The results are shown in Figure 4.7a and 4.7b.

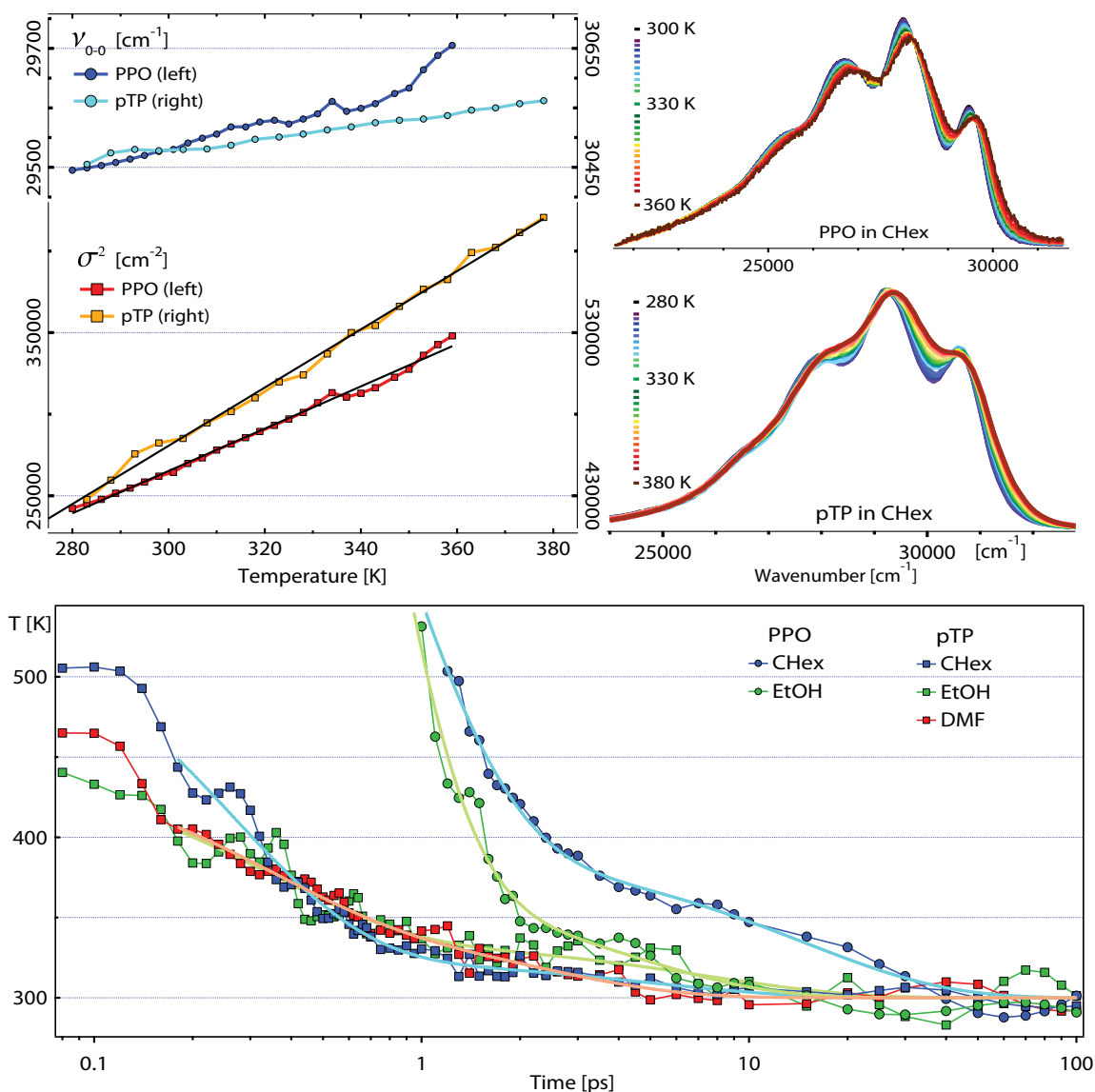


Figure 4.7: a) Zero-phonon-line and width obtained from the F-C fit of the fluorescence spectra of PPO in cyclohexane and ethanol at different temperature (b). c) Molecular temperature of PPO and pTP in various solvents as a function of time.

The zero-phonon-line shifts to the blue as the temperature increases (200 and 100 cm^{-1} over 100 K, for PPO and pTP, respectively), suggesting a breakdown of the linear coupling approximation, with an average frequency $\langle \nu \rangle$ smaller in the excited state. This observation confirms that the temperature estimated with the ground vibrational frequencies is slightly

underestimated. The bandwidth of fluorescence of PPO (pTP) increases of 20 (15) % over 80-100 K. The variance σ^2 is linear with temperature, revealing that we are in a regime of temperature where eq.(4.3) holds. In this regime, the width of the fit of the transient spectra (σ^2) is thus directly proportional to the internal temperature of the dye molecule. Figure 4.7c shows the molecular temperature of PPO in CHex and EtOH, and of pTP in CHex, EtOH and DMF as a function of time. In DMF, the fluorescence spectrum of PPO is not structured enough to reliably extract the individual bandwidth.

For PPO, the maximum temperature observed (~ 500 K) corresponds to the previously estimated temperature for 4500 cm^{-1} of excess vibrational energy. This value is found at ~ 1 ps and the spectra at earlier time delays cannot be satisfactorily fitted with the Franck-Condon progression. Yet, the main narrowing occurs in the first ps, as indicates the decrease of $M_2(t)^{1/2}$ from 2100 to 1850 cm^{-1} . However, such a value of $M_2^{1/2}$ at time zero would correspond to an initial temperature > 3000 K, strongly deviating from the calculated temperature and physically meaningless. This argument is even stronger if we take into account the fact that, as previously mentioned, the early spectra are cut on the blue side, i.e. that the calculated values of M_2 at early times are likely underestimated.

In the case of pTP, the initial temperature extrapolated on Figure 4.7c are 460 K for EtOH, 500 K for DMF and 520 K for CHex, with an uncertainty of ~ 40 K. These values exceed the previously estimated temperature of 420 K. The slight underestimation of this temperature due to the use of ground state vibrational frequencies cannot account for these values. The intramolecular temperature is reached at ~ 200 fs, i.e. at the end of the excitation pulse. Table 4.3 reports the temperature amplitudes associated with the decay time obtained from a bi-exponential fit performed from 200 fs to the latest time.

These observations confirm that in the early transient regime (< 1 ps for PPO and < 200 fs for pTP), the fluorescence cannot be described by a FC treatment. In this regime, important structural change occurs, with non statistical redistribution of excess of vibrational energy. The cooling dynamics is surprisingly fast. The main part of the cooling (80-90 K) occurs on a sub-ps timescale (200-300 fs, Table 4.3), whereas only 40 K are still thermalizing on the picosecond timescale. The fast decay is independent on the solvent for pTP, whereas it is accelerated in the polar one for PPO. Within our uncertainty, we do not observe any effect of the solvent on the slowest decay times.

Table 4.3: Time constants obtained from bi-exponential fit of $T(t)$ from Figure 4.7c. The fitting function used is reported in the appendix, eq. A.13. Amplitudes are in parenthesis.

<i>Solvent</i>	<i>PPO</i>		<i>pTP</i>	
	τ_1 [fs] (T [K])	τ_2 [ps] (T [K])	τ_1 [fs] (T [K])	τ_2 [ps] (T [K])
CHex	700 ± 60 (125 ± 10)	20 ± 3 (75 ± 7)	270 ± 30 (90 ± 10)	4.2 ± 1.2 (30 ± 5)
EtOH	400 ± 50 (130 ± 10)	5.6 ± 1.6 (70 ± 7)	300 ± 50 (80 ± 10)	7.6 ± 2.8 (40 ± 5)
DMF	-	-	310 ± 40 (80 ± 10)	2.3 ± 0.5 (40 ± 5)

4.3 Summary

The set of data presented above allows us to draw a description of the vibrational relaxation mechanisms of 2,5-diphenyloxazole and para-terphenyl excited with a large excess of vibrational energy (respectively 4500 and 2500 cm^{-1}). The main part of intramolecular Stokes shift is almost instantaneous (< 60 fs), meaning that the energy initially localized in the bright high frequency modes (1544 (1614) cm^{-1} , $\nu = 3(2)$ for PPO (pTP)) is very rapidly redistributed to lower frequency modes.

In the case of PPO, the broad spectrum oscillates around its average equilibrium position within the first picosecond, with a period of ~ 350 fs. A coherent wavepacket is generated during excitation involving mainly a 89 cm^{-1} torsional mode,¹⁴¹ evolving in the bottom of the excited state potential well and showing up as a time dependent shift of the band. The decoherence of this wavepacket accompanies the initial fast narrowing of the band.

For pTP, no coherent vibrations are observed, but a sub-ps red shift characterizes the first moment of the band. This feature, as for PPO, is the last step of IVR, and more specifically, a vibrational relaxation of the phenyls torsional motion. However, the contribution from IVR is less than in the case of PPO, since the FC fit is still satisfactory at time zero, and the estimated temperature is reached after only ~ 200 fs. These results suggest a faster IVR mechanism in pTP. This acceleration can be explained by the larger number of atoms in pTP, the presence of heavier atoms (N, O) in the oxazole ring of PPO, as well as the higher symmetry of pTP compared to PPO.

The vibrational energy transfer to the solvent is bi-exponential for both dyes. Its sub-picosecond onset occurs on the same timescale as the IVR process described above, while the complete thermalization is achieved in tens of ps. This biphasic vibrational cooling could tentatively be explained by a two-step energy transfer: in the first picosecond the chromophore transfer its energy to the closest solvent molecule (solute-to-solvent transfer), while the subsequent cooling is limited by transfer of the heat to the bulk (solvent-to-solvent transfer). This local heating effect, giving rise to the initial cooling dynamics, is enhanced by the polarity of the solvent, which strengthens the solute-solvent interaction.⁵³ Accordingly, the initial cooling rate of pTP is independent on solvent polarity, as expected for an apolar solute.

We have thus been able to evidence the presence of sub-picosecond entangled IVR and VET mechanisms, separated from the slower energy dissipation to the bulk. This study

reveals the importance of consideration of conformational changes on the fluorescence spectrum at short delay time after photoexcitation. Moreover, it illustrates the limits of the definition of the temperature of a molecule in the femtosecond domain, in particular when IVR processes interfere with cooling dynamics.

Chapter 5

Relaxation dynamics of aqueous Tryptophan

- 5.1 Fluorescence up-conversion data
 - 5.1.1 Anisotropy
 - 5.1.2 Solvation and intramolecular dynamics
- 5.2 Non-equilibrium Molecular Dynamics Simulations
- 5.3 Conclusions

In biology, most of the key chromophore molecules absorb in the UV⁶ and there is growing interest in using natural chromophores to probe dynamics of larger biological systems. Fluorescence up-conversion technique has already been implemented in the UV for the study of DNA bases photodamage mechanisms.³¹³⁻³¹⁵ The aromatic amino acids (phenylalanine, tyrosine and tryptophan) constitutes another set of natural UV chromophores, giving the opportunity to probe proteins dynamics in a non-invasive way. Trp is the most widely used residue in UV time-resolved spectroscopy. In particular, femtosecond up-conversion experiments have been applied to Trp in view to probe local hydration dynamics at the protein surface^{164,316} as well as energy/charge transfer processes.^{165,317}

The picosecond relaxation dynamics of Trp, introduced in chapter 2, is characterized by an overlap of solvation, internal conversion and vibrational cooling dynamics. We acquired the femtosecond-resolved fluorescence of aqueous Trp with broad-band detection and polarization dependence in order to unambiguously disentangle the different processes. A time-dependent analysis of the experimental results in terms of spectral moment was confronted to a MD simulation study to obtain a clear distinction between all electronic and vibrational relaxation processes.

5.1 Fluorescence up-conversion data

Figure 5.1A and B show time-wavelength plots of the fluorescence of tryptophan in water, in the first 5 ps for parallel and orthogonal detection. We detect a broad emission from 300 to 450 nm which shifts to lower energies in the first ps. We construct the time-energy plot of the anisotropy according to eq. (5.1) (Figure 1C), which shows a spectral dependence at time zero in the range 26000-32000 cm^{-1} that disappears within the pulse width (Figure 1D).

$$r_{tot}(\nu, t) = \frac{I_{\parallel}(\nu, t) - I_{\perp}(\nu, t)}{I_{\parallel}(\nu, t) + 2 \cdot I_{\perp}(\nu, t)} \quad (5.1)$$

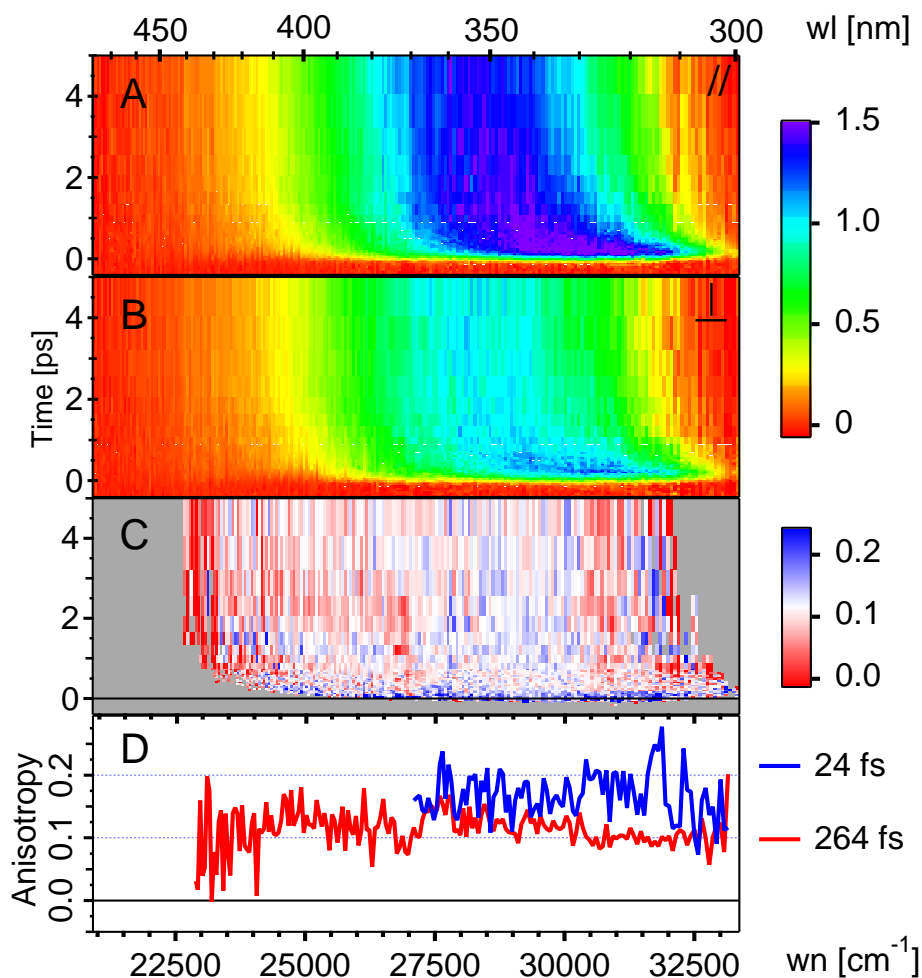


Figure 5.1: Time-wavenumber plots of time-resolved fluorescence spectrum of tryptophan in water, in the first 5 ps, with parallel (panel A) and orthogonal (panel B) polarization. C) Time-wavenumber plot of the anisotropy over the first 5 ps. The black horizontal line corresponds to the time zero. [Intensity is colour coded according to the legend on the right side] D) Selected anisotropy spectra at 24 and 264 fs.

5.1.1 Anisotropy

Figure 2 reports the anisotropy as a function of time obtained both from broadband and single-wavelength detected fluorescence signal, the latter having a better temporal resolution (120 fs). A maximum value of 0.25 is found, which decays in less than 200 fs to 0.13 and finally vanishes on a time scale of tens of ps. The latter is due to rotational diffusion and by fitting the 250 ps range with an exponential decay, we find a rotational diffusion time of $34 \text{ ps} \pm 4 \text{ ps}$, in agreement with the literature.^{161,185,318,319}

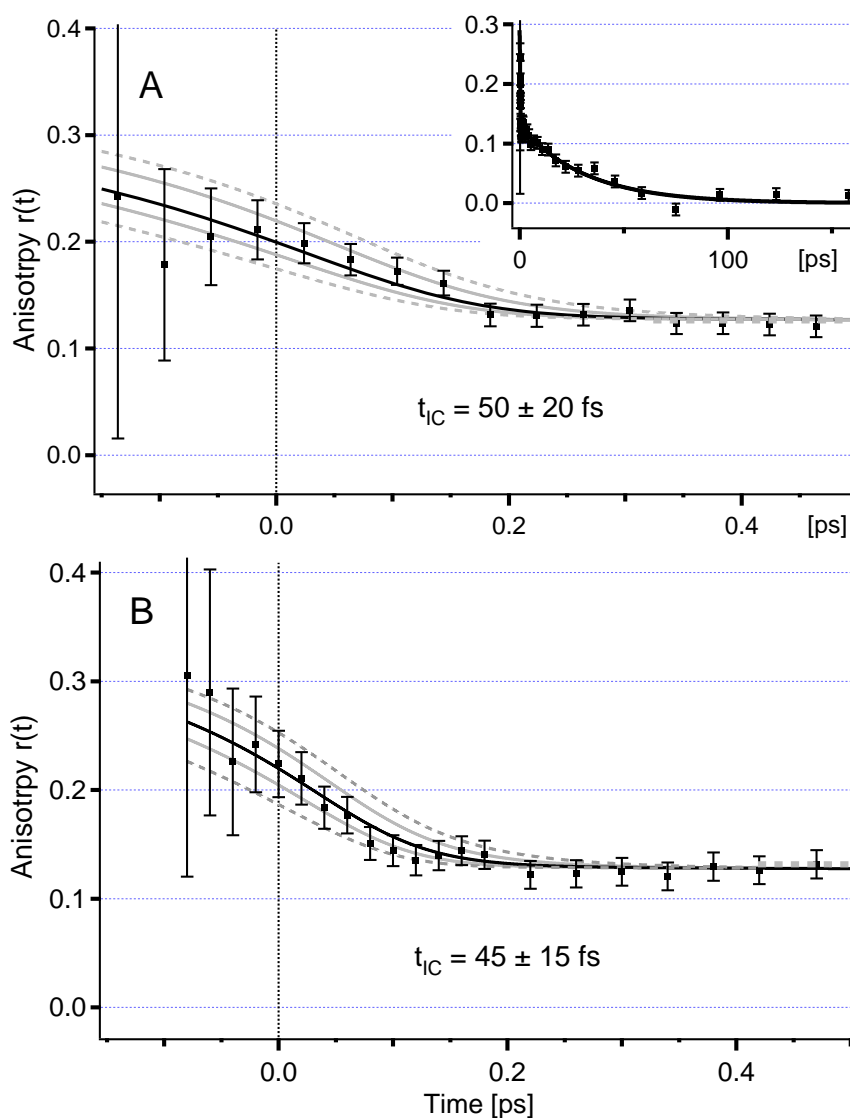


Figure 5.2: A) Time-resolved anisotropy from the fluorescence spectrum of Figure 1A and B (*irf* width of 180 fs). Inset shows the total probed range up to 260 ps. B) Time-resolved anisotropy from the set of kinetic traces across the spectrum with an *irf* (instrumental response function) width of 120 fs. Black dots are the data with error bars and the black line is the best fit. The corresponding τ_{IC} and uncertainty $\Delta\tau_{IC}$ are reported. The grey solid (dashed) lines show the fit function corresponding to $\tau_{IC} \pm \Delta\tau_{IC}$ ($\tau_{IC} \pm 2 \cdot \Delta\tau_{IC}$).

Concerning the ultrafast dynamics, the expected time-zero anisotropy value is 0.4, and the smaller value found here speaks for dynamics faster than our time resolution. This is indeed the case, as derived in ref. ¹⁶⁵ (< 80 fs), which reported an anisotropy close to 0.4, due to ${}^1L_b \rightarrow {}^1L_a$ IC. To estimate more precisely the IC time, we model it in terms of the time-dependent population of both states. We assume that for both 1L_a and 1L_b states, the transition dipole moment of excitation is collinear to the emission one. At time zero, we excite a mixture of molecules in the 1L_a and 1L_b state. The latter will undergo internal conversion to the 1L_a state in less than 100 fs while the former will undergo solvation dynamics and rotational diffusion on longer time scales. Defining $n_a(t)$ and $n_b(t)$ as the respective populations of 1L_a and 1L_b states at time t , and μ_a and μ_b as the respective emission transition dipole moments, one can write the following set of equations, assuming a Gaussian instrumental response function (*irf*) with width σ_{irf} :

$$\begin{aligned} n_a(t) &= \left[n_a^0 \cdot e^{-t/\tau_{L_a}} \right] \odot e^{-\left(\frac{t-t_0}{\sigma_{irf}}\right)^2} \\ n_b(t) &= \left[n_b^0 \cdot e^{-t(\frac{1}{\tau_{ic}})} \right] \odot e^{-\left(\frac{t-t_0}{\sigma_{irf}}\right)^2} \\ n_{ba}(t) &= \left[n_b^0 - n_b^0 \cdot e^{-t(\frac{1}{\tau_{ic}})} \right] \odot e^{-\left(\frac{t-t_0}{\sigma_{irf}}\right)^2} \end{aligned} \quad (5.2)$$

n_a^0 and n_b^0 being, respectively, the populations of the 1L_a and 1L_b states excited at time zero t_0 , n_{ba} being the population of molecules in the 1L_a state stemming from the IC (initially in the 1L_b state), τ_{ic} is the IC time constant and τ_{L_a} is the lifetime of 1L_a state. Knowing the time-dependent dipole moments through the time-dependent populations. The derivation of contributions to the parallel and orthogonal intensities is reported in the appendix C. The final anisotropy expression is:

$$\begin{cases} I_z = \left(\frac{\mu^2}{5}\right) \left[\left(n_a(t) + \alpha^2 n_b(t) \right) \cdot \left(\frac{5}{3} + \frac{4}{3} e^{-\frac{t}{\tau_{rot}}} \right) + n_{ba}(t) \cdot \left(\frac{5}{3} - \frac{2}{3} e^{-\frac{t}{\tau_{rot}}} \right) \right] \\ I_x = \left(\frac{\mu^2}{5}\right) \left[\left(n_a(t) + \alpha^2 n_b(t) \right) \cdot \left(\frac{5}{3} - \frac{2}{3} e^{-\frac{t}{\tau_{rot}}} \right) + n_{ba}(t) \cdot \left(\frac{5}{3} + \frac{1}{3} e^{-\frac{t}{\tau_{rot}}} \right) \right] \end{cases} \Rightarrow r = \frac{2(n_a + \alpha^2 n_b(t)) - n_{ba}(t)}{5[n_a + \alpha^2 n_b(t) + n_{ba}(t)]} \cdot e^{-\frac{t}{\tau_{rot}}} \quad (5.3)$$

where $\alpha = \mu_b/\mu_a$ (μ_a and μ_b are known from experimental and theoretical results¹⁶⁶) and τ_{rot} is the rotational diffusion time constant.

According to eqs (5.2) and (5.3) the 0.13 value at 0.5 ps (see Figure 5.2), after IC is finished and rotational dynamics are still negligible ($\tau_{rot} = 34$ ps), is a direct measurement of the ratio of initial 1L_a and 1L_b populations. We estimate the percentage of 1L_b (1L_a) population to be around 45% (55%), in agreement with the relative absorption intensity of both states.¹⁶¹ The solid lines in Figure 2 are the best fits based on eqs (5.2) and (5.3), with the corresponding parameters given in Table 1.

Table 1: Parameters resulting from the fit on data in Figure 5.2.

Parameter	Fraction of initially excited tryptophan in the 1L_a state, n_a^0	${}^1L_a / {}^1L_b$ transition dipole moment ratio, α ¹⁶⁶	FWHM irf , $2\sqrt{\ln 2} \cdot \sigma_{irf}$	1L_a fluorescence decay time, τ_{L_a} ¹⁸³	Rotational diffusion time constant, τ_{rot}	IC time constant, τ_{IC}
value	0.55	0.455	180/120 fs	3 ns	34 ps	45 fs
uncertainty	± 0.01	fixed	fixed	fixed	± 8 ps	± 10 fs

The agreement with experimental data in the temporal region of the internal conversion is excellent. This is even more remarkable since to describe the dynamics, the IC time constant is the only free important parameter, while all other parameters (n_a^0 , α , τ_{rot} , τ_{L_a} , σ_{irf}) are unequivocally determined by the experimental values at longer time or by independent measurements. We find $\tau_{ic} = 50 \pm 20$ fs and 45 ± 15 fs, from the analysis of broadband and single-wavelength detected measurements, respectively. These values and their relative uncertainties are supported by the comparison of the experimental data with the curves corresponding to the upper and lower value of τ_{ic} ($\tau_{ic} \pm \Delta\tau_{ic}$). These curves are indeed just within the error bars, and considering $\tau_{ic} \pm 2 \cdot \Delta\tau_{ic}$ we obtain unsatisfactory curves (Figure 5.2).

Figure 5.1C shows the time-energy plot of the anisotropy over the first 5 ps. On this plot, one can clearly distinguish at time zero, a broad band between 28000 cm^{-1} and 32000 cm^{-1} . This spectral dependence can be appreciated by comparing the anisotropy spectrum close to time zero and after the IC at 260 fs, on the panel D of Figure 5.1, and is indeed the signature of the 1L_b emission band prior to IC. More information on earliest dynamics (IC dynamics) will be obtained by analysis of spectral width kinetic, reported in the following paragraphs.

5.1.2 Solvation and intramolecular dynamics

From the parallel and orthogonal components of the fluorescence intensity, we reconstruct the intensity as measured at magic angle (Figure D.1), i.e. free from rotational diffusion, according to

$$I(\nu, t) = \frac{1}{3} (I_{\parallel}(\nu, t) + 2 \cdot I_{\perp}(\nu, t)) \quad (5.4)$$

From these data, we calculate the spectral moments. M_0 shows an instantaneous rise followed by a small and long decay over the observed 250 ps (Figure D.2), that we tentatively assign to the 0.5 ns decay component related to Trp rotamer dynamics.¹⁸² M_1 (Figure 5.3) exhibits a remarkable Stokes shift of 2000 cm^{-1} complete in 10 ps. In the 10 to 260 ps range (Figure 5.3, inset), one can see a 100 cm^{-1} red shift due to the 0.5 ns radiative decay component which has an associated spectrum slightly blue shifted with respect to the steady state spectrum.¹⁸²

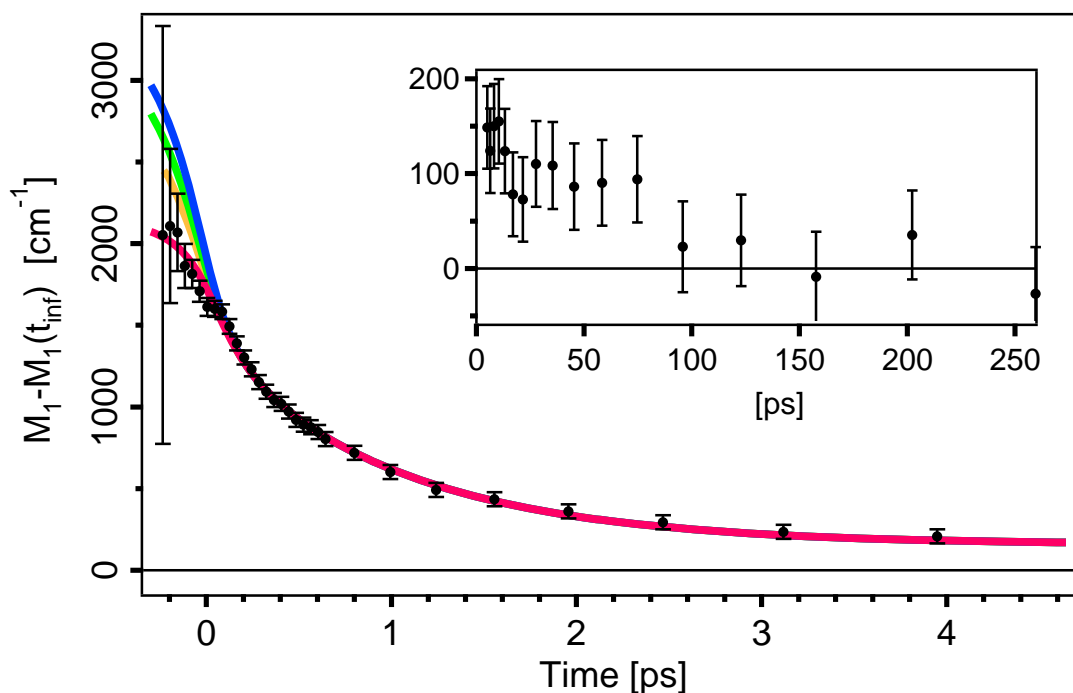


Figure 5.3: Average emission frequency (difference between the first spectral moment and its long time value (for $t > 200$ ps)) of Trp emission band (black dots). Solid red curve shows the best fit according to eq. (A.13), (see text). Orange, green and blue solid curves are the same function with an additional exponential component with 1700 cm^{-1} amplitude and, 10, 20 and 30 fs time constant respectively. The inset shows the first spectral moment on a 250 ps temporal window.

We fitted eq. A.13 with two exponential components, in the 0-10 ps range and the result is plotted in Figure 5.3. The resulting timescales with their respective amplitude are summarized in Table 2. We obtain relaxation times (amplitudes) of 160 ± 40 fs (720 ± 110 cm^{-1}) and 1.02 ± 0.12 ps (1330 ± 120 cm^{-1}), corresponding to a total shift of 2050 cm^{-1} . A mirror image of the Trp absorption band yields an emission spectrum centred at ~ 32000 cm^{-1} . This value is in good agreement with measurement of Trp emission spectrum in glassy matrices at cryogenic temperature (see chapter 2).¹⁷⁷ Indeed this would correspond to the exact spectrum of Trp surrounded by an unrelaxed solvent. Compared to the steady state emission centred at 28200 cm^{-1} (355 nm), this gives a total expected Stokes shift of ~ 3800 cm^{-1} , implying that a shift of 1700 - 1800 cm^{-1} has occurred on a timescale within our temporal resolution, as already supported by Callis *et al.*¹⁷⁰ and confirmed by our MD simulations (see below). In Figure 5.3, the resulting fitting function with the same parameters is plotted, with an additional ultrafast exponential component having an amplitude of 1700 cm^{-1} : a relevant discrepancy of the curve is observable for decay constants longer than 10 fs. The orange curve of Figure 5.3 (10 fs additional component) characterizes the most acceptable discrepancy from the data and gives an upper limit of 10 fs to the timescale of this dynamics.

Concerning the width of the emission band, the square root of the variance has also been computed (Figure 5.4), showing a fast rise in few tens of femtoseconds corresponding to a broadening of 500 cm^{-1} followed by a bi-exponential decay of 0.5 and 7 ps over which the width decreases of 180 cm^{-1} .

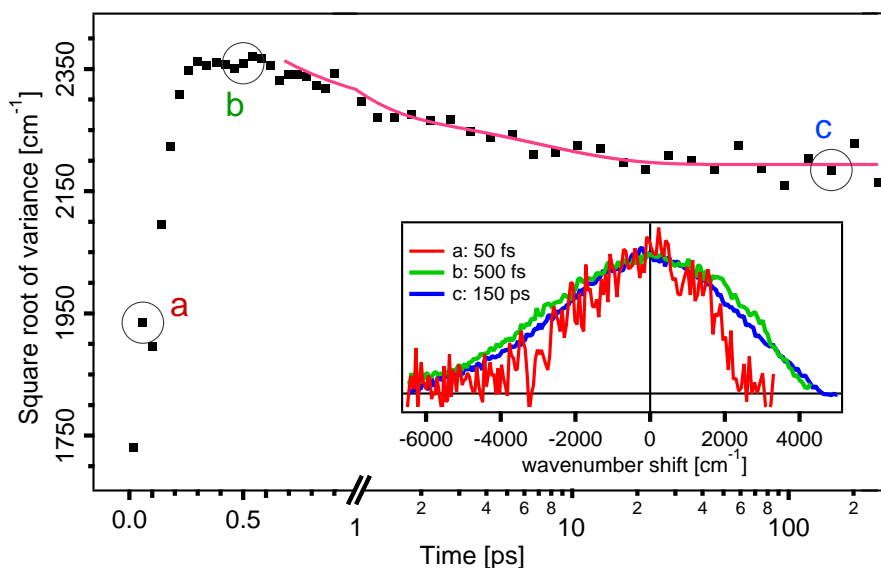


Figure 5.4: Square root of the variance of the Trp emission spectrum. Solid red line is the best fit in terms of bi-exponential decay. Inset shows normalized spectra at the three characteristic times as labelled on the main graph at 50 fs (a), 500 fs (b) and 150 ps (c). The spectra have been shifted to zero to better compare the spectral shape differences.

This behaviour can be observed by directly comparing the shape of normalized spectra at different times (inset of Figure 5.4). The two slowest timescales do not agree with water solvation times found by M_I analysis, indicating that these dynamics are not solvation driven. We tentatively assign them to vibrational cooling, since they are very similar to the cooling timescales of the UV chromophores (see chapter 4). Concerning the fastest component, it is so fast that we can exclude also cooling dynamics, signifying an intramolecular origin. In particular, it can be explained as a signature of IC process on the profile of the emission band. We consider that due to their different permanent dipole moments, the 1L_a and 1L_b states generate emission bands at different wavelengths. We can model the overall emission as the sum of two different spectral components each with its own spectral profile ($g_1(\nu, t)$ and $g_2(\nu, t)$). The IC process will induce a time dependent profile as described by the following equations:

$$\begin{aligned} g(\nu, t) &= \alpha(t) \cdot g_1(\nu) + [1 - \alpha(t)] \cdot g_2(\nu) \\ \langle \nu \rangle &= \alpha(t) \langle \nu \rangle_1 + (1 - \alpha(t)) \langle \nu \rangle_2 \\ \sigma^2 &= \alpha(t) \sigma_1^2 + (1 - \alpha(t)) \sigma_2^2 + \alpha(t)(1 - \alpha(t)) |\langle \nu \rangle_1 - \langle \nu \rangle_2|^2 \end{aligned} \quad (5.5)$$

where $g(\nu, t)$ is the total emission profile with first moment $\langle \nu \rangle$ and variance σ^2 (the index 1 and 2 refer to the respective single components) and $\alpha(t)$ takes into account the IC from 1L_b to 1L_a states. Figure 5.5 shows the kinetic model described above for some indicative but meaningful values, corroborating the idea that the fast rise observed stems from the difference in the 1L_a and 1L_b emission spectra, and only to a lower extent to IVR. To take into account the decay following the rise, experimentally observed on longer times, we should just include cooling narrowing assuming time dependent σ_2 ($\sigma_2(t) = \sigma_2^{Max} - 150(1 - e^{t/\tau_{cooling}})$).

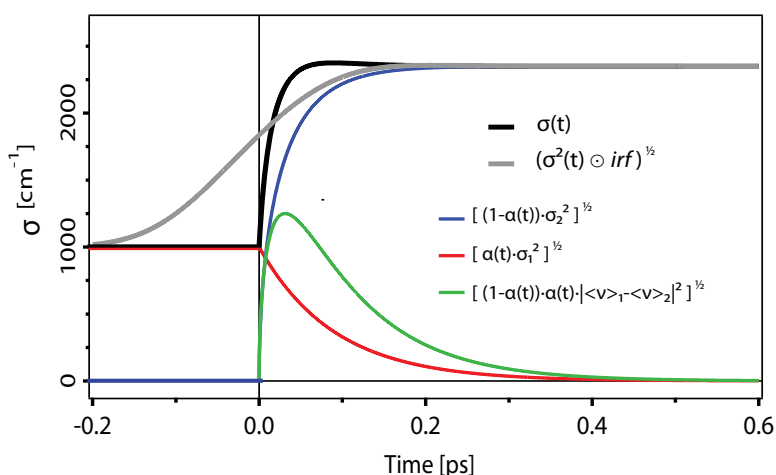


Figure 5.5: Square root of the variance kinetics model (black), using eqs (5.5) and assuming $\sigma_1 = 1000 \text{ cm}^{-1}$, $\sigma_2 = 2350 \text{ cm}^{-1}$, a 2500 cm^{-1} separation between the two spectra (indicative values), and an IC time of 45 fs from an initial condition of equally populated 1L_a and 1L_b states. The blue, red and green lines show respectively the first, second and third terms of the eq. (5.5). The grey line shows this function convoluted with the *irf*.

5.2 Non-equilibrium Molecular Dynamics Simulations

Simulations were run using Trp in its neutral zwitterionic form (which is dominant at pH = 7) placed in a cubic box with sides of 3 nm length, surrounded by 882 water molecules. Periodic boundary conditions were applied. Classical trajectories were calculated using the program package GROMACS.³²⁰ We used the GROMOS96 force field and the SPC/E water model, which was previously used to study Trp in water,^{321,322} a Lys-Trp-Lys tripeptide³¹⁸ and Trp in apomyoglobin.³²³ A cutoff of 0.9 nm was used to produce the non-bonded pair list. Similarly, we used 0.9 nm as cutoff for the calculation of the van der Waals interactions and short-range electrostatic interactions and the particle mesh Ewald algorithm^{324,325} (PME) was used to deal with the long-range interactions. We constrained bond lengths using LINCS,³²⁶ which allowed the use of a 2 fs time step.

The S_0 ground state of Trp was modeled using the GROMOS96 parameters, including atom charges. The 1L_a excited electronic state was modeled as having exactly the same parameters (equilibrium bond distances, force constants, etc.) as the ground state, but different site charges. These charges were obtained by adding the charge differences obtained in the ab-initio calculations of ref³²⁷ to the ground-state partial charges of the GROMOS96 force-field, following previous work.^{318,319} We used a similar procedure to simulate the 1L_b excited state. Basically the simulation assumes that the equilibrium structure of the indole group is the same in the two excited states as in the ground state. In this way, the simulations give information on the spectral evolution due mostly to solvent relaxation. Its drawback is an underestimation of the spectral widths.

Equilibrium ground state simulations were run in the NVT ensemble. A constant temperature of 295 K was maintained by coupling the system to a Berendsen thermostat.³²⁸ First the system was equilibrated by starting with energy minimization followed by an equilibration run of 0.5 ns. The production of a 10 ns trajectory was obtained. In a similar way, using the partial charges of the excited Trp, we obtained 10 ns equilibrium trajectories for the 1L_a and 1L_b excited electronic states. The time-dependent fluorescence process for 1L_a (1L_b) was simulated as follows: 500 initial conditions were obtained from the ground state trajectory by picking one configuration every 20 ps, which is a time long enough to consider these configurations as independent. Each configuration was used in a new 10 ps simulation obtained using the 1L_a (1L_b) potential. In this way, we obtained 500 excited

states trajectories each 10 ps long for 1L_a (1L_b). The excited state trajectories were run using the NVE ensemble, to avoid artefacts due to temperature coupling.

For a given configuration of the system, the energy difference between an excited electronic state and the ground state can be written:

$$\Delta E = E_e - E_g = \nu_0 + \Delta E^{IT} + \Delta E^{TS} \quad (3) \quad (5.6)$$

Where ΔE^{IT} is the difference between excited and ground state of the electrostatic interactions between the indole and the charged Trp groups - mainly NH^{3+} and COO^- (IT stands for Intra-Tryptophan), ΔE^{TS} is the difference in electrostatic interactions between the indole charges and water (TS stands for Tryptophan-Solvent), and ν_0 is the difference between the minima of the excited state and ground state potentials in vacuum. Actually the value of the latter cannot be obtained by this type of calculation that gives information only on shifts relative to this frequency. For convenience, we use as energy reference the equilibrium average $\Delta E \leftarrow \Delta E - \langle \Delta E \rangle_{e,\infty}$. For each excited state, using the 500 non-equilibrium trajectories we obtained at each time-step the histogram of energy differences, which represents the emission spectrum. This spectrum was characterized in a similar way as the experimental one, by calculating the time-dependent average frequency (Stokes shift) and standard deviation (bandwidth). For the shift we have, explicitly:

$$\Delta \nu(t) = \frac{\langle \Delta E \rangle_{e,t} - \langle \Delta E \rangle_{e,\infty}}{h} \quad (5.7)$$

Where the notation “ e,t ” stands for averaging over the excited state ensemble at time t . To simulate the effect of the 180 fs experimental instrumental response for broad band detection, we also obtained spectra by convoluting the simulated spectrum with a gaussian of 180 fs FWHM.

Results

The time-dependent fluorescence of Trp in different environments has been the subject of several theoretical investigations.^{122,157,170,318,319} Most studies assumed the validity of the Linear Response Approximation (LRA), which relates the time-dependent Stokes shift to the autocorrelation function of the energy difference in the ground (or excited) state. A recent study applied the LRA to separate the water and protein contributions to the time-dependent Stokes shift of Trp in the protein monellin and Trp in water.³¹⁹ Also, non-equilibrium Molecular Dynamics simulations were performed on a Trp in a

tripeptide³¹⁸ and apomyoglobin.³²³ These simulations can separate the different contributions to the fluorescence dynamics, and helps interpreting the experimental results. Using non-equilibrium simulations, we obtained time-dependent emission spectra for the excited electronic states 1L_a and 1L_b . The 1L_a and 1L_b simulated emission spectra are shown in Figure D.2, along with the calculated first moment, whereas Figure D.3 shows their respective square root of variance. The spectrum for 1L_b is qualitatively similar, but much narrower and the Stokes shift ($\sim 20 \text{ cm}^{-1}$) is negligible in comparison to that of 1L_a . Noteworthy, these spectral evolutions are mostly due to solvent relaxation as previously discussed. The underestimation of the spectral widths and the impossibility to estimate the frequency for the gas-phase 0-0 transitions make unfeasible the combination of 1L_a and 1L_b theoretical spectra to be compared with experimental spectral profiles. However, even if the spectra cannot be combined, since the 1L_b state is very short lived ($\tau_{ic} \sim 45 \text{ fs}$), beyond the first 100 fs, we are left with 1L_a as the only emitting state. This, together with the fact that the experimental temporal response is 180 fs and that more than 50 % of the molecules are directly excited to 1L_a , allows us to consider the experimental spectrum at magic angle to be mainly due to 1L_a , at least after the first 100 fs.

For a more detailed analysis, we calculate the first and second moments of the spectra. Figure 5.6 shows the average frequency for the simulated 1L_a spectrum. The reference is the frequency averaged over the interval that goes from 9 ps to 10 ps. We fit the time-dependent profile using three exponentials (Figure 5.6) covering a shift of $\sim 3750 \text{ cm}^{-1}$ after excitation: a large rapid shift with time constant (amplitudes) of 9 fs (1250 cm^{-1}), followed by further shifts with time constants 175 fs (1560 cm^{-1}) and 1.2 ps (950 cm^{-1}). For 1L_a we have a total (static) Stokes shift of $\sim 3870 \text{ cm}^{-1}$, calculated using the equilibrium ground and excited state trajectories. Therefore, after the initial 10 ps there is a further shift to the red of $\sim 100 \text{ cm}^{-1}$, which is probably due to re-equilibration of the Trp rotamers, occurring on the ns timescale. We find an excellent agreement of the time zero value with the expected total Stokes shift and of the 9 fs time constant with the experimentally determined 10 fs upper limit. The other two relaxation times agree with previous work³²⁹ and are in very good agreement with the values of 160 fs, and 1.02 ps obtained in the present experiments, whose assignment is discussed below. This confirms the validity of the assumption that the observed spectral behaviour is mainly taken into account by 1L_a dynamics, even at the earliest times. In particular, it proves that the origin of the

“instantaneous” Stokes shift is mostly related to the effect of solvent inertial response^{98,122} on the 1L_a state. The main difference between the theoretical (3760 cm^{-1}) and experimental (2050 cm^{-1}) Stokes shift is accounted for by convolution of the simulated spectra with a gaussian *irf* of 180 fs FWHM, which yields a Stokes shift of $\sim 2300\text{ cm}^{-1}$ (green trace in Figure 5.6). To further analyze the processes underlying the frequency shift, it is instructive to separate it into Intra-Tryptophan (IT) and Tryptophan-Solvent (TS) contributions, which can be done in the simulations since the Coulomb energy is additive.

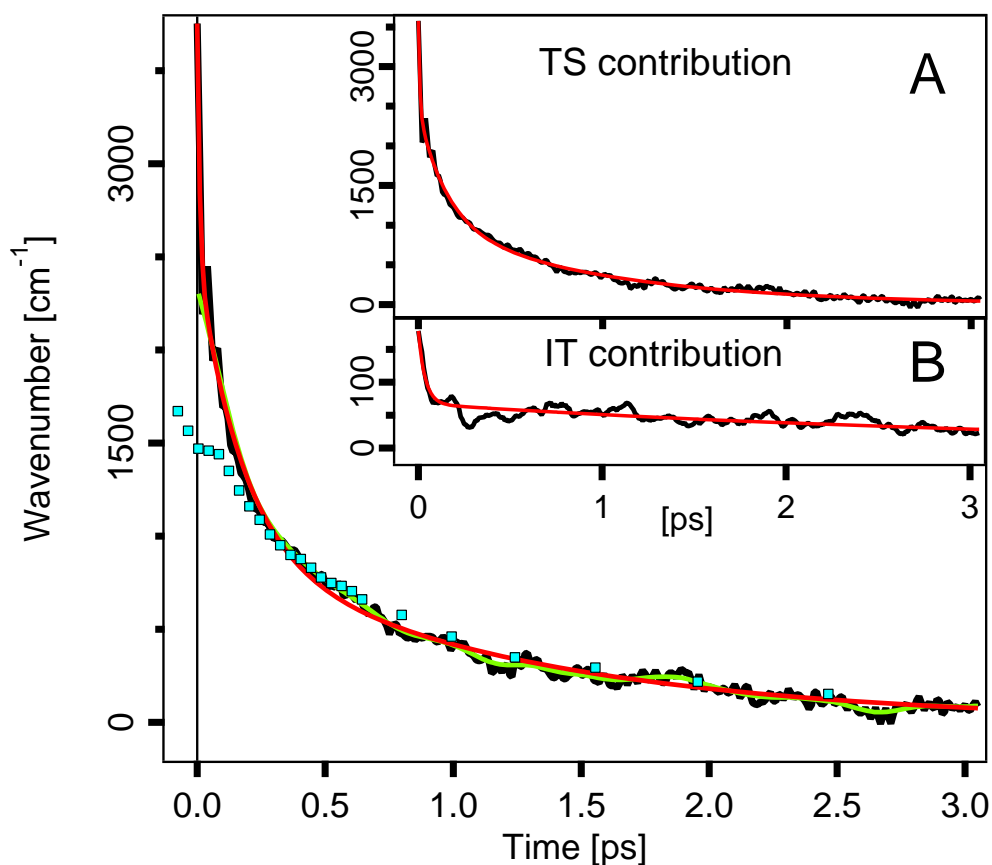


Figure 5.6: Experimental average emission frequency (first spectral moment) of 1L_a emission band (blue square dots) along with the fit (red solid line) and convolution with instrumental response (solid green line) of the computed average emission frequency (black solid line). Inset A reports the Tryptophan-Solvent contribution (squares) with its best fit (red solid line). Inset B reports the Tryptophan-Tryptophan contribution with its best fit (red solid line).

Indeed, even if the adopted simulation approach excludes IT contribution due to structural rearrangement, we have IT consisting of the interaction between the Trp partial charges. The IT contribution to the static Stokes shift is 214 cm^{-1} while the TS contribution is 3655 cm^{-1} , i.e. 5.5% and 94.5% respectively of the overall static Stokes shift, in good agreement with previous work that used a different water model.³¹⁹ In Figure 5.6 we show

the time-frequency plots corresponding to the TS (panel A) and IT (panel B) contributions. The TS contribution is adequately fitted ($R = 0.99$) using three exponentials with relaxation times (amplitudes) of 8 fs (1134 cm^{-1}), 154 fs (1397 cm^{-1}), and 0.95 ps (1045 cm^{-1}). The IT contribution can be fitted with two exponentials of relaxation times 37 fs (110 cm^{-1}) and 3.6 ps (68 cm^{-1}). As expected, the fit to the total Stokes shift discussed previously only shows the relaxation times due to solvent relaxation. We will see next, however, that the experimental methodology here adopted will allow us to study the dynamics of internal (IT) motions analyzing the bandwidths.

We calculate the second moment of the simulated spectra, which for the 1L_b state is small ($\sim 60 \text{ cm}^{-1}$) and constant. However, as shown in Figure 5.7A (red trace), the second moment of the simulated 1L_a spectrum is time-dependent, with an initial rise of $\sim 140 \text{ cm}^{-1}$ followed by a decrease of $\sim 170 \text{ cm}^{-1}$ with lifetime of ~ 1 ps. This decrease is in accordance with the narrowing of the experimental emission band occurring in 0.5 ps and attributed to Vibrational Cooling (Figure 4 and Table 2). The fast rise would speak for an increase of Trp temperature and therefore for an IVR mechanism in the first 10s of fs. However, the initial rise disappears when convoluting the spectrum with a Gaussian of 180 fs FWHM, so that it will be missed in the experiment. This confirms that the initial rise of the experimental spectrum is due to IC rather than IVR. We should note here that the simulated bands are much narrower than the experimental ones. The reason for this is that we model the excitation just as a change in partial charges of Trp, at fixed intramolecular geometry, which underestimates the effect of excitation on the equilibrium structure. However, the simulations correctly reproduce the experimentally observed narrowing of the band.

Figure 5.7A compares the local temperature of Trp (calculated from the average kinetic energy of the Trp atoms) with the square root of the variance of the simulated emission spectrum. It can be seen that there is a qualitatively similar behaviour between the bandwidth profile (red) and the temperature profile (black), confirming the origin of the rise of the simulated spectra. The initial heating of the chromophores would result in the initial broadening, and the subsequent cooling down would contribute to the narrowing of the emission band. Furthermore Figure 5.7B shows that the initial drop of the frequency shift due to intra-Trp interactions (IT component shown in Figure 5.6B) clearly follows the initial temperature rise (plotted in inverted scale, for better comparison). We rationalize these dynamics as a rapid IVR in the solute: IT contribution to the Stokes shift is due to a

rearrangement of the COO^- and NH^{3+} groups as a response to the different charge distribution of the indole group in the $^1\text{L}_a$ state with respect to the ground state. There is a rapid decrease in potential energy of Trp (earliest frequency shift in Figure 5.6B), which results in an increase of the kinetic energy of Trp atoms, thus of the temperature (Figure 5.7). After this initial increase, there is a further, slower, decrease of the potential energy (slow red-shift in Figure 6B), but the temperature keeps decreasing because of a heat transfer to the environment (vibrational cooling). The simulated bandwidth profile is consistent with the experimental profile. In particular, it is well fitted by a biexponential function with the time constants of 450 fs and 7 ps found for experiment. Moreover, the experimental first moment M_1 tells us that after 5 ps the solvation dynamics are almost completely over, meaning that this 7 ps narrowing could not be solvation-driven or at most at a lower extent. These results support the interpretation of the time-profile of the bandwidth in terms of IC/IVR and vibrational cooling.

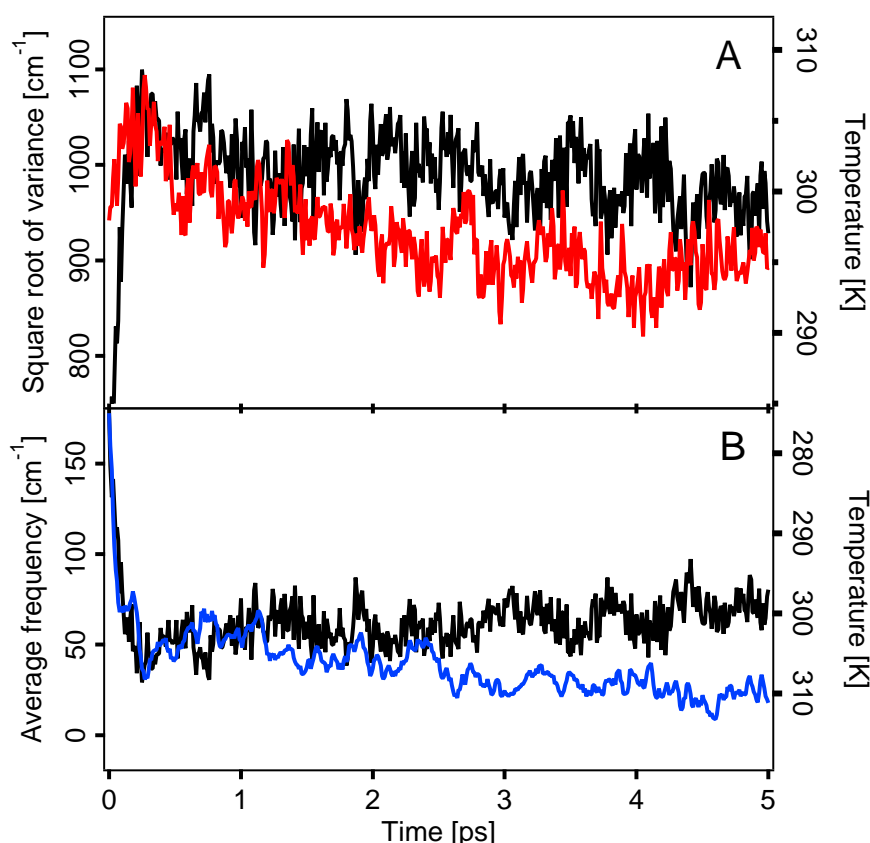


Figure 5.7: A) Square root of the variance of the emission band (red) compared to local temperature of Trp (black). B) IT contribution to the average frequency of the emission band (blue) from Figure 6B compared to local temperature of Trp (black). Please observe that the temperature scale of panel B is inverted with respect to panel A for a better comparison.

The earlier (first 4 ps, Figure 5.7A) narrowing down of the band is not only due to a decrease in temperature, but to a strengthening of the solute-solvent interactions in the excited 1L_a state. The bandwidth corresponding to $t = 0$ can be better estimated as the variance of the energy-difference over the equilibrium 10 ns ground-state trajectory, which gives a value of $\sim 910 \text{ cm}^{-1}$ for 1L_a . Similarly, the stationary emission bandwidth can be calculated from the equilibrium 10 ns 1L_a trajectory, which gives 800 cm^{-1} . Therefore, there is an overall narrowing of the spectrum of 110 cm^{-1} , as measured by the square root of the variance. These bandwidths are calculated from equilibrium trajectories at constant (295 K) temperature. Therefore, this narrowing is not due to temperature variations, but is rather evidence of the excited state Trp-Water interaction being stronger than in the ground state. Thus, the narrowing observed in Figure 5.4 and 5.7 has two origins: temperature transients due to IVR and vibrational cooling, and an actual strengthening of the solute-solvent interaction.

Noteworthy is that in previous experimental studies of Trp fluorescence with lower time resolution and monochromatic detection, vibrational cooling was explicitly dismissed.^{165,330} Although IVR and vibrational cooling are well known phenomena which are noticeable when the excess vibrational energy is very high, of the order of hundreds of K,^{312,331} here we are able to detect an internal cooling by as little as 30 K showing the sensitivity of the present experimental approach (also noted in the UV chromophores,^{192,193} see chapter 4). A point to note is that both the strengthening of the interaction and the temperature transients should imply a breakdown of the Linear Response Approximation (LRA) according to which.³¹⁹

$$\Delta\nu(t) \approx \frac{C_g(t)}{hk_B T} \approx \frac{C_e(t)}{hk_B T} \quad (5.8)$$

Where h is Planck's constant k_B is Boltzmann's constant and $C_g(t)$ and $C_e(t)$ are the excitation energy correlation functions for the ground and excited state respectively. The LRA is usually assumed to be a good approximation for Trp. However, we shall see later that it cannot deal with some of the results reported in this work.

It is important to deal with this issue because without further consideration the LRA is frequently assumed. According to the LRA, the Stokes shift is related to the energy-difference autocorrelation function calculated either in the ground state or the excited state. Replacing $t = 0$ into eq. (5.8) we obtain

$$\Delta\nu(0) \approx \frac{C_g(0)}{hk_B T} \approx \frac{C_e(0)}{hk_B T} \quad (5.9)$$

where by definition $C_g(0) = \langle \Delta E^2 \rangle_g$ and $C_e(0) = \langle \Delta E^2 \rangle_e$ are variances of the initial $t = 0$ emission and stationary emission bands, respectively. As said before, for 1L_a the “exact” static Stokes shift calculated with eq. (5.7) is $\sim 3870 \text{ cm}^{-1}$, whereas using eq. (5.9) we obtain $\sim 4050 \text{ cm}^{-1}$ and $\sim 3130 \text{ cm}^{-1}$ for the ground or excited correlation functions, respectively. In this way, we see that using the LRA with the ground state correlation overestimates the total shift by $\sim 10\%$, whereas with the excited state one, it underestimates it by $\sim 20\%$. These errors could and have been considered to be negligible in the sense that they are of the order of expected errors due to the approximate nature of the used theoretical force fields.³¹⁹ However, we stress that eq. (5.9) implies that the initial and final bandwidths are expected to be the same. Moreover, implicit to eq. (5.8) is the assumption of constant temperature throughout the relaxation process. We have shown before that none of these assumptions are valid. Therefore, even though for certain purposes the LRA can be used as a reasonable approximation, it cannot account qualitatively for aspects of the dynamics observed in this work, namely, the processes responsible for the variations of the emission bandwidth with time. Therefore, we think that equilibrium perturbative approximations are inadequate to deal with the detailed ultrafast spectral dynamics, as observed using the sensitive experimental techniques reported here, and that non-equilibrium theoretical treatments are unavoidable.

5.3 Conclusions

In summary, we presented UV broad-band fluorescence up-conversion measurements of tryptophan in bulk water with polarization detection, and compared them with non-equilibrium MD simulations of 1L_a and 1L_b relaxation dynamics. The experimental and simulation results presented above allow us to draw the following conclusions:

a) The time-resolved fluorescence anisotropy of tryptophan in water clearly exhibits a signature of an $^1L_b \rightarrow ^1L_a$ IC in 45 ± 15 fs, confirming previous predictions.^{161,165} Our observation of the wavelength dependence of the anisotropy provides evidence for emission from the 1L_b state.

b) The MD simulations confirm the biphasic relaxation of Trp in water with 160 fs and 1 ps exponential components. These times are attributed to collective motions and independent diffusion of several proximal water molecules.⁹⁸

c) We found a sub-10 fs decay which account for ~ 1700 cm^{-1} shift of the total Stokes shift of 3800 cm^{-1} . The occurrence of sub-10 fs frequency shifts was recently observed on a variety of different systems.^{52,128,186-188,192,193} Contrary to these systems, where such a fast Stokes shift is clearly intramolecular, we find here that the origin of this dynamics is intermolecular, i.e. due to solvation. It comes from the inertial motion of the water molecules, and is associated to their independent rotational motion, as already predicted.¹⁷⁰

d) The broadband detection provides reliable variance kinetics so that cooling dynamics can be sensitively followed. The excess vibrational energy, corresponding to a 30 K heating of the Trp, is responsible for ~ 6 % of the final, thermalized, width and is released to the solvent in a biphasic way with 0.5 and 7 ps time constants. The former component could also take into account slower IVR processes among low frequency vibrational modes. In this respect, due to the concurrent effects of IC and IRF convolution the observed value of 0.5 ps could be slightly shorter. The different decay times found in the case of variance and first moment kinetics show that the latter are only solvation dynamics related. The most important result of the variance analysis is the experimental evidence of a ~ 50 fs rise corresponding to a broadening of 500 cm^{-1} ($\sim 30\%$ of the thermalized width). This behaviour is directly reflecting the IC process.

e) The present study shows the sensitivity of fs broad-band UV fluorescence up-conversion of Trp and is promising for its use in biological systems.

Chapter 6

Relaxation dynamics of porphyrins

6.1 Free base porphyrins

- 6.1.1 Non-sequential electronic relaxation*
- 6.1.2 S₂→S₁ internal conversion of H₂TPP*
- 6.1.3 Vibrational relaxation*
- 6.1.4 Wavepacket dynamics*
- 6.1.5 Nonradiative channel*
- 6.1.6 Summary*

6.2 Zn (TP and OE) porphyrins

- 6.2.1 Ultrafast dynamics of Zn porphyrins*
- 6.2.2 Sequential electronic relaxation*
- 6.2.3 Summary*

6.3 Transition metal (TP and OE) porphyrins

- 6.3.1 Ultrafast emission*
- 6.3.2 Parameters affecting the relaxation processes*

6.4 Conclusion

Porphyrins have been and are still at the center of an intense research activity. Their peculiar photophysics is at the core of a wide panel of applications, based on photoactivated processes, and of the study of numerous biochemical systems (see chapter 2). These systems play indeed a fundamental role as a cofactor in several biomolecules, and in particular in haemoproteins which is the main topic of the next chapter.

The early stages of the photocycle of porphyrin systems have been extensively studied with various femtosecond resolved spectroscopic techniques.^{1,223-226,234,252,332-341} More specifically, several studies with single wavelength time-resolved emission have been reported.^{226,332,334-336,341} A complex, entangled electronic and vibrational relaxation was evidenced. Nevertheless, some questions still remain: How the polarization affects the electronic relaxation of the free base porphyrins? What is the origin of the unusual Soret emission decay in ZnTPP? Which is the electronic relaxation pathway leading to the ultrafast charge transfer in the transition metal porphyrins?

As already discussed in the previous chapters, the unique ability to spectrally resolve the emission with fs resolution provides a more detailed and conclusive picture with respect to these techniques. With the aim to clarify several aspects of the photocycle of such an important class of molecules and to provide a solid base to interpret results on the biological samples (haemoproteins), we revisited the relaxation dynamics of a wide series of porphyrin derivatives.

This chapter aims at giving a detailed picture of the relaxation dynamics of photo-excited porphyrin systems and some hints on the influence of various parameters on this relaxation. In particular, the role of the metal atom and its electronic structure, the presence of substituents on different positions on the porphyrin macrocycle and the attachment of a ligand to the metal are investigated. We will first discuss the energetic relaxation of the free base porphyrins before moving on to different metallo-porphyrins.

6.1 Free base porphyrins

6.1.1 Non-sequential electronic relaxation

Figure 6.1a (6.1b) shows the time-wavelength plot of the fluorescence from H₂TPP (H₂OEP) in cyclohexane, excited at 400 nm and measured at the magic angle. Figure 6.1c and 6.1d show a selection of spectra at various time delays. The strong peak at 452 nm corresponds to the 2900 cm⁻¹ Raman response of cyclohexane. In the 420-500 nm region, a large band below 500 nm vanishes in 200 fs and 100 fs for H₂TPP and H₂OEP, respectively. This band is ascribable to the Soret emission,³⁴² since it is positioned close to the Soret absorption band (Figure 2.7). Indeed, as a general feature of porphyrins, the Soret emission is expected to have a very small Stokes shift.^{226,332,341} The reason is that the observed Franck-Condon progression in absorption shows a weak linear coupling constant and that porphyrins are apolar chromophores.

Above 500 nm, where emission from the *Q* bands is expected, a broad emission with three maxima appears immediately. The two blue most bands (500-610 nm) vanish with increasing lifetime going towards longer wavelengths, whereas the red most band decays only on the nanosecond timescale. The two bands at 560 and 610 nm for H₂TPP and 530 and 580 nm for H₂OEP can be assigned to *Q_y*(1,0) and *Q_y*(0,0) transitions, respectively, on the basis of mirror image symmetry of the absorption band (Figure 6.1g and 6.1h). Similar considerations lead us to assign the band at 650 nm (625 nm) for H₂TPP (H₂OEP) to emission from the *Q_x*(0,0) transition, which is long-lived (~10 ns). The system then undergoes intersystem crossing to the lowest triplet state T₁.¹ Emission from the *Q_x*(0,1) transition is not observed here, because it is out of the detectable range. We indeed set deliberately the blue-most limit of the CCD camera around 420 nm in order to observe emission from the Soret, at the expense of red most part of the fluorescence spectrum.

No rise of the emission is observed across the entire spectrum. Apart from a weak and long 30 ps component in the *Q_x*(0,0) band, all bands are instantaneously populated within our *irf*. The selection of kinetic traces for H₂TPP in Figure 6.1i illustrates the absence of rise time in the first 5 ps, and in particular in the *Q_x*(0,0) emission. This observation rules out any sequential relaxation cascade by internal conversion (IC), before reaching to the lowest excited state (*Q_x*(0,0)). In the latter case, the increasing lifetime going from short to long wavelength would be accompanied by a corresponding rise.

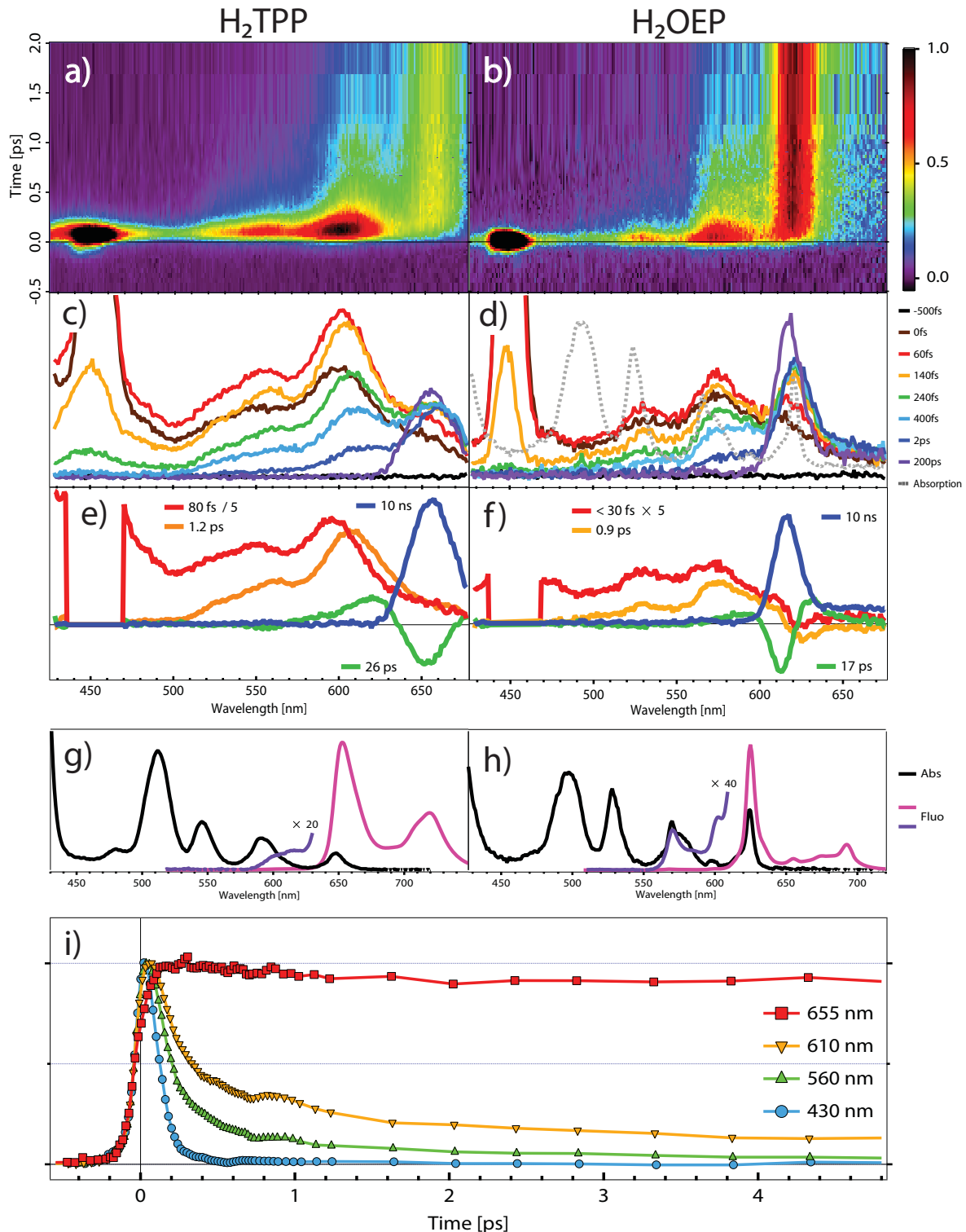


Figure 6.1: a) (b) Time-wavelength fluorescence intensity plot of H₂TPP (H₂OEP) in cyclohexane excited at 400 nm. The strong peak at 453 nm the Raman response of cyclohexane (2900 cm⁻¹). c) (d) Fluorescence spectra of H₂TPP (H₂OEP) selected at various delay time after excitation from panel a) (b). e) (f) Decay associated spectra of H₂TPP (H₂OEP), obtained after Singular Value Decomposition and global fitting analysis. g) (h) Static absorption and fluorescence spectra of H₂TPP (H₂OEP) in cyclohexane. i) Normalized kinetic trace of fluorescence of H₂TPP in cyclohexane, at the 4 different detection wavelengths (430, 560, 610 and 655 nm).

This suggests that the excited states that decay fast between 500 and 600 nm do not feed the $Q_x(0,0)$ state, but an optically silent state or the ground state. We have compared the relative QY of $Q_x(0,0)$ fluorescence under $Q_x(1,0)$ excitation and Soret excitation, and we found an emission almost 20 times smaller when excited in the Soret (10 times smaller for H₂OEP). Thus, molecules excited within the Soret band experience more than one relaxation channel, of which one is an optically silent state. The nature of the latter will be discussed in §6.1.5.

The transient spectra in Figure 6.1c and 6.1d show that the most intense band at time zero (610 nm and 580 nm) shifts to the red as it decays. However, this shift is only the result of an overlap of two closely lying bands with different decay times (see Figure 6.1i for H₂TPP). The following SVD analysis will confirm this behavior. Figure 6.1e and 6.1f show the Decay Associated Spectra (DAS) obtained after analysis of the SVD of data from Figure 6.1a and 6.1b. We now discuss the assignment of all the observed dynamics:

< 100 fs DAS: The fastest spectral component (red lines) is broad, covering the 420 to 780 nm region. Data in the 430-470 nm range, distorted by the Raman peak, were neglected during the analysis. At $\lambda < 500$ nm, this component corresponds clearly to the Soret emission decay. For $\lambda > 500$ nm, it exhibits a clear vibronic progression with 2 main bands at 560 (535) and 605 (580) nm for H₂TPP and 535 and 580 nm for H₂OEP. This structured emission looks fairly like the mirror image symmetry of the $Q_y(1,0)$ and $Q_y(0,0)$ transitions and we can assign its two components to the $Q_y(0,0)$ and $Q_y(0,1)$ emission bands. This is a first surprising result since emission from the Soret and Q_y bands are decaying with the same lifetime.

0.9-1.2 ps DAS: The second DAS (orange lines) has the same structure as the <30/80 fs one, but with no contribution in the Soret region. This decay is thus attributed to $Q_y(0,0)$ and $Q_y(0,1)$ emission alone. No rise (negative contribution) with the same timescale is observed in other regions of the spectrum, and in particular in the lower energy region. This single decay confirms that the Q_y population relaxes to a dark state, with inefficient IC to the Q_x state.

10 ns and 17-26 ps DAS: The longest spectral component (blue lines), is unambiguously ascribable to emission from the $Q_x(0,0)$ transition. The larger width of this band compared to the steady state one, is due to a lower spectral resolution in the fluorescence up-conversion experiment (see chapter 3). The spectral component associated with a 26 and

17 ps lifetime (green lines) for H₂TPP and H₂OEP, is constituted of positive and negative contributions, corresponding to decay and rise on the same timescale. This feature will be discussed in details in the next paragraph.

6.1.2 $S_2 \rightarrow S_1$ internal conversion of H₂TPP

While the Q states are populated within our *irf*, the Soret emission is not pulse-limited but decays with 80 fs in the case of H₂TPP. This bimodal behavior suggests the presence of more than one electronic state in the Soret band, likely B_x and B_y . These observations agree with the excitation of a mixture of B_x and B_y states, each undergoing IC to Q_x and Q_y , respectively. The relaxation mechanism appears clearly separated into x and y polarization, without IC between states of different polarization. Indeed, the instantaneously populated Q_x and Q_y states deactivate on distinct timescales. In addition, the parallel and orthogonal fluorescence polarization do not show any difference over the entire spectrum (data not shown), confirming the fact that the polarization is preserved during the electronic relaxation.

6.1.3 Vibrational relaxation

In this paragraph, we take a closer look to the long-lived $Q_x(0,0)$ emission band. The DAS corresponding to the 26 ps (17ps for H₂OEP) lifetime (Figure 6.1e and 6.1f) describes a narrowing concomitant with a shift of the 10 ns band ($Q_x(0,0)$ emission). These dynamics are typical of a cooling process. The related spectral shape and the corresponding timescale make no doubt on its assignment.^{332,343} Figure 6.2a and 6.2b show the wavelength-resolved emission from the $Q_x(0,0)$ band (from Figure 6.1a and 6.1b), over 200 ps. Both bands are shifting to the blue on tens of ps. The first spectral moment of these bands, plotted in Figure 6.2c, confirms that a blue shift occurs on the same timescale as the cooling, preceded by a fast red shift on ~ 1 ps. This behavior has already been observed and explained:³⁴⁴ it is due to a vibrationally induced reduction of the energy gap by anharmonic expansion of the porphyrin ring. After the fast red shift, the hot and red-shifted $Q_x(0,0)$ band recover its initial position (~ 3 nm blue shift) as the cooling occurs. The presence of emission on the blue side of the band decaying with the same timescale does not allow an accurate measure of the expansion time, but we can conclude to an upper limit of 1 ps.

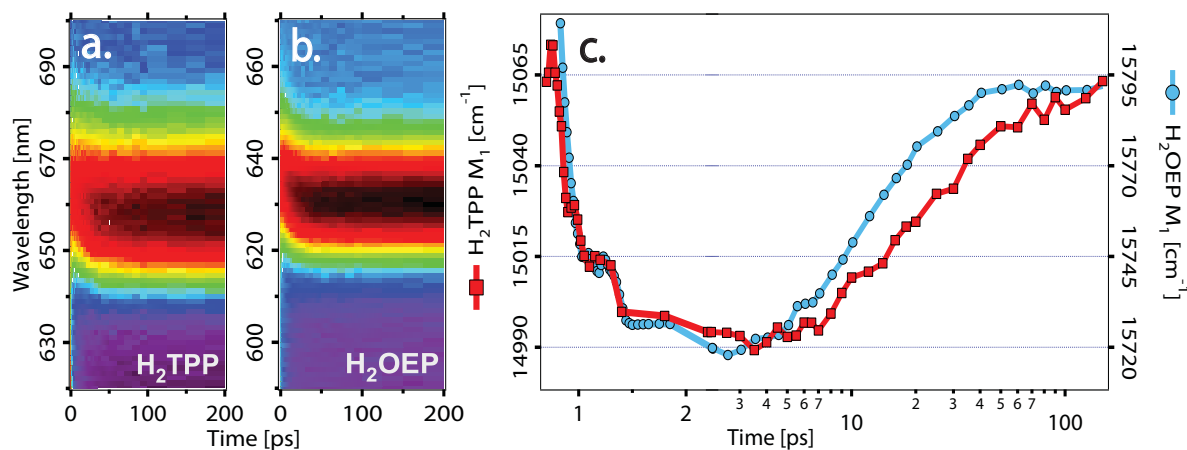


Figure 6.2: a) (b) Time-wavelength fluorescence intensity plot of H₂TPP (H₂OEP) from Figure 6.1a and 6.1b, in the 600-700 nm region and until 200 ps. c) First spectral moment of the Q_x(0,0) emission band from H₂TPP (red squares) and H₂OEP (blue circles) from data of panel a) and b).

In the static fluorescence spectrum (Figure 6.1d and 6.1g), a weak shoulder is observed on the blue side of the Q_x(0,0) band. The latter is observable on the corresponding spectra multiplied by a factor of 20 and 40 for TPP and OEP, respectively (Figure 6.1e and 6.1f). This feature has been attributed to a hot band, disappearing at low temperature.³⁴⁵ When integrating our data over the 200 ps, the spectrum fits the static fluorescence, including the weak shoulder (not shown). Consequently, the origin of the latter is confirmed: it is emission of a “hot” vibrational level, namely the Q_x(1,0) transition. Accordingly, the related decay (17-26 ps) contains also contribution from vibrational relaxation.

6.1.4 Wavepacket dynamics

Closer examination of Figure 6.1a, reveals a recurrence at around 1 ps delay time in the 600-620 nm region. To elucidate the origin of this revival, we have performed the same measurements but with different data acquisition conditions (smaller time window (3 ps) and longer integration time) to improve the signal to noise ratio. The results presented in Figure 6.3a and 6.3b, reveal a clear oscillating behavior in the 550-650 nm region, as nicely show the kinetic traces in Figure 6.3c and 6.3d. To extract the frequencies involved in the oscillatory pattern, we performed on each kinetic trace a Fourier transform (FT) of the residual of a multi-exponential fit. The FT spectra are shown in Figure 6.4a and 6.4b. These results are confirmed by a fit of the kinetic traces taking into account 3 damped oscillations of frequencies $36 \pm 4 \text{ cm}^{-1}$, $80 \pm 5 \text{ cm}^{-1}$ and $110 \pm 7 \text{ cm}^{-1}$ (Figure 6.3c and 6.3d). The damping factor obtained varies from 0.3 to 1 ps. Remarkably, the frequency dominating the oscillating pattern is wavelength-dependent.

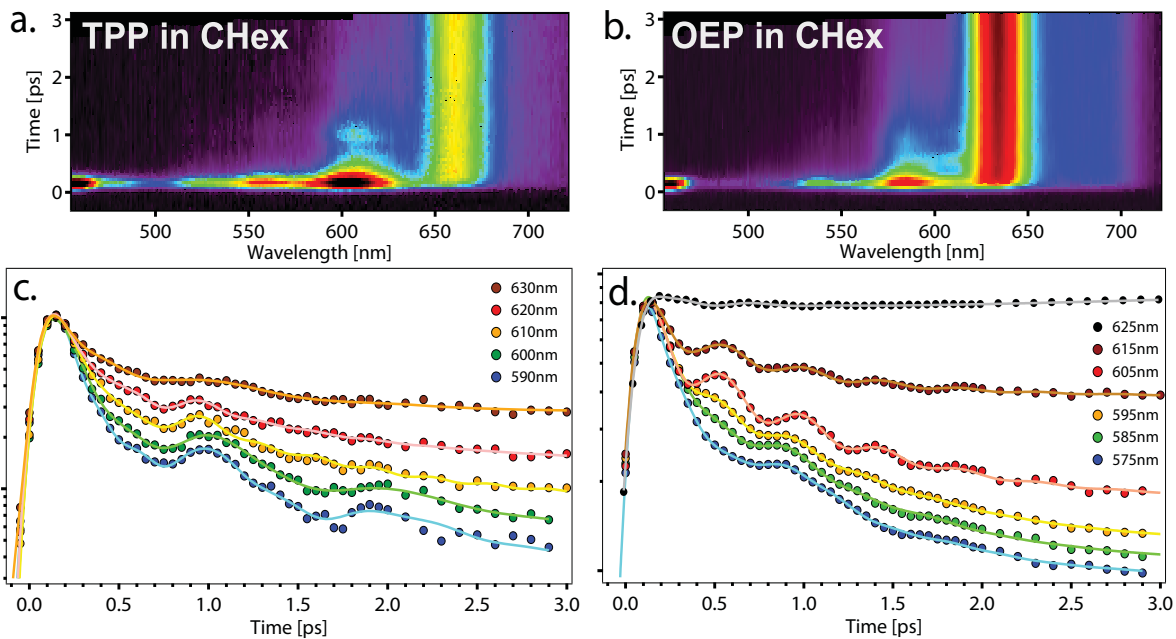


Figure 6.3: a.(b.) Time-wavelength fluorescence intensity plot of H₂TPP (H₂OEP) in cyclohexane excited at 400 nm. c.(d.) Normalized fluorescence kinetic trace of H₂TPP (H₂OE), at the detection wavelengths indicated in the legend, integrated over 5 nm, along with their fit, including 3 exponential decays and 3 cosinus. A logarithmic intensity scale was chosen since the oscillations are superimposed with a fast decay.

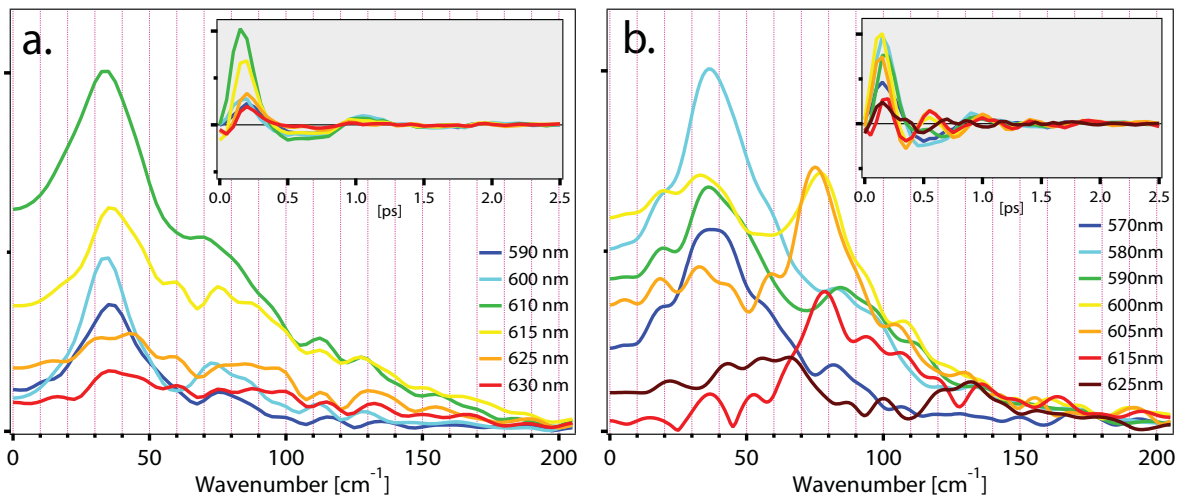


Figure 6.4: a) (b) Fourier Transform spectra of the oscillations pattern of H₂TPP (H₂OE) at different wavelengths, from the kinetic traces of the fluorescence data of Figure 6.3c (d). The insets show the residuals of the multi-exponential fits.

The FT spectra show a strong peak around 37 cm^{-1} , common to H₂TPP and H₂OEP. Moving to redder wavelengths, in the case of H₂OEP, the 37 cm^{-1} peak decreases in intensity while a peak at 75 cm^{-1} increases. In the case of H₂TPP this behavior appears only as a shoulder in the $70\text{-}90\text{ cm}^{-1}$ region. The spectral region where the oscillations are taking place ($590\text{-}630\text{ nm}$ for H₂TPP, $570\text{-}630\text{ nm}$ for H₂OEP) corresponds to the 610 nm (580 nm) band observed in the early transient spectra of H₂TPP (H₂OEP) (Figure 6.1c and 6.1d). A third weak band appears at $120\text{-}130\text{ cm}^{-1}$ in the red-most region. A two dimensional Fourier transform of the data in Figure 6.3a and 6.3b confirms the presence of this band (data not shown). We will now discuss the assignment of each frequency.

A progression (37 , 77 and 111 cm^{-1}) has been observed experimentally in the fluorescence spectrum at 7 K of H₂OEP in n-octane,³⁴⁶ confirmed by the calculations of Schlücker et al.,³⁴⁷ who reported a doming mode of 37 cm^{-1} ($\sim 900\text{ fs}$). While a 130 cm^{-1} vibrational mode has been reported by Singh *et al.*,³⁴⁶ but not assigned, no $\sim 80\text{ cm}^{-1}$ mode has ever been calculated nor observed for this compound. It is clearly present, at least in H₂OEP, as confirmed by the inset of Figure 6.4b. Other metallo-porphyrins have shown wavepacket dynamics on a longer timescale, but always with higher frequencies.^{225,342} However, the two lowest frequencies ($\sim 37\text{ cm}^{-1}$ and $\sim 80\text{ cm}^{-1}$) have been already reported by Champion and co-workers in femtosecond coherent spectroscopy (FCS) studies of haemoproteins.³⁴⁸⁻³⁵⁴ While in these experiments the doming mode $\sim 40\text{ cm}^{-1}$ is well characterized and used as a benchmark of ligand photolysis, the origin of the 80 cm^{-1} mode is supposed to be a combination of haem doming with other out-of-plane low frequency modes. The 40 and 80 cm^{-1} modes evidenced by Champion have strong damping factor ($< 1\text{ ps}$), similar to the ones observed here. They also observed oscillations in the $100\text{-}150\text{ cm}^{-1}$ frequency region, but did not assign them to a particular vibrational mode. They suggest that these modes are associated with out-of-plane vibrations, as saddling, ruffling or waving.

The presence of wavepacket dynamics corroborates the idea that the lowest excited singlet states (Q_x and Q_y) are instantaneously populated. While the Q_x is long-lived, a nonradiative channel depopulates the Q_y state with 100 fs and 1 ps decay times. We discuss the nature of the accepting state in the next §.

6.1.5 Nonradiative channel

This study brings the evidence that the no $Q_y \rightarrow Q_x$ IC occurs, as would be expected. Instead, these two instantaneously populated states undergo their own relaxation channel. While Q_x is long-lived, Q_y relaxes to another state in ~ 1 ps. We now discuss the nature of this accepting electronic state. The latter could be of different nature: i) the ground state; ii) a dark electronic state; iii) the triplet state.

An ultrafast ISC to a triplet state can be excluded, since 1) such a rapid spin crossing is improbable in the free base porphyrins,³⁵⁵ and 2) the Zn porphyrins exhibit slower relaxation mechanism despite an increased spin-orbit coupling (see next section). No excited singlet state underlying the Q_x state is expected, ruling out IC to a lower dark singlet state. Another possibility would be that the photoexcitation at 400 nm is degrading the molecule, for example by electron transfer to the solvent, as observed for ZnTPP in CH_2Cl_2 .²²⁶ No such photodegradation was observed after the measurements at least in the static absorption spectrum. The most probable nonradiative channel responsible for this decay is IC to the ground state through better vibrational couplings at high energy. This issue has already been investigated with transient absorption measurements,^{332,356} but the overlap of the strong and broad absorption of the lowest singlet state with the stimulated emission did not allow to identify the accepting level.

The photophysical properties of porphyrins highly depend on whether their structure is planar or nonplanar.^{1,357-359} Non-planar porphyrins show some characteristic differences in the absorption and emission spectra with respect to the planar ones: red shift of the absorption bands, larger Stokes shift, broader and less structured fluorescence spectrum and reduced fluorescence yield. Chirovny *et al.* investigated the role of porphyrin distortion on the fluorescence lifetime shortening of the diprotonated forms of H_2TPP and H_2OEP ($\text{H}_4\text{TPP}^{2+}$ and $\text{H}_4\text{OEP}^{2+}$).¹ These compounds are known, from computed structures and X-ray data, to undergo strong non-planar saddle shape distortion. They attributed the radiationless deactivation to IC to the ground state, enhanced by out-of-plane distortion of the porphyrin ring. Indeed, the greater conformational flexibility of the photo-excited species allows wide exploration of the excited state potential surface. This flexibility gives access to (non-planar) configurations with reduced energy gaps between the ground and excited states, leading to a funnel geometry where the IC is dramatically enhanced. This scheme proposed by Chirvony *et al.* is shown in Figure 6.5. Beside the original 10 ns decay

of Q_x fluorescence due to ISC to triplet state, a faster component appears on the ns timescale. The energy barrier necessary to access these quenching configurations has been estimated to $\sim 1400 \text{ cm}^{-1}$ by temperature dependence of the Q_x fluorescence decay time. The situation is quite different for the parent molecules H_2TPP and H_2OEP , herein investigated, since they show a near-planar geometry already in the ground state. Accordingly, the radiationless deactivation yield of Q -band excited H_2TPP is relatively small (0.1-0.2). However, when exciting the Soret, the latter is significantly higher (see §6.1.1). One could imagine that the large excess of vibrational energy under 400 nm excitation allows exploring a wide area of the excited state potential surface, inducing non-planar distortion. Moreover, the wavepacket dynamics observed around 570-650 nm corresponds to the doming motion of the porphyrin. This non-planar vibration could be thought to enhance the rate of the IC to ground state. Indeed, the oscillations are superimposed to a rapid decay, and we cannot exclude that the formers modulate the IC rate, i.e. the decay.

Another important aspect leads to an alternative explanation: the IC rate of H_2TPP has been shown to be affected by deuteration of the center hydrogen atoms, suggesting an important role of the N-H vibration.^{360,361} In addition, the $\text{S}_2 \rightarrow \text{S}_1$ IC rate has been investigated by Tripathy and co-workers for a large selection of free base and Zn porphyrins. They suggested that for the free base, the $\text{S}_2\text{-S}_1$ interstate coupling is greatly enhanced by the N-H vibration. These evidences suggest that the mode involving N-H vibration play the role of accepting mode during the $\text{S}_1 \rightarrow \text{S}_0$ relaxation. In this picture, it is expected a very different FC overlap of the Q_y and Q_x levels with those of the ground state, since the origin of the splitting between these states is the presence of the H atoms (see Figure 2.4). The corresponding scheme is depicted in Figure 6.6.

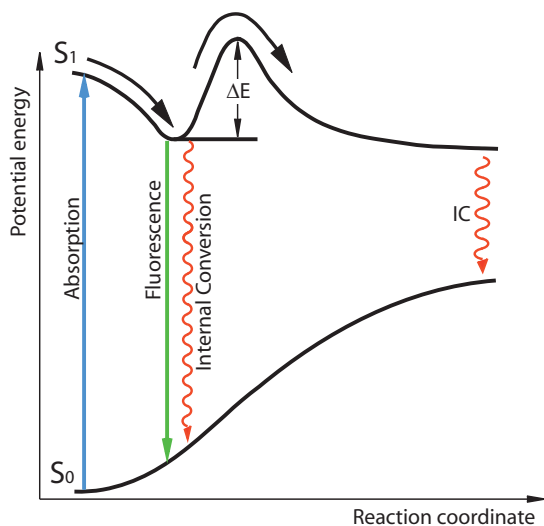


Figure 6.5: Schematic potential-energy surface diagram showing a proposed funnel geometry at which the excited-state nonradiative deactivation is enhanced compared to internal conversion at the equilibrium configuration at which fluorescence is predominantly observed. A small energy barrier must be surmounted to reach the funnel point(s). From Figure 5 of ref. ¹.

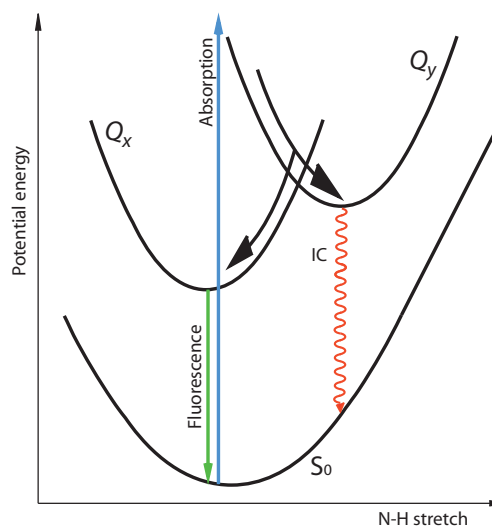


Figure 6.6: Schematic potential-energy surface diagram showing a proposed geometry of the excited singlet state Q_x and Q_y , potential surface projected on the N-H coordinate.

6.1.6 Summary

The Soret excitation leads to a very similar relaxation scheme for H₂TPP and H₂OEP. The only difference lie in the decay of the Soret emission, shortened by a factor of ~ 3 in H₂OEP (< 30 fs against 80 fs). This can be explained by an enhanced vibronic coupling induced by the OE substituent, also suggested by the broader Soret band (Figure 2.7). Nevertheless, for H₂TPP, the absence of 80 fs rise in the population of the lower states speaks for a pulse-limited $S_2 \rightarrow S_1$ IC. This observation indicates that the Soret excited H₂TPP experiences a branching mechanism, with two different de-excitation channels. This behavior suggests that two closely lying states constitute the Soret band, probably B_x and B_y , as proposed by Yu et al for ZnTPP.²²⁶

The subsequent relaxation is characterized by a branching, with instantaneous population of the lowest Q_y and Q_x states. These states are likely being separated by an energy barrier, which prevents the $Q_y \rightarrow Q_x$ IC to occur. While the Q_x deactivates through radiative and ISC to Triplet states on the ns timescale, Q_y deactivates by IC to the ground state. The latter transition is favored by either the N-H vibration or the non-planar distortion of the porphyrin. To clarify this issue, investigation of the effects of deuteration on the

fluorescence from Q_y is required. The Q_x emission is only affected by cooling process on the time window here investigated (200 ps).

This relaxation scheme is different from that proposed by Baskin *et al.*,³³² which is characterized by a cascade relaxation through all the states. In this pathway, after $B \rightarrow Q_y$ IC, a fast $Q_y \rightarrow Q_x$ IC occurs with a subsequent IVR and solvent-induced IVR (100-200 fs and 1.4 ps) followed by cooling (10-20 ps). However, this interpretation is based on the analysis of only few kinetic traces, and in particular one at 635 nm, which contains a non negligible contribution of the 100 fs and 1 ps components. Our data provide evidence that these decays are related to the depopulation of the Q_y state, which undergoes IC to the ground state via either non-planar distortion or through the N-H vibrations.

Finally, we report the detailed description of the full photocycle of the free base TPP and OEP. The relaxation pathway is found to be polarization dependent. Within the manifold of excited states (B_y , B_x , Q_y and Q_x), no change of polarization occurs during the relaxation. While Q_x is long-lived, Q_x relaxes directly to the ground state. Therefore, the protonation of the pyrrole nitrogen plays a crucial role in the global electronic relaxation of the free base porphyrins. The vibrational relaxation is also complex, with an instantaneous population of the ground vibrational level of each Q state, in parallel with population of a hot level in the Q_x state. The IVR mechanism heats the porphyrin macrocycle, which undergoes a thermal expansion. The macrocycle recovers its initial size during the cooling process. The heat transfer to the solvent is controlled by the peripheral substituents.

The next step of this study consists in exploring the influence of the substitution of the two central H atoms by a metal atom on the relaxation pathway.

6.2 Zn TPP and OEP

6.2.1 Ultrafast dynamics of Zn porphyrins

As for the free base corresponding porphyrins, an extensive study has already been carried out on the electronic relaxation of the ZnTPP and ZnOEP compounds through fluorescence up-conversion or transient absorption techniques,^{223-226,341} but no spectrally resolved femtosecond fluorescence has been reported. Yu *et al.*²²⁶ have investigated the electronic relaxation through an extended study in different solvent and for different excitation wavelengths. The general picture coming out from these measurements is the following: under 400 nm excitation, the S_2 state relaxes to S_1 in 1 to 2 ps, followed by vibrational relaxation (IVR and vibrational cooling) on a timescale of tens of ps. Several other experiments showed a polarization independent 60-90 fs rise of the Soret emission, assigned to spectral relaxation due to solvation and vibrational relaxation processes in the S_2 state.^{223,225} For Soret band excitation, the initial rise time of Q band emission deviates from the mono-exponential decay of the Soret emission, suggesting complex dynamics. In the Soret region, the presence of two independent and at most weakly coupled states designated as S_2 and S_2' , which undergo different relaxation dynamics, was proposed to explain this behavior.²²⁶ In addition, one of the first fluorescence up-conversion measurement on ZnTPP, carried out by Gurzadyan *et al.*,²²³ identified a degenerate excited electronic state in the Soret band region, through a 0.7 initial anisotropy value decaying to 0.1 with a 0.2 ps time constant. More recently, Schalk *et al.*³³⁹ have studied the electronic dark states in the vicinity of the Soret band of a very similar Zn porphyrin (Zn Tetratolylporphyrin), and concluded that above the S_2 state at 2.97 eV, at least 3 other states lie at 3.11 eV (1E_g), 3.25 eV ($^1A_{2g}$) and $\gg 3.3$ eV ($^1B_{2g}$). With femtosecond coherence spectroscopy (pump-probe) experiment on ZnTPP and ZnOEP, Yoon *et al.*²²⁵ obtained information on the excited potential energy surface (curvature and displacement), as well as excited state dynamics and subsequent structural changes.²²⁵ They observed that in ZnOEP, where the potential energy surface of the S_1 state is different from that of ZnTPP (contrary to ZnTPP, ZnOEP has only a small displacement of the equilibrium position but has a wider curvature), the $S_2 \rightarrow S_1$ internal conversion is much faster (estimated to be < 20 fs from the lack of S_2 emission). Tripathy *et al.* investigated the origin of the unusual S_2 - S_1 IC rate in an extensive study of Mg, Zn and Cd porphyrins.^{335,341} All compounds show an S_2 - S_1 IC with unit efficiency, except for the Cd porphyrin where ISC, enhanced by spin-orbit

coupling, competes with the IC. They concluded that no general explanation could be applied to all the compounds studied, but some trends are observed. First the β -alkyl substitution increases the S_2 - S_1 coupling strength and in this case a conical intersection is likely to occur. Second, the meso-substitution has little effect on the IC rate. Third, the non-planar porphyrins show an increased S_2 - S_1 coupling, however it does not seem to be the only factor governing the non-radiative decay.

6.2.2 Sequential electronic relaxation

Figure 6.7a shows the time-wavelength plot of the fluorescence of ZnTPP in cyclohexane impulsively excited at 400 nm. Figure 6.7c shows a representative selection of spectra at various time delays. Figures 6.7b and 6.7d are the same plots for ZnOEP in DMF. The choice of DMF for the ZnOEP compound was dictated by a solubility issue. This choice was influencing the result to a minor extent since the small Stokes shift indicates a minor contribution from solvation dynamics, and the obtained lifetimes were confirmed by single wavelength detection measurements done in cyclohexane (data not shown). The strong peak at 452 nm (454 nm) corresponds to the 2900 cm^{-1} Raman response of the cyclohexane (DMF) solvent molecule. In the 420-510 nm region, a large band appears in 100 fs and vanishes in 10 ps (150 fs for H₂OEP). This band is easily ascribable to the Soret emission, as it resembles the mirror image of the Soret absorption, also shown in panels g and h of Figure 6.7, if one takes into account the strong re-absorption which decreases the blue-most intensity, i.e. the 0-0 transition. Above 510 nm, where emission from the Q bands is expected, the ZnTPP has a broad spectrum with 2 maxima at 560 and 645 nm, showing up in 500 fs. Thereafter, the 560 nm band decreases while those at 645 nm and 600 nm increase and then decay on the nanosecond timescale. The latter two red-most bands are emissions from the $Q(0,0)$ and $Q(0,1)$ transitions, quenched by intersystem crossing to the lowest triplet state T_1 in $\sim 2\text{ ns}$.^{362,363} From the stationary absorption spectrum, we can assign the transient band at 560 nm to the “hot” $Q(1,0)$ transition.

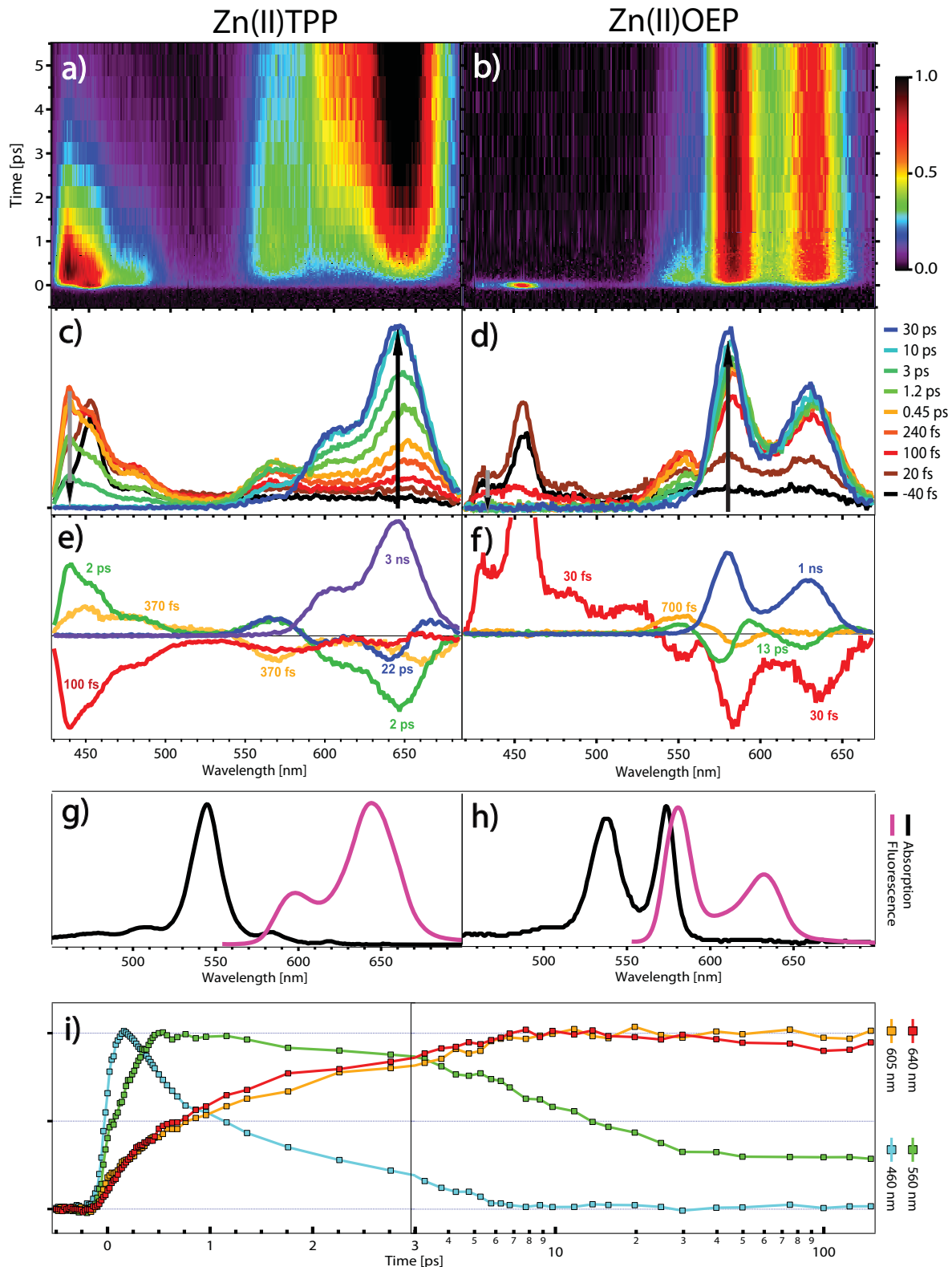


Figure 6.7: a) (b) Time-wavelength fluorescence intensity plot of Zn(II)TPP (Zn(II)OEP) in cyclohexane (DMF) excited at 400 nm. The strong peak at 453 nm is the Raman response of the solvent ($\sim 2900\text{ cm}^{-1}$). c) (d) Fluorescence spectra of Zn(II)TPP (Zn(II)OEP) selected at various delay time after excitation from panel a) (b). e) (f) Decay associated spectra of Zn(II)TPP (Zn(II)OEP), obtained after Singular Value Decomposition and global fitting analysis of data from panel a) (b). i) Normalized kinetic trace of fluorescence of H₂TPP in cyclohexane.

Figure 6.7e and 6.7f show the Decay Associated Spectra (DAS) obtained from SVD and global fit analysis of data shown on Figure 6.7a and 6.7b. We consider first the ZnTPP molecule in cyclohexane (Figure 6.7e).

100 fs DAS: The fastest spectral component obtained from the analysis (red line) has the shape of the Soret emission band, but with negative values. We can thus associate it to a 100 fs exponential rise time τ_{Soret}^r of the Soret fluorescence. It also contains a weak negative contribution at wavelengths longer than 510 nm. The latter contribution is only a residual artifact from the SVD decomposition. Indeed the amplitude is weak compared to other DAS, when taking into account the fact that the related timescale is close to the irf. Moreover, imposing the pre-exponential factor of this lifetime to be zero in a global fit analysis leads to satisfactory fits.

370 fs DAS: The second DAS (orange line) has a broad shape and a maximum at 440 nm in the Soret region, and thus clearly corresponds to emission from the S_2 state. In the Q band region, it appears as two negative bands at 555 nm and 660 nm. We can thus attribute it to the rise time of the two bands present at 500 fs and will be referred as the IC time constant τ_1^{IC} .

2 ps DAS: This spectral component (green line) has also the shape of the Soret emission in the 420 to 500 nm region, with a maximum at 430 nm. Therefore it also corresponds to S_2 emission that decays with a slower timescale. In the Q band region, it shows a positive band at 570 nm and two negative bands at 610 nm and 650 nm with the same shape as the long time spectrum (see Figure 6.7c). The concomitant Soret decay and $Q(0,0)$ and $Q(0,1)$ emission rise, suggest that this time corresponds to another IC time constant τ_2^{IC} . The decay of the “hot” $Q(1,0)$ emission occurs with the same time constant, meaning that this DAS contains also contribution from vibrational relaxation (VR), with τ_{VR} being similar to τ_2^{IC} .

22 ps DAS: As discussed in the case of the free base porphyrins, this DAS (blue line) corresponds to the narrowing and shift of the $Q(0,0)$ band, which reflects cooling dynamics ($\tau_{cooling}$). The lifetime obtained here is in agreement with the literature²²⁶ and the one found in H₂TPP (26 ps).

3 ns DAS: This contribution corresponds to the long time emission spectrum of the $Q(0,0)$ and $Q(0,1)$ transition, decaying with a lifetime $\tau_{Q_{0-0}} \approx 2$ ns.³³⁵

In the ZnOEP molecule, the dynamics are faster, as shown in the transient spectra of Figure 6.7d. The Soret emission decay and the Q band emission rise occur within the excitation pulse. While the “hot” Q band at 550 nm is still present, it rises and decays faster than in ZnTPP. The analysis of the SVD confirms these behaviors and gives the following timescales:

< 30 fs DAS: The fastest spectral component obtained (red line) has a positive broad shape in the Soret region at wavelengths shorter than 540 nm. The blue-most part of the spectrum is filtered out by the cut-off filter at 420 nm. We associate it to the tail of the Soret band emission. At wavelengths longer than 540 nm, this DAS shows a negative contribution with three bands, mirror image of the spectrum at $t = 100$ fs (red trace in Figure 6.7d), with respect to the zero axis. Accordingly, this negative contribution is assigned to the rise of emission from the Q bands. The lifetime $\tau_1^{IC} < 30$ fs corresponds to the $S_2 \rightarrow S_1$ IC rate.

700 fs DAS: This DAS (orange line) describes a positive contribution at 550 nm and a smaller negative contribution at 590 nm. The former band corresponds to the hot emission band, by analogy with the free base parent compound. While this hot level depopulates, the $Q(0,0)$ increases on the same timescale (negative contribution). Accordingly, the related lifetime corresponds to vibrational relaxation and is referred to as τ_{IVR} in the following.

13 ps DAS: Still by analogy with the free base porphyrins and ZnTPP, this DAS is associated to the cooling process. The obtained lifetime $\tau_{cooling}$ of 13 ps is similar to that of H₂OEP (17 ps).

1 ns DAS: This contribution corresponds to the long time emission spectrum of the $Q(0,0)$ and $Q(0,1)$ transition, decaying with a ns lifetime $\tau_{Q_{0-0}}$.³³⁵

Table 6.1: Time constants obtained from the SVD analysis of data shown in Figure 6.7a and 6.7b.

Porphyrin	τ_{Soret}^r	τ_1^{IC}	τ_2^{IC}	τ_{IVR}	$\tau_{cooling}$	$\tau_{Q_{0-0}}$
TPP	100 ± 20 fs	370 ± 50 fs	2 ± 0.2 ps	2 ± 0.2 ps	22 ± 3 ps	3 ns (fixed)
OEP	-	< 30 fs	-	700 ± 50 fs	13 ± 2 ps	1 ns (fixed)

6.2.3 Summary

Contrary to the parent free base porphyrins, in Zn porphyrins each decay in the high energy range is associated to a rise in the lower energy transitions (Figure 6.7i). Moreover, the photoluminescence excitation spectra of Q band emission is very similar to the static absorption spectrum (not shown). Tripathy *et al.* have reported that these Zn porphyrins have an S_2 - S_1 IC efficiency between 0.9 and 1.0.³³⁵ The present data confirms a sequential electronic and vibrational relaxation through all the excited states of the porphyrin. The substitution of the H atom by a metal dramatically affects the efficiency of the S_1 - S_0 IC.

The difference induced by the peripheral group (TP and OE) lies in the dynamics of the S_2 state. In ZnTPP, the population of the latter rises in 100 fs and then undergoes a biphasic (370 fs and 2 ps) IC to S_1 . Since the polarization detection was set at the magic angle, we exclude that the rise stems from IC between two orthogonal dipole transitions. The fluorescence anisotropy measurements of Gurzadyan *et al.* have already shown that this was not the case.²²³ The biphasic IC speaks for a branching mechanism in the S_2 state, implying at least two different states with different IC rates to S_1 . However, on the contrary to the free base porphyrins, these states are likely two vibrational levels of the S_2 state. The 400 nm excitation of ZnTPP corresponds to excitation in the vibronic replica of the Soret band (Figure 2.8a). While the 100 fs rise in the Soret emission is due to vibrational relaxation to the “hot” level of S_2 , the ground vibrational level of the latter is only populated in 2 ps, in the course of a second-step vibrational relaxation. The same type of relaxation occurs in the Q band, since the same lifetime is obtained for the transfer of population from the hot to the ground vibrational level of the S_1 state. The $S_2 \rightarrow S_1$ IC occurs from both ground and first vibrational levels of S_2 , with a lifetime of 370 fs, i.e. faster than the vibrational relaxation. Consequently, the bimodal decay of the Soret emission reflects the IC rate (370 fs)⁻¹ (from the hot level) and a rate limited IC from the ground level. The IVR relaxation in the high vibrational levels of S_1 is < 370 fs and is thus also rate limited. This photocycle, resumed in the scheme of Figure 6.8, agrees with the results of Yu *et al.*,²²⁶ which observed an increase in the amplitude of the fast decay (240 fs) of Soret emission under two photon absorption at 550 nm, i.e. with higher excess vibrational energy. Finally, we answer the long-standing question of the origin of the unusually long Soret emission lifetime:^{334-336,341} the peculiarity of ZnTPP lies in its specific vibrational relaxation mechanism, in particular in the S_2 state, limiting the IC efficiency.

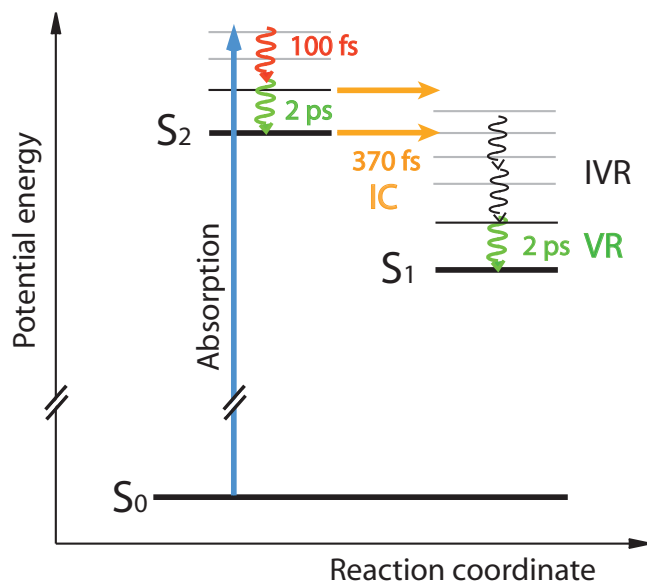


Figure 6.8: Schematic energy diagram of the electronic and vibrational relaxation of ZnTPP.

Conversely, in ZnOEP this IC occurs in < 30 fs, supporting a strong influence of the substituent on the S_2 - S_1 coupling. As mentioned above, Tripathy *et al.* suggested that β -alkyl substitution affects the macrocycle stretching frequencies, probably leading to a conical intersection.³³⁵

After IC and the main part of the IVR mechanism, hot vibrational levels of S_1 are populated (the three bands between 20 and 100 fs in Figures 6.7e and 6.7d), corresponding to the Hertzberg-Teller (HT) progression (see §2.3). The last step of VR occurs in 700 fs and 2 ps for ZnOEP and ZnTPP, respectively, corresponding to a transfer of population from the HT high frequency vibrations to the low frequency modes (decreasing of the $Q(1,0)$ band, increasing and broadening the $Q(0,0)$ and $Q(0,1)$ bands). The hot porphyrin cools down by dissipating the excess vibrational energy to the solvent in 13 ps and 22 ps for ZnOEP and ZnTPP, respectively. The difference in cooling times indicates an important role of the substituent on this process. The presence of phenyl groups probably reduces significantly the number of cyclohexane molecules in direct contact with the porphyrin ring, decreasing the heat transfer efficiency. As in the case of the free base, a thermal expansion effect is observed with similar amplitude.

In order to better describe the dynamics in haemoproteins, we studied the role of the electronic structure of the central metal atom of the porphyrins on the electronic relaxation dynamics.

6.3 Transition metal TPP and OEP

6.3.1 Ultrafast emission

Figure 6.9 reports the transient fluorescence spectra in the visible of Ru- (with CO as ligand), Cu-, Ni- and Co-TPP and OEP in cyclohexane, excited at 400 nm. The full time-wavelength plots, reported in Figure E.1, show that no significant emission is observed in the Soret region. The fluorescence spectra appear within the instrumental response for all compounds, and decreases to less than 10% in 300 fs. The spectra are broad and featureless in the case of TPP complexes, whereas they have a clear vibronic structure, mirror-image of the absorption, for the OEP complexes, except for Co-OEP which resembles the TPP. In all compounds, the large $\sim 7000\text{ cm}^{-1}$ Stokes shift occurs in < 50 fs. However, a pulse-limited emission is observed at wavelengths shorter than 500 nm. In the region of the *Q* band (500-700 nm), the fluorescence decay is wavelength independent, as shown by the normalized kinetic traces in Figure E.2. The fluorescence decay of OEPs, excluding Co-OEP, is slower than that of TPPs. The kinetic traces at 550 nm are shown in Figure 6.10 for all the compounds, along with their exponential fit. The obtained time constants are reported in table 6.2. In the case of M-TPP, a longer component of a few percent ($< 10\%$), fixed at 1 ps, is found, which is absent in OEP.

Table 6.2: Time constants obtained from exponential fits of kinetic traces of fluorescence from Ru, Cu, Ni and Co TPP and OEP in cyclohexane (Figure 6.10), according to function A.10.

<i>Transition metal</i>	<i>OEP</i> [± 20 fs]	<i>TPP</i> [± 20 fs]
Ru ²⁺	120	47 (0.93)
Cu ²⁺	80	50 (0.97)
Ni ²⁺	90	60 (0.94)
Co ²⁺	67	61 (0.97)

As a first observation, all transition metal porphyrins exhibit a strongly quenched fluorescence, as expected from the extremely weak steady state fluorescence ($QY < 10^{-4}$) of these compounds.³⁶⁴ The similarity between the absorption spectrum of all metal porphyrin including Zn (Figure 2.8 and ref. ³⁶⁵) suggests that the relaxation mechanism quenching the fluorescence involves the open-shell orbital structure of the metal, rather than a change in the electronic or conformational structure of the porphyrin macrocycle.

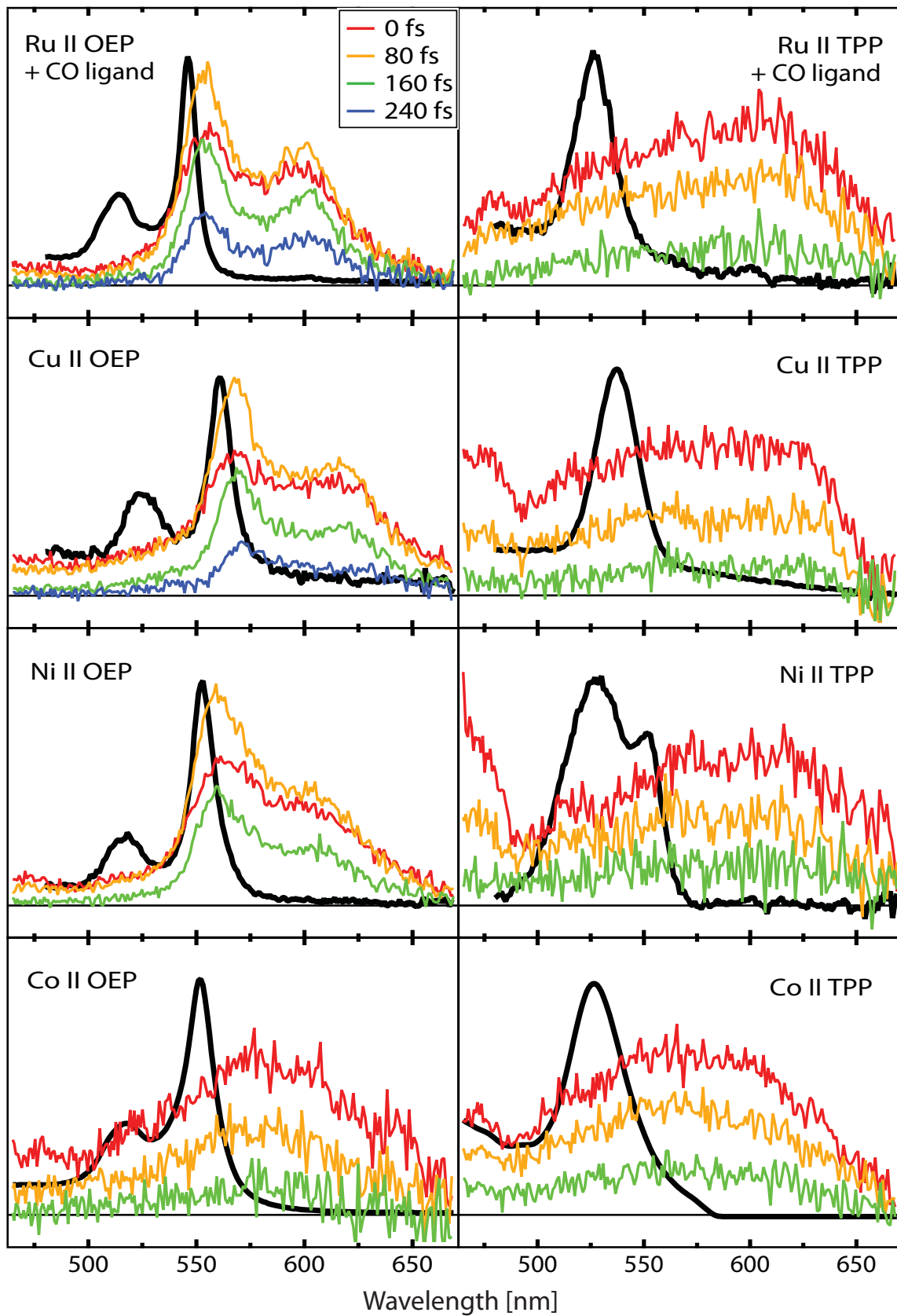


Figure 6.9: Representative selection of fluorescence spectra at different time delays from Ru, Cu, Ni and Co OEP (right panels) and TPP (left panels) in cyclohexane upon 400 nm excitation. The static absorption spectrum is shown in black.

The long-lived fluorescence from the Q band of Zinc porphyrin reported in the previous section excludes any metal to ring charge transfer process. This mechanism was also excluded in the photoelectron study of Sorgues *et al.*, which argues that ionization of metalloporphyrins involves electrons from the ring.^{252,366} Moreover, the results of Holten *et al.*^{343,356} as well as various works on Ni-TPP,³⁶⁷⁻³⁷⁰ indicate a transient (d, d^*) state on the picosecond timescale. All these considerations point to a relaxation leading to population of a metal d-state as the only possible quenching mechanism of the Q band fluorescence. This is confirmed by X-ray transient absorption and photoelectron spectroscopy.^{368,371,372} A transfer of the excitation energy from the ring to the metal is improbable, since it corresponds to a double change in the electron configuration and since d-d transitions are orbitally forbidden.²⁵² The only remaining possible mechanism is an electron transfer from the porphyrin ring to an empty d orbital of the metal center. This explanation is well accepted and it is furthermore believed to be at the origin of the ligand photolysis, which is attached to the metal center.^{234,250,251,373}

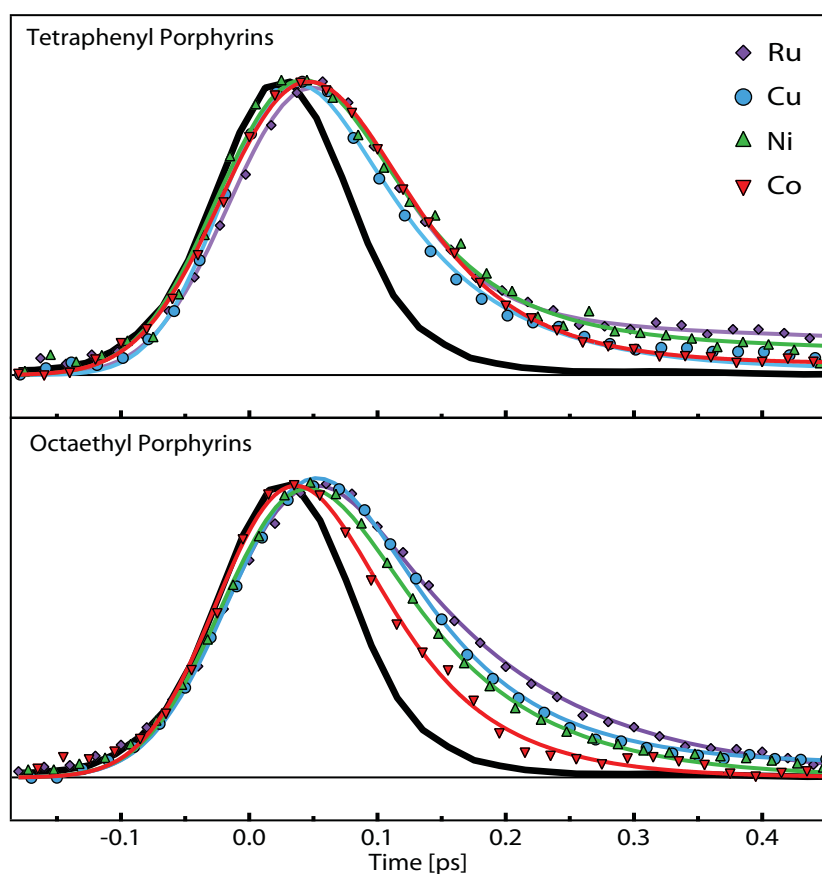


Figure 6.10: Kinetic traces at 550 nm ($\sim 18000 \text{ cm}^{-1}$) of fluorescence from Ru, Cu, Ni, and Co tetraphenylporphyrin (top) and octaethylporphyrin (bottom) (symbols), along with their fit (lines). The kinetic trace of the Raman signal from cyclohexane corresponds to the irf (thick black line).

6.3.2 Parameters affecting the relaxation processes

Effect of the peripheral substituent

The substituent does not affect strongly the observed kinetic behavior occurring on the 50-150 fs timescale for all complexes. However, the OEPs show globally slower decay of the Q band emission, with a minor effect of the central atom on the overall IC process. In a similar way than for the free base porphyrins with the N-H vibrations, the N-M bond might be the major coordinate involved in the IC between porphyrin and metal centered states. The S_2 - S_1 IC in the Zn porphyrins is slowed by the displacement of S_1 potential surface compared to S_2 for ZnTPP (Yoon *et al.*).²²⁵ If the same coordinate is responsible for the $S_1 \rightarrow d$ IC, the displacement might in this case favor the latter transition, i.e. the porphyrin to metal charge transfer. This relaxation scheme is illustrated in Figure 6.11. The effect of the central metal would be a minor vertical shift or a narrowing of the potential energy surface (PES) of the d and S_1 states. In the case of OEPs, this shift would modulate the barrier height. In the case of TPPs, where the d state crosses the S_1 PES in the minimum, no effect is expected.

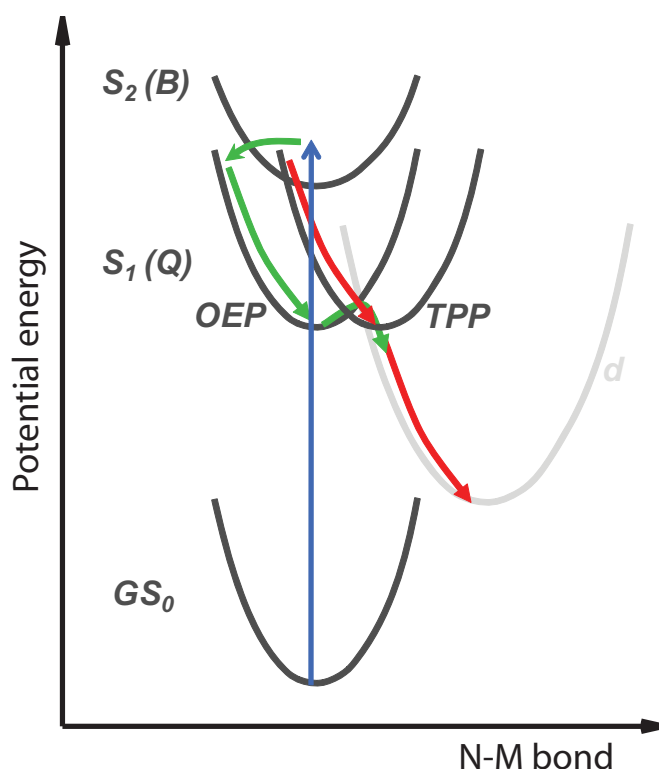


Figure 6.11: Potential energy diagram of ZnOEP and ZnTPP, with the proposed relaxation pathways. The difference between OEP and TPP lies in the displacement of the S_1 potential surface with respect with other states.

Effect of transition metal electronic structure

The decay of the S_1 state of the OEPs is sensitive to the transition metal, whereas no trend is observed in the TPPs (Table 6.2). Liao and Scheiner have reported an extensive DFT investigation of the electronic structure of few transition metal TPPs.³⁷⁴ Unfortunately, such a study is not available for OEPs, apart from Fe-OEP.³⁷⁵ Comparing Fe-TPP and Fe-OEP, the effect of substituent seems to be only a global shift to higher energy of all orbitals. Such a comparison is however difficult since a small change in the energies of the ($a_{2u}e_g$) and ($a_{1u}e_g$) states dramatically changes the photophysics of the porphyrin (see chapter 2). Nevertheless, the consideration of the d -orbital energies of each transition metal does not lead to a clear explanation of the CT rate decrease with the trend $Co > Cu > Ni > Ru$ for the OEPs.

Effect of axial ligation

In the case of Ru-OEP and Ru-TPP compounds a carbon monoxide (CO) axial ligand is attached to the central Ru atom. Compared to other transition metal porphyrins, the kinetic behavior is similar. While the investigation of only one ligated compound is not enough to conclude about the influence of ligation, this result suggests that the electronic relaxation is not strongly affected by the presence of the axial ligand, although the latter is known to dissociate upon photoexcitation.²⁵² This observation was also suggested by Shafizadeh *et al.* which have studied a larger series of ligated and unligated metalloporphyrins.²⁵⁰

6.4 Conclusion

The transient femtosecond-resolved fluorescence of the different porphyrins compounds investigated here reveals some trends, which are helpful to understand the various electronic and vibrational dynamics occurring in haemoproteins.

The unusual relaxation mechanism of free base porphyrins evidenced here suggests that the presence of the H atoms constitute a crucial factor of interstate coupling, affected by the peripheral substituent, and to a minor role of the macrocycle non-planar distortion. The influence of the substituent is better revealed in the Zn porphyrins. Indeed, while the vibrational relaxation in all excited singlet states (S_2 and S_1) limits the overall electronic relaxation in ZnTPP, the higher density of vibrational levels of ZnOEP (broader Soret band in Figure 2.8a) leads to a more efficient vibrational and electronic relaxation.

The central open-shell metal atom remarkably changes the relaxation dynamics of the porphyrins, by opening new efficient non-radiative channel, which are the partially filled d -orbitals of the transition metals. The influence of the peripheral substituent on the $S_1 \rightarrow d$ IC rate is weak, but can be interpreted in a similar way as for the other porphyrins. The reaction coordinate of this $S_1 \rightarrow d$ charge transfer is likely the nitrogen-metal bond, which is affected by the tetraphenyl substituent, if we consider the a_{2u} orbital (Figure 2.4). In addition, the electronic structure of the transition metal, i.e. the energy of the accepting d -orbitals, does not influence significantly the IC rate.

The relaxation dynamics of porphyrins is intrinsically related to its basic photophysics, described by the Gouterman theory. Indeed, weak electronic perturbation of the ring leads to important changes in the absorption and emission spectra. As we have seen, such perturbation also governs the interstate couplings and thus the relaxation pathways.

Chapter 7

Protein dynamics

7.1 Cytochrome c

- 7.1.1 Introduction*
- 7.1.2 Time-resolved fluorescence*
- 7.1.3 Transient Absorption*
- 7.1.4 Discussion*
- 7.1.5 Conclusion*

7.2 Myoglobin

- 7.2.1 Dual UV fluorescence*
- 7.2.2 Local Trp7 dynamics*
- 7.2.3 Haem electronic relaxation*
- 7.2.4 Summary*

7.1 Cytochrome c

7.1.1 Introduction

The mechanism of ligand release and rebinding has been extensively studied in haemoglobin and myoglobin by ultrafast pump-probe spectroscopy in which an impulsive photoexcitation leads to dissociation of the ligand, and evolution of the system is followed using a time delayed second pulse.²²⁷⁻²³⁵ However, the details of the electronic structure changes that are responsible for the photodissociation are still not elucidated. In particular, from which electronic excited state does the bond breaking occur and how fast does the system reaches this state are still unanswered questions. To address these issues, here we focus on the photo-induced dynamics of horse heart Cytochrome c (hh Cyt c, Cyt c in the following). The general photophysics of Cyt c is presented in chapter 2. While the Met80 photodissociates in its ferrous form, only cooling dynamics occurs in the ferric form, with no signature of ligand photolysis. Here we present our study on the whole photocycle of ferric and ferrous form, until the recovery of the electronic ground state. We measured the time-gated fluorescence from hh Cyt c in both oxidation states. In addition, in the framework of collaboration with Cristina Consani, we measured ultrafast broadband transient absorption (a brief description of the set-up is reported in appendix F, p.202). *Q* band, Soret band and 290 nm excitations were achieved in both experiments in order to explore the relaxation pathways of higher energy haem states, but also of aromatic amino acids such as Tryptophan. Moreover, these different excitations would induce an increase of the haem temperature by 300 K, 400 K and 550 K, respectively, allowing us to study the role of excess vibrational energy on the observed dynamics.³¹²

As in the previous chapter, the data are analyzed in term of SVD and global fit (Appendix A), providing us the decay associated spectra which are then discussed.

7.1.2 Time-resolved fluorescence

a) Results

Figures 7.1a and 7.1b present spectra at different delays, selected from the time-wavelength plot of the emission of ferrous and ferric Cyt c under 286 nm excitation, shown in Figures F.1a and F.1b. In both forms, the emission is broad and spans the 300-500 nm region. It decays on a sub-ps timescale, with a faster decay component in the 400-500 nm region which is pulse-limited, as it disappears at the same time as the water Raman peak at

317 nm. Moreover, no rise of the emission can be observed over the whole spectral range. This result reveals that two different spectral contributions are present from $t = 0$ but decay with different time constants. The slower decay observed in the blue region is faster in the ferrous compared to the ferric form.

Figure 7.1c and 7.1d present spectra at different delays, selected from the time-wavelength plot of the emission of ferrous and ferric Cyt c upon 400 nm excitation (Figures F.1c and F.1d). The two oxidation states show drastically different emission decays and spectral shapes. In the case of ferrous Cyt c, the emission spectra show a clear vibronic progression at all times, corresponding to the mirror image of the static absorption. The spectrum narrows in 10s of fs, as can be seen by comparing the time zero (red line) and the 60 fs (orange line) spectra. The whole spectrum vanishes within 500 fs. In contrast, the emission spectrum of ferric Cyt c is broad, unstructured and disappears in less than 200 fs. Under 520-530 nm excitation, the same behaviour are observed (inset of Figure F.1c and F.1d). However, in the case of ferrous Cyt c, the vibronic band (600 nm) at time zero is narrower compared to 400 nm excitation (Figure F.2).

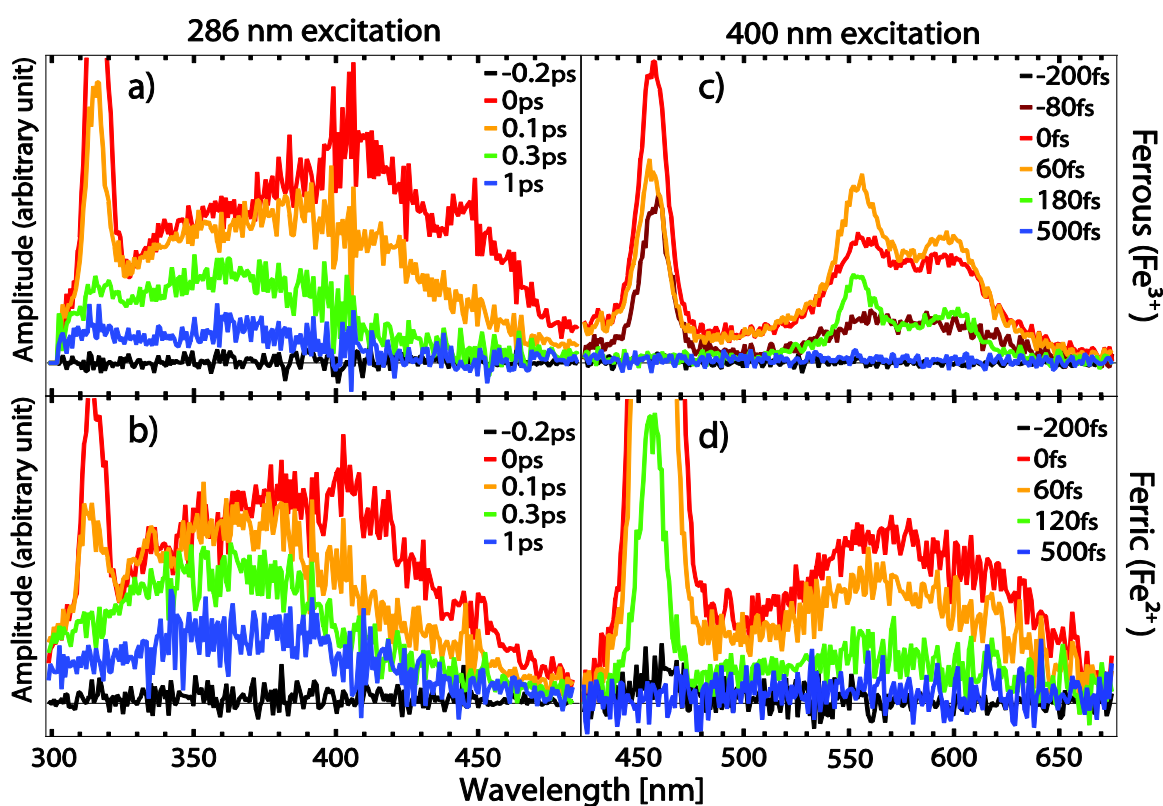


Figure 7.1: Representative Selection of emission spectra at different time delays from ferrous and ferric Cyt c (top and bottom panels, respectively) upon 286 nm and 400 nm excitation (left and right panels, respectively). The strong peak at 317 nm and 463 nm for the UV and visible excitation correspond to the instantaneous Raman signal from water.

b) Spectral and temporal decomposition

Figure 7.2 shows the resulting DAS of ferrous and ferric Cyt c for both UV and Vis excitation. Upon UV (286 nm) excitation, a broad (300-450 nm) spectrum is centered around 370 nm, associated to a 350 fs and 700 fs decay time for ferrous and ferric Cyt c, respectively (blue traces), overlapping with a narrower band around 370-470 nm associated to a < 40 fs decay (red trace). Under 400 nm excitation, as already observed, the two oxidation forms behave clearly differently. The ferric form shows only one broad positive spectral contribution associated with < 40 fs decay (red trace). The ferrous form exhibits two structured DAS. The slowest clearly corresponds to the mirror image of the absorption (in black) and is associated with a 105 fs decay time (green trace). The fast contribution (red trace) is associated with a < 40 fs time constant and looks like a positive, broad and unstructured band with two minima at positions corresponding to the peaks of the slow decay component (green trace). This indicates that this DAS represents two distinct contributions: a broad emission, which is instantaneously populated, and a negative contribution describing the rise of the slower component.

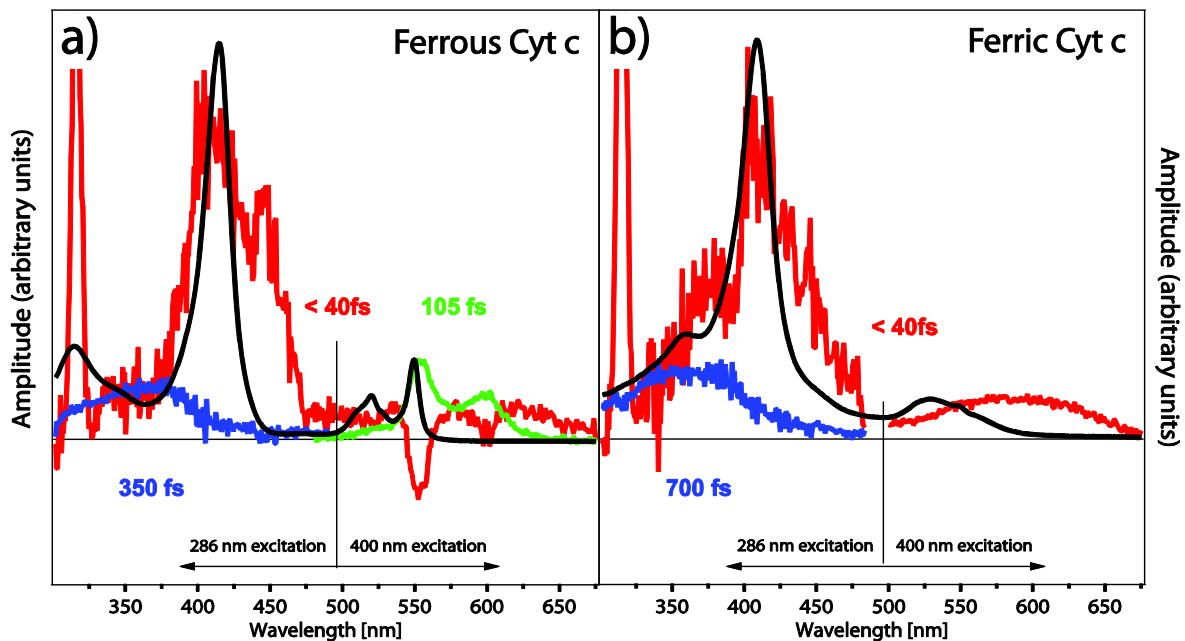


Figure 7.2: Decay Associated Spectra resulting from the SVD analysis of time-resolved fluorescence of ferrous (a) and ferric (b) Cyt c of data of Figure F.1, along with the corresponding stationary absorption (black line).

7.1.3 Transient Absorption

The top panel of Figure 7.3 (F.3) shows a representative selection of TA spectra from ferric (ferrous) Cyt c under UV excitation. We observe a complicated behaviour where positive signals, due to excited state absorption (ESA), are mixed with ground state recovery and cooling dynamics. To disentangle these different contributions we analyzed the SVD of the experimental data according to the procedure previously discussed, in order to obtain the different DAS components. The outcome of this analysis is presented in the bottom panel of Figure 7.3, where five components, with relative time constant spanning from 100's of fs to 10s of ps, are found.

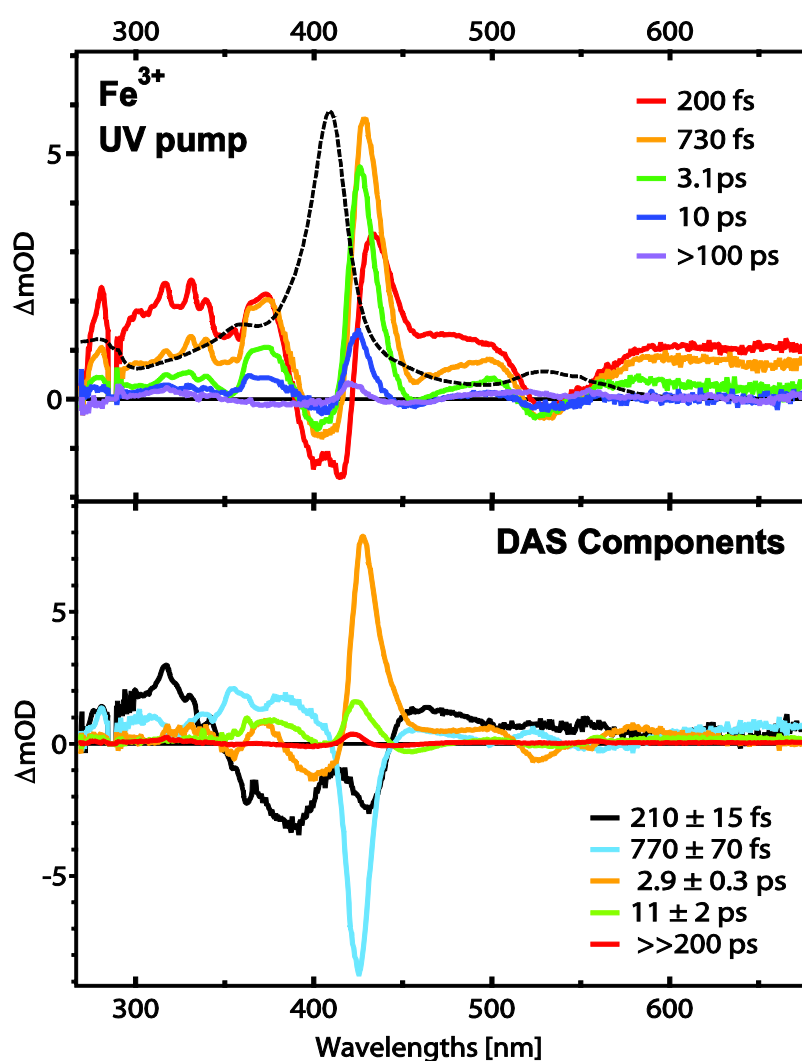


Figure 7.3: (top) A representative selection of transient absorption spectra at different delay times from ferric Cyt C under UV (288 nm) pump. The dashed line represents the ground state absorption spectrum in arbitrary units. (bottom) DAS from analysis of femtosecond TA measurements of ferric Cyt c excited at 288 nm (top panel).

For the purpose of the work, which focuses on the electronic relaxation mechanisms of Cyt c, only the sub-ps components are considered. The long, cooling-related dynamics are discussed in details in an article.³⁷⁶ For each redox form and under both UV and visible excitation, we observe a 150-220 fs component with a similar spectrum over all the investigated spectral range. Based on this strong invariance and on an overall absorption character (except where the Soret band dominates) we assign it to ESA on the porphyrin macrocycle. It will be referred as the excited state (ES) decay time τ_{ES} in the following. In the case of ferrous Cyt c upon visible excitation, this component contains contribution from a rise of the subsequent photoproduct signal. Under UV excitation, an additional component of 350 fs and 770 fs have been detected in the ferrous and ferric forms, respectively. From arguments exposed in the discussion, this time constant will be attributed to the decay of the Trp excited state (τ_{Trp}). Table 7.1 summarizes the time constants obtained from analysis of the transient absorption and fluorescence data.

Table 7.1: Time constants obtained from exponential fits of the SVD of transient absorption and fluorescence from ferrous and ferric Cyt c under 286 (288 for TA), 400 and 530 nm excitation.

<i>Oxidation form,</i> <i>Excitation [nm]</i>		<i>Transient Absorption</i>		<i>Fluorescence up-conversion</i>		
		τ_{ES} [fs]	τ_{Trp} [fs]	τ_{Trp} [fs]	τ_{Soret} [fs]	τ_Q [fs]
Ferrous	286	155 ± 12	350 (fixed)	350 ± 20	< 40	120 ± 40 [70%] 340 ± 140 [30%]
	400			-	< 40	145 ± 3
	530	160 ± 15	-	-	-	105 ± 2
Ferric	286	210 ± 15	770 ± 70	690 ± 30	< 40	< 40
	400			-	< 40	< 40
	530	220 ± 20	-	-	-	< 40

7.1.4 Discussion

The results reported here constitute experimental evidence for various relaxation dynamics of Trp and haem in Cyt c. We will now discuss in detail the different observed processes for both redox forms.

a) Trp Emission

We assign the slowest component at 370 nm (τ_{Trp} in Table 1) to emission from the Trp, even if a more blue-shifted spectrum could be expected for such a deeply protein-embedded Trp. Indeed, the inner protein environment is hydrophobic, and in such a medium the fluorescence from Trp is known to show a blue shift compared to the bulk steady state fluorescence.¹⁵⁷ However, the spectrum, slightly cut on the blue side due to the excitation cut-off filter, is red-shifted (~ 10 - 20 nm) with respect to that of aqueous Trp, indicating that the Trp residue is located in a relatively polar environment.³⁷⁷ Moreover, this emission does not show any dynamical red shift and therefore is free of any fs or ps solvation mechanism. The lack of environment response on this timescale reveals its rigidity and the fast Trp de-excitation (350 fs and 700 fs) excludes any response on longer timescales. These Trp decay times are unusually short compared to its fluorescence lifetime in bulk water (3 ns and 0.5 ns). However, this result is in full agreement with the observation in UV-TA measurements of a 350 fs and a 770 fs component for the ferrous and ferric forms respectively (lower panels of Figure 7.3 and Figure F.3), unambiguously assigned to Trp excited state absorption (ESA). Moreover in the visible region, where only haem contribution is expected, a rise of the subsequent haem absorption signal is observed on the same timescales, and this, only upon UV excitation.³⁷⁸ This delayed haem population, also observed in the haem emission (see § c) *Delayed haem excitation*), is concomitant with the Trp de-excitation and constitute the unambiguous proof that the 350 fs and 700 fs correspond to a very efficient Trp-haem energy transfer, as expected by fluorescence QY measurements as a function of pH.^{245,249}

The different decay times in the ferrous and ferric forms speak for a less efficient energy transfer in the latter form. As can be seen in Figure 2.9, the dependence of the energy transfer efficiency cannot be ascribed to spectral changes of the haem absorption: if one takes the stationary emission spectrum of aqueous Trp as a reference, the overlap integral in the ferric form is 15% larger than in the ferrous form.²⁴⁵ This confirms the different relative orientation and distance between the Trp residue and the haem cofactor in the two

forms, as found by structure determination (PDB: 1HRC and 1OCD). In addition, Visible circular dichroism spectroscopy has revealed a different orientation of the haem transition dipole moment in the two oxidation states.³⁷⁹ The oxidation state³⁸⁰ and the nature of the protein fold in both oxidation states are known to have a non negligible influence on the tertiary protein structure of the haem pocket region.²⁴⁶ In addition, compressibility measurements of Cyt c have pointed out that the ferric form has a more open tertiary structure than the ferrous one.³⁸¹ These observations agree with the experimental timescales obtained here, because they would reflect a less efficient energy transfer in the ferric case.

b) Haem emission

In the 370 to 500 nm region, the pulse-limited contribution (red curve of Figure 7.2) matches well the *B* absorption (Soret) band, and therefore we assign it to ultrafast emission from the S_2 state, responsible for the Soret band. It has to be noted here that the strong absorption of the Soret band of our sample (> 1 OD) might strongly affect the shape of the emission in the 400 - 430 nm region. This result agrees with the fact that, as seen in the previous chapter, for porphyrin molecules in general the Soret emission has a very small Stokes shift.^{226,332,382} The reason is that a weak vibronic coupling is usually observed and that porphyrins are apolar chromophores. These results are to our knowledge the first time-resolved emissions from the Soret band of a haemoprotein and prove that the haem group of Cyt c contributes to its UV fluorescence, as previously mentioned.²⁴⁹ Our instrumental response (160 fs) was too long to resolve the decay time (τ_{Soret}) of the S_2 state and we can just provide an upper value of 40 fs. The time zero reference of the Raman band of water shows that the rise time of this emission is within our time resolution. From the excitation (at 286 nm) to the Soret band (400 nm), 1.22 eV is instantaneously dissipated. Moreover, as will be pointed out from the *Q* band emission treated in the next paragraph, the haem undergoes internal conversion (IC) to lower electronic excited states within 40 fs. These measurements allow us to calculate the relative emission QY of Trp and haem moieties and to compare our time-resolved measurements with steady state studies. From the area of the Soret and the Trp absorption bands we can indeed estimate a radiative rate for the Soret transition approximately 10 times greater than that of Trp (one can roughly estimate this ratio from the absorption amplitudes of 120'000 and 6000 $\text{cm}^{-1}\text{Mol}^{-1}$ for the Soret and Trp absorption, respectively, taking into account that the Trp band is twice broader than the Soret band). With a total lifetime of 40 fs and 350 fs, respectively,

we derive that the emission quantum yield is the same for both the haem and the Trp moieties. Interestingly Löwenich *et al.*²⁴⁹ observed that upon excitation at 280 nm and at pH 7, the porphyrin system contributes about 80 % and tryptophan about 20 % to the total stationary fluorescence. This is not far from our aforementioned contributions of 72% and 28% of haem and Trp to the total absorption, therefore a similar estimation for the QY is derived.

In the 500 to 700 nm region, the observed emission is basically a mirror image of the *Q* band absorption. We observe a prompt broad emission that disappears in < 30 fs, overlapped with the rise of the structured emission, which then decays with a 105 fs time constant. This indicates that a weak and broad hot emission spectrum is instantaneously present and evolves during the excitation pulse to a more intense, narrow vibronic progression expected from the mirror image symmetry of the absorption spectrum (Figure 7.2a). It agrees with the sub-40 fs S₂ → S₁ internal conversion (from Soret to *Q* band) and IVR (Internal Vibrational Redistribution). The rise of the *Q* band emission is also observed upon UV and Soret excitation as shown in Figure 7.4.

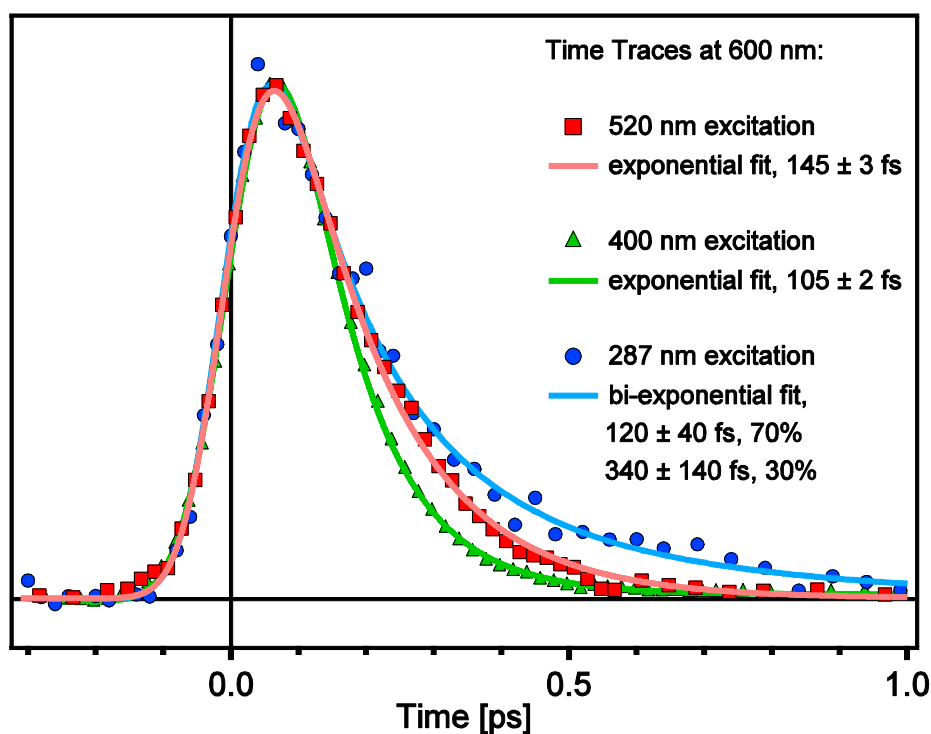


Figure 7.4: Normalized kinetic traces of fluorescence from Cyt c in buffer solution pH7 at 600 nm, under 286 nm (blue curve), 400nm (green curve) and 520 nm (red) excitation.

The emission decays with a time constant changing from ~ 150 to ~ 100 fs depending on whether we excite into the *Q* band or into the Soret band. This observation suggests an acceleration of the S_1 fluorescence quenching by excess vibrational energy. The timescale obtained here is in accordance with the expected S_1 lifetime of ~ 0.2 ps from QY measurements.³⁸³

Contrary to the ferrous state, the ferric form shows only one DAS in the 500 to 700 nm region, with a shape corresponding still to the mirror image of the stationary absorption band (grey trace), but broader and associated to a pulse-limited (< 40 fs) decay time, as is the Soret emission (Figure 7.2b). This lifetime is also expected from QY measurements.³⁸³ As in the ferrous form, the $S_2 \rightarrow S_1$ internal conversion is virtually instantaneous, but the subsequent S_1 state relaxation dramatically changes with oxidation state.

c) Delayed haem excitation

The energy transfer from the Trp to the haem leads to a delayed population of the S_2 state, which then emits. We tracked down the energy transfer contribution from the Trp to the haem by monitoring the S_1 emission decay at 600 nm exciting in the UV (286 nm), within the Soret and *Q* bands (400 nm and 520 nm), as reported in Figure 7.4. Here the decay of the S_1 emission is integrated over the spectral width of the red-most band (600 ± 20 nm, Figure F.1c). Indeed, we see that the kinetics observed under Soret and *Q* band excitations are well described by a single decay, while the UV excited emission shows a biphasic behavior. This additional slower decay of amplitude 30% of the total signal is very close to the 28% contribution of the Trp absorption. The fit parameters are reported in the last column of Table 7.1. An identical effect is observed with the TA analysis where the rise of haem-related signals is observed with the same time constant as the Trp lifetime (Table 7.1 and Figures 7.3 and F.3).³⁷⁸ These observations lead us to conclude that this signal stems from the portion of haem molecules indirectly excited via energy transfer from Trp.

This contribution should also show up in the Soret emission. As the haem emission is < 40 fs while the Trp lifetime is at least 10 times longer, this signal decays with the longest time constant, i.e. it is rate-limited. In other words, it should appear in the DAS of the Trp emission. Indeed, the blue curves in Figure 7.2a and 7.2b show a weak signal in the 400-480 nm region. This signal roughly matches the haem emission spectrum observed (red curve) when the latter is scaled by the excitation and time scale ratio (Figure F.4).

a) Haem electronic relaxation

Under 400 nm excitation, an “instantaneous” population of the S_1 state is observed. In spite of its speed, this is not the main depopulation channel from S_2 , as only $\sim 14\%$ of the excited molecules undergo $S_2 \rightarrow S_1$ IC in ferrous Cyt c.^{383,384} The remaining 86% are believed to relax towards metal-centred (MC) states, triggering the ultrafast bond-cleavage.^{240,252} Concerning the ferric form, branching ratios from higher states are unknown, because the very short excited states lifetimes prevent static measurements. Since the ligand photodissociation QY is almost unitary ($>80\%$)²⁴⁰ whether we excite the Q , B or δ band, the accepting metal-centred state is likely the empty anti-bonding d_{z^2} state, since it is lower than all the aforementioned porphyrin excited states and the lower metal centered d_{xy} state is fully occupied.³⁷⁵ In both oxidation states, the S_1 state (Q band) is instantaneously populated, but it is depopulated in 105 fs and 40 fs in the ferrous and ferric forms, respectively. These values are definitively shorter than the ESA decay times from the TA measurements (150-220 fs), suggesting the presence in the latter of an intermediate state (a low-lying dark state or a hot ground state) involved in the haem-photocycle, that lengthens the recovery of the pristine porphyrin electronic ground state.

As previously discussed, the S_1 state generated upon 400 nm excitation in the ferrous systems is initially very hot and it appears mirror-like to the static absorption band in a few tens of fs. This points to the presence of a very effective IVR in damping the porphyrin high frequency modes, as will be seen in the next chapter on metal-polypyridine complexes.³⁸⁵ More important, it suggests that this emission stems from a 6-fold coordinated ferrous haem ($6cFe^{2+}$), rather than a 5-fold coordinated one ($5cFe^{2+}$). Indeed the latter shows an unstructured broad absorption band, very similar to the 6-fold coordinated ferric haem ($6cFe^{3+}$).^{239,240,378} Thus the observed 100-150 fs decay time describes a CT from the porphyrin to an empty d -orbital of the metal (likely the d_{z^2}), and the subsequent ligand photolysis, under direct excitation of the Q band (Inset of Figure F.1c). It implies that the earliest TA dynamics reflects also a $6cFe^{2+} \rightarrow 5cFe^{2+}$ conversion and not a porphyrin ESA only. This is almost one order of magnitude slower than the photolysis process upon 400 nm excitation²⁴⁰ and than the generally assumed value if comparing with other similar systems.^{227,233,251} Noteworthy, when we consider the ferric form, the S_1 lifetime is pulse-limited regardless of the excitation. This reveals an important

role of the iron oxidation state and in particular of the d -orbital occupancy, involved in the porphyrin-iron ligand.

Moving to UV excitation, Figures 7.2a and 7.2b show that the pulse-limited signal matches well the expected S_2 emission in the overlap region 480-500 nm, confirming that the δ -state relaxes to S_2 . Thanks to the tryptophan emission, which plays the role of an internal reference, we can estimate the QY of S_2 population by calculating the relative emission area at time zero in Figure 7.2a and 7.2b, integrated over the frequency domain. This ratio is equal to the ratio of the initial number of emitters times the ratio of the radiative rates. The latter can easily be calculated as the ratio of the respective static absorption bands. The emission band ratio (S_2/Trp) is ~ 4 , while the Soret radiative rate is ~ 7 times larger than the Trp one. Taking into account that for each excited Trp, 3 haems are excited, we obtain that 20% of the excited haems end up in the S_2 state. Since the amplitude of the Soret band is distorted by a strong reabsorption, this value surely constitutes a lower limit.

Assuming that the relaxation pathway from S_2 does not depend dramatically on the excess vibrational energy deposited in the haem (direct excitation at 400 nm vs indirect excitation from higher states), molecules relaxing to S_2 will behave as the directly excited ones. Remarkably, regardless of the excited state, all the lower electronic levels of the porphyrin are involved, with an instantaneous redistribution (population) among them. This is clear from Figure 7.4, where the rise of the signal at the lower transition is excitation wavelength independent.

To provide a unified description of these observations we propose the photocycle summarized in Figure 7.5: in the ferrous form, upon excitation above the Q band (B or δ band), the system reaches the S_2 state where it experiences a branching with 86 % of molecules undergoing immediate internal conversion to the antibonding d_{z^2} metal center state (channel A), inducing ligand photodissociation. Afterward, the pristine configuration is recovered by a back electron transfer directly from the d_{z^2} state or indirectly from another d state (e.g. a $d_{xy} \rightarrow \text{GS}_P$ CT followed by a $d_{z^2} \rightarrow d_{xy}$ electron-hole recombination). The lifetime of the porphyrin ESA corresponds to the time of this back donation. The remaining 14 % undergoing internal conversion to the Q band (channel B) reaches the same antibonding metal center state through a less energetically favourable crossing point, that then trigger a delayed photodissociation. The more favourable path to d_{xy} (channel C) is prevented by the full occupancy of this state. The hypothesis of a phonon-assisted process

to overcome the crossing point is corroborated by the shortening of the Q emission lifetime with the excitation energy (Table 1), and in Figure 7.5 it is represented by the height of crossing point with respect to the minimum of S_1 .

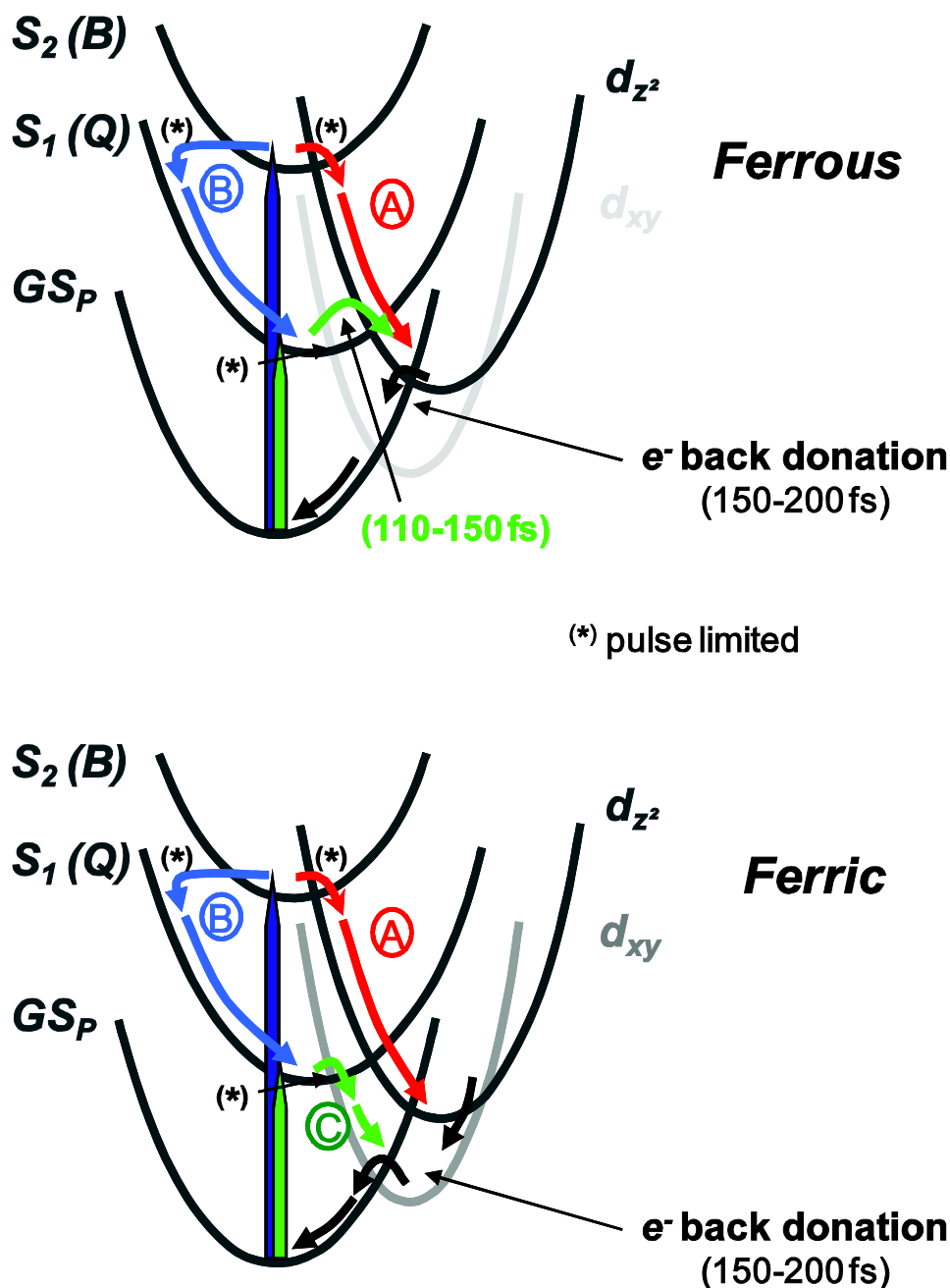


Figure 7.5: Potential energy diagram of ferrous and ferric Cyt c haem, with the proposed relaxation pathways. If the d_{z^2} metal center orbital is empty in both oxidation forms, the d_{xy} one is half filled in the ferric form and completely filled in the ferrous form (see Figure 7 for a simplified scheme). Channels A and B correspond to the branching that occur in ferrous Cyt c under Soret or δ band excitation. In the ferric form, since the d_{xy} orbital is half filled, IC to d_{xy} (channel C) is allowed and more efficient than the 100-150 fs IC to d_{z^2} (end of channel B). Regardless the relaxation channel, the final step is an electron back donation to the porphyrin microcycle.

In the ferric form, the most favourable relaxation pathway through the partially occupied d_{xy} is open, allowing a faster de-excitation without triggering the bond-cleavage.²³⁹ The lack of photo-dissociation also upon excitation in the *B* band suggests that the hole on the d_{xy} orbital can open a similar relaxation via the non antibonding state from S_2 . Alternatively, the first electron transfer still ends up on the d_{z^2} state, but the presence of an empty hole on the lower d_{xy} allows intra-metal orbital IC able to depopulate the antibonding state before any bond-cleavage occurs (in the Figure 7.5, it would correspond to the crossing point between the d_{z^2} and d_{xy} surfaces). After 150-200 fs the system reaches the same state, responsible of the ESA signal, regardless of the oxidation state and the excitation frequency.

It is important not to over-interpret Figure 7.5, where the different parabolae depict multidimensional surfaces projected on a generalized coordinate that takes into account all the possible normal modes. In particular, the different crossing points are in general located along different coordinates on the multidimensional surfaces. For instance the axial d_{z^2} potential energy is expected to depend mainly on the ligand-iron distance, while the d_{xy} energy should be more related to the porphyrin nitrogen-iron distance.

7.1.5 Conclusion

Femtosecond-resolved fluorescence studies of Cyt c upon UV excitation have been carried out, revealing a sub-picosecond energy transfer from the Trp to the Haem, strongly dependent on the oxidation state of the latter. This stress the different geometries (distance and relative orientation) of the Trp-haem pair in ferrous and ferric Cyt c. The Trp emission is instantaneously Stokes shifted to $\lambda > 350$ nm,³⁷⁷ indicating a rigid and polar environment. We reported for the first time fluorescence from the photo-excited haem group, which reveals a complex multi-channel electronic relaxation. The broad detection range as well as the excitation tunability of the transient fluorescence and absorption allowed us to follow the different relaxation steps and to propose one model explaining the origin of the ligand photolysis in ferrous Cyt c. The photolysis is triggered by a charge transfer from the excited states of the porphyrin ring to the d_{z^2} antibonding orbital of the iron. This relaxation channel is < 40 fs from S_2 or from upper energy levels, but 105-145 fs from S_1 , this time constant strongly depending on the excess of vibrational energy. In the ferric form, the presence of the partially unoccupied d_{xy} orbital constitutes a faster decay channel, preventing the ligand from dissociating.

7.2 Myoglobin

The fluorescence of Trp has been extensively used as probe of local protein environment in Myoglobin (Mb). Various techniques have been employed to distinguish the different contributions of the two Trp present in this haemoprotein.^{169,241,323,386-389} Most often, the use of mutant or of important concentration of quencher alter the protein structure and bias the interpretation of the observations. Here we apply our femtosecond broad-band fluorescence technique to the wild type Horse Heart Myoglobin in the Metform (metMb), in order to discriminate spectrally and temporally the contributions from the two Trp.

Additionally, to extend the investigation of haem electronic relaxation, we tracked down the *Q* band fluorescence of Mb and Hemin in water. MetMb and Hemin are both in the ferric oxidation state, but while in the former the Fe atom is 6 coordinated (two axial ligand, an Histidine residue and a water molecule), it is five coordinated with only one axial ligand, a chlorine atom, in the latter. Interestingly, a pulse-limited emission is observed in both cases, like the *Q* band emission of ferric Cytochrome c.

7.2.1 Dual UV fluorescence

The time-wavelength plot of fluorescence from metMb is shown in Figure 7.6a. A representative selection of transient spectra in Figure 7.6b indicates an important spectral evolution on tens of picoseconds, characterized by a broadening of the band.

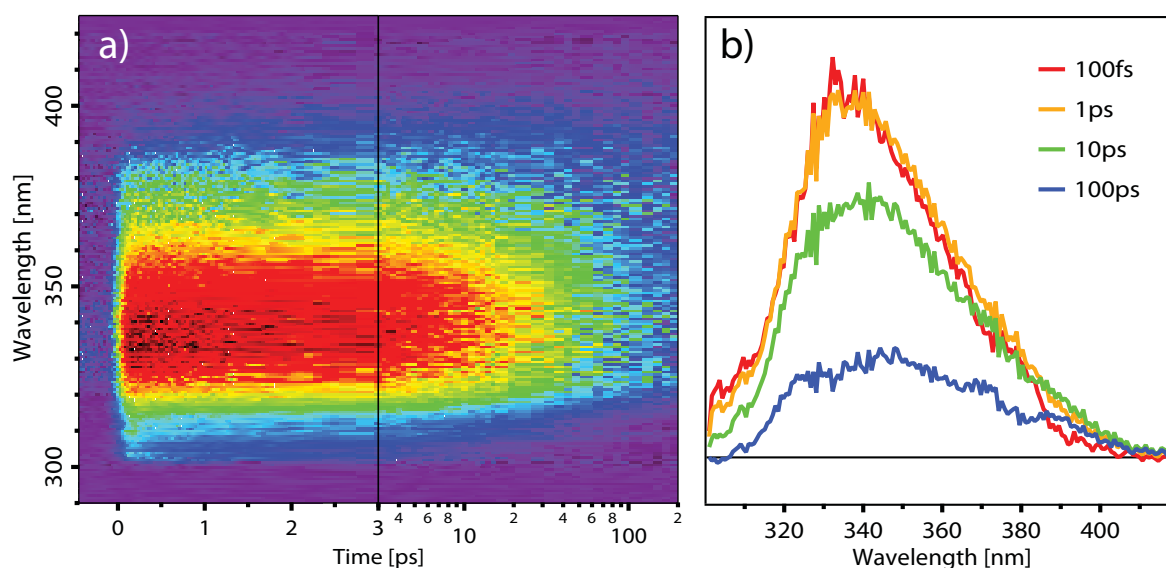


Figure 7.6: a) Time- and wavelength-resolved fluorescence of MetMb in buffer solution (pH = 7) excited at 290 nm, in the 290-420 nm range. The Raman signal from water has been measured independently and subtracted from the raw data. b) Selection of spectra at various time delays from the data on panel a).

Mb contains two Trp, namely W7 and W14, with different local environment and thus different fluorescence spectra (See section 2.4.2).¹⁶⁹ The photo-excited Trps are known to undergo Förster-Dexter resonance energy transfer to the haem group, in ~ 20 and 130 ps for W14 and W7, respectively.²⁴¹ The spectral change observed here is likely due to the overlap of the two different spectra, each vanishing with a different time constant. The disentanglement of the individual emission spectra is not trivial, since the fluorescence profile of each Trp undergoes its own dynamics (spectral shift, narrowing or broadening). The access to the spectrally resolved emission allows us to overcome this issue by considering the integrated spectral area, i.e. the zero moment M_0 . The time evolution of the latter reflects only the depopulation of the excited state of both Trps. In this way, each contribution can be temporally discriminated. Figure 7.7 shows M_0 as a function of time with a biexponential fit. The two obtained lifetimes (15 ± 1 and 140 ± 10 ps) are in agreement with the values reported in the literature (~ 20 and 130 ps).^{169,241,388,390} However, these values were obtained by means of frequency domain fluorescence spectroscopy and time-resolved fluorescence with streak camera, the time resolutions of which are > 5 ps. Therefore, while the deviation of the long component is due to our too short temporal window (200 ps), a more accurate value of the fastest decay time is obtained here, thanks to our femtosecond resolution. The latter is associated to W14 de-excitation, whereas the former corresponds to that of W7, positioned respectively at a distance of ~ 15 and 20 Å from the haem group.¹⁶⁹ The decays have one order of magnitude of difference, allowing us to temporally separate both contributions. At the delay time of 70 ps, the contribution from W14 is $< 1\%$ and the spectrum corresponds almost to emission from W7 only. Provided that no important spectral changes occur in the first tens of ps, it is possible to subtract this contribution (properly scaled) to the spectrum at earlier times, when contribution from W14 is significant. However, the first moment $M_1(t)$ reported in Figure 7.8, indicates that a red shift of the band occurs on different timescales. The attribution of each timescale is non-trivial and will be treated in the next section.

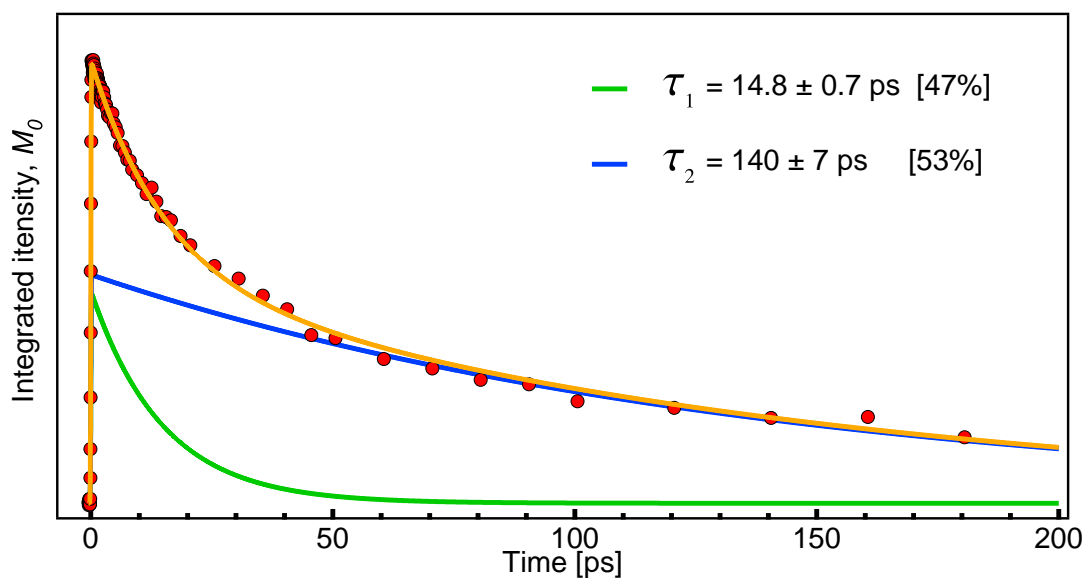


Figure 7.7: $M_0(t)$ (red points) with a bi-exponential fit (orange line). The obtained exponential contribution of 14.8 and 140 ps are plotted in green and blue lines respectively.

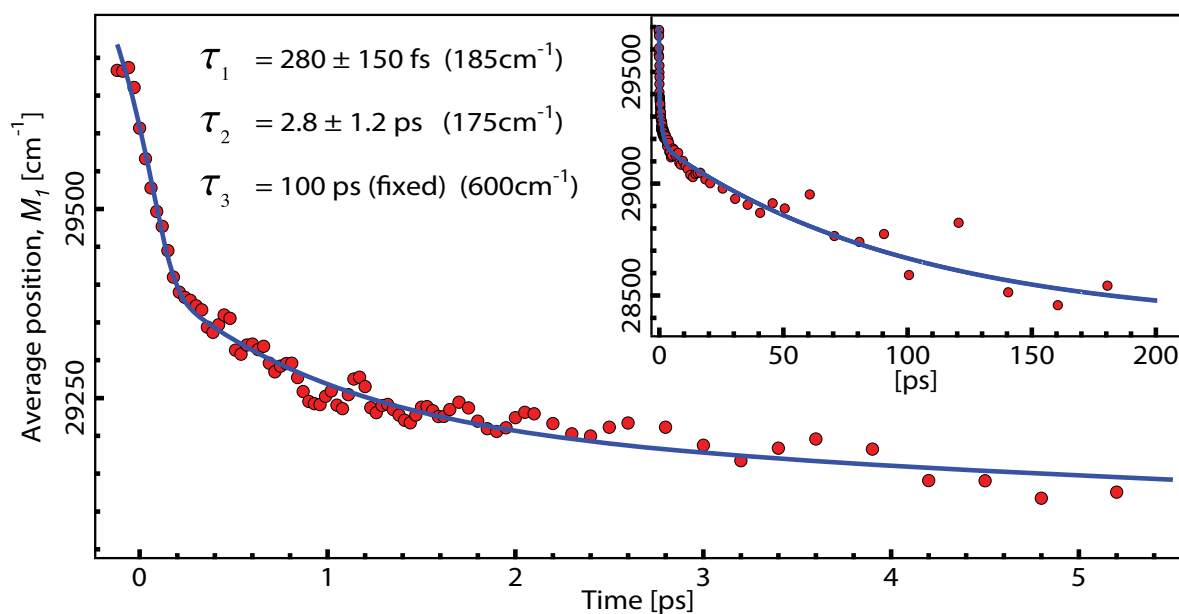


Figure 7.8: $M_1(t)$ (red points) with a tri-exponential fit (blue line), in the first 5 ps. The inset shows the same plot extended to 200 ps.

The fluorescence spectral profile of each Trp has been determined in apomyoglobin with the technique of quenching perturbation, in which the emission intensity from one Trp, more exposed to the external environment, is monitored by variation of quencher concentration.^{386,387} The maxima of fluorescence of W14 and W7 were observed at ~ 335 nm and ~ 345 nm, respectively, and the spectrum of W7 was found broader than that of W14. Both features are expected from the position of W7, closer to the protein surface and thus more exposed to water molecules. On the other hand, W14 is in a hydrophobic medium, and shows accordingly a blue-shifted fluorescence compared to the bulk water (see chapter 5). The different positions ($\Delta\nu^{max} \approx 800$ cm^{-1}) and decay times (15 and 140 ps) of W14 and W7 should appear as a red shift in $M_I(t)$ that amounts to ~ 400 cm^{-1} between 0 and 50 ps. This shift must occur with the fastest decay, i.e. $\tau_1 = 15$ ps (Figure 7.7). At 10 ps, the intensity from W14 is half and thus half of the total shift (200 cm^{-1}) has occurred. Between 10 and 70 ps, the spectrum should still shift of 200 cm^{-1} . This estimation is in agreement with what is observed in our data (Figure 7.8). This observation ensures that in this time window, the spectral shift is only due to the presence of two DAS. A reasonable time delay to extract a confident fluorescence spectrum of W14 from the total fluorescence is 10 ps. The spectral decomposition in W7 and W14 fluorescence intensity, shown in Figure 7.9, confirms the expected spectral profiles, i.e. broad and red shifted for W7 and narrower and blue shifted for W14.

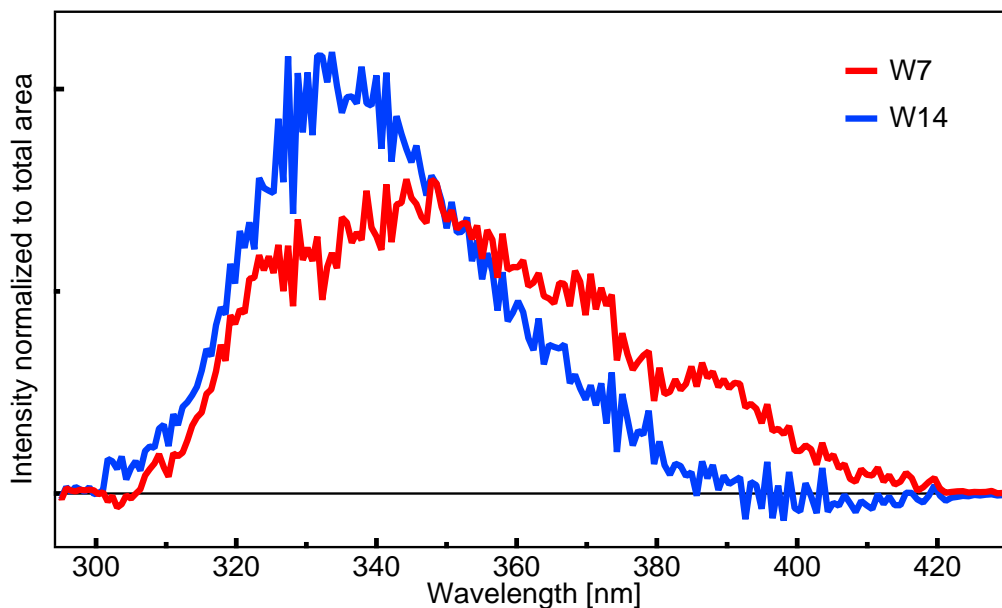


Figure 7.9: Spectral decomposition of W7 and W14. The intensity has been normalized to the integrated area of the spectrum.

7.2.2 Local Trp7 dynamics

The contributions to the total Stokes shift ($M_I(t)$, Figure 7.8) are various and hard to disentangle: beside the shift due to the dual fluorescence (Figure 7.9), each Trp undergoes its relaxation dynamics, reflected in spectral shifts, those might occur on different timescales. The assignment of the decays observed in $M_I(t)$ are now discussed.

As argued in the previous §, the intermediate timescale (1-50 ps) should be dominated by the quenching of W14. The spectral and temporal decomposition obtained in the previous section can be used to identify the influence of this effect on $M_I(t)$. Figure 7.10 shows the first moment from the data (from Figure 7.8) and that of the time-wavelength plot reconstructed from the addition of the individual Trp contributions (spectra of Figure 7.9 multiplied by kinetic traces of Figure 7.7).

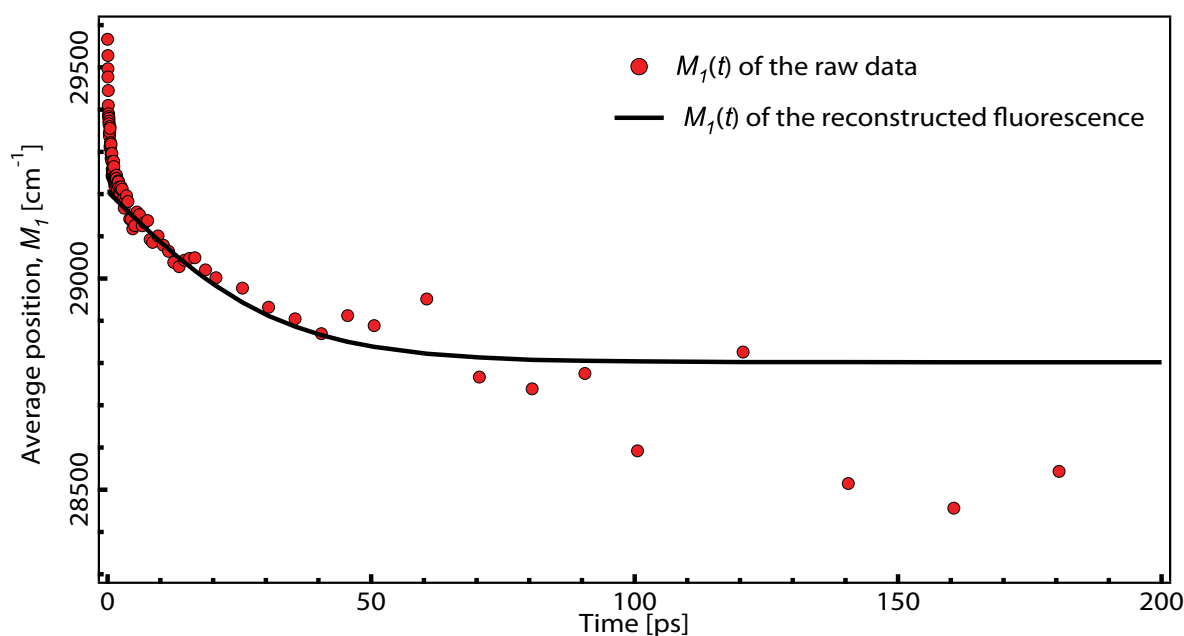


Figure 7.10: First spectral moment $M_I(t)$ of: the raw time-wavelength fluorescence data of Figure 7.6 (red disks); the sum of fluorescence of W7 and W14 contributions, reconstructed from their kinetic and spectral profiles (black trace); the fluorescence contribution of W7 only, i.e. the raw fluorescence minus the contribution from W14.

Apart from the first picosecond, the first moment from the reconstructed time-wavelength matrix matches the raw data points for time shorter than 70 ps. After that time, $M_I(t)$ still shifts to the red. This long decay belongs only to W7. Such a relaxation has been observed in a mutant apomyoglobin containing only W7.^{61,323} A 87 ps relaxation of 420 cm⁻¹ was assigned to coupled water-protein response, sustained by MD simulation. The weak signal

intensity from W7 in the present wild type Myoglobin in this timescale does not allow a good determination of the time constant related to this surface hydration relaxation. Nevertheless, a shift of $\sim 300 \text{ cm}^{-1}$ is observed in this time window (50-200 ps).

In the sub-50 ps temporal window, both Trp should contribute to the total spectral shift. However, as mentioned before, W14 is embedded in a hydrophobic area in the protein and is almost not exposed to water molecules. Accordingly, its environment is only constituted of the rigid polypeptide structure. On the picosecond timescale, the mechanical response of this local structure to the dipole moment change of W14 is less significant than the water relaxation around W7. It is thus reasonable to assume that the picosecond red shift of the band is only due to solvation dynamics of W7, located on the protein surface. Figure 7.11 shows $M_I(t)$ of the fluorescence of W7, obtained by subtracting the fluorescence of W14, reconstructed from its kinetic and spectral profiles, to the raw data (Figure 7.6). A bi-exponential fit of the resulting trace gives two lifetimes of 430 fs and 2.8 ps.

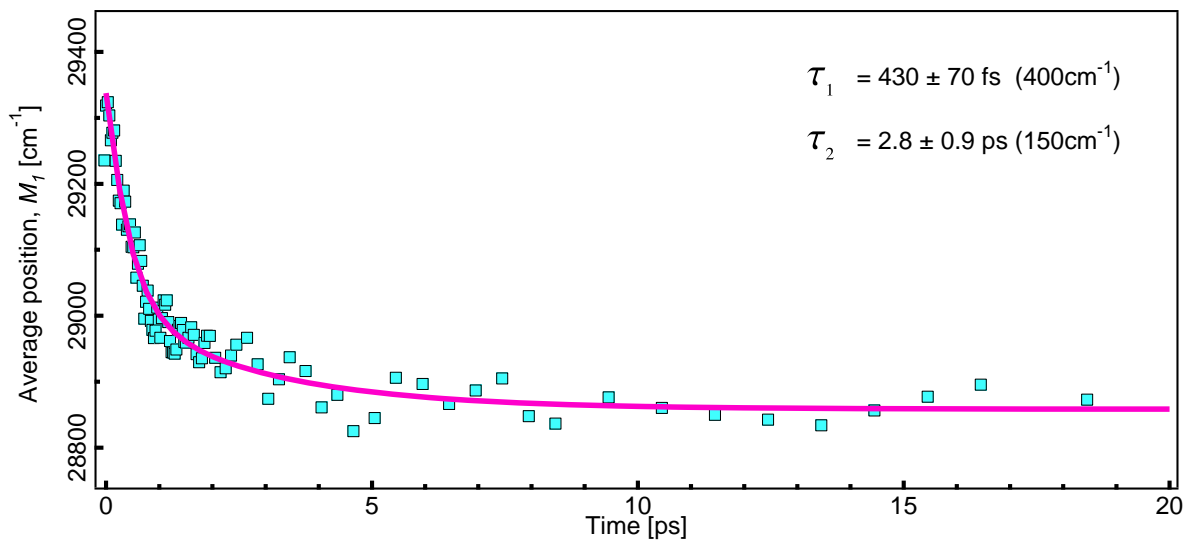


Figure 7.11: First spectral moment $M_I(t)$ of the fluorescence contribution of W7 only, i.e. the raw fluorescence minus the reconstructed contribution from W14 (blue squares), along with a bi-exponential fit (purple trace).

These initial relaxation times are due to the response of the local environment of W7, which is in direct contact with the water molecules from the hydration layer. However, the local flexibility of free water molecules is constrained by the strong protein-water interactions at the interface. The initial $< 10 \text{ fs}$ water relaxation evidenced in the bulk (see chapter 5) is still not detectable here. However, this response, due to inertial rotation of

water, should not be affected by the interactions with the protein surface. The 430 fs and 2.8 ps could tentatively be assigned to the same solvation mechanisms than in bulk water, but slowed down in the hydration layer. In a series of articles, Zhong *et al.*^{59,185,391} have observed at least two different picoseconds solvation times at lipid-water and protein-water interfaces that they attributed to two different hydration layers, namely a first well-ordered mono-molecule layer (strong interaction) and a second quasi-bound layer. The solvation contribution from the latter corresponds to water network rearrangement and is expected to occur on tens to hundreds of picoseconds. It can also be viewed as the bound-to-free transition rate, in the description of the protein hydration layer proposed by A. Zewail.⁶⁰ This rate highly depends on the local surface sites in such a way that the local water fluctuations “slave” the local protein motion.⁶¹ The fastest time, on 1-10 ps, originates from collective rotational and translational motion of the former quasi-bound water layer. This mechanism is probably reflected in the 2.8 ps observed in our data, corresponding to the ~1ps relaxation of bulk water response, slowed down by the protein-water interactions. Indeed, Zhang *et al.*⁶¹ observed two decays of 3-5 ps and 80-90 ps in the correlation function of a mutant myoglobin, containing only W7. The ultrafast response of 430 fs, is likely due to contribution from the bulk water. The separation of these free water molecules from Trp by the hydration layer makes this contribution smaller than what is observed in bulk water: 400 cm⁻¹ against 2000 cm⁻¹ for the 160 fs and 1ps times gathered (see chapter 5). These dynamics are also reflected in the second spectral moment reported in Figure 7.12. While the fluorescence spectrum of W14 is assumed static, the spectral shift of fluorescence of W7 should appear as a broadening of the total band. Beside the broadening observed on 10 ps due to the quenching of W14, an initial broadening occurs on 450 fs, resulting from modulation of the width by the time-dependent relative position of W7 and W14 spectra in the the initial relaxation (430 fs).

In the next §, we discuss the contribution of the haem group to the UV-visible fluorescence of metMb.

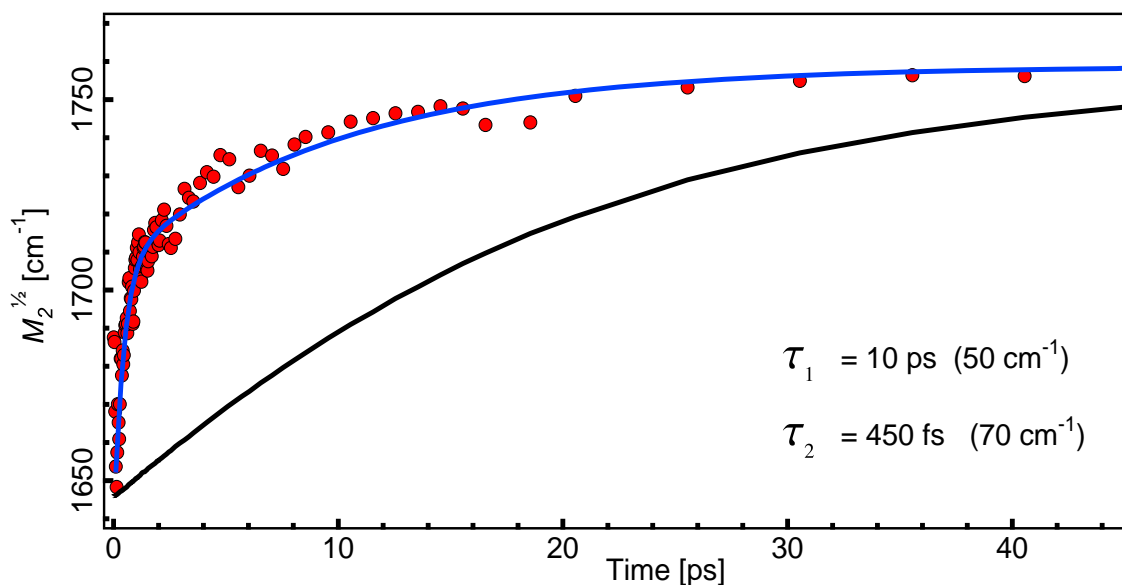


Figure 7.12: Square root of the second spectral moment $M_2(t)$. The data points (red disks) are well fitted with a bi-exponential rise of 450 fs and 10 ps (amplitudes in parenthesis). The black line corresponds to the second spectral moment of the sum of fluorescence of W7 and W14 contributions, reconstructed from their kinetic and spectral profiles.

7.2.3 Haem electronic relaxation

Conversely to Cytochrome *c*, no emission of the haem is observed in the UV range. Moreover, to our knowledge, emission of the haem of Mb has never been reported yet, neither in the UV nor in the visible. We have looked over the *Q* band fluorescence of metMb under Soret excitation (400 nm). In parallel, we performed the same measurement on the haem-like compound in bulk water: Fe^{III} protoporphyrin IX chloride also called hemin. The iron atom of both samples is in the ferric oxidation state. The time-wavelength fluorescence plots are shown in Figure 7.13.

The *Q* band fluorescence of the two samples are almost identical, and resemble the one of ferricytochrome *c*, i.e. broad and featureless, mirror image symmetry of the absorption band. The intensity appears and vanishes within the *irf*, indicating a decay time < 50 fs. Figure 7.14a reports a selection of kinetic traces and Figure 7.14b the spectrum a time zero of fluorescence of metMb, confirming this observation. This result corroborates the idea that the quenching mechanism of ferric porphyrins is intrinsically related to the presence of a hole in a specific iron *d*-orbital. The speed of the porphyrin → metal electron transfer speaks for the occurrence of a conical intersection between the two involved excited states. However, to confirm this behavior, more measurements on Fe²⁺ porphyrins are necessary, as for instance on iron protoporphyrin IX. Moreover, Ha-Thi *et al.*²⁵⁰ have observed

identical relaxation decay rates for Fe^{2+} protoporphyrin IX and its associated salt Fe^{3+} protoporphyrin IX chloride (Hemin), questioning the importance of the iron electronic structure in the relaxation pathway.

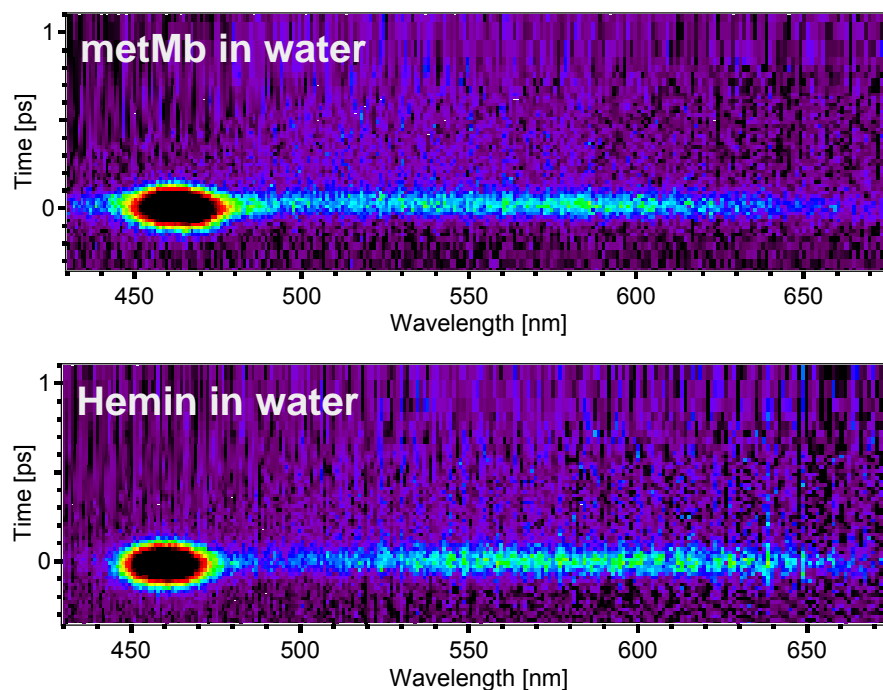


Figure 7.13: Time- and wavelength plots of fluorescence of metMb and Hemin in buffer solution pH7 under 400 nm excitation

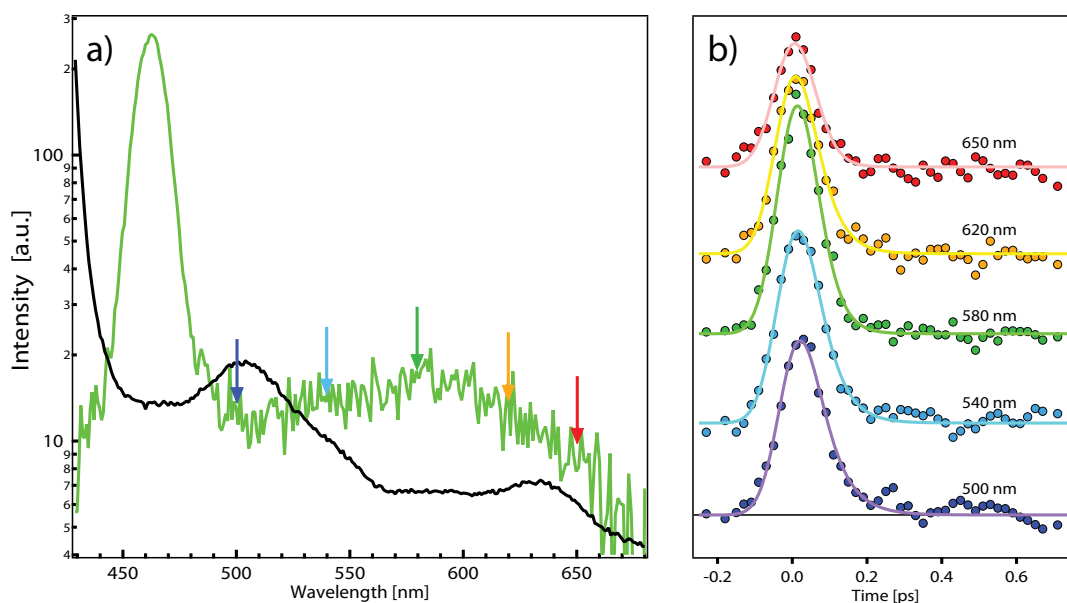


Figure 7.14: a) Time-zero spectrum and b) representative selection of kinetic traces of fluorescence of metMb (Figure 7.13)

7.2.4 Summary

The UV fluorescence of metMb reveals the relaxation dynamics of Trp as energy transfer and solvation. In particular our broad-band detection allowed us to spectrally and temporally separate the contribution from W7 and W14. It is then possible to extract the solvation timescales of W7, and this, in the wild-type protein. The maximum of the timezero spectrum is already close to the static spectrum, i.e. displaced by more than 5000 cm^{-1} from the absorption maximum. Consequently, the initial ultrafast ($< 10\text{ fs}$) shift observed in the bulk (chapter 5) is still present but not detectable. The longer timescales, characteristic of the bulk solvation (150 fs, 1 ps) are clearly slowed down by the protein-water interactions to 430 fs and 2.8 ps. A slower $> 50\text{ ps}$ component is observed, likely due to the hydration layer “bound-to-free” transition rate.

The electronic relaxation of the haem, followed through the emission of the Q band, is similar to that of haem-like systems in the same oxidation state, ferricytochrome c and hemin. This preliminary study of metMb is promising for a prospective systematic investigation of the other forms of Mb, i.e. deoxy-Mb or Mb with different ligand (O_2 , CO, CN, etc...).

Chapter 8

Metal-polypyridine complexes and Dye Sensitized Solar Cells

8.1 Solution phase studies

8.1.1 Time zero Stokes shift

8.1.2 Excitation dependence of $M(bpy)_3^{2+}$

8.1.3 Ultrafast IVR mechanism

8.1.4 Solvent effect

8.1.5 Solar cell sensitizer: RuN719

8.2 RuN719 adsorbed on semiconductor thin films

8.2.1 RuN719 adsorbed on injecting and non injecting substrates

8.2.2 Electron injection process

8.3 Conclusion

One of the most important applications of the study of ultrafast relaxation dynamics of photo-excited molecules lies in the great development of artificial solar energy conversion devices in the last decades. Among the various types of photovoltaics cells, the dye sensitized solar cells (DSSC), invented by Mickael Grätzel and Brian O'Regan in 1991,^{277,280} are one of the most efficient low-cost devices. This system is such promising that numerous studies are managed in order to improve every constituting component (sensitizer, semiconductor, electrolyte solution, etc...).

The principle of the dye sensitized solar cells (DSSC) is based on the use of mainly metal-based molecular complexes,²⁷⁷ of which the RuN3 ($[\text{Ru}(\text{dcbpyH}_2)_2(\text{NCS})_2]^{2+}$) dye is the most popular. The initial process of light harvesting is performed by such a dye molecule, adsorbed onto a semiconductor substrate (usually TiO_2). Upon absorption of visible light by the singlet metal-to-ligand-charge-transfer ($^1\text{MLCT}$) state of the dye, injection of an electron into the conduction band of the substrate occurs.²⁹⁴ A central issue for the optimization of the efficiency of dye-sensitized solar cells is the detailed understanding of the mechanism and time scale of electron injection.

To address this issue, we have performed femtosecond-resolved broadband fluorescence studies of $[\text{M}(\text{bpy})_3]^{2+}$ ($\text{M} = \text{Fe}, \text{Ru}$), RuN3 and RuN719 complexes in solution and of RuN719 adsorbed on TiO_2 and Al_2O_3 substrates. We investigated the pump wavelength dependence of the fluorescence of aqueous $[\text{Fe}(\text{bpy})_3]^{2+}$ and the solvent and ligand dependence of the fluorescence of Ru-complexes excited at 400 nm. The experimental procedures are reported in appendix G.

8.1 Solution phase studies

Recently, our group reported polychromatic time-resolved fluorescence studies on $[\text{Ru}(\text{bpy})_3]^{2+}$ and $[\text{Fe}(\text{bpy})_3]^{2+}$ in aqueous solutions, detecting not only their short lived $^1\text{MLCT}$ fluorescence but also their $^3\text{MLCT}$ phosphorescence.^{52,186} For both complexes, the decay time of the $^1\text{MLCT}$ emission was determined to be ≤ 30 fs, and the fluorescence exhibited fairly similar features, characterized by a strongly Stokes shifted $^1\text{MLCT}$ fluorescence already at zero time delay, having a mirror-like profile with respect to the absorption band (Figure 8.1). This implies sub-30 fs intramolecular energy relaxation processes preceding the $^1\text{MLCT}$ fluorescence, such as internal conversion (IC) in the manifold of $^1\text{MLCT}$ states and intramolecular vibrational redistribution (IVR), that should therefore compete with the injection when the dyes are adsorbed on a semiconductor substrate. Since DSSCs usually operate with RuN3 or RuN719 ($(\text{Bu}_4\text{N})_2[\text{Ru}(\text{dcbpyH})_2(\text{NCS})_2]^{2+}$) complexes, we decided to extend our studies to these complexes, while revisiting the $[\text{M}(\text{bpy})_3]^{2+}$ complexes to investigate the pump wavelength and solvent dependences of their ultrafast intramolecular relaxation processes.

8.1.1 Time zero Stokes shift

Figure 8.1 shows the steady state absorption spectra and the previously reported fluorescence spectra at zero time delay of the $[\text{Ru}(\text{bpy})_3]^{2+}$ and $[\text{Fe}(\text{bpy})_3]^{2+}$ complexes.^{52,186} The observed time zero Stokes shift is quite similar in both cases and as already mentioned, the fluorescence exhibits a near-mirror image with respect to the absorption spectra, as expected for a vibrationally cold emission, despite the fact that we excite both to high vibrational levels ($\nu = 2$ and 4, respectively) of the high frequency 1607 cm^{-1} mode which makes up the dominant progression of the absorption band (Figure 8.2). To clarify this behaviour, we measured the time-zero fluorescence spectra as a function of excitation energy, thus allowing us to deposit different amounts of excess vibrational energy in the excited electronic state. This was only possible for $[\text{Fe}(\text{bpy})_3]^{2+}$ because its absorption band best matches the range of excitation wavelengths available with our set-up.

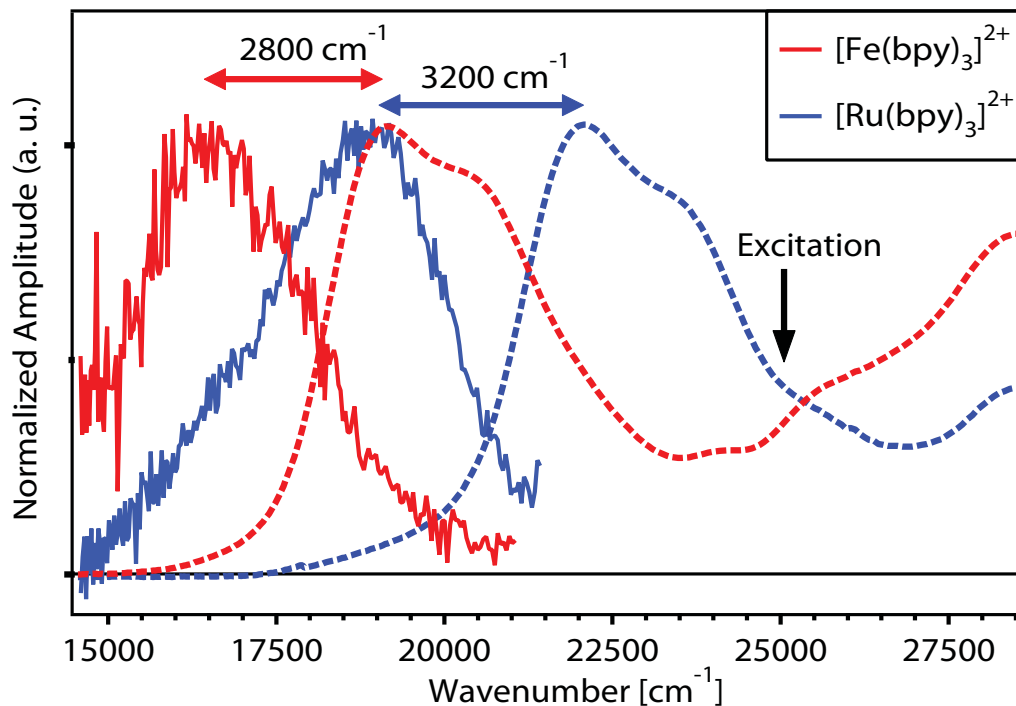


Figure 8.1. Steady-state absorption spectra showing the $^1\text{MLCT}$ absorption band (dashed traces) and time-zero fluorescence spectra of $[\text{Fe}(\text{bpy})_3]^{2+}$ and $[\text{Ru}(\text{bpy})_3]^{2+}$ in water, excited at 25000 cm^{-1} (black arrow). The horizontal arrows indicate the respective absorption-emission Stokes shift (from refs ⁵² and ¹⁸⁶).

8.1.1 Excitation dependence of $[\text{Metal}(\text{bpy})_3]^{2+}$

Figure 8.2 shows the absorption spectrum of aqueous $[\text{Fe}(\text{bpy})_3]^{2+}$ along with its decomposition¹⁸⁶ using a progression of the high frequency Franck-Condon (FC) mode at 1607 cm^{-1} with a Huang-Rhys factor $S=0.8$, whose bands are represented by Gaussian line shapes. The different pump wavelengths used to excite the system are indicated by arrows. The highest excitation frequency used is close to the spectral position of the $\nu=4$ vibrational level of the FC mode, while the others excite the $\nu=0$ and $\nu=1$ levels. The corresponding time-zero emission spectra are also shown. Over the detection range allowed by the corresponding excitation cut-off filter, they clearly show no dependence on the excitation wavelength. Also worthy to note is that the only slight disagreement is observed in the region around 18000 cm^{-1} where partial re-absorption (sample-dependent, but always $\leq 25\%$) of the emitted fluorescence occurs due to the onset of the $^1\text{MLCT}$ band. In all cases the decay of the $^1\text{MLCT}$ fluorescence is found to occur in $\leq 30\text{ fs}$, as previously reported under 400 nm excitation and proven to be a consequence of ultrafast intersystem crossing to the $^3\text{MLCT}$ state.¹⁸⁶

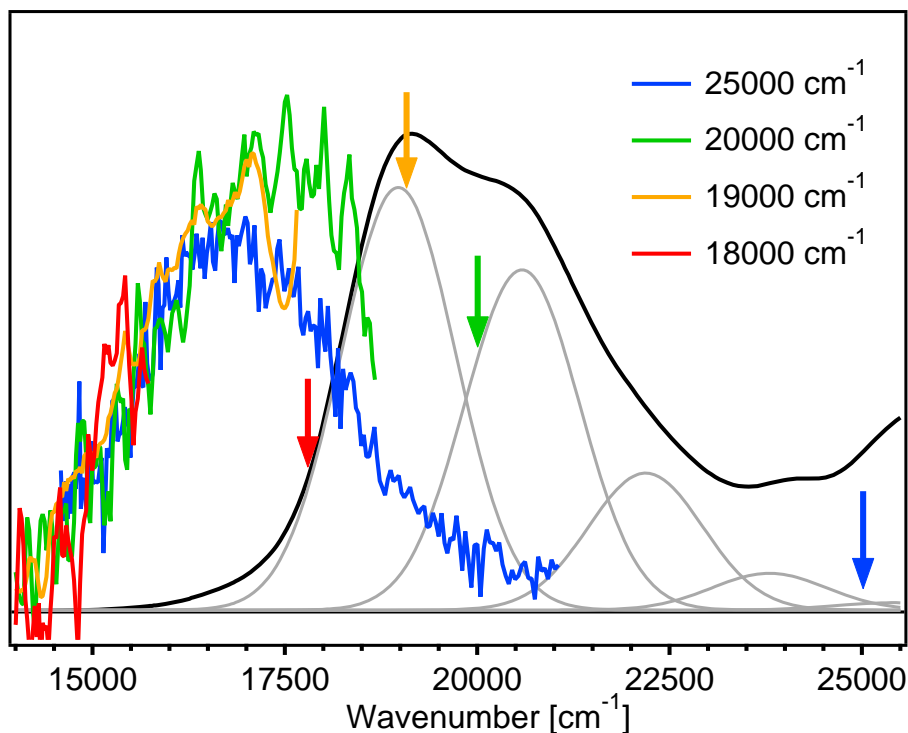


Figure 8.2. Ground state absorption of $[\text{Fe}(\text{bpy})_3]^{2+}$ in water (black trace) with its decomposition in terms of a progression of the Franck-Condon 1607 cm^{-1} vibrational mode (grey lines).¹⁸⁶ The coloured traces show the time-zero emission spectra for different excitation wavelengths (marked by vertical arrows with the respective colours). The emission spectra are cut-off on the blue side according to the corresponding filter used to reject excitation light.

Note that the mirror-symmetric time-zero emission observed for $[\text{Ru}(\text{bpy})_3]^{2+}$ (Figure 8.1) is also consistent with the lack of excitation wavelength dependence seen in Figure 8.2, since the 400 nm excitation corresponds to the $\nu = 2$ level in the former. Together with Figure 8.1, this confirms that the $^1\text{MLCT}$ fluorescence is vibrationally relaxed on ultrashort time scales. This implies that the time scale of such a relaxation must be significantly shorter than 30 fs. We should remark that the concept of a “cold” $^1\text{MLCT}$ fluorescence is with respect to the high frequency Franck-Condon mode making up the main progression in absorption (Figure 8.2), while silent lower frequency modes may be populated.

8.1.3 Ultrafast IVR mechanism

Starting from the fact that the $^1\text{MLCT}$ fluorescence exhibits an upper lifetime $\tau_{\text{ISC}} \sim 30$ fs, determined by the intersystem crossing (ISC) to the $^3\text{MLCT}$ state both in $[\text{Ru}(\text{bpy})_3]^{2+}$ and $[\text{Fe}(\text{bpy})_3]^{2+}$,^{52,186} one can obtain a rough estimate of the relaxation time τ_H (H for hot) leading to the observed “cold” signal from the ratio R of the peak fluorescence signal to that of the background on the blue most side of the spectrum, namely $\tau_H \sim R^{-1}\tau_{\text{ISC}}$. To see how this arises, let us consider the case of excitation of $[\text{Fe}(\text{bpy})_3]^{2+}$ at 400 nm. In first approximation, this will basically populate only the $^1\text{MLCT}$ sublevel with $\nu = 4$. In absence of any relaxation, such an initially prepared state should yield a characteristic hot emission $I_H(E)$ arising from the transitions from the $\nu = 4$ level to the manifold of vibrational levels within the ground electronic state. By calculating the shape of $I_H(E)$ via the known Frank-Condon parameters of $[\text{Fe}(\text{bpy})_3]^{2+}$ it turns out that most of the $I_H(E)$ emission intensity ($\sim 65\%$) is concentrated in the “hot” region $E_H > 19000 \text{ cm}^{-1}$, much higher than the centre of gravity of our signal (Figure G.1 and G.2). Hence, to be consistent with the observed Stokes-shifted fluorescence, such an initially prepared hot state must be (incoherently) depopulated in a time scale τ_H , leading to a “cold”(C) emitting state with emission $I_C(E)$ that subsequently decays in τ_{ISC} . Since both τ_{ISC} and τ_H are significantly shorter than the 100 fs *irf*, the dynamics is pulse-limited, meaning that time-zero populations of H and C will be basically proportional to τ_H and τ_{ISC} , respectively. We can thus express the normalized fluorescence line shape as a weighted combination of hot and cold emission line shapes:

$$I(E) = \frac{\tau_H I_H(E) + \tau_{\text{ISC}} I_C(E)}{\tau_H + \tau_{\text{ISC}}} \quad (8.1)$$

namely $\tau_H/(\tau_H + \tau_{\text{ISC}})$ corresponds to the weight of the “hot” contribution to the whole lineshape. Since $I_H(E)$ is negligible in the region E_C where the signal peaks, and since $I_C(E)$ is negligible in the E_H energy region, the last expression implies that $\tau_H \sim R^{-1}\tau_{\text{ISC}}$ within a factor of the order of unity (basically corresponding to the width ratio between the line shapes $I_C(E)$ and $I_H(E)$).

The ratio R can be assessed by comparing in Figure 8.2 the signal at 16500 cm^{-1} to that at $20000\text{-}21000 \text{ cm}^{-1}$ for the spectrum excited at 25000 cm^{-1} , yielding $R \sim 10\text{:}1$ (It is worth noting that reabsorption effects are negligible for this sample both at E_H and E_C). This implies a lifetime of < 3 fs for the intermediate states lying between the excitation energy

and the fluorescence. Since relaxation is a cascade among intermediate states, we conservatively estimate to ≤ 10 fs the appearance of the Stokes shifted $^1\text{MLCT}$ fluorescence in $[\text{M}(\text{bpy})_3]^{2+}$ ($\text{M} = \text{Ru}, \text{Fe}$). This would mean that the “cold” $^1\text{MLCT}$ emission is formed on sub-vibrational time scales. Such a fast relaxation can only be due to ultrafast IC and IVR.²¹ In support of this, we note that the vibrational progression of the highest frequency mode (1607 cm^{-1}) dominating the $^1\text{MLCT}$ absorption band of $[\text{M}(\text{bpy})_3]^{2+}$ ($\text{M} = \text{Ru}, \text{Fe}$) features a line width of $\sim 1700 \text{ cm}^{-1}$ of each vibronic line.^{52,186} At cryogenic temperature, the line width was observed to be $400\text{-}500 \text{ cm}^{-1}$,²⁷¹ which would correspond to a lifetime of 10-15 fs, assuming a fully homogenous lifetime broadening mechanism. While the observed $^1\text{MLCT}$ fluorescence stems from a “cold” electronic level with respect to the high frequency Franck-Condon mode, we remark again that optically silent lower frequency modes may be populated. Actually they are expected to be, since cooling of the molecule by the solvent is unlikely to occur within such a short time scale. The high local temperature of the molecule after IVR should lead to a structure less fluorescence at early times, as opposed to the vibrational structure that shows up in absorption. Such a broadening of bands at time zero and their narrowing at later times was for example clearly visible in our fluorescence up-conversion study of the 2,5-diphenyloxazole (PPO) dye in cyclohexane (see chapter 4).¹⁹³ This does not occur here because the $^1\text{MLCT}$ lifetime is too short to allow for cooling.

8.1.3 Solvent effect

The above estimate of ≤ 10 fs for the dynamical Stokes shift is significantly shorter than any solvation times.³⁹² However, given the measurable solvent effects on the absorption spectrum (see e.g., ref. ³⁹³ for the case of $[\text{Ru}(\text{bpy})_3]^{2+}$), we nevertheless explored their possible influence in the initial intramolecular relaxation. Figure 8.3 shows the 2D time-wavelength plots of the emission of $[\text{Ru}(\text{bpy})_3]^{2+}$ excited at 400 nm in various solvents. They all feature a short-lived singlet emission band centred around 500-525 nm, and a longer lived $^3\text{MLCT}$ emission centred around 600-650 nm as previously reported.⁵² Except for minor spectral shifts among the different solvents, their dynamics are clearly identical. Given that the used solvents differ significantly in their dielectric constants, we can safely conclude that the dynamics at ultrashort times is entirely governed by intramolecular processes.

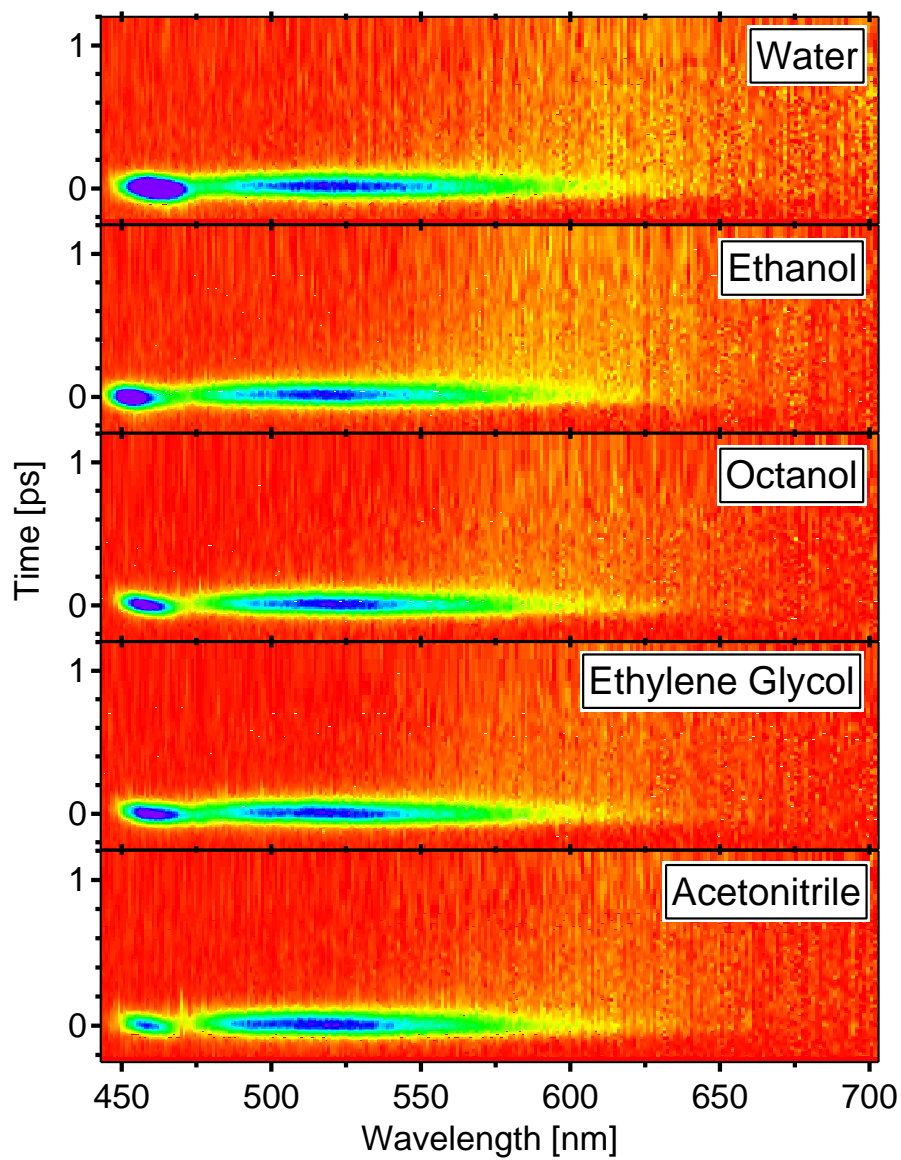


Figure 8.3: 2D time-wavelength plots of the emission of $[\text{Ru}(\text{bpy})_3]^{2+}$ excited at 400 nm in different solvents. The plots are normalized to the maximum of the fluorescence (~ 520 nm).

8.1.4 Solar cell sensitizer: RuN719

Because the RuN3 and RuN719 are the most commonly used complexes in DSSCs, we also investigated their dynamics in solution and on semiconductor substrates, concentrating on RuN719. As already mentioned in section 2.5.2, the static absorption spectrum of RuN719 features two ¹MLCT bands (Figure 8.4) located at 500-530 nm and 375-385 nm. Excitation into these bands leads to the steady-state phosphorescence spectrum that peaks at 740-780 nm (Figure 8.4). Both absorption and phosphorescence spectra exhibit clear solvent effects with ethanol and acetonitrile having rather similar features while water clearly stands out. The time-wavelength plots of the ultrafast fluorescence of N719 in water, ethanol and acetonitrile excited at 400 nm are also shown in Figure 8.4. Because of the fast photo-aggregation on the walls of the flow cell, the integration time used in EtOH and ACN was shorter than in H₂O, leading to a poorer signal to noise ratio. The behaviour of RuN719 appears to be qualitatively identical to what is observed above in [Ru(bpy)₃]²⁺ (Figure 8.3): the dominant signal in all solvents is the fast-decaying pulse-limited fluorescence around 550-575 nm. Figure G.3 shows the static absorption spectra and the time-zero fluorescence spectrum on the same energy scale. The latter is strongly Stokes-shifted and mirror symmetric with respect to the first absorption band around 500 nm. This points to an ultrafast internal conversion (IC) from the upper to the lower ¹MLCT state, that takes place on a time scale significantly shorter than the fluorescence lifetime (≤ 30 fs, see below). ³MLCT phosphorescence is not measured in this case since it falls outside our detection region. Overall, these results (and those for RuN3 in EtOH, not shown here) show that also for RuN719 and RuN3 the short time dynamics is dominated by intramolecular relaxation faster than the ISC and that fluorescence arises from a “cold” state. In conclusion, IVR/IC processes occur on the same ultrafast time scales for all Ru-complexes studied here, suggesting a weak influence of the nature and symmetry properties of the ligands coordinating to the central atom.

More information on the decay kinetics of RuN719 and RuN3 can be obtained by a detailed analysis of their kinetic traces. In Figure 8.5, we show the kinetic traces at different emission wavelengths and the time-gated emission spectra at different time delays of [Ru(bpy)₃]²⁺, RuN719 and RuN3, which are extracted from 2D time-wavelength emission plots (i.e. those of Figure 8.4 for RuN719, and of ref. ⁵² for [Ru(bpy)₃]²⁺).

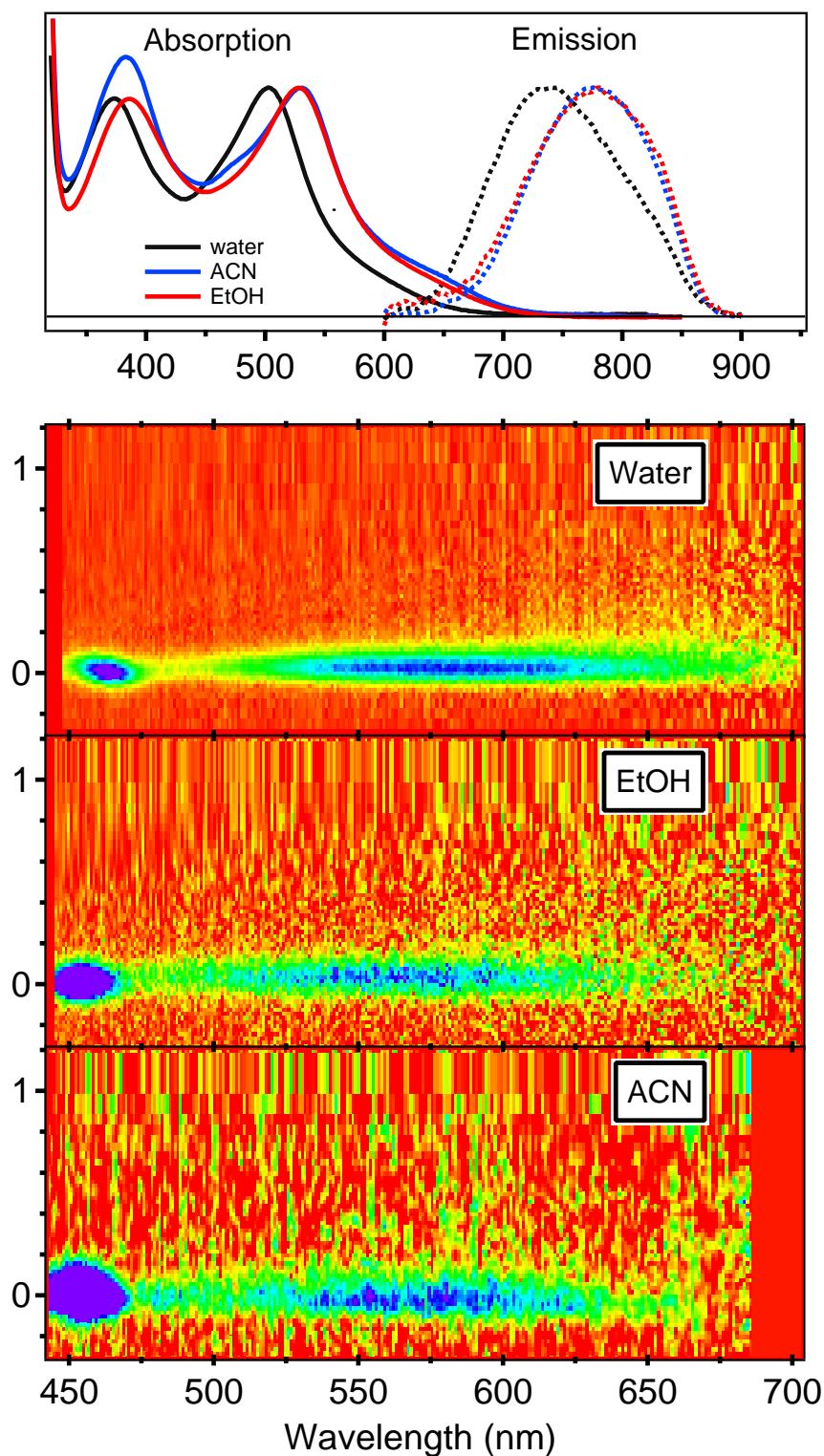


Figure 8.4: Top panel: Static absorption and emission spectra of RuN719 in several solvents. Other panels: 2D time-wavelength plots of the emission of RuN719 excited at 400 nm in several solvents normalized to the maximum of the fluorescence (~570 nm).

These traces include the solvent Raman line in the region around 460 nm, which serves as a crosscorrelator. It can be seen that the kinetic traces on the blue wing of the fluorescence overlap quite well that of the Raman line, but exhibit a longer decay than the latter, as already reported for $[\text{Ru}(\text{bpy})_3]^{2+}$,⁵² and shown to be due to the ultrafast decay (in ≤ 30 fs) of the $^1\text{MLCT}$ state by intersystem crossing to the $^3\text{MLCT}$ state. The overall behaviour of RuN3 and RuN719 appears to be identical. By convoluting with the cross-correlation time of our experiment (~ 110 fs), fits of the kinetic traces at 500 nm (corresponding to the range of the $^1\text{MLCT}$ emission free from longer-lived contributions, see Figure G.4) yield decay times of ≤ 30 fs for RuN719 and ≤ 45 fs for RuN3. However, in all three dyes the decay becomes longer for longer detection wavelengths. For example, in the case of RuN3 the fit gives a time constant of ~ 60 fs for the trace at 600 nm, wavelength at which Sundström and co-workers²⁹¹ reported a 70 fs lived SE. As this value does not reflect the lifetime of the $^1\text{MLCT}$ at maximum, it may be due to longer-lived lower lying $^1\text{MLCT}$ states or a weak contamination by the $^3\text{MLCT}$ emission, which for RuN3 is peaked at ~ 800 nm.²⁹³ For reasons outlined below, we believe that the first option is more likely.

To investigate further the nature of this longer component in RuN719 and RuN3, we performed a global fit analysis of the 2D time-wavelength plot of RuN719 in water, which was chosen because it has the best signal to noise ratio. The result yields two different decay times, corresponding to different spectral components shown in Figure G.5. The first, centred around 570 nm, is pulse-limited (≤ 30 fs) and can safely be associated to the $^1\text{MLCT}$ fluorescence. The second component has a longer decay time (~ 190 fs) and lies further to the red, but it does not occur in the range where the $^3\text{MLCT}$ phosphorescence is expected (compare with top of Figure 8.4). Density functional theory (DFT) and time-dependent density functional theory (TD-DFT) calculations by Selloni *et al.*³⁹⁴ reported the existence of a manifold of closely spaced MLCT singlet electronic states in RuN3, many of which have reasonable oscillator strengths. The analogues of these states for RuN719 may be responsible for this emission.

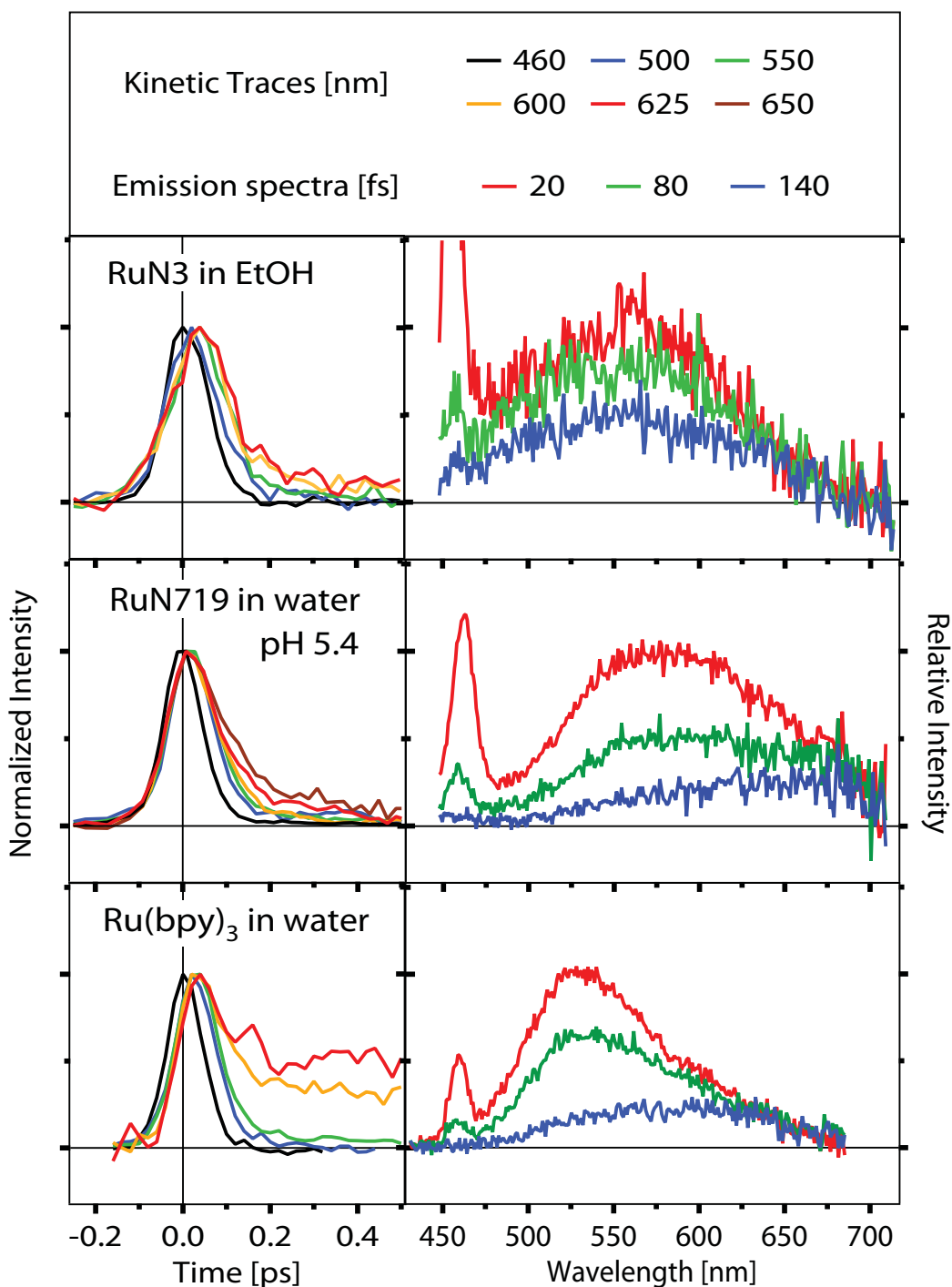


Figure 8.5: Representative kinetic traces (left panels) and spectra (right panels) from 2D time-wavelength emission plots of RuN3 in ethanol and RuN719 and $[\text{Ru}(\text{bpy})_3]^{2+}$ in water. For a better comparison of the kinetic behavior, the time traces are normalized to the maximum. The longer lived signal in $[\text{Ru}(\text{bpy})_3]^{2+}$ is due to the $^3\text{MLCT}$ emission as already discussed in ref. ⁵². See also Figure G.4 where the emission spectra are normalised to 510 nm, highlighting the longer lived red emission in RuN719 and $[\text{Ru}(\text{bpy})_3]^{2+}$.

8.2 RuN719 adsorbed on semiconductor thin films

8.2.1 RuN719 adsorbed on injecting and non injecting substrates

Figure 8.6 (upper panel) shows the absorption spectra of RuN719 adsorbed on mesoporous TiO₂ and Al₂O₃, along with the spectra of the substrates only. The emission centred around 750 nm stems from the ³MLCT state, as seen in ethanol and acetonitrile (Figure 8.4). The absence of this signal in the case of TiO₂ is evidence of an efficient injection from the excited states of the dye. The lower panel shows the resulting time-wavelength plots under 400 nm excitation. The plots are normalized to 1 at the maximum of the fluorescence (~570 nm).

Although a Raman reference is lacking in these cases, the kinetic behaviour of the fluorescence on TiO₂ and Al₂O₃ is identical to the solution samples, as can be seen in Figure 8.7 from the normalized kinetic traces and from the time gated spectra. We also performed a global analysis of the 2D plots of Figure 8.6, and the results are also shown in Figure G.5. Just as for the water solvent, two components are recovered with comparable time scales, indicating that the kinetic behaviour is identical in solutions and on the two substrates. In particular, the evolution of the kinetic traces as a function of detection wavelength is very similar in all three cases, pointing to the fact that the “cold” fluorescence is basically unaffected by the presence of an injecting substrate such as TiO₂. Assuming the hypothesis that the injection proceeds from non-thermalized states and given the time resolution of our experiment, it is not surprising that the time profiles are similar in solution, on an injecting substrate and on a non-injecting one. The only criterion that could identify the effect of injection under these circumstances is the intensity of the fluorescence at $t = 0$ in the different media, since it would affect the population of remaining molecules that emit. Comparing intensities is however impossible due to differences in the number and geometry of adsorbed molecules, and in the absorption and scattering properties of the two substrates.

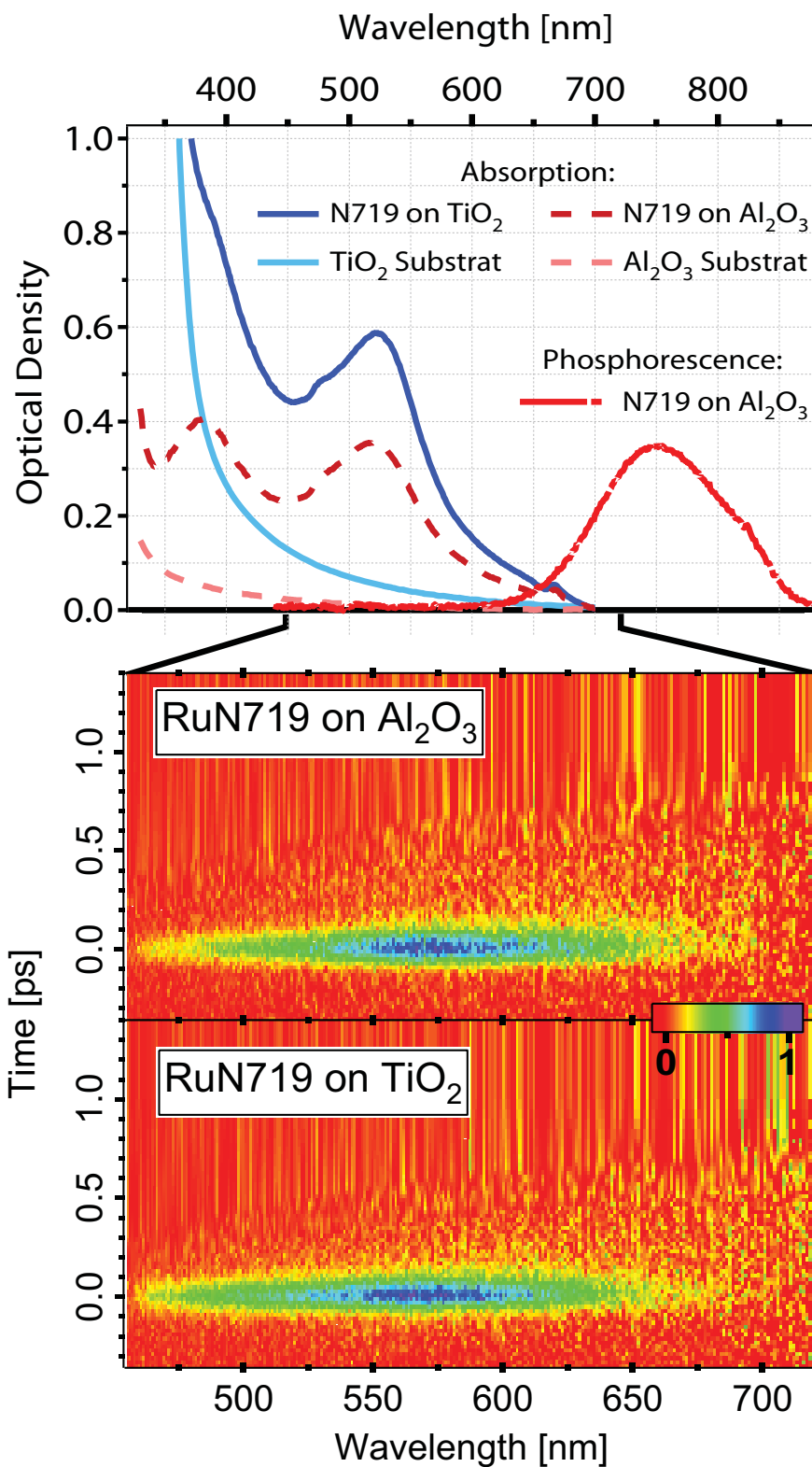


Figure 8.6: Upper panel shows the steady-state absorption of the RuN719 dye adsorbed on TiO₂ (blue line) and on Al₂O₃ (red dashed line) along with their substrate alone (corresponding light color). Lower panels: 2D time-wavelength plots of the emission of RuN719 adsorbed on mesoporous TiO₂ and Al₂O₃ under 400 nm excitation.

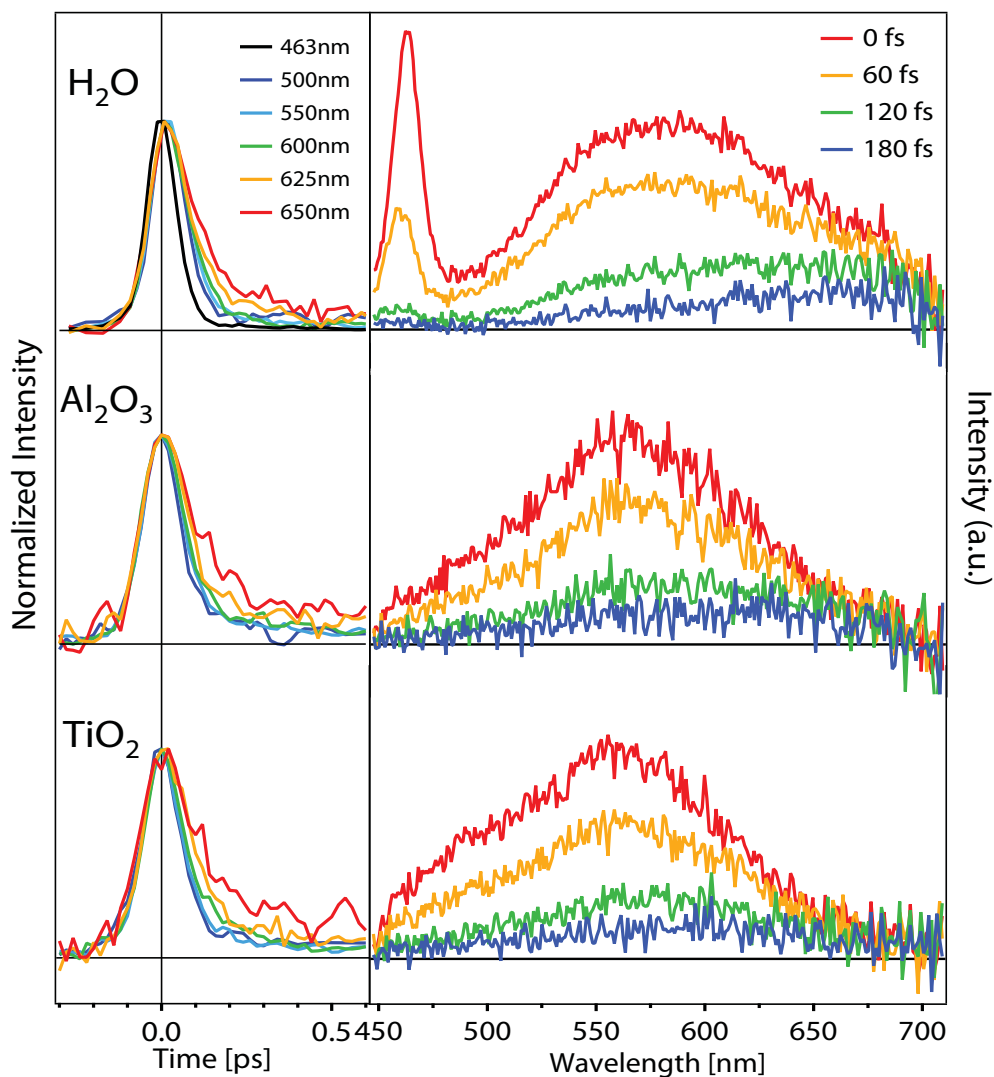


Figure 8.7. Representative kinetic traces and spectra from emission time-wavelength plot of RuN719 in water at pH5.4 and adsorbed on Al_2O_3 and TiO_2 . For a better comparison of the kinetic behavior, the time traces are normalized to the maximum.

8.2.2 Electron injection process

The results of Figures 8.1-3 clearly show that the singlet emission bands of both $[\text{Ru}(\text{bpy})_3]^{2+}$ and $[\text{Fe}(\text{bpy})_3]^{2+}$ stem from a vibrationally cold state, as far as the high frequency Franck-Condon modes are concerned. Since the time-zero emission spectra exhibit mirror image symmetry with respect to the absorption band and show no solvent dependence, we can exclude solvation dynamics as being responsible for this behaviour. That the Stokes shift occurs on such an ultrashort time scale, which we estimate to ≤ 10 fs for $[\text{M}(\text{bpy})_3]^{2+}$, is quite remarkable given the large amount of energy it represents, and the fact that we are dealing with sub-vibrational time scales, since the highest frequency

optically coupled (FC) mode has a period of ~ 20 fs (1607 cm^{-1}). As a matter of fact, if the system is thought of as a classical damped oscillator, the 10 fs decay time would be associated to a damping ratio as high as ~ 0.2 , corresponding to $\sim 90\%$ energy loss within the first oscillation.

As already discussed, this time zero Stokes shift is due to IC and IVR processes causing an ultrafast departure from the initially excited vibronic level(s). This occurs in the same fashion in Fe- and Ru-complexes and, for the latter, it is influenced neither by the ligands, nor by the solvent. Furthermore, such a behaviour appears to be quite general, since it is not only observed for metal complexes,³⁹⁵ but also for organic dyes (see chapter 4).^{193,127} As mentioned above, the excess energy is redistributed in lower frequency modes that are optically silent.

These observations have a direct incidence on the functioning of the DSSCs. In this respect, the important result here is the invariance of the $^1\text{MLCT}$ decay for RuN719 in solution and on TiO_2 and Al_2O_3 substrates. This confirms that injection in TiO_2 occurs efficiently from the initially excited level(s), prior to IVR/IC, but is then significantly slowed down when the system is in the cold $^1\text{MLCT}$. A particularly strong evidence for this is the presence of the 120-190 fs component in all three environments (Figure G.5). Furthermore, injection from the $^3\text{MLCT}$ state occurs on even longer time scales.³⁹⁶ There is therefore a dramatic drop of injection rate by almost one order of magnitude over ~ 0.85 eV corresponding to the energy difference between the initial excitation and the singlet fluorescence. An additional drop of injection rate occurs in the triplet state,³⁹⁶ which corresponds to a further decrease in energy by ~ 0.65 eV, if we refer to the case of RuN719. Along with the dye electronic and molecular structure and the way it is adsorbed onto the substrate, which determine the electronic coupling,³⁹⁷ a key parameter that influences the injection efficiency is the relative position of the dye excited state(s) relative to the bottom of the conduction band of the TiO_2 substrate. This formally determines the driving force for the excited state electron injection into the manifold of the unoccupied states of the substrate.

8.3 Conclusion

Several theoretical studies have been reported aimed at rationalizing the electron injection mechanism and its timescale, mostly focussing on organic dyes adsorbed on TiO₂.³⁹⁷⁻⁴⁰¹ Recent DFT/TDDFT studies of RuN719 on TiO₂^{401,402} reported the density of states (DOS) of the bare and loaded substrate. They predict an ultrafast, almost instantaneous electron injection component on the basis of the strong coupling and of the matching of the visible absorption spectrum and density of TiO₂ unoccupied states. Quite surprisingly, despite this almost direct injection mechanism, the absorption profile of the adsorbed dye is almost identical to that in solution, even though the underlying excited states have a drastically different nature. This work also concluded that there is no lower limit to the injection time except the electron dephasing times in the semiconductor, which are typically < 10 fs. These calculations, however, did not consider structural changes upon excitation of the MLCT states,⁴⁰³ although these should occur on a longer time scale due to nuclear inertia. Our results introduce IC and IVR as intramolecular processes that compete with the injection. Since IC and IVR occur on a sub-10 fs time scale, this implies that the injection from non-thermalized levels is competing with them and it should therefore also occur on a < 10 fs time scale, which is significantly shorter than the upper limit (50 fs) derived by Sundström and co-workers.²⁹¹ Although this is an extremely short injection time it is nevertheless in agreement with the above simulations of a delocalized adsorbate/substrate excited state.⁴⁰¹ It also agrees with the following experimental results obtained with different dyes on SC substrates and with different techniques: a) Huber *et al.* investigated alizarin anchored at the surface of TiO₂ and ZrO₂ semiconductor colloids in solution, using transient absorption spectroscopy with 20 fs time resolution. For the alizarin/TiO₂ system, a very fast electron injection from the photoexcited dye to the conduction band of TiO₂ was found to occur in 6 fs, which was not observed for non-injecting alizarin/ZrO₂ system,^{404,405} b) Schnadt *et al.*⁴⁰⁶ identified electron injection from RuN3 adsorbed onto TiO₂ by comparing the resonant photoemission (RPE) spectrum with the X-ray absorption spectrum at the K-edge of nitrogen. Deviations appeared between them as a disappearance of the LUMO+1 and LUMO+2 bands in the RPE spectrum, while no such effect was observed on the LUMO band, the latter lies below the conduction band of TiO₂ while the former lies within it. In the presence of the core hole an electron residing in the LUMO can therefore not be transferred into the substrate, while for an electron in the LUMO+1 and

LUMO+2 a transfer is energetically feasible. Based on the N K-edge core hole lifetime, the authors estimated the time scale for electron injection into the substrate to < 3 fs.

The one order of magnitude drop in injection rate from the initially excited levels to the $^1\text{MLCT}$ lowest emitting level that is inferred from our measurements can be accounted for by the DOS of RuN719 on TiO_2 reported by De Angelis *et al.*⁴⁰¹ However, the further drop as the system ends up in the $^3\text{MLCT}$ state is not reflected in the DOS and is probably due to the adsorption geometry and/or the spin of the excited state.

Figure 8.8 summarizes our conclusions. The initially excited level(s) undergo(es) competing electron injection and IC/IVR processes on similar timescales of < 10 fs. Once the system reaches the emitting $^1\text{MLCT}$ state, has the injection rate dropped by more than an order of magnitude as witnessed by the presence of a > 150 fs fluorescence component. In the $^3\text{MLCT}$ state, the injection time further extends to several picoseconds.^{396,407} If the first two steps can be accounted for by the energy variation of the DOS, the last drop is due to factors such as adsorption geometry and nature of the electronic state. These observations are of importance for optimizing the performance of DSSCs.

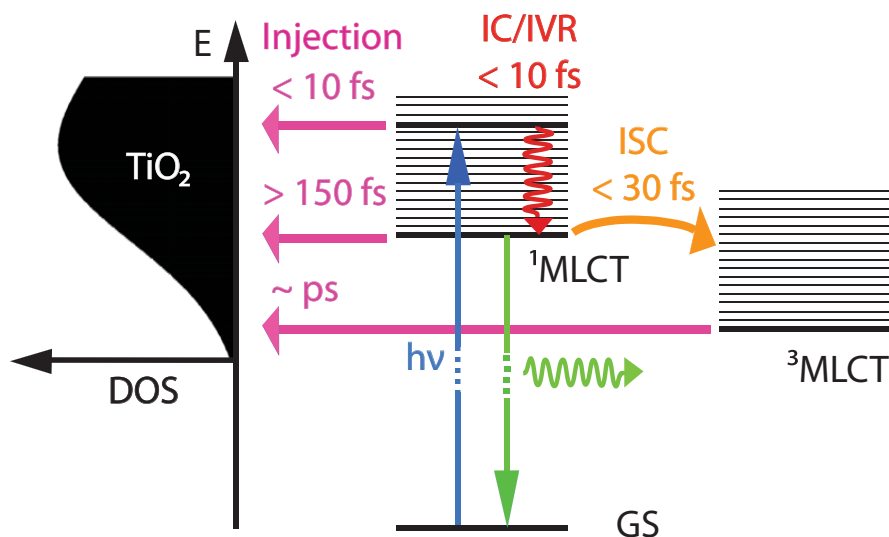


Figure 8.8: Schematic representation of the photophysical processes occurring in RuN719 adsorbed on TiO_2 , revealed in the present study. Note the dramatic dependence of the electron injection rate on the relative position of the dye excited state with respect to the density of states (DOS) of the conduction band of TiO_2 .

Chapter 9

Conclusions and perspectives

Polychromatic femtosecond-resolved fluorescence spectroscopy was applied to the study of intra- and intermolecular dynamics in different molecular systems, whose relevance spans from biomolecules (as Trp and haem in haemoproteins) to artificial photodevices (as RuN719 in dye-sensitized solar cells). These results clarified with an unmatched detail the earliest electronic excited state dynamics in all the investigated chromophores, providing a definitive picture of the respective energetics.

The experimental and simulation studies of aqueous Tryptophan allowed us to investigate the role of solvation, internal conversion and vibrational cooling in the relaxation dynamics of this amino acid. The results clearly evidence the distinction between the electronic and vibrational relaxation processes. While the time-resolved anisotropy exhibits a signature of an ${}^1L_b \rightarrow {}^1L_a$ IC in 45 ± 15 fs, the MD simulations confirm the biphasic water relaxation with 160 fs and 1 ps exponential components, respectively attributed to collective motions and independent diffusion of several proximal water molecules. In addition, we confirm the occurrence of a large (~ 1700 cm^{-1}) sub-10 fs frequency shift over the total Stokes shift (3800 cm^{-1}), coming from the inertial motion of the water molecules, and associated to their independent rotational motion.

A transient fluorescence of an extensive series of porphyrins elucidates crucial aspects of the electronic and vibrational dynamics occurring in such an important class of chromophores and subsequently in the active site of haemoproteins.

In particular, results on Zn and free base porphyrins show the crucial role of structure on the overall relaxation pathway. While ZnTPP show an unusually long vibrational relaxation, even in the S_2 state, substitution of the Zn atom by protonation of 2 nitrogens as

well as change in the peripheral substituent (with OE) improve the interstate coupling. In parallel, the nature of the central metal atom remarkably changes the relaxation dynamics of the porphyrin. While the Zn (full d-shell) porphyrins show a long-lived fluorescence, the transition metal porphyrins see their relaxation pathway dramatically affected by the presence of efficient non-radiative channels, which are the empty *d*-orbitals. These channels correspond to a Ligand-to-Metal-Charge-Transfer, responsible for the ligand photodissociation in haemoproteins. The $S_1 \rightarrow d$ IC, likely occurring via the nitrogen-metal bond, is affected by the substituent. Indeed, while a conical intersection may occur in the case of TPPs, the potential energy surface of S_1 in OEPs is likely shifted, resulting in a barrier slowing down the IC. The electronic structure of the transition metal does not influence the IC rate.

The former study and the clarified relaxation scheme supply us with a solid base for the investigation of phototriggered relaxations in two representative haemoproteins: cytochrome c (Cyt c) and myoglobin (Mb).

In these systems the fluorescence dynamics observed contain contributions from the two previously investigated chromophores, Trp and haem groups. In both proteins we followed the Trp \rightarrow haem resonant energy transfer through the decay of Trp's fluorescence. In Mb, we separated the spectral contribution of each of the two Trp (W7 and W14), and observed the hydration relaxation dynamics of W7 (400 fs, 3 ps and > 50 ps), located at the surface of the protein. In Cyt c, a sub-picosecond energy transfer from the Trp to the haem, strongly dependent on the oxidation state of the latter, is revealed. Consequently, while in both case the emission spectrum shows an instantaneous Stokes shift close to that in bulk water indicating a rigid and polar environment, a different geometry (distance and relative orientation) of the Trp-haem pair in ferrous and ferric Cyt c is evidenced. This result is promising for prospective investigation of the structural changes occurring upon photodissociation. Indeed a perspective measurement would consist in carrying out the same femtosecond UV fluorescence measurement of Cyt c, but with a pre-excitation of the haem group by an additional 400 nm pulse. The change in fluorescence decay would then give information about the new Trp-haem geometry.

The fluorescence of the photo-excited haem group reveals a complex multi-channel electronic relaxation. The broad detection range as well as the excitation tunability of the

transient fluorescence and absorption allowed us to follow the different relaxation steps and to propose a model explaining the origin of the ligand photolysis in ferrous Cyt c. The photolysis is triggered by a charge transfer from the excited states of the porphyrin ring to the d_{z^2} antibonding orbital of the iron. This relaxation channel is < 40 fs from S_2 or from upper energy levels, but 100-150 fs from S_1 , this time constant strongly depending on the excess of vibrational energy. In the ferric form, the presence of the partially unoccupied d_{xy} orbital constitutes a faster decay channel, preventing the ligand from dissociating. This picture agrees with the previous study of transition metal porphyrins and with the results on metMb and hemin. Indeed, the latter systems are in the ferric state (Fe^{3+}) and show relaxation dynamics identical to those of ferricytochrome c. Nevertheless, to corroborate and generalize this model, it would be interesting to probe other haem-like systems with different oxidation states (Fe^{2+} , Fe^{3+}).

Last, the ultrafast fluorescence of the several metal-polypyridine complexes were investigated, in order to understand the features controlling the electron injection in DSSCs. The solution phase study shows a recurrent < 10 fs IVR mechanism in all compounds, and an almost inexistent role of solvation on the initial electronic relaxation mechanism, i.e. IC, IVR and ISC. When adsorbed on the substrate, our results revealed the important role of IC and IVR, as intramolecular processes that compete with the injection. Since IC and IVR occur on a sub-10 fs time scale, it implies that the injection from non-thermalized levels competes with them and should therefore also occur on a sub-fs time scale. Although this injection time is extremely short, it is nevertheless in agreement with several experimental and computational works.^{401,404-406} In particular, the density of state (DOS) of RuN719 on TiO_2 reported by De Angelis *et al.*⁴⁰¹ agrees with the one order of magnitude drop in injection rate from the initially excited levels to the 1MLCT lowest emitting level that is inferred from the presence of a > 150 fs fluorescence component. In the 3MLCT state, the injection time further extends to several picoseconds.^{396,407} If the first two steps can be accounted for by the energy variation of the DOS, the last drop is due to factors such as adsorption geometry and nature of the electronic state. These observations are of importance for optimizing the performance of DSSCs.

Appendix

A. Time-resolved spectral analysis

The intra- and intermolecular dynamics described in the previous sections are observed through the time- and frequency-resolved emission spectrum $I(\nu, t)$. Depending on the complexity of the dynamics observed, different analysis was performed. We describe here the two different approaches.

Moment analysis

In the case of emission stemming from one specific radiative transition, the information is contained in a unique spectral band. It is the case when only intermolecular interactions are affecting the early time-resolved emission, for instance after an instantaneous IVR. Therefore the intra-band dynamics have to be extracted from the temporal evolution of the band. This is possible through an analysis in terms of spectral moment: For each time step, the first three spectral moments of the emission spectrum are calculated:

$$M_0(t) = \sum_{\nu_1}^{\nu_2} I(\nu, t) \cdot d\nu \quad (\text{A.1})$$

$$M_1(t) = \frac{1}{M_0} \sum_{\nu_1}^{\nu_2} \nu \cdot I(\nu, t) \cdot d\nu \quad (\text{A.2})$$

$$M_2(t) = \frac{1}{M_0} \left[\sum_{\nu_1}^{\nu_2} \nu^2 \cdot I(\nu, t) \cdot d\nu \right] - M_1^2 \quad (\text{A.3})$$

where M_i is the i -th spectral moment. The zero order moment (M_0) corresponds to the frequency-integrated intensity, and the first (M_1) and second (M_2) order correspond respectively to the average spectral position and spectral variance. The uncertainty on the first spectral moment can be derived as follows, defining $m_1(t)$ as the non normalized first moment (numerator of eq.(A.2)):

$$m_1(t) = \sum_{i=0}^N \nu \cdot I_i(\nu, t) \cdot d\nu_i \quad (\text{A.4})$$

The uncertainty ΔI does not depend on time or frequency (position on the CCD camera)

$$\Delta M_0(t) = \sum_{i=0}^N \Delta I_i(\nu, t) \cdot d\nu_i = \frac{\langle \Delta I \rangle}{\sqrt{N}} \sum_{i=0}^N d\nu_i \quad (\text{A.5})$$

$$\Delta m_1(t) = \sum_{i=0}^N \nu \cdot \Delta I_i(\nu, t) \cdot d\nu_i = \frac{\langle \Delta I \rangle}{\sqrt{N}} \sum_{i=0}^N \nu \cdot d\nu_i \quad (\text{A.6})$$

Hence the final expression for the uncertainty on the first spectral moment:

$$\begin{aligned} \Delta M_1(t) &= \left| \frac{\partial M_1}{\partial m_1} \right| \cdot \Delta m_1 + \left| \frac{\partial M_1}{\partial M_0} \right| \cdot \Delta M_0 = \left| \frac{1}{M_0} \right| \cdot \Delta m_1 + \left| -\frac{m_1}{M_0^2} \right| \cdot \Delta M_0 \\ &= \frac{1}{M_0} \cdot \left(\frac{\langle \Delta I \rangle}{\sqrt{N}} \sum_{i=0}^N \nu \cdot d\nu_i + M_1 \cdot \frac{\langle \Delta I \rangle}{\sqrt{N}} \sum_{i=0}^N d\nu_i \right) \\ &= \frac{\langle \Delta I \rangle}{M_0(t) \cdot \sqrt{N}} \cdot \left(\sum_{i=0}^N \nu \cdot d\nu_i + M_1(t) \cdot \sum_{i=0}^N d\nu_i \right) \end{aligned} \quad (\text{A.7})$$

A similar reasoning gives the following expression for $\Delta M_2(t)$:

$$\Delta M_2(t) = \frac{\langle \Delta I \rangle}{M_0 \cdot \sqrt{N}} \cdot \left(\sum_{i=0}^N \nu^2 \cdot d\nu_i \right) + (M_2 + M_1^2) \frac{\Delta M_0}{M_0} + 2M_1 \Delta M_1 \quad (\text{A.8})$$

Kinetic analysis

The kinetic behaviour observed in the time-resolved emission reflects time evolution of concentrations, described by linear differential equations (rate equations). The solution of this first order kinetics is given by a linear combination of exponential decays (§1.1.4). Therefore, the basic fitting function used in the analysis of our data is an exponential multiplied by a step function $u(t_0, t)$ to simulate the impulsive excitation at time zero (t_0). Our experiment has an intrinsic time instrumental response function (*irf*, see §3.5.3) inherent to the gaussian temporal profile of the laser pulses. This *irf* is taken into account by convolution with a gaussian of width σ_{irf} . In the thesis, we hold the gaussian function has the following expression:

$$Gauss(\sigma, x_0, x) = A e^{-\left(\frac{x-x_0}{\sigma}\right)^2} \quad (\text{A.9})$$

One has to multiply σ by a factor of 1.6651 to obtain the full width at half maximum (*fwhm*). For sake of clarity, the obtained basic function is defined as:

$$\text{erfexp}(\sigma_{irf}, t_0, \tau, t) = \left(e^{\left(\frac{t}{\tau}\right)} \cdot u(t_0, t) \right) \odot e^{-\left(\frac{t-t_0}{\sigma_{irf}}\right)^2} \quad (\text{A.10})$$

This function is in fact the product of an error function with an exponential of time constant τ , hence its name *erfexp*. For instance, $M_0(t)$ and the emission intensity at a selected wavelength $I(\lambda_j, t)$ are fitted with a linear combination of *erfexp* functions:

$$M_0(t) = \sum_i M_0^i \cdot \text{erfexp}(\sigma_{irf}, t_0, \tau_i, t) \quad (\text{A.11})$$

$$I(\lambda_j, t) = \sum_i I_0^i(\lambda_j) \cdot \text{erfexp}(\sigma_{irf}, t_0, \tau_i, t) \quad (\text{A.12})$$

where M_0^i/I_0^i and τ_i are the amplitude and time constants of the i -th exponential contribution. On the other hand, $M_i(t)$ is no longer a simple linear combination, because of normalization by $M_0(t)$:

$$M_1(t) = \frac{\sum_i M_1^i \cdot \text{erfexp}(\sigma_{irf}, t_0, \tau_i, t)}{\text{erfexp}(\sigma_{irf}, t_0, \tau_{L_a}, t)} \quad (\text{A.13})$$

One should note that this fitting function is no longer a simple linear combination of exponential decays. On a timescale comparable with the *irf*, the *erfex* denominator makes the function to diverge from the multiexponential decay behaviour. The only free parameters involved in fit performed with this function are the different time constants and their associated amplitudes, the time zero and *irf* being characterized independently (for instance on the Raman of the solvent or on $M_0(t)$). Similar considerations on eq.(A.3) lead to the same function for the second spectral moment.

Spectral decomposition

In the case of contribution from more than one radiative transition to the total emission, the possible overlap of signals makes the analysis more difficult and a spectral decomposition of the data is needed. The goal of such decomposition is to extract the spectra associated with each time constant found by means of a global analysis (GA) of the data: the Decay Associated Spectra (DAS). This is possible by performing a global fitting of the data, with a fit function corresponding to a proposed kinetic model including all dynamics contained in the data.

This global fitting can be performed directly on the raw data, by selecting a set of kinetic traces $I(\lambda_j, t_k)$ from the 2 dimensional matrices. The DAS are reconstructed from the wavelength dependent pre-exponential factors $I_0^i(\lambda_j)$.

Before the global fitting analysis, it is possible to apply a mathematical treatment of the 2 dimensional data in order to separate the physically-relevant information from the statistical noise by means of Singular Value Decomposition (SVD). The data set $I(\lambda_j, t_k) = I_{jk}$ is a matrix of $J \times K$ dimension, that can be decomposed in a product of 3 matrices:

$$I = USV^T \quad (\text{A.14})$$

where U and V^T are orthogonal matrices of dimensions $J \times J$ and $K \times K$ composed of kinetic and spectral singular vectors, respectively. The diagonal matrix S is composed of the eigenvalues $s_n = S_{nn}$ ($S_{mn} = 0$ for $m \neq n$). The number of non zero eigenvalues N is the rank of the matrix I , and these eigenvalues constitute a weight associated to each spectral + kinetic basis component. In our case, the noise-free ideal data matrix would contain only few basis component –typically less than ten- compared to the rank of the real data. The remaining SVD components is due to the random noise. As a consequence, it is possible to reduce the rank of the data matrix to a number M , in order to get rid of the noise contribution. This is done by careful selection of the component with higher singular values. Figure A.1 shows the SVD of the time and frequency resolved fluorescence from ZnTPP in cyclohexane. This procedure does not provide any physical information, but reduces the amount of data necessary to perform the GA and in particular removes the undesired statistical noise.

The GA can then be performed on the new basis set of kinetic and spectral vectors. At this stage, two approaches may be use to analyze the data: the spectral shape or the kinetic model. It is indeed possible either to fit the spectra according to a specific model and to obtain the related kinetics, or to fit the kinetics with a global scenario and to extract the related spectra. A spectral analysis is difficult to perform since the shape of transient bands is hard to predict, especially if some bands show spectral changes as a function of time (shift, change of width, etc...). We rather use a kinetic approach, for which a physically relevant model is easier to establish. Again, the fitting function is a linear combination of *erfexp* functions:

$$\begin{cases} U_0(t) = \sum_i U_0^i \cdot \text{erfexp}(\sigma_{irf}, t_0, \tau_i, t) \\ \dots \\ U_M(t) = \sum_i U_M^i \cdot \text{erfexp}(\sigma_{irf}, t_0, \tau_i, t) \end{cases} \quad (\text{A.15})$$

Where $U_m(t)$ are the kinetic basis vectors and U_0^i and τ_i are the amplitude and time constants of the i -th exponential contribution. The related DAS are linear combinations of the spectral vectors:

$$\text{DAS}_{\tau_i}(\lambda) = \sum_m s_m \cdot U_m^i \cdot V_m \quad (\text{A.16})$$

One DAS represent the spectral contribution from all population of excited species decay with the same time constant τ_i , involved in the relaxation mechanism of the photo-excited molecule.

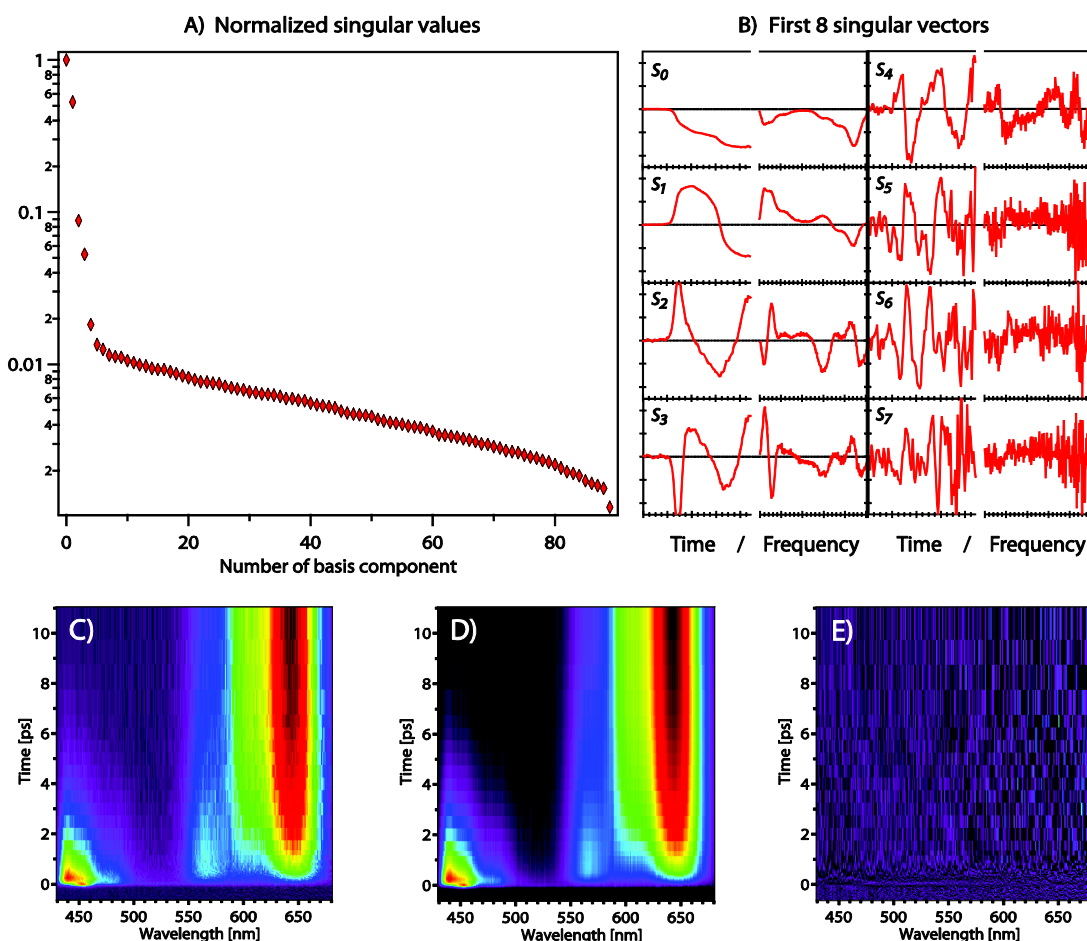


Figure A.1: Singular Value Decomposition of the time and frequency resolved emission from ZnTPP in cyclohexane (§...): A) normalized singular values, B) first 8 kinetic and spectral singular vectors, C) raw data matrix, D) matrix reconstructed from the first 5 singular vectors ($M = 5$), E) difference between raw and reconstructed matrix.

B. Fluorescence and vibrations calculation of UV dyes

Figure B.1: Energy- and time-resolved fluorescence from PPO in cyclohexane (top), ethanol (middle) and dimethylformamide (bottom). Experimental conditions are reported on the right.

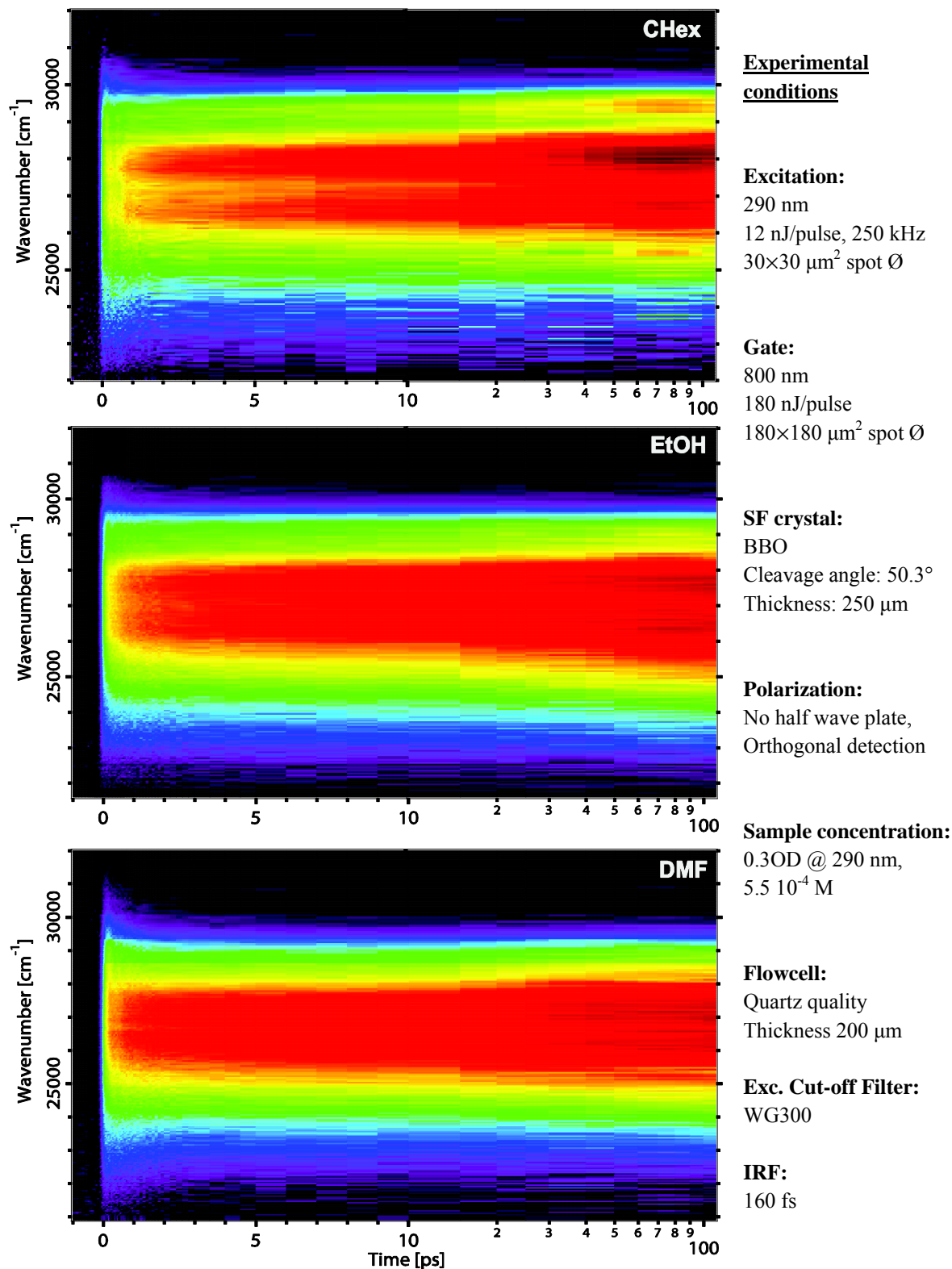


Figure B.2: Wavelength- and time-resolved fluorescence from pTP in cyclohexane (top), ethanol (middle) and dimethylformamide (bottom). Experimental conditions are reported on the right.

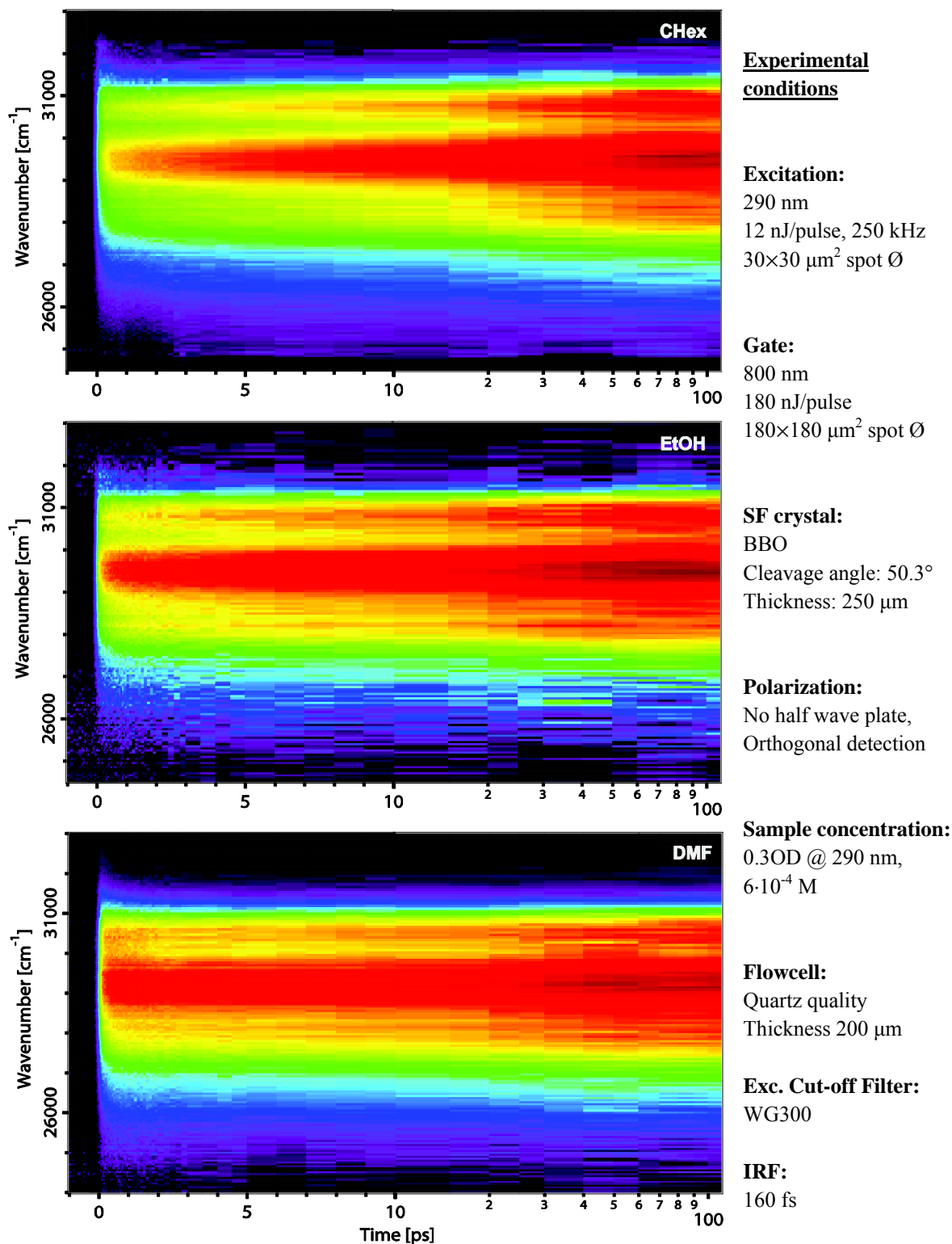
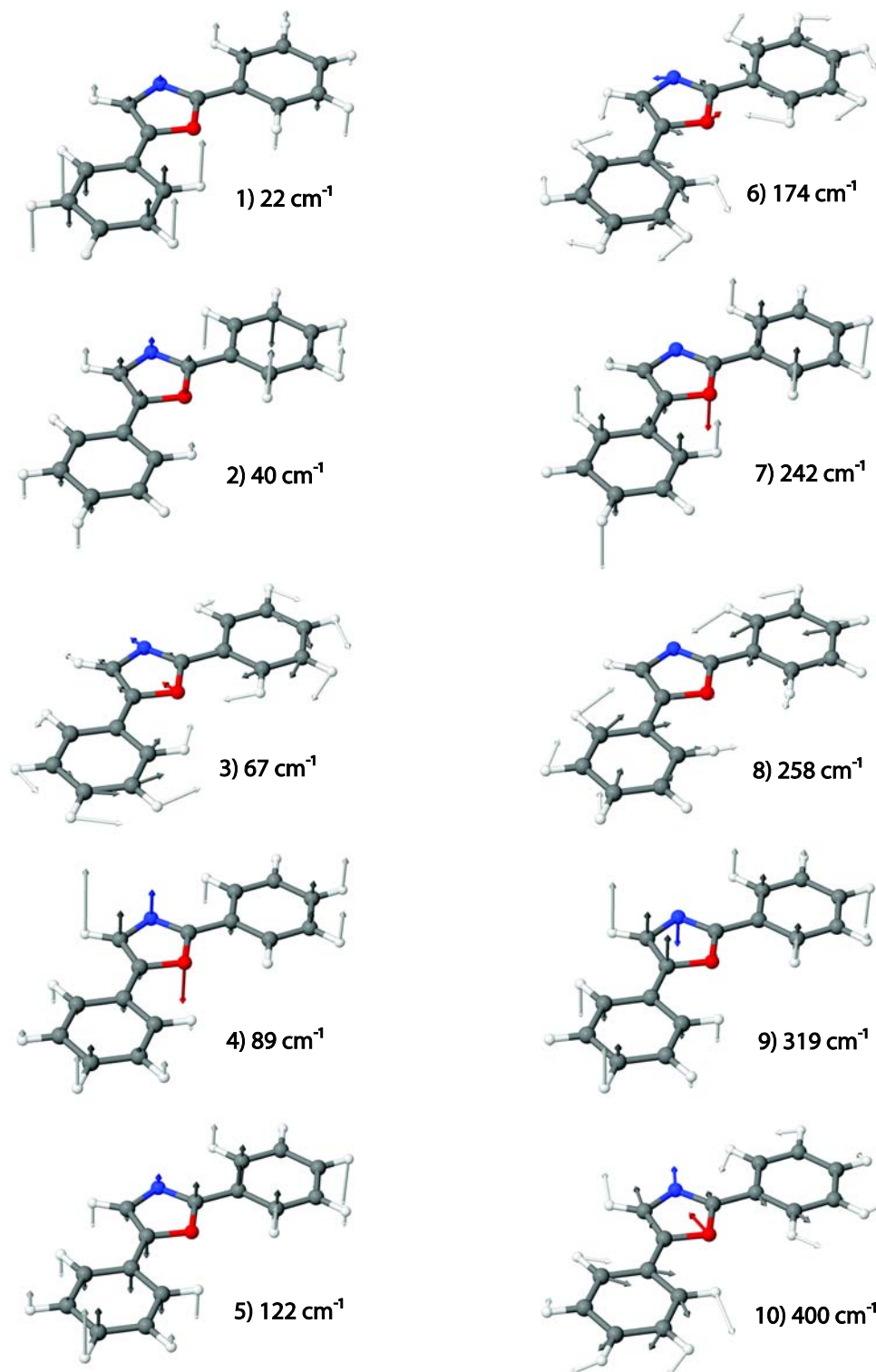


Table B.1: Calculated vibration frequencies [cm^{-1}] of 2,5-diphenyloxazole and paraterphenyl.

<i>2,5-diphenyloxazole (PPO)</i>			<i>Paraterphenyl (pTP)</i>		
22.197	938.7524	1539.4182	37.7187	860.5789	1345.4495
40.2357	954.2725	1582.3989	47.4843	861.0484	1355.5449
67.6381	965.8029	1619.732	69.4205	861.3511	1367.6649
89.4556	971.9922	1639.4616	87.9371	927.6518	1371.5828
122.0644	976.867	1643.289	122.7754	932.8443	1448.1141
173.5672	995.3387	1663.7843	139.0202	967.9381	1487.9403
241.6276	1001.6684	1666.3279	215.0135	969.658	1500.1635
257.5644	1016.0801	3185.0718	246.9088	971.4618	1535.0512
319.2458	1017.8459	3186.3794	297.1848	974.8939	1545.8631
400.0564	1052.3597	3192.6291	394.0119	994.9557	1570.6982
406.9497	1054.435	3196.4892	408.653	995.2094	1603.2985
410.7374	1088.8785	3202.698	416.1202	1016.3638	1635.7485
413.9902	1100.5253	3208.5221	420.6936	1016.8208	1639.8412
496.3827	1110.9995	3212.0968	422.1402	1022.3019	1660.7169
514.5934	1116.4951	3221.3173	424.9697	1027.6059	1662.3851
529.8725	1180.9504	3222.9266	526.6883	1054.0312	1669.5754
632.3677	1193.9611	3226.665	531.738	1068.2838	3180.4798
633.1824	1194.694	3276.598	584.7982	1076.2961	3180.6818
670.5191	1212.3933		625.1915	1113.1741	3185.6531
690.0808	1217.3336		631.7496	1113.6052	3187.3301
703.6642	1286.7216		634.3505	1151.9461	3187.6086
705.137	1324.5321		657.6552	1193.2208	3190.1498
717.1158	1329.3375		712.5691	1193.3584	3197.3372
725.0532	1347.6493		714.5254	1214.8069	3198.5421
777.857	1370.3619		715.091	1217.437	3201.6201
791.5841	1372.9701		739.8167	1229.9471	3203.9834
841.9122	1383.9495		772.1614	1306.4653	3206.1212
855.2303	1494.6534		787.7941	1314.256	3206.7577
863.2776	1495.7825		791.4184	1317.5643	3211.4557
923.3448	1529.9907		856.6086	1322.3169	3212.063

Figure B.3: Eigenvectors and frequencies of the first 8 calculated low frequency normal modes of PPO molecule showing distinctive distortions: 1) torsion, 2) torsion plus out-of-plane bending, 3) and 6) in plane bending, 4) torsion plus waving, 5) waving, 6) cycles rotations, 7) torsion plus waving, 8) phenyl-oxazole-phenyl in-plane bending.



C. Time-resolved anisotropy of Trp

Modelling the anisotropy decay of the ${}^1L_b \rightarrow {}^1L_a$ transition

We want here to find the expression of the parallel and orthogonal intensities observed and to deduce the final expression of the anisotropy decay, from the time dependent population of both states. Here we assume that for both 1L_a and 1L_b states, the transition dipole moment of excitation and emission are collinear. We will derive the time-resolved anisotropy equation with the following assumptions: I) at time zero, we excite a mixture of molecules in the 1L_a and 1L_b state; II) the formers will undergo only solvation dynamics and rotational diffusion while III) the latter will undergo an internal conversion to 1L_a state. In the laboratory coordinate, xyz system, we excite the sample with polarization in the z direction (figure 18). Defining $n_a(t)$ and $n_b(t)$ as the respective population of 1L_a and 1L_b states at time t, μ_a and μ_b as the respective emission transition dipole moment of 1L_a and 1L_b state, one can write the next equation, distinguishing for 1L_a the population parallel (\parallel) and orthogonal (\perp) to excitation polarization:

$$n_b(t) = n_b(0) \cdot e^{-t/\tau} \quad (\text{C.1})$$

$$n_a(t) = n_a^{\parallel} + n_a^{\perp}(t) = n_a^0 + n_a^{\perp}(t) = n_a^0 + n_b(0) - n_b(t) \quad (\text{C.2})$$

For simplicity, we will adopt for the next derivations the notation $n_a^{\parallel} = n_a^0$ and $n_a^{\perp}(t) = n_b(0) - n_b(t) = n_{ba}(t)$, n_a^0 being the population of 1L_a state excited at time zero and n_{ba} being the population of molecule in the 1L_a state initially in the 1L_b state. In this way, we consider three different populations:

$$\begin{aligned} n_a &= n_a^{\parallel}(t) \\ n_b(t) &= n_b^0 \cdot e^{-t/\tau} \\ n_{ba}(t) &= n_a^{\perp}(t) = n_b^0 - n_b(t) \end{aligned} \quad (\text{C.3})$$

We have now to derive the time dependent electric dipole moments of each population, in a way to obtain their contribution to the parallel and orthogonal intensities.

The transition dipole moment of 1L_a and 1L_b states are known to be almost orthogonal and of different amplitude. We can write $\mu_b = \alpha \cdot \mu_a$ for the amplitude relation. Although α is expected to be around 0.5, we will keep this general notation. During the transition, since the angle between the two transition dipole is close to 90° , the dipole moments μ_a stemming from the 1L_b state converted to orthogonal 1L_a state, are spread over 2π in the

plane perpendicular to the xy plane. We have thus to integrate all around this angle to obtain the perpendicular intensities:

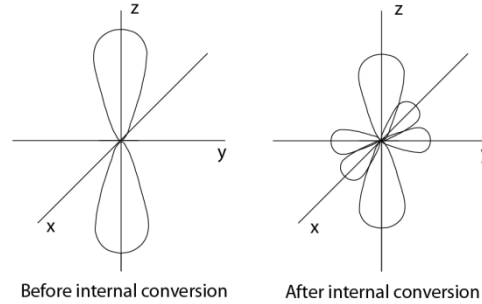


Figure 18 Distribution of excited chromophores just after excitation, and after internal conversion (decomposed in x and y contribution)

Assuming a transition dipole μ with a parallel component (i.e. along z) μ_{\parallel} and an orthogonal one, μ_{\perp} , which is uniformly distributed on the xy plane (i.e. $\langle \mu_x^2 \rangle = \langle \mu_y^2 \rangle = \frac{1}{2} \mu_{\perp}^2$), we have

$$\mu_{\parallel} \Rightarrow \bar{I}(\mu_{\parallel}) = \left[\left(\frac{1}{5} \mu_{\parallel}^2 \right)_x ; \left(\frac{1}{5} \mu_{\parallel}^2 \right)_y ; \left(\frac{3}{5} \mu_{\parallel}^2 \right)_z \right] \quad (\text{C.4})$$

$$\mu_{\perp} \Rightarrow (\mu_x; \mu_y) \Rightarrow \begin{cases} \mu_x \Rightarrow \bar{I}(\mu_x) = \left[\left(\frac{3}{10} \mu_{\perp}^2 \right)_x ; \left(\frac{1}{10} \mu_{\perp}^2 \right)_y ; \left(\frac{1}{10} \mu_{\perp}^2 \right)_z \right] \\ \mu_y \Rightarrow \bar{I}(\mu_y) = \left[\left(\frac{1}{10} \mu_{\perp}^2 \right)_x ; \left(\frac{3}{10} \mu_{\perp}^2 \right)_y ; \left(\frac{1}{10} \mu_{\perp}^2 \right)_z \right] \end{cases} \quad (\text{C.5})$$

$$I_{\parallel} = I_z = I(\mu_{\parallel})_z + I(\mu_x)_z + I(\mu_y)_z \quad I_{\perp} = I_x (= I_y) = I(\mu_{\parallel})_x + I(\mu_x)_x + I(\mu_y)_x \quad (\text{C.6})$$

This generalized set of equation for the detected intensities is derived from the well known integration of a dipole moment distribution after excitation. With the following detection scheme: z axis = parallel axis; x axis = orthogonal axis,

$$I_z = \frac{3}{5} \mu_{\parallel}^2 + \frac{1}{5} \mu_{\perp}^2 \quad I_x = \frac{1}{5} \mu_{\parallel}^2 + \frac{2}{5} \mu_{\perp}^2 \quad (\text{C.7})$$

This is true for one dipole only¹. Since the emission signal is incoherent, in the case of an ensemble of identical dipoles the overall signal is just proportional to the number of dipole, so:

$$I_z = \left(\frac{3}{5} \mu_{\parallel}^2 + \frac{1}{5} \mu_{\perp}^2 \right) \cdot n \quad I_x = \left(\frac{1}{5} \mu_{\parallel}^2 + \frac{2}{5} \mu_{\perp}^2 \right) \cdot n \quad (\text{C.8})$$

If different dipoles (or dynamics) coexist we have just to add a contribution for each family:

$$\begin{aligned} I_z &= \left(\frac{3}{5} \mu_{\parallel a}^2 + \frac{1}{5} \mu_{\perp a}^2 \right) \cdot n_a + \left(\frac{3}{5} \mu_{\parallel b}^2 + \frac{1}{5} \mu_{\perp b}^2 \right) \cdot n_b + \dots \\ I_x &= \left(\frac{1}{5} \mu_{\parallel a}^2 + \frac{2}{5} \mu_{\perp a}^2 \right) \cdot n_a + \left(\frac{1}{5} \mu_{\parallel b}^2 + \frac{2}{5} \mu_{\perp b}^2 \right) \cdot n_b + \dots \end{aligned} \quad (\text{C.9})$$

In the case of Trp we have two kinds of dipoles, the L_a - and L_b -transition related ones, from now on a - and b -type. For more clarity again, we will consider the molecules in the 1L_a state converted from the 1L_b state as own population n_{ba} of dipoles μ_{ba} . In the following we assumed: $\mu_a = \mu_{ba} = \mu_b / \alpha = \mu$,

The a -family gives:

$$\begin{cases} \mu_{\parallel}^2 = n_a \mu^2 \\ \mu_{\perp}^2 = 0 \cdot \mu^2 \end{cases} \Rightarrow \begin{cases} I_z^a = \frac{3}{5} n_a \mu^2 \\ I_x^a = \frac{1}{5} n_a \mu^2 \end{cases} \quad (\text{C.10})$$

where we assume no interconversion between μ_{\parallel} and μ_{\perp} (i.e. nether rotational diffusion nor intramolecular relaxations) even if, in principle n_a could be time dependent.

Concerning the b -type we have:

$$\begin{cases} \mu_{\parallel}^2 = n_b (\alpha \cdot \mu)^2 \\ \mu_{\perp}^2 = 0 \cdot \mu^2 \end{cases} \Rightarrow \begin{cases} I_z^b = \frac{3}{5} \alpha^2 n_b \mu^2 \\ I_x^b = \frac{1}{5} \alpha^2 n_b \mu^2 \end{cases} \quad (\text{C.11})$$

¹ For an excitation along the z axis, the intensities observed corresponding to one dipole in the z direction are $I_{/z} = 3/5$, $I_{\perp x} = 1/5$, $I_{\perp y} = 1/5$.

And finally the ba -type we have:

$$\begin{cases} \mu_{\parallel}^2 = 0 \cdot \mu^2 \\ \mu_{\perp}^2 = (n_b^0 - n_b) \cdot \mu^2 \end{cases} \Rightarrow \begin{cases} I_z^{ba} = \frac{1}{5} (n_b^0 - n_b) \mu^2 \\ I_x^{ba} = \frac{2}{5} (n_b^0 - n_b) \mu^2 \end{cases} \quad (\text{C.12})$$

So the overall signal is:

$$\begin{cases} I_z = I_z^a + I_z^b + I_z^{ba} = \left[3n_a + n_b^0 + (3\alpha^2 - 1)n_b \right] \frac{\mu^2}{5} \\ I_x = I_x^a + I_x^b + I_x^{ba} = \left[n_a + 2n_b^0 + (\alpha^2 - 2)n_b \right] \frac{\mu^2}{5} \end{cases} \Rightarrow r = \frac{2n_a - n_b^0 + (2\alpha^2 + 1)n_b}{5[n_a + n_b^0 + (\alpha^2 - 1)n_b]} \quad (\text{C.13})$$

At $t = 0$ ($n_b(0) = n_b^0$) we obtain indeed $r = 0.4$. This is a quite general expression, where no assumption is done about the ratio of excited molecules (n_a^0 and n_b^0 are free) and about the change of the dipole intensity after the internal conversion (α).

We can extract from this some direct observables. First the anisotropy at time zero does not of course depend on the state population and has the expected value of $2/5$. The amplitude of the anisotropy decay is governed by the population ratio:

$$r_{\infty} = \frac{2n_a^0 - n_b^0}{5(n_a^0 + n_b^0)} = \frac{2}{5} \frac{n_a^0}{n} - \frac{1}{5} \frac{n_b^0}{n} = \frac{2}{5} N_a - \frac{1}{5} N_b \quad (\text{C.14})$$

Where $n = n_a^0 + n_b^0$ the total amount of excited molecules, and $N_a = \frac{n_a^0}{n}$, $N_b = \frac{n_b^0}{n}$ the proportion of initial 1L_a and 1L_b population.

Since in our case, according to figure 4 and 5, we excite approximately 50% - 50% (i.e. $n_a^0 = n_b^0 = n_0$), and that $n_a(t)$ is a step function ($n_a(t > 0) = n_a(0) = n_0$) and $n_b(t) = n_0 e^{-t/\tau}$, we have:

$$\begin{cases} I_z = \frac{n_0 \mu^2}{5} [4 + (3\alpha^2 - 1)e^{-t/\tau}] \\ I_x = \frac{n_0 \mu^2}{5} [3 + (\alpha^2 - 2)e^{-t/\tau}] \end{cases} \Rightarrow r = \frac{1 + (2\alpha^2 + 1)e^{-t/\tau}}{5[2 + (\alpha^2 - 1)e^{-t/\tau}]} \quad (\text{C.15})$$

We can keep now in mind the more general expression of the anisotropy:

$$r(t) = \frac{I_{\parallel}(t) - I_{\perp}(t)}{I_{\parallel}(t) + 2 \cdot I_{\perp}(t)} = \frac{2n_a^0 - n_b^0 + (2\alpha^2 + 1)n_b^0 \cdot e^{-t/\tau}}{5[n_a^0 + n_b^0 + (\alpha^2 - 1)n_b^0 \cdot e^{-t/\tau}]} \quad (\text{C.16})$$

We can remark that the parameter α governs the temporal behavior of the decay. In the particular case where $\alpha = 1$, meaning that $\mu_a = \mu_b$, the anisotropy decay is exactly monoexponential, a deviation from this value induces a deviation from the monoexponential behavior, r being a ratio of two different exponential function. This fact may also be observed in the individual intensities (I_{\parallel} and I_{\perp} from eq. C.15) where in the particular case of $\alpha = \sqrt{2}$, all the transition is observed in the parallel component and no contribution is seen in the orthogonal one. On the contrary, in the other particular case where $\alpha = 1/\sqrt{3}$, only the orthogonal component exhibits a temporal feature and not the parallel one. In our case, we will give α the value of 0.455, calculated from values given in ref¹⁶⁶.

Introducing rotational diffusion

We would like now to add the rotational diffusion contribution to the final expressions of parallel and orthogonal intensities. In this way, we could perform a global fit of the data, and extract all the values in a correct way. To add this contribution, we have to take into account the rotation of the dipole moments. The rotational Brownian is described by the next diffusion equation:

$$dW(\theta, \varphi, t) / dt = D_{rot} \nabla^2 W(\theta, \varphi, t) \quad (\text{C.17})$$

Where the rotational diffusion coefficient D_{rot} is related to the viscosity of the solvent, the Van der Waals volume of the solute and the temperature through the relation: $D_{rot} = kT / 6V\eta$. First, regardless this specific distribution, we calculate the intensities resulting from a rotation of the angle θ with respect to the initial geometry: For the

contribution of one population i of dipole moments, we have the intensity $d_\theta I_z^i$, at the angle θ (eq. C.8):

$$\begin{aligned} d_\theta I_z^i &= \left(\frac{3}{5} \mu_i^2 \cos^2 \theta + \frac{1}{5} \mu_i^2 (1 - \cos^2 \theta) \right) \cdot dn_\theta^i \\ d_\theta I_x^i &= \left(\frac{1}{5} \mu_i^2 \cos^2 \theta + \frac{2}{5} \mu_i^2 (1 - \cos^2 \theta) \right) \cdot dn_\theta^i \end{aligned} \quad (\text{C.18})$$

With $dn_\theta^i = n_i \cdot W(\theta, t) \cdot \sin \theta \cdot d\theta$, the intensities integrated along θ are:

$$\begin{aligned} I_z^i &= \int_0^{\pi/2} d_\theta I_z^i = \left(\frac{\mu_i^2}{5} \right) \cdot (1 + 2 \langle \cos^2 \theta \rangle_i) \cdot n_i \\ I_x^i &= \int_0^{\pi/2} d_\theta I_x^i = \left(\frac{\mu_i^2}{5} \right) \cdot (2 - \langle \cos^2 \theta \rangle_i) \cdot n_i \end{aligned} \quad (\text{C.19})$$

Introducing the new intensities I_z^a , I_x^a , I_z^b , I_x^b , I_z^{ba} , I_x^{ba} , with the terms $\langle \cos^2 \theta \rangle_i$ decaying exponentially, we finally have:

$$\begin{cases} I_z = \left(\frac{\mu^2}{5} \right) \left[\left(n_a + \alpha^2 n_b(t) \right) \cdot \left(\frac{5}{3} + \frac{4}{3} e^{-\frac{t}{\tau_{rot}}} \right) + n_{ba}(t) \cdot \left(\frac{5}{3} - \frac{2}{3} e^{-\frac{t}{\tau_{rot}}} \right) \right] \\ I_x = \left(\frac{\mu^2}{5} \right) \left[\left(n_a + \alpha^2 n_b(t) \right) \cdot \left(\frac{5}{3} - \frac{2}{3} e^{-\frac{t}{\tau_{rot}}} \right) + n_{ba}(t) \cdot \left(\frac{5}{3} + \frac{1}{3} e^{-\frac{t}{\tau_{rot}}} \right) \right] \end{cases} \quad (\text{C.20})$$

$$\Rightarrow r = \frac{2 \left(n_a + \alpha^2 n_b(t) \right) - n_{ba}(t)}{5 \left[n_a + \alpha^2 n_b(t) + n_{ba}(t) \right]} \cdot e^{-\frac{t}{\tau_{rot}}} \quad (\text{C.21})$$

These three relations describe the general fluorescence anisotropy signal due to emission from two states with transition dipole $\mu_a = \mu_b / \alpha$ perpendicular to each other where one interconvert into the other, together with an isotropic rotational diffusion. These are the set of equation we will use to analyze the experimental data reported in the previous section.

D. Fluorescence and Molecular Dynamics simulation of Trp in water.

Figure D.1: Wavelength- and time-resolved fluorescence from aqueous Trp (top), integrated area (bottom).

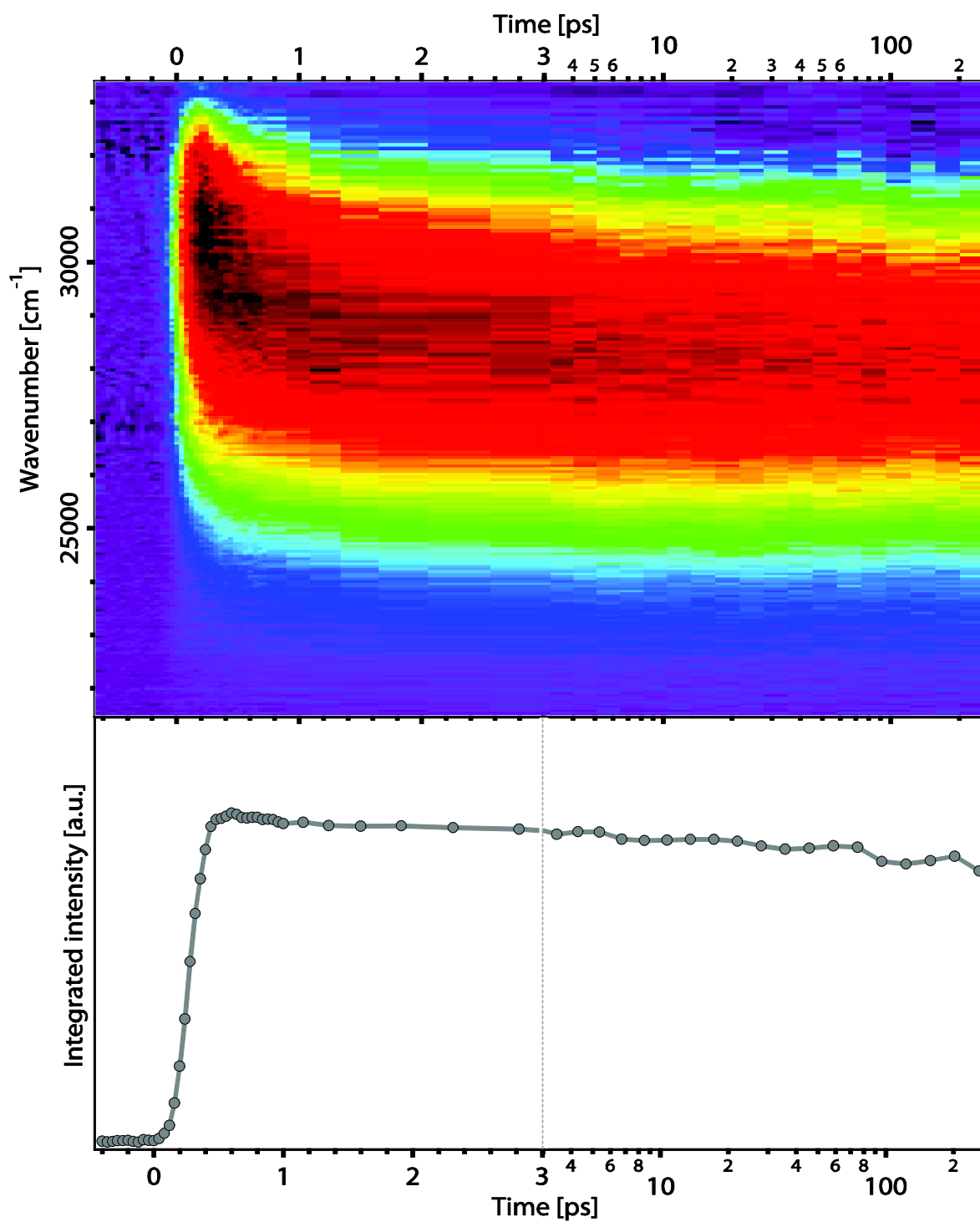


Figure D.2: Time-dependent emission spectra of the 1L_b and 1L_a states of Trp obtained from non-equilibrium MD simulations along with the computed first moment (solid pink line).

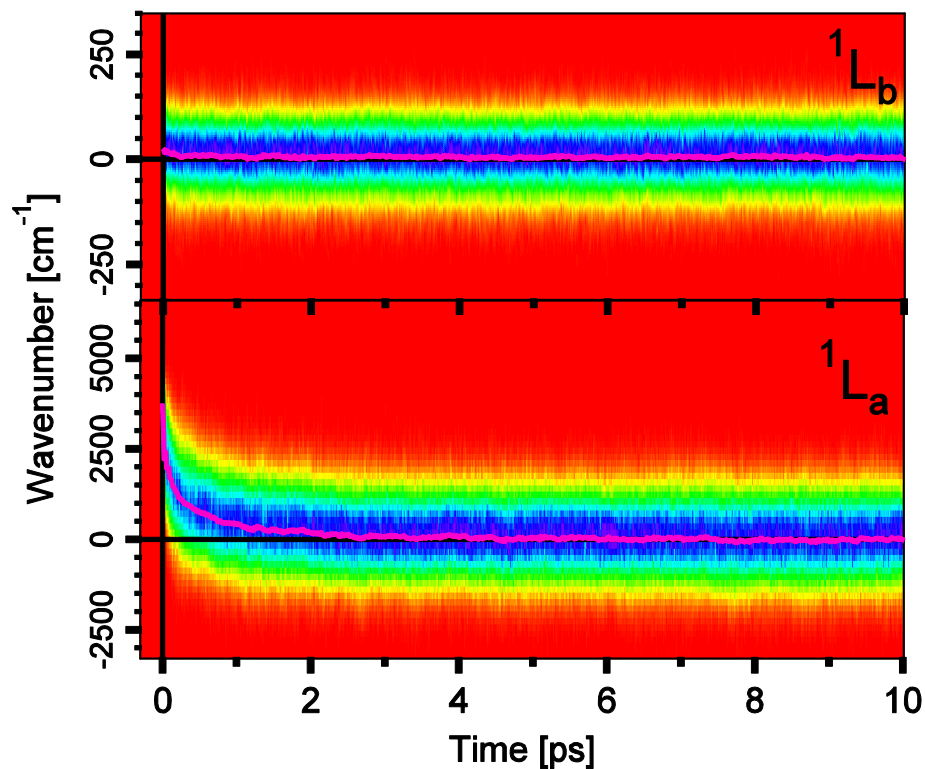
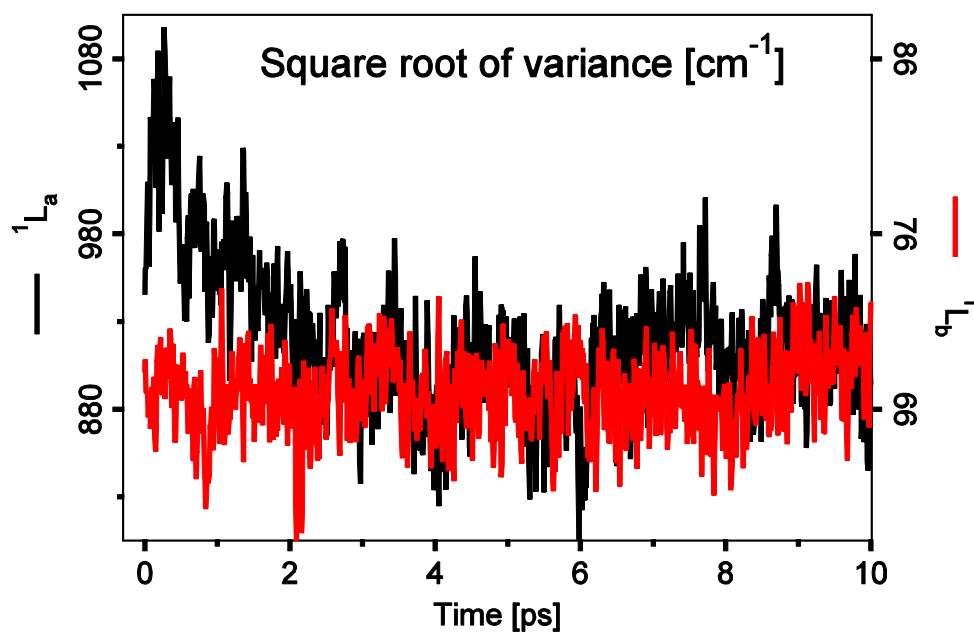


Figure D.3: Square root of the variance of the 1L_b (red) and 1L_a (black) emission band from Figure S2.



E. Transient fluorescence of Transition metal porphyrins.

Figure E.1: Wavelength- and time-resolved fluorescence of Ru, Cu, Ni and Co TPP and OEP in cyclohexane impulsively excited at 400 nm. The peaks at ~ 450 nm are Raman signal from cyclohexane.

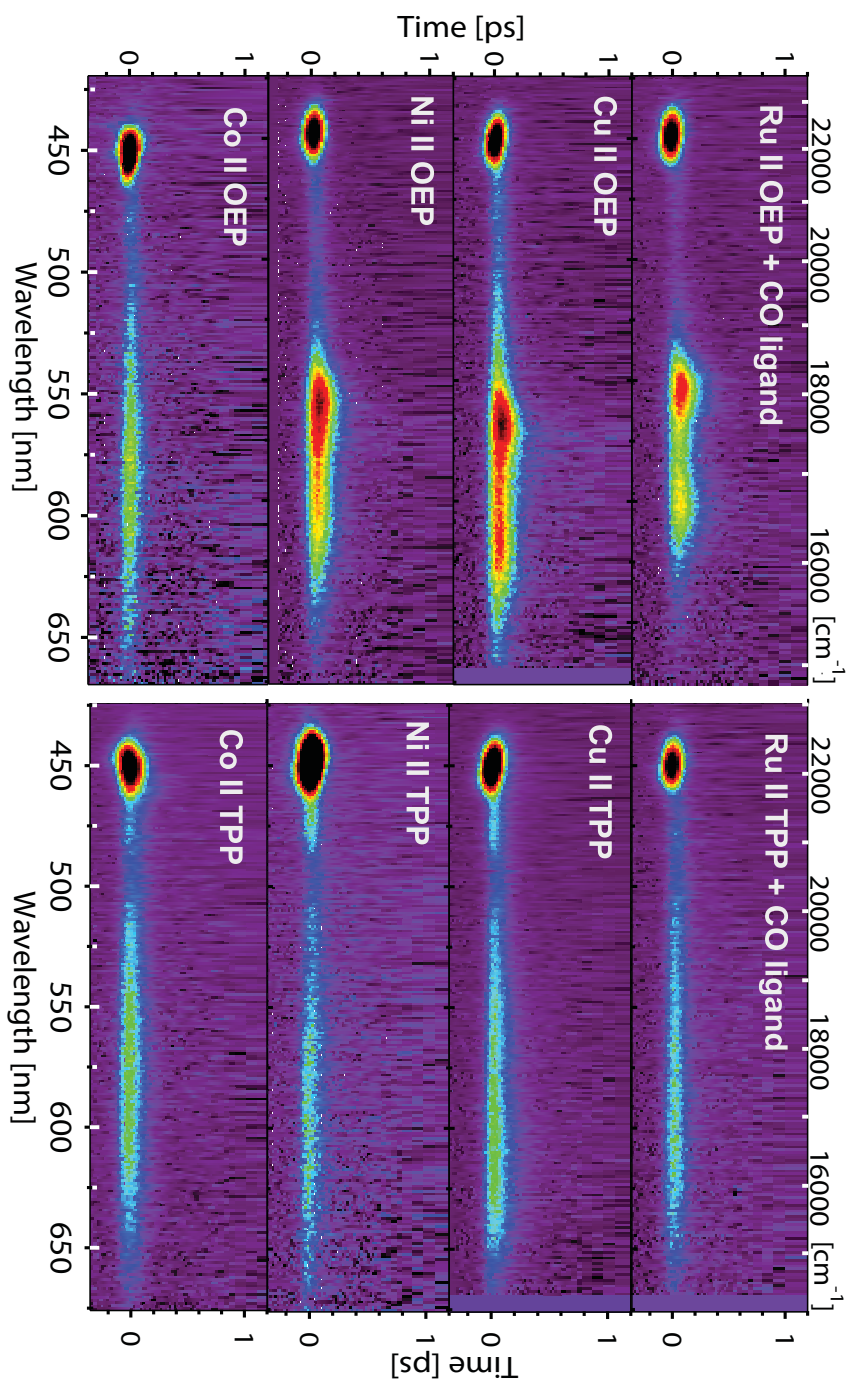
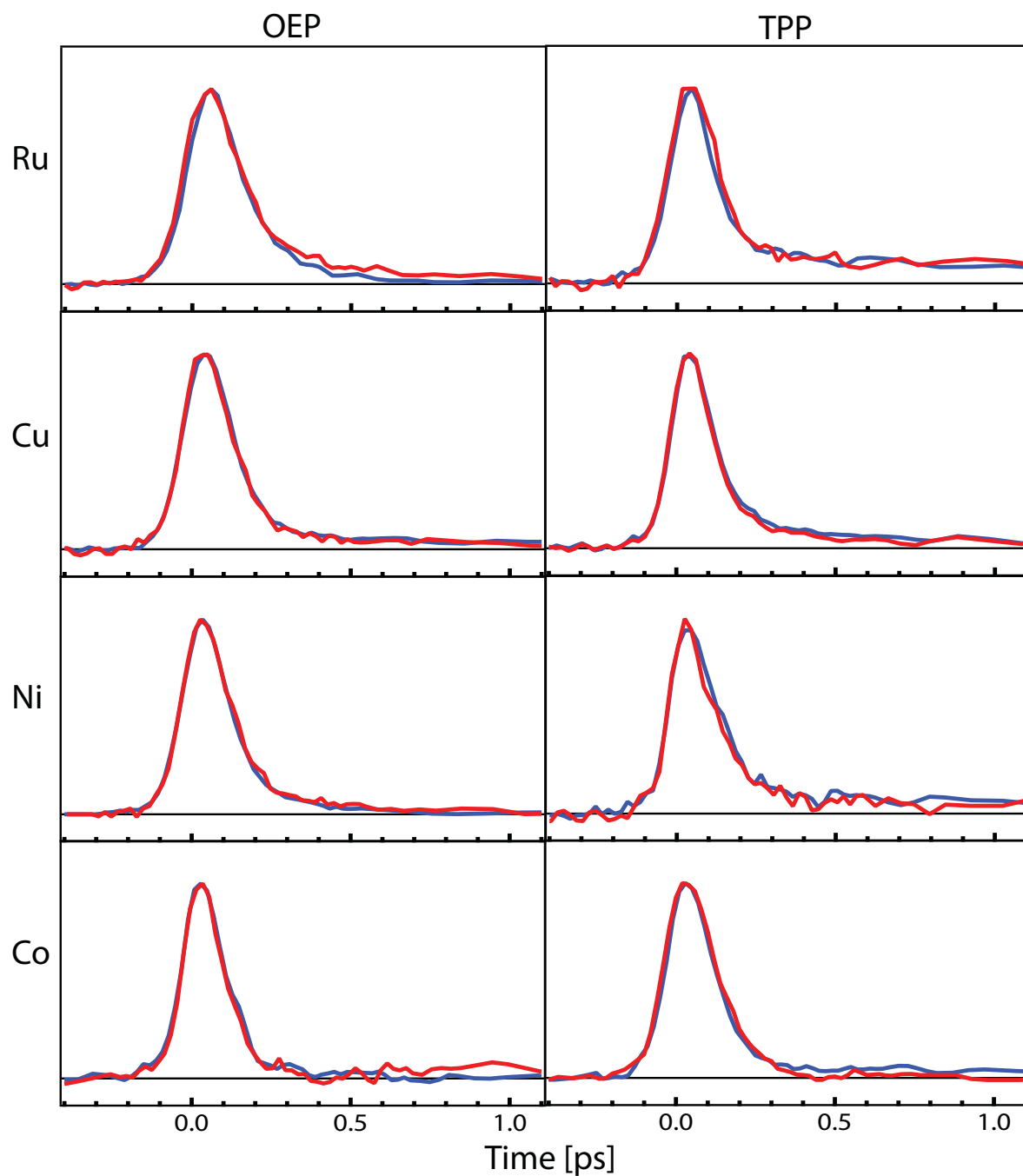


Figure E.2: Normalized kinetic traces from the 2D fluorescence data shown in Figure E.1, at $\sim 18000\text{ cm}^{-1}$ (blue trace) and $\sim 16000\text{ cm}^{-1}$ (red trace). Only the CuTPP complex show a wavelength dependent behavior. For this latter, an intermediate kinetic trace at $\sim 17000\text{ cm}^{-1}$ is added (green trace).



F. Transient fluorescence and absorption of Cyt c.

Figure F.1: Wavelength- and time-resolved fluorescence of ferrous (a, c) and ferric (b, d) Cyt c upon 286 nm (a, b) and 400 nm (c, d) excitation. The inset of panels c and d represents the emission upon 530 nm excitation. The peaks at 317 nm and 460 nm (640 nm in the inset) are Raman signal from water.

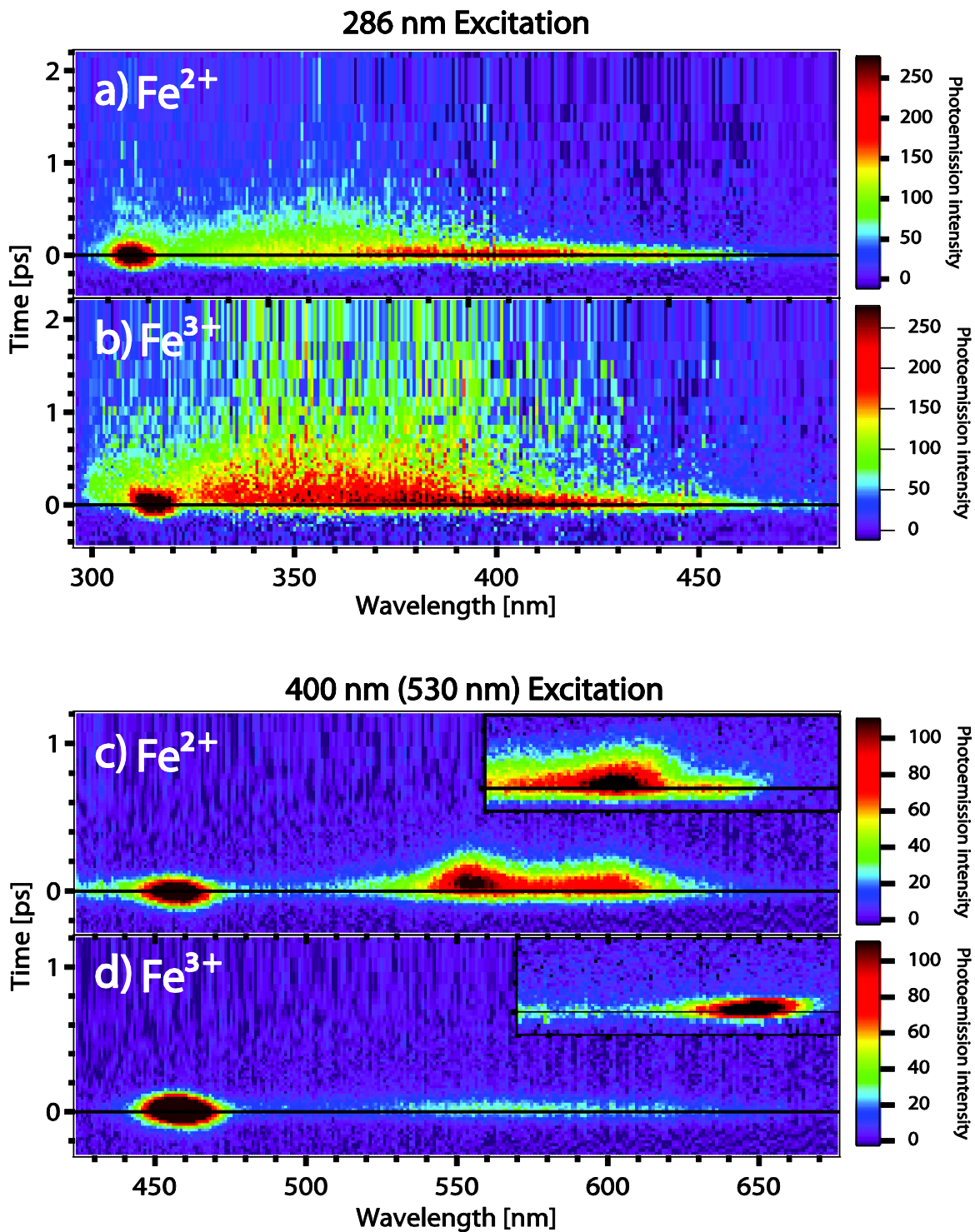


Figure F.2: Emission spectra at 0 fs (red and blue traces) and 120 fs (orange and light blue traces) time delays from ferrous Cyt c under 400 nm (red and orange traces) and 520 nm (blue and light blue traces) excitation. Spectra upon 520 nm excitation are cut on the blue side due to excitation filtering and show a bump at 635 nm corresponding to the Raman signal from water.

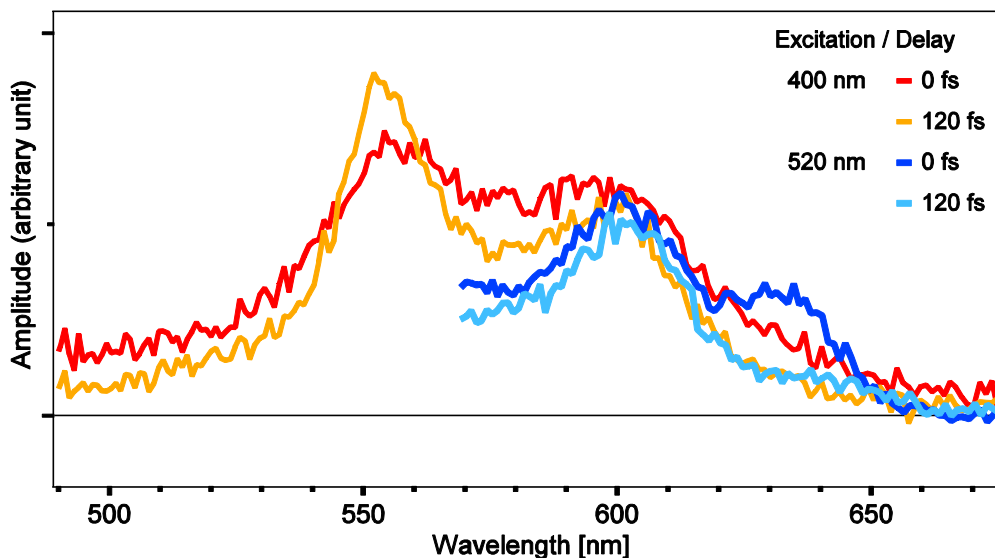


Figure F.3: (top) A representative selection of transient absorption spectra at different delay times from ferrous Cyt C under UV (288 nm) pump. The dashed line represents the ground state absorption spectrum in arbitrary units. (bottom) DAS from analysis of femtosecond TA measurements of ferrous Cyt c excited at 286 nm (top panel).

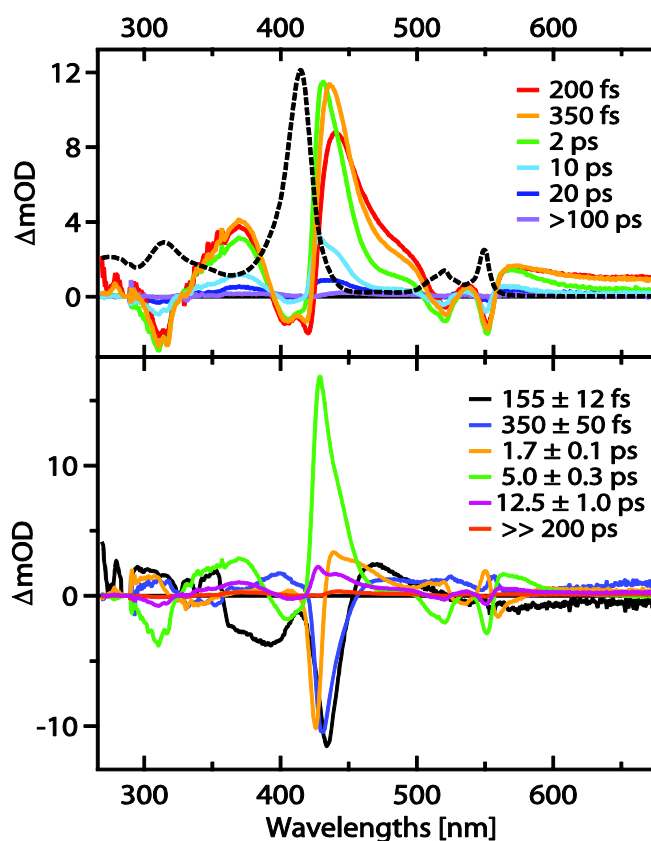
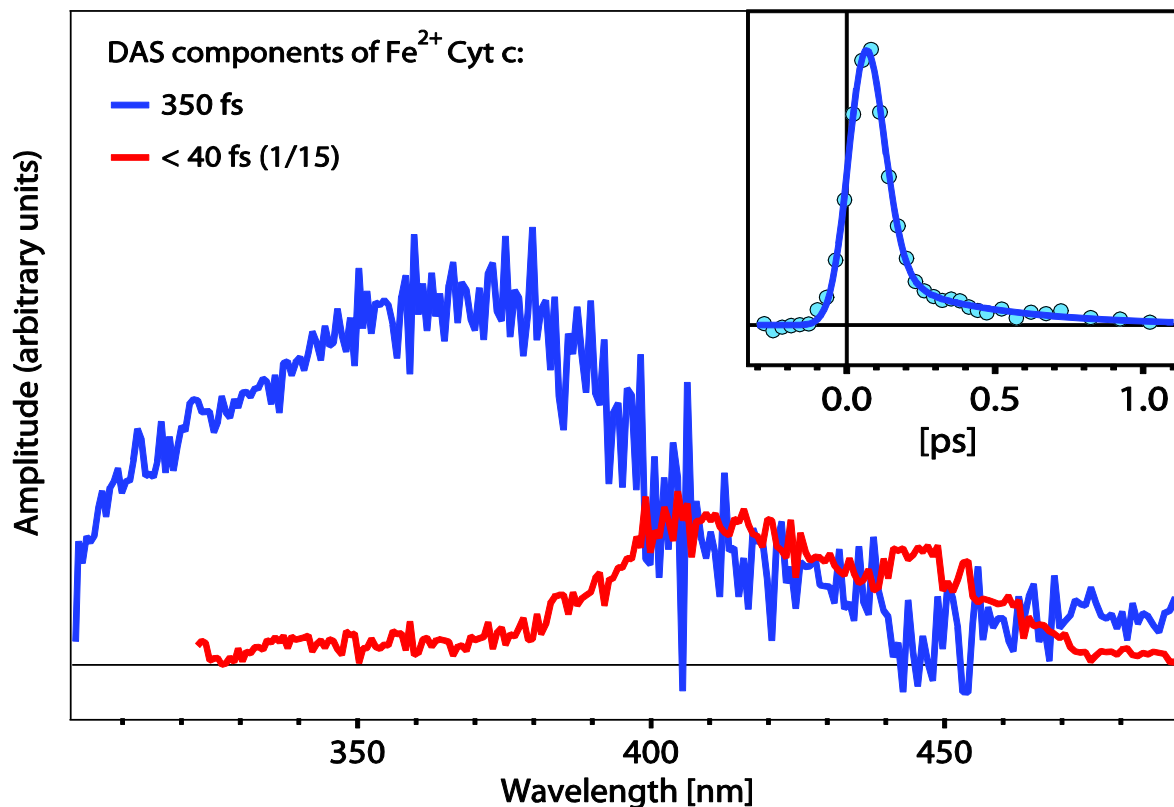


Figure F.4: Decay associated spectra (DAS) decomposition from reduced Cyt c excited at 286 nm from figure 2, but with the DAS related to Haem emission scaled by a factor of 1/15, deduced from the ratio of excitation of 2.5 and of time constant ratio ~ 6 . In inset is shown the kinetic trace of fluorescence at 460 nm along with its bi-exponential fit.



TA experimental set-up:

A detailed description of the transient absorption set-up has been recently reported.⁴⁰⁸ We use 288 nm pulses with a spectral width of ~ 5 nm and a temporal width of ~ 70 fs at a repetition rate of 1 kHz. The UV-excited sample is then probed with a 50 nm broad pulse and 3 different scans were used to cover the 263-375 nm region. The time response of 130 fs was obtained via cross-correlation measurement in pure water. Cross-phase modulation signals were dominant in the first 100s of fs, so that in order to avoid artefacts, the first 300 fs signals were not considered the analysis. The 286-290 nm region was also removed due to scattering by the pump pulse.

G. Metal-polypyridine complexes

Experimental procedures

Tris(2,2'-bipyridine)iron(II) chloride hexahydrate ($[\text{Fe}^{\text{II}}(2,2'\text{-bipyridine})_3]\text{Cl}_2 \times 6\text{H}_2\text{O}$) was synthesized according to ref⁴⁰⁹. Deionized water was used as the solvent. Room temperature aqueous solutions of $[\text{Fe}(\text{bpy})_3]^{2+}$ were circulated in a 0.2 mm thick quartz flow-cell at a speed of 1 m/s to avoid photo-damage. With the above experimental conditions, the excitation pulses hit the same spot ~ 8 times. However, since the ground state recovery is ~ 600 ps¹⁸⁶, all excited molecules relax to the ground state between two pulses. The concentration was chosen to have typically 0.3 OD at the excitation wavelength.

The RuN3 ($[\text{Ru}(\text{dcbpyH}_2)_2(\text{NCS})_2]^{2+}$) and RuN719 ($(\text{Bu}_4\text{N})_2[\text{Ru}(\text{dcbpyH})_2(\text{NCS})_2]^{2+}$) dyes were synthesized according to ref.⁴¹⁰ and dissolved in ethanol, acetonitrile and water at two different pH's (5.4 and 7). Because of the very fast photo-aggregation on the flowcell wall, the integration time of RuN3 and RuN719 dye dissolved in ethanol is smaller and thus the signal to noise ratio relatively lower compared to other solvents. Concerning the RuN719/substrate samples, the dye was adsorbed onto nanocrystalline titanium dioxide and aluminium oxide films by soaking them into 0.05 mM RuN719 solutions in ethanol for 12 h.²⁹⁴ For the fluorescence measurements, the adsorbed dye molecules were covered with a film of the redox inactive ionic liquid (1-ethyl-2-methylimidazoliumbis-(trifluoromethylsulfonyl)imide).⁴¹¹ Typical data acquisition times were of the order of half an hour for one scan, the scans were repeated ten times. Special care was taken to ensure that the measurements on both substrates were taken under identical laser conditions. During the ten scans, no significant intensity variation of the fluorescence signal was observed from scan to scan in the case of both samples. The laser flux was verified before and after each measurement. To minimize photo-damage, the solid samples were mounted on a spinning cell coupled with a horizontal motorized translation stage. In spite of these precautions, damage became visible for data acquisition times of the order of 5 hours, even if absorption spectra recorded before and after the measurements show negligible differences. The damage appeared as a very small background signal which was found to slowly increase from scan to scan in the 2D emission plot, particularly for Al_2O_3 . As a consequence, we decided to use for the averaging the first 2 scans for Al_2O_3 and the first 4

for TiO₂, to record data as background-free as possible. The optical density at 400 nm of the dye on each substrate was precisely determined, after subtraction of the absorption of the substrates. In this way the intensity of the up-converted fluorescence could be perfectly normalized to the number of excited molecules. Finally, the data were analyzed by performing a global fit (GF) of kinetic traces averaged over 5 nm steps using eq. (A.10) in which we assume two characteristic times (τ_1 , τ_2) for the emission decay. In the GF procedure, the time constants have been considered as common kinetic parameters at all wavelengths, whereas the amplitudes A_1 and A_2 have been determined for each wavelength (See section A). In order to reconstruct the time-integrated spectrum associated to each time constant obtained, we multiplied the pre-exponential factors A_1 and A_2 by the respective decay times and plotted them as a function of wavelength.

Supplementary Figures

Figure G.1: Simulated emission from the $n=4$ and $n=0$ vibrational sublevels of the excited electronic state for $\text{Fe}(\text{bpy})_3$. Experimental absorption and emission curves (emission excited at 400nm) are reported for comparison.

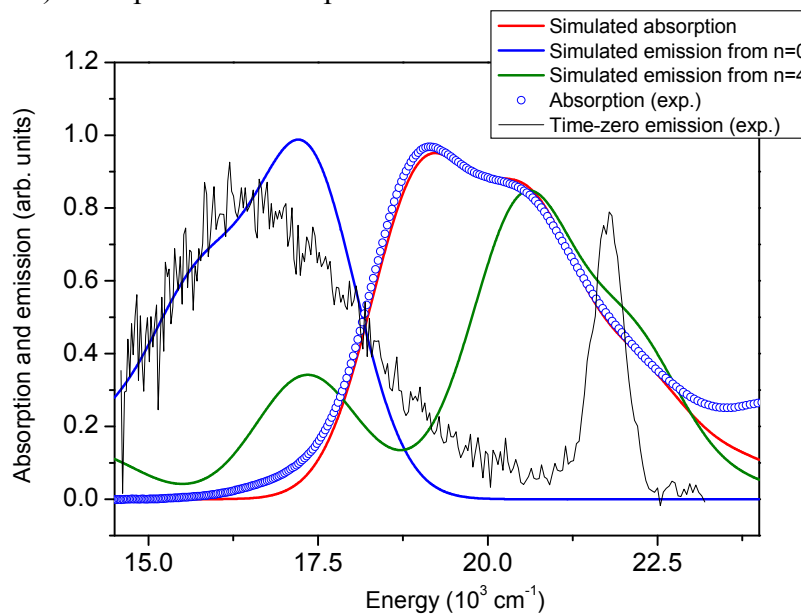


Figure G.2: Simulated emission from the $n=4$ and $n=0$ vibrational sublevels of the excited electronic state for $\text{Fe}(\text{bpy})_3$. Experimental absorption and emission curves (emission excited at 500nm) are reported for comparison.

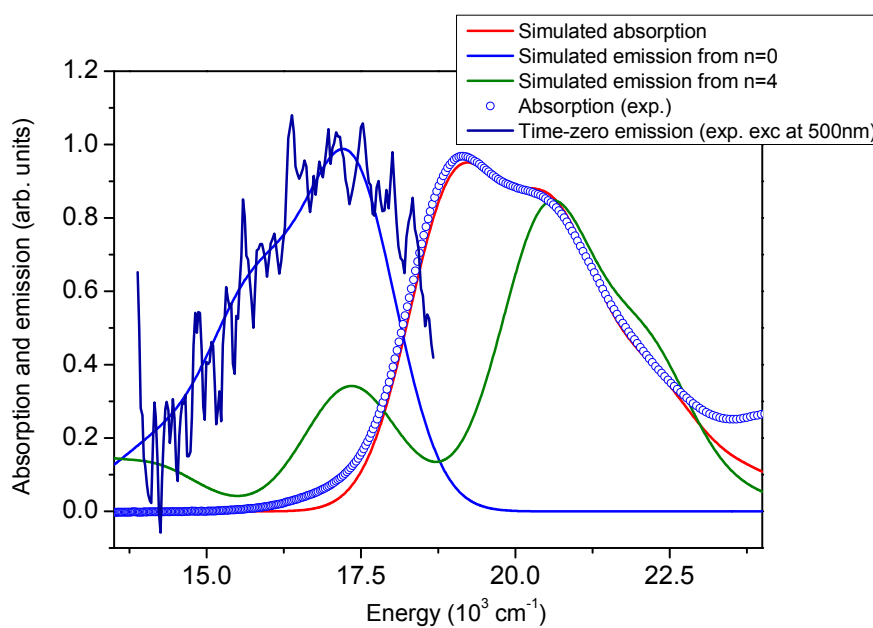


Figure G.3: steady-state absorption spectra of RuN719 in different solvents (red traces) and the time gated fluorescence recorded at zero time delay (blue traces).

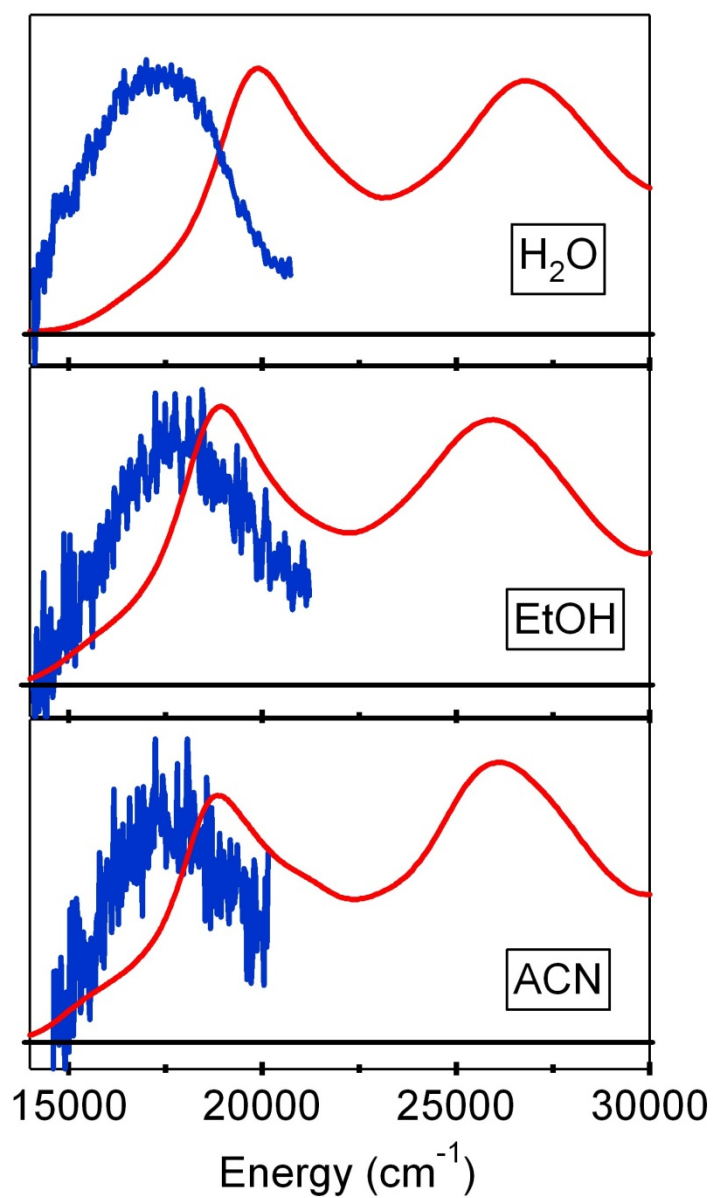


Figure G.4: Representative spectra of emission intensity of RuN3 in ethanol, RuN719 in water at pH5.4, and aqueous $[\text{Ru}(\text{bpy})_3]^{2+}$, normalized at the wavelength of 525 nm, which is dominated by the fluorescence. This normalization shows the increase with time of longer lived $^1\text{MLCT}$ states emission for RuN719, and of the phosphorescence contribution for $[\text{Ru}(\text{bpy})_3]^{2+}$.

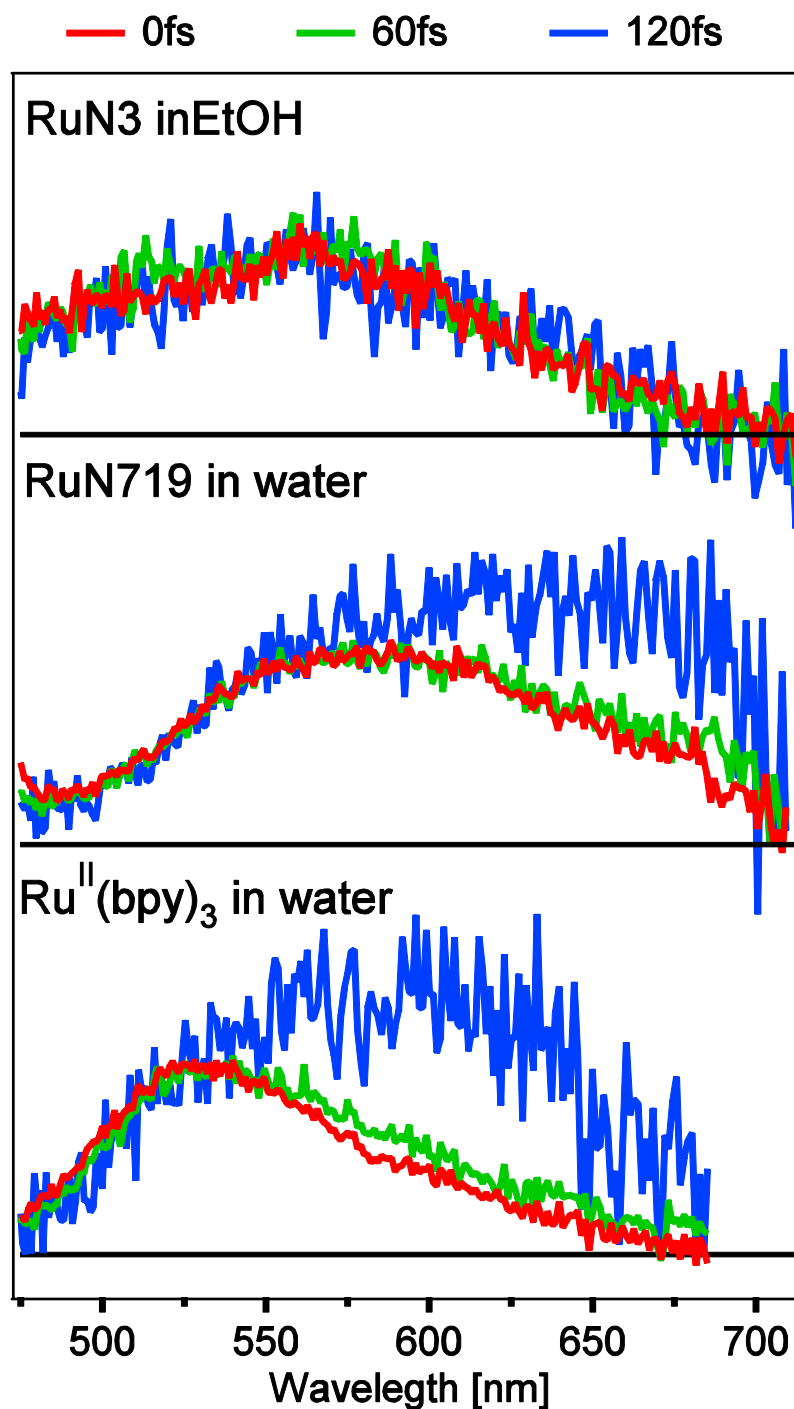
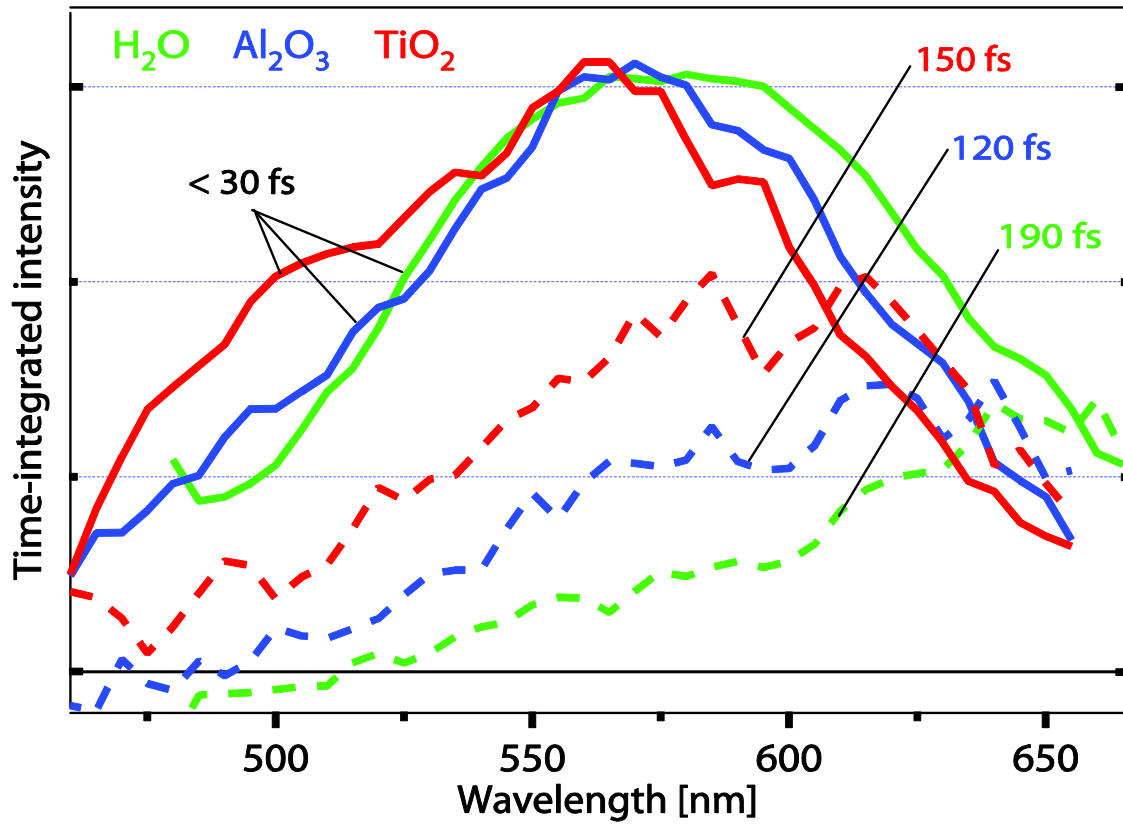


Figure G.5: Time-integrated reconstructed spectra (pre-exponential factor multiplied by time constant, plotted as a function of the emission wavelength) obtained with a global fit analysis of data for RuN719 in water reported in figure 4. The uncertainty on the lifetimes of the long component is estimated to be ± 30 fs.



Abbreviations

ASE.....	amplified stimulated emission	MD.....	molecular dynamics
BBO.....	β -BaB ₂ O ₄	Met80.....	methionine residue
CCD.....	charge coupled device	MO.....	molecular orbital
CHex.....	cyclohexane	MLCT....	metal-to-ligand-CT
CT.....	charge transfer	OEP.....	octaethylporphin
CW.....	continuous wave	OPA.....	optical parametric amplifier
Cyt c.....	cytochrome c	PDB.....	protein data bank
DAS.....	Decay associated spectrum	PPO.....	2,5-diphenyloxazole
DFT.....	density functional theory	pTP.....	para-terphenyl
DMF.....	dimethylformamide	QY.....	quantum yield
DSSC.....	dye-sensitized-solar-cell	SE.....	stimulated emission
ESA.....	excited state absorption	SF.....	sum frequency
EtOH.....	ethanol	SFG.....	sum frequency generation
FC.....	Franck-Condon	SHG.....	second harmonic generation
FT.....	Fourier transform	SS.....	Stokes shift
FWHM.....	full width at half maximum	SVD.....	singular value decomposition
GA.....	global analysis	TA.....	transient absorption
GSB.....	ground state bleach	TD-DFT..	time-dependent DFT
GVD.....	group velocity dispersion	TPP.....	tetraphenylporphin
GVM.....	group velocity mismatch	Trp.....	tryptophan
H18, H93....	histidine residue	TRSS.....	time-resolved SS
HOMO.....	highest occupied MO	UV.....	ultraviolet
HT.....	Hertzberg-Teller	VET.....	vibrational energy transfer
IC.....	internal conversion	VR.....	vibrational relaxation
IRF.....	instrumental response function	W7, W14.	tryptophan residue
ISC.....	intersystem crossing		
IT.....	Intra-tryptophan		
LMCT.....	ligand-to-metal-CT		
LUMO.....	lowest unoccupied MO		
Mb.....	myoglobin		

Bibilography

- 1 V. S. Chirvony, A. van Hoek, V. A. Galievsky, I. V. Sazanovich, T. J. Schaafsma,
and D. Holten, *Journal of Physical Chemistry B* **104** (42), 9909 (2000).
- 2 P. W. Atkins and R. Friedman, *Molecular Quantum Mechanics*. (Oxford University
Press, USA; 4 edition 2005).
- 3 H. Sponer and E. Teller, *Reviews of Modern Physics* **13** (2), 0075 (1941).
- 4 B. Valeur, *Invitation à la fluorescence moléculaire*. (De Boeck 2004).
- 5 B. Valeur, *Molecular Fluorescence: Principles and Applications*. (Wiley-VCH,
2001).
- 6 J. R. Lakowicz, *Principles of fluorescence spectroscopy*. (New York, 1983).
- 7 S. E. Braslavsky, *Pure and Applied Chemistry* **79** (3), 293 (2007).
- 8 M. Kasha, *Discussions of the Faraday Society* (9), 14 (1950).
- 9 C. Reichardt, *Chemical Reviews* **94** (8), 2319 (1994).
- 10 L. Onsager, *Journal of the American Chemical Society* **58**, 1486 (1936).
- 11 E. G. Mcrae, *Journal of Physical Chemistry* **61** (5), 562 (1957).
- 12 Y. Ooshika, *Journal of the Physical Society of Japan* **9** (4), 594 (1954).
- 13 M. Ravi, A. Samanta, and T. P. Radhakrishnan, *Journal of Physical Chemistry* **98**
(37), 9133 (1994).
- 14 A. Marini, A. Munoz-Losa, A. Biancardi, and B. Mennucci, *Journal of Physical
Chemistry B* **114** (51), 17128 (2010).
- 15 A. C. Yu, C. A. Tolbert, D. A. Farrow, and D. M. Jonas, *Journal of Physical
Chemistry A* **106** (41), 9407 (2002).
- 16 S. Kinoshita and N. Nishi, *Journal of Chemical Physics* **89** (11), 6612 (1988).
- 17 J. C. Owrutsky, D. Raftery, and R. M. Hochstrasser, *Annual Review of Physical
Chemistry* **45**, 519 (1994).
- 18 D. Boyall and K. L. Reid, *Chemical Society Reviews* **26** (3), 223 (1997).
- 19 D. J. Nesbitt and R. W. Field, *Journal of Physical Chemistry* **100** (31), 12735
(1996).
- 20 P. M. Felker and A. H. Zewail, *Journal of Chemical Physics* **82** (7), 2961 (1985).
- 21 P. M. Felker and A. H. Zewail, *Journal of Chemical Physics* **82** (7), 2975 (1985).
- 22 P. M. Felker and A. H. Zewail, *Journal of Chemical Physics* **82** (7), 2994 (1985).
- 23 P. M. Felker, W. R. Lambert, and A. H. Zewail, *Journal of Chemical Physics* **82** (7),
3003 (1985).
- 24 P. S. H. Fitch, C. A. Haynam, and D. H. Levy, *Journal of Chemical Physics* **74** (12),
6612 (1981).
- 25 J. E. Gambogi, J. H. Timmermans, K. K. Lehmann, and G. Scoles, *Journal of
Chemical Physics* **99** (11), 9314 (1993).
- 26 J. L. Scott, D. Luckhaus, S. S. Brown, and F. F. Crim, *Journal of Chemical Physics*
102 (2), 675 (1995).
- 27 A. Callegari, Princeton University 1998.
- 28 K. K. Lehmann, G. Scoles, and B. H. Pate, *Annual Review of Physical Chemistry*
45, 241 (1994).
- 29 C. G. Elles, M. J. Cox, and F. F. Crim, *Journal of Chemical Physics* **120** (15), 6973
(2004).
- 30 H. S. Yoo, M. J. DeWitt, and B. H. Pate, *Journal of Physical Chemistry A* **108** (8),
1348 (2004).

- 31 H. S. Yoo, M. J. DeWitt, and B. H. Pate, *Journal of Physical Chemistry A* **108** (8),
1365 (2004).
- 32 H. S. Yoo, D. A. McWhorter, and B. H. Pate, *Journal of Physical Chemistry A* **108**
(8), 1380 (2004).
- 33 H. J. Bakker, P. C. M. Planken, and A. Lagendijk, *Nature* **347** (6295), 745 (1990).
- 34 A. Charvat, J. Assmann, B. Abel, D. Schwarzer, K. Henning, K. Luther, and J.
Troe, *Physical Chemistry Chemical Physics* **3** (12), 2230 (2001).
- 35 K. Sekiguchi, A. Shimojima, and O. Kajimoto, *Chemical Physics Letters* **356** (1-2),
84 (2002).
- 36 K. Sekiguchi, A. Shimojima, and O. Kajimoto, *Chemical Physics Letters* **370** (3-4),
303 (2003).
- 37 R. S. von Benten and B. Abel, *Chemical Physics* **378** (1-3), 19 (2010).
- 38 T. Elsaesser and W. Kaiser, *Annual Review of Physical Chemistry* **42**, 83 (1991).
- 39 F. Laermer, T. Elsaesser, and W. Kaiser, *Chemical Physics Letters* **156** (4), 381
(1989).
- 40 F. Laermer, W. Israel, and T. Elsaesser, *Journal of the Optical Society of America*
B-Optical Physics **7** (8), 1604 (1990).
- 41 J. Y. Liu, W. H. Fan, K. L. Han, W. Q. Deng, D. L. Xu, and N. Q. Lou, *Journal of*
Physical Chemistry A **107** (50), 10857 (2003).
- 42 J. Y. Liu, W. H. Fan, K. L. Han, D. L. Xu, and N. Q. Lou, *Journal of Physical*
Chemistry A **107** (12), 1914 (2003).
- 43 A. M. Weiner and E. P. Ippen, *Chemical Physics Letters* **114** (5-6), 456 (1985).
- 44 W. Wild, A. Seilmeier, N. H. Gottfried, and W. Kaiser, *Chemical Physics Letters*
119 (4), 259 (1985).
- 45 D. Schwarzer, C. Hanisch, P. Kutne, and J. Troe, *Journal of Physical Chemistry A*
106 (35), 8019 (2002).
- 46 A. J. Taylor, D. J. Erskine, and C. L. Tang, *Chemical Physics Letters* **103** (5), 430
(1984).
- 47 M. J. Rosker, F. W. Wise, and C. L. Tang, *Physical Review Letters* **57** (3), 321
(1986).
- 48 C. H. B. Cruz, R. L. Fork, W. H. Knox, and C. V. Shank, *Chemical Physics Letters*
132 (4-5), 341 (1986).
- 49 A. Mokhtari, A. Chebira, and J. Chesnoy, *Journal of the Optical Society of America*
B-Optical Physics **7** (8), 1551 (1990).
- 50 T. Hasche, S. H. Ashworth, E. Riedle, M. Woerner, and T. Elsaesser, *Chemical*
Physics Letters **244** (1-2), 164 (1995).
- 51 S. H. Ashworth, T. Hasche, M. Woerner, E. Riedle, and T. Elsaesser, *Journal of*
Chemical Physics **104** (15), 5761 (1996).
- 52 A. Cannizzo, F. van Mourik, W. Gawelda, G. Zgrablic, C. Bressler, and M.
Chergui, *Angewandte Chemie-International Edition* **45** (19), 3174 (2006).
- 53 S. A. Kovalenko, R. Schanz, H. Hennig, and N. P. Ernsting, *Journal of Chemical*
Physics **115** (7), 3256 (2001).
- 54 T. Kasajima, S. Akimoto, S. Sato, and I. Yamazaki, *Chemical Physics Letters* **375**
(1-2), 227 (2003).
- 55 T. Kiba, S. Sato, S. Akimoto, T. Kasajima, and I. Yamazaki, *Journal of*
Photochemistry and Photobiology a-Chemistry **178** (2-3), 201 (2006).
- 56 A. Pigliucci, G. Duvanel, L. M. L. Daku, and E. Vauthey, *Journal of Physical*
Chemistry A **111** (28), 6135 (2007).

- 57 U. Sukowski, A. Seilmeier, T. Elsaesser, and S. F. Fischer, *Journal of Chemical*
58 *Physics* **93** (6), 4094 (1990).
- 59 P. Li and P. M. Champion, *Biophysical Journal* **66** (2), 430 (1994).
- 60 J. Kim, W. Y. Lu, W. H. Qiu, L. J. Wang, M. Caffrey, and D. P. Zhong, *Journal of*
61 *Physical Chemistry B* **110** (43), 21994 (2006).
- 62 S. K. Pal and A. H. Zewail, *Chemical Reviews* **104** (4), 2099 (2004).
- 63 L. Y. Zhang, L. J. Wang, Y. T. Kao, W. H. Qiu, Y. Yang, O. Okobiah, and D. P.
64 Zhong, *Proceedings of the National Academy of Sciences of the United States of*
America **104** (47), 18461 (2007).
- 65 D. Aherne, V. Tran, and B. J. Schwartz, *Journal of Physical Chemistry B* **104** (22),
66 5382 (2000).
- 67 P. L. Geissler and D. Chandler, *Journal of Chemical Physics* **113** (21), 9759 (2000).
- 68 R. M. Stratt and M. Maroncelli, *Journal of Physical Chemistry* **100** (31), 12981
69 (1996).
- 70 A. E. Bragg, M. C. Cavanagh, and B. J. Schwartz, *Science* **321** (5897), 1817 (2008).
- 71 T. Fonseca and B. M. Ladanyi, *Journal of Physical Chemistry* **95** (6), 2116 (1991).
- 72 G. H. Tao and R. M. Stratt, *Journal of Chemical Physics* **125** (11) (2006).
- 73 N. G. van Kampen, *Stochastic Processes in Physics and Chemistry*. (Amsterdam,
74 1981).
- 75 U. M. B. Marconi, A. Puglisi, L. Rondoni, and A. Vulpiani, *Physics Reports-*
Review Section of Physics Letters **461** (4-6), 111 (2008).
- 76 P. Langevin, *Comptes Rendus Hebdomadaires Des Seances De L Academie Des*
Sciences **146**, 530 (1908).
- 77 G. E. Uhlenbeck and L. S. Ornstein, *Physical Review* **36** (5), 0823 (1930).
- 78 B. Bagchi and B. Jana, *Chemical Society Reviews* **39** (6), 1936 (2010).
- 79 R. A. Nome, *Journal of the Brazilian Chemical Society* **21** (12), 2189 (2010).
- 80 N. T. Hunt, A. A. Jaye, and S. R. Meech, *Physical Chemistry Chemical Physics* **9**
81 (18), 2167 (2007).
- 82 H. Shirota, T. Fujisawa, H. Fukazawa, and K. Nishikawa, *Bulletin of the Chemical*
Society of Japan **82** (11), 1347 (2009).
- 83 Q. Zhong and J. T. Fourkas, *Journal of Physical Chemistry B* **112** (49), 15529
84 (2008).
- 85 M. H. Cho and G. R. Fleming, *Journal of Chemical Physics* **98** (4), 2848 (1993).
- 86 S. Park, J. Kim, A. M. Moran, and N. F. Scherer, *Physical Chemistry Chemical*
Physics **13** (1), 214 (2011).
- 87 S. A. Passino, Y. Nagasawa, and G. R. Fleming, *Journal of Chemical Physics* **107**
88 (16), 6094 (1997).
- 89 M. Born, *Zeitschrift Fur Physik* **1**, 45 (1920).
- 90 B. Bagchi, *Annual Review of Physical Chemistry* **40**, 115 (1989).
- 91 B. Bagchi, E. W. Castner, and G. R. Fleming, *Journal of Molecular Structure* **194**,
92 171 (1989).
- 93 H. Block and S. M. Walker, *Chemical Physics Letters* **19** (3), 363 (1973).
- 94 E. W. Castner, G. R. Fleming, and B. Bagchi, *Journal of Chemical Physics* **89** (6),
95 3519 (1988).
- 96 S. Ehrenson, *Journal of Computational Chemistry* **2** (1), 41 (1981).
- 97 S. Ehrenson, *Journal of Physical Chemistry* **91** (7), 1868 (1987).
- 98 A. Declémy and C. Rulliere, *Chemical Physics Letters* **146** (1-2), 1 (1988).

- 88 A. Declémy, C. Rulliere, and P. Kottis, *Chemical Physics Letters* **133** (5), 448 (1987).
- 89 V. Nagarajan, A. M. Brearley, T. J. Kang, and P. F. Barbara, *Journal of Chemical Physics* **86** (6), 3183 (1987).
- 90 J. D. Simon and S. G. Su, *Journal of Chemical Physics* **87** (12), 7016 (1987).
- 91 S. G. Su and J. D. Simon, *Journal of Physical Chemistry* **91** (11), 2693 (1987).
- 92 D. Bingemann and N. P. Ernsting, *Journal of Chemical Physics* **102** (7), 2691 (1995).
- 93 E. W. Castner, M. Maroncelli, and G. R. Fleming, *Journal of Chemical Physics* **86** (3), 1090 (1987).
- 94 T. Fonseca and B. M. Ladanyi, *Journal of Molecular Liquids* **60** (1-3), 1 (1994).
- 95 M. L. Horng, J. A. Gardecki, A. Papazyan, and M. Maroncelli, *Journal of Physical Chemistry* **99** (48), 17311 (1995).
- 96 W. Jarzaba, G. C. Walker, A. E. Johnson, and P. F. Barbara, *Chemical Physics* **152** (1-2), 57 (1991).
- 97 W. Jarzaba, G. C. Walker, A. E. Johnson, M. A. Kahlow, and P. F. Barbara, *Journal of Physical Chemistry* **92** (25), 7039 (1988).
- 98 R. Jimenez, G. R. Fleming, P. V. Kumar, and M. Maroncelli, *Nature* **369** (6480), 471 (1994).
- 99 M. A. Kahlow, W. Jarzaba, T. J. Kang, and P. F. Barbara, *Journal of Chemical Physics* **90** (1), 151 (1989).
- 100 M. A. Kahlow, T. J. Kang, and P. F. Barbara, *Journal of Physical Chemistry* **91** (26), 6452 (1987).
- 101 M. Maroncelli, *Journal of Chemical Physics* **94** (3), 2084 (1991).
- 102 S. J. Rosenthal, R. Jimenez, G. R. Fleming, P. V. Kumar, and M. Maroncelli, *Journal of Molecular Liquids* **60** (1-3), 25 (1994).
- 103 S. J. Rosenthal, X. L. Xie, M. Du, and G. R. Fleming, *Journal of Chemical Physics* **95** (6), 4715 (1991).
- 104 B. Bagchi and A. Chandra, *Journal of Chemical Physics* **90** (12), 7338 (1989).
- 105 B. Bagchi and A. Chandra, *Chemical Physics Letters* **155** (6), 533 (1989).
- 106 D. F. Calef and P. G. Wolynes, *Journal of Chemical Physics* **78** (6), 4145 (1983).
- 107 A. Chandra and B. Bagchi, *Chemical Physics Letters* **151** (1-2), 47 (1988).
- 108 L. E. Fried and S. Mukamel, *Journal of Chemical Physics* **93** (2), 932 (1990).
- 109 P. J. Rossky, *Annual Review of Physical Chemistry* **36**, 321 (1985).
- 110 D. Q. Wei and G. N. Patey, *Journal of Chemical Physics* **93** (2), 1399 (1990).
- 111 P. G. Wolynes, *Journal of Chemical Physics* **86** (9), 5133 (1987).
- 112 J. B. Hubbard, R. F. Kayser, and P. J. Stiles, *Chemical Physics Letters* **95** (4-5), 399 (1983).
- 113 P. J. Stiles and J. B. Hubbard, *Chemical Physics* **84** (3), 431 (1984).
- 114 G. Vanderzwan and J. T. Hynes, *Physica A* **121** (1-2), 227 (1983).
- 115 M. Maroncelli and G. R. Fleming, *Journal of Chemical Physics* **86** (11), 6221 (1987).
- 116 M. Maroncelli and G. R. Fleming, *Journal of Chemical Physics* **89** (2), 875 (1988).
- 117 J. S. Bader and D. Chandler, *Chemical Physics Letters* **157** (6), 501 (1989).
- 118 M. Maroncelli and G. R. Fleming, *Journal of Chemical Physics* **89** (8), 5044 (1988).
- 119 M. J. Lang, X. J. Jordanides, X. Song, and G. R. Fleming, *Journal of Chemical Physics* **110** (12), 5884 (1999).

- 120 C. Silva, P. K. Walhout, K. Yokoyama, and P. F. Barbara, *Physical Review Letters* **80** (5), 1086 (1998).
- 121 P. R. Callis, *Methods in Enzymology* **278**, 113 (1997).
- 122 P. L. Muino and P. R. Callis, *Journal of Chemical Physics* **100** (6), 4093 (1994).
- 123 S. K. Pal, J. Peon, B. Bagchi, and A. H. Zewail, *Journal of Physical Chemistry B* **106** (48), 12376 (2002).
- 124 B. Bagchi, *Journal of Chemical Physics* **100** (9), 6658 (1994).
- 125 M. Berg, *Journal of Physical Chemistry A* **102** (1), 17 (1998).
- 126 P. Larregaray, A. Cavina, and M. Chergui, *Chemical Physics* **308** (1-2), 13 (2005).
- 127 A. A. Oskouei, O. Braem, A. Cannizzo, F. van Mourik, A. Tortschanoff, and M. Chergui, *Chemical Physics* **350** (1-3), 104 (2008).
- 128 A. A. Oskouei, O. Bram, A. Cannizzo, F. van Mourik, A. Tortschanoff, and M. Chergui, *Journal of Molecular Liquids* **141** (3), 118 (2008).
- 129 A. A. Oskouei, A. Tortschanoff, O. Bram, F. van Mourik, A. Cannizzo, and M. Chergui, *Journal of Chemical Physics* **133** (6) (2010).
- 130 D. Franco, G. Consolati, and D. Trezzi, *Physical Review C* **83** (1) (2011).
- 131 Y. Homma, Y. Murase, and K. Sonehara, *Applied Radiation and Isotopes* **38** (2), 91 (1987).
- 132 P. Ramasamy, N. Balamurugan, and A. Arulchakkaravarthi, *Journal of Crystal Growth* **310** (7-9), 2115 (2008).
- 133 H. L. Xiao, X. B. Li, D. Zheng, J. Cao, L. J. Wen, and N. Y. Wang, *Chinese Physics C* **34** (11), 1724 (2010).
- 134 C. Hariharan, V. V. and A. K. Mishra, *Journal of Luminescence* **75** (3), 205 (1997).
- 135 B. Steyer and F. P. Schafer, *Applied Physics* **7** (2), 113 (1975).
- 136 A. T. Balaban, I. Bally, M. Bacescu, E. Cioranescu, L. Birladeanu, and P. T. Frangopol, *Tetrahedron* **19** (1), 169 (1963).
- 137 A. T. Balaban, Z. Simon, P. T. Frangopol, L. Birladeanu, I. Bally, and M. Mocanu, *Tetrahedron* **19** (12), 2199 (1963).
- 138 S. Ionescu, D. Popovici, A. T. Balaban, and M. Hillebrand, *Spectrochimica Acta Part a-Molecular and Biomolecular Spectroscopy* **62** (1-3), 252 (2005).
- 139 A. A. Elazhary, A. A. Ghoneim, and M. E. Elshakre, *Journal of Chemical Research-S* (9), 354 (1995).
- 140 A. E. Obukhov, *Zhurnal Fizicheskoi Khimii* **69** (6), 1015 (1995).
- 141 E. A. Mangle, P. R. Salvi, R. J. Babbit, A. L. Motyka, and M. R. Topp, *Chemical Physics Letters* **133** (3), 214 (1987).
- 142 N. Boens, W. W. Qin, N. Basaric, J. Hofkens, M. Ameloot, J. Pouget, J. P. Lefevre, B. Valeur, E. Gratton, M. Vandeven, N. D. Silva, Y. Engelborghs, K. Willaert, A. Sillen, G. Rumbles, D. Phillips, A. J. W. G. Visser, A. van Hoek, J. R. Lakowicz, H. Malak, I. Gryczynski, A. G. Szabo, D. T. Krajcarski, N. Tamai, and A. Miura, *Analytical Chemistry* **79** (5), 2137 (2007).
- 143 S. Ionescu, D. Popovici, A. T. Balaban, and M. Hillebrand, *Spectrochimica Acta Part a-Molecular and Biomolecular Spectroscopy* **66** (4-5), 1165 (2007).
- 144 I. B. Berlman, *Handbook of Fluorescence Spectra of Aromatic Molecules*. (Academic Press, 1971).
- 145 J. C. delValle, M. Kasha, and J. Catalan, *Chemical Physics Letters* **263** (1-2), 154 (1996).
- 146 J. C. delValle, M. Kasha, and J. Catalan, *Journal of Physical Chemistry A* **101** (18), 3260 (1997).

- 147 J. Saltiel, R. A. Ivanov, D. A. Gormin, T. S. R. Krishna, and R. J. Clark, *Molecular*
148 *Physics* **104** (5-7), 957 (2006).
- 149 W. P. Ambrose and W. E. Moerner, *Nature* **349** (6306), 225 (1991).
- 150 W. E. Moerner and D. P. Fromm, *Review of Scientific Instruments* **74** (8), 3597
151 (2003).
- 152 W. E. Moerner and M. Orrit, *Science* **283** (5408), 1670 (1999).
- 153 M. T. Bernius, M. Inbasekaran, J. O'Brien, and W. S. Wu, *Advanced Materials* **12**
154 (23), 1737 (2000).
- 155 M. Gross, D. C. Muller, H. G. Nothofer, U. Scherf, D. Neher, C. Brauchle, and K.
156 Meerholz, *Nature* **405** (6787), 661 (2000).
- 157 G. Heimel, M. Daghofer, J. Gierschner, E. J. W. List, A. C. Grimsdale, K. Mullen,
158 D. Beljonne, J. L. Bredas, and E. Zojer, *Journal of Chemical Physics* **122** (5)
(2005).
- 159 C. Kryschi, W. Klufner, and H. Kupka, *Chemical Physics* **146** (1-2), 231 (1990).
- 160 C. Kryschi, W. Klufner, and H. Kupka, *Journal of Luminescence* **48-9**, 381 (1991).
- 161 J. M. Beechem and L. Brand, *Annual Review of Biochemistry* **54**, 43 (1985).
- 162 J. T. Vivian and P. R. Callis, *Biophysical Journal* **80** (5), 2093 (2001).
- 163 P. R. Callis and B. K. Burgess, *Journal of Physical Chemistry B* **101** (46), 9429
(1997).
- 164 J. R. Lakowicz, *Photochemistry and Photobiology* **72** (4), 421 (2000).
- 165 B. Schuler and W. A. Eaton, *Current Opinion in Structural Biology* **18** (1), 16
(2008).
- 166 X. H. Shen and J. R. Knutson, *Journal of Physical Chemistry B* **105** (26), 6260
(2001).
- 167 S. K. Pal, J. Peon, and A. H. Zewail, *Chemical Physics Letters* **363** (1-2), 57 (2002).
- 168 J. Peon, S. K. Pal, and A. H. Zewail, *Proceedings of the National Academy of*
169 *Sciences of the United States of America* **99** (17), 10964 (2002).
- 170 S. K. Pal, J. Peon, and A. H. Zewail, *Proceedings of the National Academy of*
171 *Sciences of the United States of America* **99** (4), 1763 (2002).
- 172 D. P. Zhong, S. K. Pal, D. Q. Zhang, S. I. Chan, and A. H. Zewail, *Proceedings of*
173 *the National Academy of Sciences of the United States of America* **99** (1), 13
(2002).
- 174 S. Schenkl, F. van Mourik, G. van der Zwan, S. Haacke, and M. Chergui, *Science*
175 **309** (5736), 917 (2005).
- 176 J. Leonard, E. Portuondo-Campa, A. Cannizzo, F. van Mourik, G. van der Zwan, J.
177 Tittor, S. Haacke, and M. Chergui, *Proceedings of the National Academy of*
178 *Sciences of the United States of America* **106** (19), 7718 (2009).
- 179 C. Zang, J. A. Stevens, J. J. Link, L. J. Guo, L. J. Wang, and D. P. Zhong, *Journal*
180 *of the American Chemical Society* **131** (8), 2846 (2009).
- 181 J. A. Stevens, J. J. Link, Y. T. Kao, C. Zang, L. J. Wang, and D. P. Zhong, *Journal*
182 *of Physical Chemistry B* **114** (3), 1498 (2010).
- 183 P. R. Callis, *Fluorescence Spectroscopy* **278**, 113 (1997).
- 184 P. R. Callis, *Journal of Chemical Physics* **95** (6), 4230 (1991).
- 185 L. S. Slater and P. R. Callis, *Journal of Physical Chemistry* **99** (21), 8572 (1995).
- 186 E. Jalviste and N. Ohta, *Journal of Chemical Physics* **121** (10), 4730 (2004).
- 187 R. Katoh, *Journal of Photochemistry and Photobiology a-Chemistry* **189** (2-3), 211
188 (2007).
- 189 B. Valeur and G. Weber, *Photochemistry and Photobiology* **25** (5), 441 (1977).

- 176 Y. Yamamoto and J. Tanaka, *Bulletin of the Chemical Society of Japan* **45** (5),
1362 (1972).
- 177 J. L. Dashnau, B. Zelent, and J. M. Vanderkooi, *Biophysical Chemistry* **114** (1), 71
(2005).
- 178 D. M. Sammeth, S. S. Siewert, L. H. Spangler, and P. R. Callis, *Chemical Physics
Letters* **193** (6), 532 (1992).
- 179 K. W. Short and P. R. Callis, *Journal of Chemical Physics* **113** (13), 5235 (2000).
- 180 K. W. Short and P. R. Callis, *Chemical Physics* **283** (1-2), 269 (2002).
- 181 B. Fender and P. R. Callis, *Chemical Physics Letters* **262** (3-4), 343 (1996).
- 182 A. G. Szabo and D. M. Rayner, *Journal of the American Chemical Society* **102** (2),
554 (1980).
- 183 J. R. Lakowicz, *Principles of fluorescence spectroscopy*. (Plenum Press, New York,
1983).
- 184 S. K. Pal, J. Peon, and A. H. Zewail, *Proceedings of the National Academy of
Sciences of the United States of America* **99** (24), 15297 (2002).
- 185 W. Y. Lu, J. Kim, W. H. Qiu, and D. P. Zhong, *Chemical Physics Letters* **388** (1-3),
120 (2004).
- 186 W. Gawelda, A. Cannizzo, V. T. Pham, F. van Mourik, C. Bressler, and M.
Chergui, *Journal of the American Chemical Society* **129** (26), 8199 (2007).
- 187 G. Zgrablic, K. Voitchovsky, M. Kindermann, S. Haacke, and M. Chergui,
Biophysical Journal **88** (4), 2779 (2005).
- 188 G. Zgrablic, S. Haacke, and M. Chergui, *Journal of Physical Chemistry B* **113** (13),
4384 (2009).
- 189 I. P. Mercer, I. R. Gould, and D. R. Klug, *Journal of Physical Chemistry B* **103**
(36), 7720 (1999).
- 190 J. E. Hansen, S. J. Rosenthal, and G. R. Fleming, *Journal of Physical Chemistry* **96**
(7), 3034 (1992).
- 191 A. J. Ruggiero, D. C. Todd, and G. R. Fleming, *Journal of the American Chemical
Society* **112** (3), 1003 (1990).
- 192 A. A. Oskouei, O. Bram, A. Cannizzo, F. van Mourik, A. Tortschanoff, and M.
Chergui, *Chemical Physics* **350** (1-3), 104 (2008).
- 193 A. Cannizzo, O. Bram, G. Zgrablic, A. Tortschanoff, A. A. Oskouei, F. van Mourik,
and M. Chergui, *Optics Letters* **32** (24), 3555 (2007).
- 194 W. M. Campbell, K. W. Jolley, P. Wagner, K. Wagner, P. J. Walsh, K. C. Gordon,
L. Schmidt-Mende, M. K. Nazeeruddin, Q. Wang, M. Gratzel, and D. L. Officer,
Journal of Physical Chemistry C **111** (32), 11760 (2007).
- 195 T. Hasobe, H. Imahori, P. V. Kamat, T. K. Ahn, S. K. Kim, D. Kim, A. Fujimoto,
T. Hirakawa, and S. Fukuzumi, *Journal of the American Chemical Society* **127** (4),
1216 (2005).
- 196 B. C. O'Regan, I. Lopez-Duarte, M. V. Martinez-Diaz, A. Forneli, J. Albero, A.
Morandeira, E. Palomares, T. Torres, and J. R. Durrant, *Journal of the American
Chemical Society* **130** (10), 2906 (2008).
- 197 K. Konig, *Journal of Microscopy-Oxford* **200**, 83 (2000).
- 198 E. D. Sternberg, D. Dolphin, and C. Bruckner, *Tetrahedron* **54** (17), 4151 (1998).
- 199 M. R. Detty, S. L. Gibson, and S. J. Wagner, *Journal of Medicinal Chemistry* **47**
(16), 3897 (2004).
- 200 G. Liebsch, I. Klimant, B. Frank, G. Holst, and O. S. Wolfbeis, *Applied
Spectroscopy* **54** (4), 548 (2000).

- 201 T. Maisch, J. Baier, B. Franz, M. Maier, M. Landthaler, R. M. Szeimies, and W.
Baumler, Proceedings of the National Academy of Sciences of the United States of
America **104** (17), 7223 (2007).
- 202 A. Mills and A. Lepre, Analytical Chemistry **69** (22), 4653 (1997).
- 203 J. S. Lindsey, New Journal of Chemistry **15** (2-3), 153 (1991).
- 204 J. M. Tour, A. M. Rawlett, M. Kozaki, Y. X. Yao, R. C. Jagessar, S. M. Dirk, D. W.
Price, M. A. Reed, C. W. Zhou, J. Chen, W. Y. Wang, and I. Campbell, Chemistry-
a European Journal **7** (23), 5118 (2001).
- 205 R. Ziessel, M. Hissler, A. El-Ghayoury, and A. Harriman, Coordination Chemistry
Reviews **178**, 1251 (1998).
- 206 M. Gouterman, L. C. Snyder, and G. H. Wagniere, Journal of Molecular
Spectroscopy **11** (2), 108 (1963).
- 207 H. C. Longuethiggins, C. W. Rector, and J. R. Platt, Journal of Chemical Physics **18**
(9), 1174 (1950).
- 208 M. Gouterman, Journal of Chemical Physics **30** (5), 1139 (1959).
- 209 M. Gouterman, Journal of Molecular Spectroscopy **6** (1), 138 (1961).
- 210 W. Moffitt, Journal of Chemical Physics **22** (2), 320 (1954).
- 211 N. S. Ham and K. Ruedenberg, Journal of Chemical Physics **25** (1), 1 (1956).
- 212 N. S. Ham and K. Ruedenberg, Journal of Chemical Physics **25** (1), 13 (1956).
- 213 N. S. Ham and K. Ruedenberg, Journal of Chemical Physics **29** (6), 1199 (1958).
- 214 N. S. Ham and K. Ruedenberg, Journal of Chemical Physics **29** (6), 1215 (1958).
- 215 M. Levantino, Q. Huang, A. Cupane, M. Laberge, A. Hagarman, and R.
Schweitzer-Stenner, Journal of Chemical Physics **123** (5) (2005).
- 216 G. Herzberg and E. Teller, Zeitschrift Fur Physikalische Chemie-Abteilung B-
Chemie Der Elementarprozesse Aufbau Der Materie **21** (5/6), 410 (1933).
- 217 F. Duschinsky, Acta Physicochimica Urss **7** (4), 551 (1937).
- 218 F. Santoro, A. Lami, R. Improta, J. Bloino, and V. Barone, Journal of Chemical
Physics **128** (22) (2008).
- 219 Y. L. Niu, Q. A. Peng, C. M. Deng, X. Gao, and Z. G. Shuai, Journal of Physical
Chemistry A **114** (30), 7817 (2010).
- 220 K. K. Humphry-Baker R., Journal of Photochemistry and Photobiology a-Chemistry
31 (1), 105 (1985).
- 221 O. Ohno, Y. Kaizu, and H. Kobayashi, Journal of Chemical Physics **82** (4), 1779
(1985).
- 222 J. P. Strachan, S. Gentemann, J. Seth, W. A. Kalsbeck, J. S. Lindsey, D. Holten, and
D. F. Bocian, Journal of the American Chemical Society **119** (46), 11191 (1997).
- 223 G. G. Gurzadyan, T. H. Tran-Thi, and T. Gustavsson, Journal of Chemical Physics
108 (2), 385 (1998).
- 224 N. Mataga, Y. Shibata, H. Chosrowjan, N. Yoshida, and A. Osuka, Journal of
Physical Chemistry B **104** (17), 4001 (2000).
- 225 M. C. Yoon, D. H. Jeong, S. Cho, D. Kim, H. Rhee, and T. Joo, Journal of
Chemical Physics **118** (1), 164 (2003).
- 226 H. Z. Yu, J. S. Baskin, and A. H. Zewail, Journal of Physical Chemistry A **106** (42),
9845 (2002).
- 227 S. Franzen, L. Kiger, C. Poyart, and J. L. Martin, Biophysical Journal **80** (5), 2372
(2001).
- 228 Y. Kholodenko, E. A. Gooding, Y. Dou, M. Ikeda-Saito, and R. M. Hochstrasser,
Biochemistry **38** (18), 5918 (1999).

- 229 M. Lim, T. A. Jackson, and P. A. Anfinrud, *Science* **269** (5226), 962 (1995).
230 M. H. Lim, T. A. Jackson, and P. A. Anfinrud, *Journal of Physical Chemistry* **100**
(29), 12043 (1996).
- 231 J. L. Martin and M. H. Vos, *Hemoglobins, Pt C* **232**, 416 (1994).
232 J. W. Petrich, J. L. Martin, D. Houde, C. Poyart, and A. Orszag, *Biochemistry* **26**
(24), 7914 (1987).
- 233 J. W. Petrich, C. Poyart, and J. L. Martin, *Biochemistry* **27** (11), 4049 (1988).
234 B. Steiger, J. S. Baskin, F. C. Anson, and A. H. Zewail, *Angewandte Chemie-
International Edition* **39** (1), 257 (2000).
- 235 X. Ye, A. Demidov, and P. M. Champion, *Journal of the American Chemical
Society* **124** (20), 5914 (2002).
- 236 D. R. Green and J. C. Reed, *Science* **281** (5381), 1309 (1998).
237 M. O. Hengartner, *Nature* **407** (6805), 770 (2000).
- 238 D. Hamada, Y. Kuroda, M. Kataoka, S. Aimoto, T. Yoshimura, and Y. Goto,
Journal of Molecular Biology **256** (1), 172 (1996).
- 239 M. Negrier, S. Cianetti, M. H. Vos, J. L. Martin, and S. G. Kruglik, *Journal of
Physical Chemistry B* **110** (25), 12766 (2006).
- 240 W. Wang, X. Ye, A. A. Demidov, F. Rosca, T. Sjodin, W. X. Cao, M. Sheeran, and
P. M. Champion, *Journal of Physical Chemistry B* **104** (46), 10789 (2000).
- 241 R. M. Hochstrasser and D. K. Negus, *Proceedings of the National Academy of
Sciences of the United States of America-Biological Sciences* **81** (14), 4399 (1984).
- 242 S. M. Janes, G. Holtom, P. Ascenzi, M. Brunori, and R. M. Hochstrasser,
Biophysical Journal **51** (4), 653 (1987).
- 243 S. R. Yeh, S. W. Han, and D. L. Rousseau, *Accounts of Chemical Research* **31** (11),
727 (1998).
- 244 Y. Goto, L. J. Calciano, and A. L. Fink, *Proceedings of the National Academy of
Sciences of the United States of America* **87** (2), 573 (1990).
- 245 K. M. Sanchez, D. E. Schlamadinger, J. E. Gable, and J. E. Kim, *Journal of
Chemical Education* **85** (9), 1253 (2008).
- 246 W. D. Butt and D. Keilin, *Proceedings of the Royal Society of London Series B-
Biological Sciences* **156** (965), 429 (1962).
- 247 T. Y. Tsong, *Journal of Biological Chemistry* **249** (6), 1988 (1974).
248 T. Y. Tsong, *Biochemistry* **15** (25), 5467 (1976).
- 249 D. Loewenich and K. Kleinermanns, *Photochemistry and Photobiology* **83** (6), 1308
(2007).
- 250 M. H. Ha-Thi, N. Shafizadeh, L. Poisson, and B. Soep, *Physical Chemistry
Chemical Physics* **12** (45), 14985 (2010).
- 251 S. Ishizaka, T. Wada, and N. Kitamura, *Photochemical & Photobiological Sciences*
8 (4), 562 (2009).
- 252 S. Sorgues, L. Poisson, K. Raffael, L. Krim, B. Soep, and N. Shafizadeh, *Journal of
Chemical Physics* **124** (11) (2006).
- 253 Q. H. Gibson and S. Ainsworth, *Nature* **180** (4599), 1416 (1957).
- 254 M. R. Armstrong, J. P. Ogilvie, M. L. Cowan, A. M. Nagy, and R. J. D. Miller,
Proceedings of the National Academy of Sciences of the United States of America
100 (9), 4990 (2003).
- 255 A. Ostermann, R. Waschipky, F. G. Parak, and G. U. Nienhaus, *Nature* **404** (6774),
205 (2000).

- 256 F. Rosca, A. T. N. Kumar, D. Ionascu, X. Ye, A. A. Demidov, T. Sjodin, D.
Wharton, D. Barrick, S. G. Sligar, T. Yonetani, and P. M. Champion, *Journal of*
257 *Physical Chemistry A* **106** (14), 3540 (2002).
- 258 M. L. Quillin, R. M. Arduini, J. S. Olson, and G. N. Phillips, *Journal of Molecular*
Biology **234** (1), 140 (1993).
- 259 J. S. Griffiths, *The Theory of Transition Metal Ions*. (Cambridge University Press,
New York, 1961).
- 260 M. Gerloch, *Coordination Chemistry Reviews* **99**, 117 (1990).
- 261 R. D. Cowan, *The Theory of Atomic Structure and Spectra*. (The University of
California, Berkeley, 1981).
- 262 J. K. McCusker, *Accounts of Chemical Research* **36** (12), 876 (2003).
- 263 W. Gawelda, *Ecole Polytechnique Fédérale de Lausanne*, 2006.
- 264 A. Cannizzo, C. J. Milne, C. Consani, W. Gawelda, C. Bressler, F. van Mourik, and
M. Chergui, *Coordination Chemistry Reviews* **254** (21-22), 2677 (2010).
- 265 J. Ferguson, F. Herren, E. R. Krausz, M. Maeder, and J. Vrbancich, *Coordination*
Chemistry Reviews **64** (May), 21 (1985).
- 266 A. Juris, V. Balzani, F. Barigelletti, S. Campagna, P. Belser, and A. Vonzelewsky,
Coordination Chemistry Reviews **84**, 85 (1988).
- 267 J. P. Paris and W. W. Brandt, *Journal of the American Chemical Society* **81** (18),
5001 (1959).
- 268 A. Vlcek, *Coordination Chemistry Reviews* **200**, 933 (2000).
- 269 M. Gratzel, *Nature* **414** (6861), 338 (2001).
- 270 J. F. Letard, P. Guionneau, and L. Goux-Capes, *Spin Crossover in Transition Metal*
Compounds Iii **235**, 221 (2004).
- 271 A. Hauser, *Spin Crossover in Transition Metal Compounds Ii* **234**, 155 (2004).
- 272 T. Schonherr, J. Degen, E. Gallhuber, G. Hensler, and H. Yersin, *Chemical Physics*
Letters **158** (6), 519 (1989).
- 273 G. Calzaferri and R. Rytz, *Journal of Physical Chemistry* **99** (32), 12141 (1995).
- 274 R. M. Berger and D. R. Mcmillin, *Inorganica Chimica Acta* **177** (1), 65 (1990).
- 275 E. M. Kober and T. J. Meyer, *Inorganic Chemistry* **21** (11), 3967 (1982).
- 276 S. Ardo and G. J. Meyer, *Chemical Society Reviews* **38** (1), 115 (2009).
- 277 F. Gao, Y. Wang, D. Shi, J. Zhang, M. K. Wang, X. Y. Jing, R. Humphry-Baker, P.
Wang, S. M. Zakeeruddin, and M. Gratzel, *Journal of the American Chemical*
Society **130** (32), 10720 (2008).
- 278 A. Hagfeldt and M. Gratzel, *Accounts of Chemical Research* **33** (5), 269 (2000).
- 279 C. J. Barbe, F. Arendse, P. Comte, M. Jirousek, F. Lenzmann, V. Shklover, and M.
Gratzel, *Journal of the American Ceramic Society* **80** (12), 3157 (1997).
- 280 B. Oregan, J. Moser, M. Anderson, and M. Gratzel, *Journal of Physical Chemistry*
94 (24), 8720 (1990).
- 281 B. Oregan and M. Gratzel, *Nature* **353** (6346), 737 (1991).
- 282 E. Galoppini, *Coordination Chemistry Reviews* **248** (13-14), 1283 (2004).
- 283 Y. Tachibana, J. E. Moser, M. Gratzel, D. R. Klug, and J. R. Durrant, *Journal of*
Physical Chemistry **100** (51), 20056 (1996).
- 284 T. Hannappel, B. Burfeindt, W. Storck, and F. Willig, *Journal of Physical*
Chemistry B **101** (35), 6799 (1997).
- J. E. Moser, D. Noukakis, U. Bach, Y. Tachibana, D. R. Klug, J. R. Durrant, R.
Humphry-Baker, and M. Gratzel, *Journal of Physical Chemistry B* **102** (18), 3649
(1998).

- 285 T. Hannappel, C. Zimmermann, B. Meissner, B. Burfeindt, W. Storck, and F.
Willig, *Journal of Physical Chemistry B* **102** (18), 3651 (1998).
- 286 R. J. Ellingson, J. B. Asbury, S. Ferrere, H. N. Ghosh, J. R. Sprague, T. Q. Lian,
and A. J. Nozik, *Journal of Physical Chemistry B* **102** (34), 6455 (1998).
- 287 J. B. Asbury, R. J. Ellingson, H. N. Ghosh, S. Ferrere, A. J. Nozik, and T. Q. Lian,
Journal of Physical Chemistry B **103** (16), 3110 (1999).
- 288 J. R. Durrant, Y. Tachibana, I. Mercer, J. E. Moser, M. Gratzel, and D. R. Klug,
*Zeitschrift Fur Physikalische Chemie-International Journal of Research in Physical
Chemistry & Chemical Physics* **212**, 93 (1999).
- 289 T. A. Heimer, E. J. Heilweil, C. A. Bignozzi, and G. J. Meyer, *Journal of Physical
Chemistry A* **104** (18), 4256 (2000).
- 290 J. Kallioinen, V. Lehtovuori, P. Myllyperkio, and J. Korppi-Tommola, *Chemical
Physics Letters* **340** (3-4), 217 (2001).
- 291 G. Benko, J. Kallioinen, J. E. I. Korppi-Tommola, A. P. Yartsev, and V. Sundstrom,
Journal of the American Chemical Society **124** (3), 489 (2002).
- 292 S. A. Haque, Y. Tachibana, R. L. Willis, J. E. Moser, M. Gratzel, D. R. Klug, and J.
R. Durrant, *Journal of Physical Chemistry B* **104** (3), 538 (2000).
- 293 A. C. Bhasikuttan and T. Okada, *Journal of Physical Chemistry B* **108** (34), 12629
(2004).
- 294 M. K. Nazeeruddin, A. Kay, I. Rodicio, R. Humphrybaker, E. Muller, P. Liska, N.
Vlachopoulos, and M. Gratzel, *Journal of the American Chemical Society* **115** (14),
6382 (1993).
- 295 A. H. Zewail, *Journal of Physical Chemistry A* **104** (24), 5660 (2000).
- 296 S. A. Kovalenko, A. L. Dobryakov, J. Ruthmann, and N. P. Ernsting, *Physical
Review A* **59** (3), 2369 (1999).
- 297 B. Schmidt, S. Laimgruber, W. Zinth, and P. Gilch, *Applied Physics B-Lasers and
Optics* **76** (8), 809 (2003).
- 298 P. Fita, Y. Stepanenko, and C. Radzewicz, *Applied Physics Letters* **86** (2) (2005).
- 299 J. Shah, *Ieee Journal of Quantum Electronics* **24** (2), 276 (1988).
- 300 R. Schanz, S. A. Kovalenko, V. Kharlanov, and N. P. Ernsting, *Applied Physics
Letters* **79** (5), 566 (2001).
- 301 L. J. Zhao, J. L. P. Lustres, V. Farztdinov, and N. P. Ernsting, *Physical Chemistry
Chemical Physics* **7** (8), 1716 (2005).
- 302 H. R. Schanz, Humboldt-Universität zu Berlin, 2002.
- 303 D. F. Zernike and J. E. Midwinter, *Applied Nonlinear Optics*. (Wiley, New York,
1973).
- 304 G. Zgrablic, Ecole Polytechnique Fédérale de Lausanne, 2006.
- 305 O. Bräm, Ecole Polytechnique Fédérale de Lausanne, 2006.
- 306 L. Placentino, E. Pace, G. Naletto, and G. Tondello, *Optical Engineering* **35** (11),
3342 (1996).
- 307 K. Kato, *Ieee Journal of Quantum Electronics* **22** (7), 1013 (1986).
- 308 D. E. Hare and C. M. Sorensen, *Journal of Chemical Physics* **93** (1), 25 (1990).
- 309 R. Luchowski, *Chemical Physics Letters* **501** (4-6), 572 (2011).
- 310 J. R. Lakowicz, I. Gryczynski, Z. Gryczynski, E. Danielsen, and M. J. Wirth,
Journal of Physical Chemistry **96** (7), 3000 (1992).
- 311 A. Cupane, M. Leone, E. Vitrano, and L. Cordone, *European Biophysics Journal* **23**
(6), 385 (1995).

- 312 E. R. Henry, W. A. Eaton, and R. M. Hochstrasser, Proceedings of the National
Academy of Sciences of the United States of America **83** (23), 8982 (1986).
- 313 T. Gustavsson, R. Improta, and D. Markovitsi, Journal of Physical Chemistry
Letters **1** (13), 2025 (2010).
- 314 D. Markovitsi, T. Gustavsson, and A. Banyasz, Mutation Research-Reviews in
Mutation Research **704** (1-3), 21 (2010).
- 315 N. K. Schwalb and F. Temps, Science **322** (5899), 243 (2008).
- 316 D. P. Zhong, L. Y. Zhang, L. J. Wang, Y. T. Kao, W. H. Qiu, Y. Yang, and O.
Okobiah, Proceedings of the National Academy of Sciences of the United States of
America **104** (47), 18461 (2007).
- 317 D. P. Zhong and A. H. Zewail, Proceedings of the National Academy of Sciences of
the United States of America **98** (21), 11867 (2001).
- 318 A. A. Hassanali, T. P. Li, D. P. Zhong, and S. J. Singer, Journal of Physical
Chemistry B **110** (21), 10497 (2006).
- 319 L. Nilsson and B. Halle, Proceedings of the National Academy of Sciences of the
United States of America **102** (39), 13867 (2005).
- 320 E. Lindahl, B. Hess, and D. van der Spoel, Journal of Molecular Modeling **7** (8),
306 (2001).
- 321 X. Daura, R. Suter, and W. F. van Gunsteren, Journal of Chemical Physics **110** (6),
3049 (1999).
- 322 P. Mark and L. Nilsson, Journal of Physical Chemistry B **106** (36), 9440 (2002).
- 323 T. P. Li, A. A. P. Hassanali, Y. T. Kao, D. P. Zhong, and S. J. Singer, Journal of the
American Chemical Society **129** (11), 3376 (2007).
- 324 T. Darden, D. York, and L. Pedersen, Journal of Chemical Physics **98** (12), 10089
(1993).
- 325 U. Essmann, L. Perera, M. L. Berkowitz, T. Darden, H. Lee, and L. G. Pedersen,
Journal of Chemical Physics **103** (19), 8577 (1995).
- 326 B. Hess, H. Bekker, H. J. C. Berendsen, and J. G. E. M. Fraaije, Journal of
Computational Chemistry **18** (12), 1463 (1997).
- 327 A. L. Sobolewski and W. Domcke, Chemical Physics Letters **315** (3-4), 293 (1999).
- 328 H. J. C. Berendsen, J. P. M. Postma, W. F. Vangunsteren, A. Dinola, and J. R.
Haak, Journal of Chemical Physics **81** (8), 3684 (1984).
- 329 X. H. Shen and J. R. Knutson, Chemical Physics Letters **339** (3-4), 191 (2001).
- 330 W. H. Qiu, L. Y. Zhang, Y. T. Kao, W. Y. Lu, T. P. Li, J. Kim, G. M. Sollenberger,
L. J. Wang, and D. P. Zhong, Journal of Physical Chemistry B **109** (35), 16901
(2005).
- 331 I. Okazaki, Y. Hara, and M. Nagaoka, Chemical Physics Letters **337** (1-3), 151
(2001).
- 332 J. S. Baskin, H. Z. Yu, and A. H. Zewail, Journal of Physical Chemistry A **106** (42),
9837 (2002).
- 333 M. Enescu, K. Steenkeste, F. Tfibel, and M. P. Fontaine-Aupart, Physical
Chemistry Chemical Physics **4** (24), 6092 (2002).
- 334 X. Liu, A. Mahammed, U. Tripathy, Z. Gross, and R. P. Steer, Chemical Physics
Letters **459** (1-6), 113 (2008).
- 335 X. Liu, U. Tripathy, S. V. Bhosale, S. J. Langford, and R. P. Steer, Journal of
Physical Chemistry A **112** (38), 8986 (2008).
- 336 M. Maiti, B. R. Danger, and R. P. Steer, Journal of Physical Chemistry A **113** (42),
11318 (2009).

- 337 N. Mataga, H. Chosrowjan, and S. Taniguchi, *Journal of Photochemistry and*
338 *Photobiology C-Photochemistry Reviews* **6** (1), 37 (2005).
- 339 Y. Mizutani and T. Kitagawa, *Bulletin of the Chemical Society of Japan* **75** (4), 623
(2002).
- 340 O. Schalk, H. Brands, T. S. Balaban, and A. N. Unterreiner, *Journal of Physical*
341 *Chemistry A* **112** (8), 1719 (2008).
- 342 M. Schmitt, B. Dietzek, G. Hermann, and J. Popp, *Laser & Photonics Reviews* **1**
(1), 57 (2007).
- 343 U. Tripathy, D. Kowalska, X. Liu, S. Velate, and R. P. Steer, *Journal of Physical*
344 *Chemistry A* **112** (26), 5824 (2008).
- 345 K. Y. Yeon, D. Jeong, and S. K. Kim, *Chemical Communications* **46** (30), 5572
(2010).
- 346 J. Rodriguez and D. Holten, *Journal of Chemical Physics* **91** (6), 3525 (1989).
- 347 J. Rodriguez, C. Kirmaier, and D. Holten, *Journal of Chemical Physics* **94** (9), 6020
(1991).
- 348 D. J. Quimby and F. R. Longo, *Journal of the American Chemical Society* **97** (18),
5111 (1975).
- 349 A. Singh and L. W. Johnson, *Spectrochimica Acta Part a-Molecular and*
350 *Biomolecular Spectroscopy* **64** (3), 761 (2006).
- 351 S. Schlücker, J. Koster, M. Nissum, J. Popp, and W. Kiefer, *Journal of Physical*
352 *Chemistry A* **105** (41), 9482 (2001).
- 353 P. M. Champion, F. Rosca, D. Ionascu, W. X. Cao, and X. Ye, *Faraday Discussions*
354 **127**, 123 (2004).
- 355 F. Gruia, M. Kubo, X. Ye, and P. M. Champion, *Biophysical Journal* **94** (6), 2252
(2008).
- 356 F. Gruia, M. Kubo, X. Ye, D. Ionascu, C. Lu, R. K. Poole, S. R. Yeh, and P. M.
357 Champion, *Journal of the American Chemical Society* **130** (15), 5231 (2008).
- 358 F. Gruia, X. Ye, D. Ionascu, M. Kubo, and P. M. Champion, *Biophysical Journal* **93**
(12), 4404 (2007).
- 359 F. Rosca, A. T. N. Kumar, D. Ionascu, X. Ye, A. A. Demidov, and P. M.
360 Champion, *Bulletin of the Chemical Society of Japan* **75** (5), 1093 (2002).
- 361 L. Zhu, P. Li, M. Huang, J. T. Sage, and P. M. Champion, *Physical Review Letters*
72 (2), 301 (1994).
- 362 F. Rosca, A. T. N. Kumar, X. Ye, T. Sjodin, A. A. Demidov, and P. M. Champion,
363 *Journal of Physical Chemistry A* **104** (18), 4280 (2000).
- 364 S. Perun, J. Tatchen, and C. M. Marian, *Chemphyschem* **9** (2), 282 (2008).
- 365 J. Rodriguez, C. Kirmaier, and D. Holten, *Journal of the American Chemical*
366 *Society* **111** (17), 6500 (1989).
- 367 S. Gentemann, C. J. Medforth, T. Ema, N. Y. Nelson, K. M. Smith, J. Fajer, and D.
368 Holten, *Chemical Physics Letters* **245** (4-5), 441 (1995).
- 369 S. Gentemann, N. Y. Nelson, L. Jaquinod, D. J. Nurco, S. H. Leung, C. J. Medforth,
370 K. M. Smith, J. Fajer, and D. Holten, *Journal of Physical Chemistry B* **101** (7), 1247
(1997).
- 371 M. Ravikanth and T. K. Chandrashekar, *Journal of Photochemistry and*
Photobiology a-Chemistry **74** (2-3), 181 (1993).
- 372 Y. Kajii, K. Obi, I. Tanaka, and S. Tobita, *Chemical Physics Letters* **111** (4-5), 347
(1984).
- 373 S. Tobita, Y. Kajii, and I. Tanaka, *Acs Symposium Series* **321**, 219 (1986).

- 362 L. Pekkarinen and H. Linschitz, *Journal of the American Chemical Society* **82** (10),
2407 (1960).
- 363 Gradyush.At and M. P. Tsvirko, *Optics and Spectroscopy-Ussr* **31** (4), 291 (1971).
- 364 A. Antipas and M. Gouterman, *Journal of the American Chemical Society* **105** (15),
4896 (1983).
- 365 L. Edwards, D. H. Dolphin, Gouterman.M, and A. D. Adler, *Journal of Molecular
Spectroscopy* **38** (1), 16 (1971).
- 366 N. Shafizadeh, S. Sorgues, and B. Soep, *Chemical Physics Letters* **391** (4-6), 380
(2004).
- 367 P. Brodard and E. Vauthey, *Chemical Physics Letters* **309** (3-4), 198 (1999).
- 368 L. X. Chen, X. Y. Zhang, E. C. Wasinger, K. Attenkofer, G. Jennings, A. Z.
Muresan, and J. S. Lindsey, *Journal of the American Chemical Society* **129** (31),
9616 (2007).
- 369 A. V. Zamyatin, A. V. Gusev, and M. A. J. Rodgers, *Journal of the American
Chemical Society* **126** (49), 15934 (2004).
- 370 X. Y. Zhang, E. C. Wasinger, A. Z. Muresan, K. Attenkofer, G. Jennings, J. S.
Lindsey, and L. X. Chen, *Journal of Physical Chemistry A* **111** (46), 11736 (2007).
- 371 O. T. Ehrler, J. P. Yang, A. B. Sugiharto, A. N. Unterreiner, and M. M. Kappes,
Journal of Chemical Physics **127** (18) (2007).
- 372 L. X. Chen, X. Y. Zhang, E. C. Wasinger, J. V. Lockard, A. B. Stickrath, M. W.
Mara, K. Attenkofer, G. Jennings, G. Smolentsev, and A. Soldatov, *Chemical
Science* **1** (5), 642 (2010).
- 373 O. Horvath, R. Huszank, Z. Valicsek, and G. Lendvay, *Coordination Chemistry
Reviews* **250** (13-14), 1792 (2006).
- 374 M. S. Liao and S. Scheiner, *Journal of Chemical Physics* **117** (1), 205 (2002).
- 375 M. S. Liao and S. Scheiner, *Journal of Chemical Physics* **116** (9), 3635 (2002).
- 376 C. Consani, O. Bräm, F. Van Mourik, A. Cannizzo, and M. Chergui, in preparation.
- 377 O. Bram, A. A. Oskouei, A. Tortschanoff, F. van Mourik, M. Madrid, J. Echave, A.
Cannizzo, and M. Chergui, *Journal of Physical Chemistry A* **114** (34), 9034 (2010).
- 378 O. B. Cristina Consani, Frank van Mourik, Andrea Cannizzo, Majed Chergui, in
preparation.
- 379 R. Schweitzer-Stenner, *Journal of Physical Chemistry B* **112** (33), 10358 (2008).
- 380 A. Schejter and B. Plotkin, *Biochemical Journal* **255** (1), 353 (1988).
- 381 D. Eden, J. B. Matthew, J. J. Rosa, and F. M. Richards, *Proceedings of the National
Academy of Sciences of the United States of America-Biological Sciences* **79** (3),
815 (1982).
- 382 R. P. Steer, U. Tripathy, D. Kowalska, X. Liu, and S. Velate, *Journal of Physical
Chemistry A* **112** (26), 5824 (2008).
- 383 P. M. Champion and R. Lange, *Journal of Chemical Physics* **73** (12), 5947 (1980).
- 384 P. M. Champion and G. J. Perreault, *Journal of Chemical Physics* **75** (1), 490
(1981).
- 385 O. Bräm, F. Messina, A. El-Zohry, A. Cannizzo, and M. Chergui, Submitted to
Journal of the American Chemical Society (2011).
- 386 K. Nakashima, K. Yuda, Y. Ozaki, and I. Noda, *Applied Spectroscopy* **57** (11),
1381 (2003).
- 387 C. Twist, C. Royer, and B. Alpert, *Biochemistry* **41** (32), 10343 (2002).
- 388 K. J. Willis, A. G. Szabo, M. Zuker, J. M. Ridgeway, and B. Alpert, *Biochemistry*
29 (22), 5270 (1990).

- 389 Z. Gryczynski and E. Bucci, *Biophysical Chemistry* **74** (3), 187 (1998).
390 E. Bismuto, G. Irace, and E. Gratton, *Biochemistry* **28** (4), 1508 (1989).
391 L. Y. Zhang, Y. T. Kao, W. H. Qiu, L. J. Wang, and D. P. Zhong, *Journal of*
Physical Chemistry B **110** (37), 18097 (2006).
392 J. Gardecki, M. L. Horng, A. Papazyan, and M. Maroncelli, *Journal of Molecular*
Liquids **65-6**, 49 (1995).
393 E. M. Kober, B. P. Sullivan, and T. J. Meyer, *Inorganic Chemistry* **23** (14), 2098
(1984).
394 S. Fantacci, F. De Angelis, and A. Selloni, *Journal of the American Chemical*
Society **125** (14), 4381 (2003).
395 A. Cannizzo, A. M. Blanco-Rodriguez, A. El Nahhas, J. Sebera, S. Zalis, A. Vlcek,
and M. Chergui, *Journal of the American Chemical Society* **130** (28), 8967 (2008).
396 J. Kallioinen, G. Benko, P. Myllyperkio, L. Khriachtchev, B. Skarman, R.
Wallenberg, M. Tuomikoski, J. Korppi-Tommola, V. Sundstrom, and A. P. Yartsev,
Journal of Physical Chemistry B **108** (20), 6365 (2004).
397 S. Meng and E. Kaxiras, *Nano Letters* **10** (4), 1238 (2010).
398 W. R. Duncan and O. V. Prezhdo, *Annual Review of Physical Chemistry* **58**, 143
(2007).
399 W. R. Duncan, W. M. Stier, and O. V. Prezhdo, *Journal of the American Chemical*
Society **127** (21), 7941 (2005).
400 J. R. Li, I. Kondov, H. B. Wang, and M. Thoss, *Journal of Physical Chemistry C*
114 (43), 18481 (2010).
401 F. De Angelis, S. Fantacci, E. Mosconi, M. K. Nazeeruddin, and M. Gratzel,
Journal of Physical Chemistry C **115** (17), 8825 (2011).
402 F. De Angelis, S. Fantacci, A. Selloni, M. K. Nazeeruddin, and M. Gratzel, *Journal*
of Physical Chemistry C **114** (13), 6054 (2010).
403 W. Gawelda, M. Johnson, F. M. F. de Groot, R. Abela, C. Bressler, and M. Chergui,
Journal of the American Chemical Society **128** (15), 5001 (2006).
404 R. Huber, J. E. Moser, M. Gratzel, and J. Wachtveitl, *Journal of Physical Chemistry*
B **106** (25), 6494 (2002).
405 R. Huber, J. E. Moser, M. Gratzel, and J. Wachtveitl, *Ultrafast Phenomena Xiii* **71**,
316 (2003).
406 J. Schnadt, P. A. Bruhwiler, L. Patthey, J. N. O'Shea, S. Sodergren, M. Odelius, R.
Ahuja, O. Karis, M. Bassler, P. Persson, H. Siegbahn, S. Lunell, and N.
Martensson, *Nature* **418** (6898), 620 (2002).
407 J. Kallioinen, G. Benko, V. Sundstrom, J. E. I. Korppi-Tommola, and A. P. Yartsev,
Journal of Physical Chemistry B **106** (17), 4396 (2002).
408 C. Consani, M. Premont-Schwarz, A. ElNahhas, C. Bressler, F. van Mourik, A.
Cannizzo, and M. Chergui, *Angewandte Chemie-International Edition* **48** (39),
7184 (2009).
409 F. M. Jaeger and J. A. van Dijk, *Zeitschrift Fur Anorganische Und Allgemeine*
Chemie **227** (3), 273 (1936).
410 Y. Tachibana, M. K. Nazeeruddin, M. Gratzel, D. R. Klug, and J. R. Durrant,
Chemical Physics **285** (1), 127 (2002).
411 P. Bonhote, A. P. Dias, N. Papageorgiou, K. Kalyanasundaram, and M. Gratzel,
Inorganic Chemistry **35** (5), 1168 (1996).

Curriculum Vitae

Personal details

Olivier Christian Bräm

Personal address:

Rue de l'Avenir 25A, 1020 Renens, Switzerland

Professional address:

EPFL SB ISIC LSU; CH H1 575; Station 6; CH-1015 Lausanne; Switzerland

Professional phone: +41216930453

Personal phone: +41788149948

Email address: olivier.braem@epfl.ch

Date of birth: 1st of February, 1983

Nationality: Swiss & French

Civil status: Married, 1 child

Education

2007-2011 PhD at the Swiss Federal Institute of Technology – Lausanne (EPFL) under the supervision of Prof. Majed Chergui, Ultrafast Spectroscopy Laboratory (LSU), Doctoral school of Physics.

2005-2007 Master of Science in Physics at EPFL in the LSU

2001-2005 Bachelor in Physics at EPFL

Project experience

2007-2011 **PhD Thesis**, Ultrafast visible and ultraviolet fluorescence studies of molecular and biological systems in solution

Fall 2006 **Master project** on fluorescence up-conversion in the UV range

Spring 2006 Photoluminescence time-resolved spectroscopic studies of C₆₀, LSU

Fall 2005 Surface Enhanced Raman Spectroscopy on silver nanoparticles, LSU

Summer 2005 Raman Spectroscopy on beta-carotene and lycopene in various solvents, Department of life science, under the direction of prof. Bruno Robert, CEA, Saclay

Languages

French (Mother tongue)

English (Fluent)

German (Beginner)

Attended courses

1. Photochemistry II, Jacques-Edouard Moser, Summer semester 2007-2008
2. Photochemistry I, Jacques-Edouard Moser, Winter semester 2007-2008
3. Modelling magnetic and spectroscopic properties of molecules containing d- and f-elements, Claude Auguste Erwin Daul, S. semester 2007-2008
4. Computation of molecular properties, François Rotzinger, S. semester 2006-2007
5. Ultrafast phenomena, Franck van Mourik, S. semester 2006-2007

Teaching experiences

- 2007-2011** PhD assistant for molecular physics course (56 h), EPFL
PhD assistant for molecular physics experiment (fs pump-probe) (60 h), EPFL
- 2004-2006** student assistant for physics practical work, EPFL
- 2003-2004** student assistant for physics courses, EPFL

Oral presentations

1. *Ultrafast electronic relaxation of metalloporphyrins: from bulk to protein environment*; O. Bräm, C. Consani, A. Cannizzo, F. van Mourik, and M. Chergui; Winter School of Ultrafast Spectroscopy, Saint-Luc, Switzerland; March 4-6, 2011.
2. *Electronic dephasing processes of non-polar solutes in both polar and non-polar solvents studied by UV 3-pulse photon echo measurements*; A. Cannizzo, A. Ajdarzadeh Oskouei, O. Bräm, F. van Mourik, A. Tortschanoff and M. Chergui, First International Conference on Ultrafast Structural Dynamics (ICUSD'10); Lausanne, Switzerland, June 2010.
3. *Solvation dynamics of p-terphenyl and tryptophan studied by UV Photon Echo and fluorescence Up-Conversion*; A. Ajdarzadeh Oskouei, A. Cannizzo, O. Bräm, C. Consani, F. van Mourik, A. Tortschanoff and M. Chergui; Post-symposium of CMDS2008 "New Frontiers in Advanced Spectroscopy of Complex Systems", Kyoto, Japan, Aug 2008.

4. *UV spectroscopies as a tool to study protein functionality*; C. Consani, A. Ajdarzadeh Oskouei, O. Bräm, F. van Mourik, A. Cannizzo, M. Chergui; Post-symposium of CMDS2008 “New Frontiers in Advanced Spectroscopy of Complex Systems”, Kyoto, Japan, Aug 2008.
5. *Photon Echo experiments in the UV: Towards investigation of protein dynamics*; A. Ajdarzadeh Oskouei, A. Tortschanoff, A. Cannizzo, O. Bräm, F. van Mourik, and M. Chergui; Swiss Physical society (SPS) annual conference, Geneva, Switzerland, March 2008.
6. *UV Photon Echo & UV fluorescence up-conversion spectroscopy*; A. Ajdarzadeh Oskouei, A. Tortschanoff, A. Cannizzo, O. Bräm, F. van Mourik, and M. Chergui; Winter School of Ultrafast Spectroscopy, Ovronnaz –Switzerland; March 7-9, 2008.
7. *Ultraviolet Photon-Echo and Broad-band Fluorescence Up-conversion studies of molecules in solvents*; A. Tortschanoff, A. Ajdarzadeh Oskouei, A. Cannizzo, O. Bräm, F. van Mourik, and M. Chergui; MARIE CURIE CHAIR CONFERENCE, "Recent advances in laser spectroscopy and laser technology", Lodz, Poland; May, 2007.
8. *A novel polychromatic femtosecond time-resolved fluorescence set-up in the UV for investigation of biological and chemical systems*; O. Bräm, A. Cannizzo, A. Ajdarzadeh Oskouei, F. van Mourik, A. Tortschanoff, M. Chergui; SCS (Swiss Chemical Society) Fall Meeting, Lausanne, Switzerland Sept. 2007.
9. *Towards investigation of femtosecond tryptophan solvation dynamics by broad-band fluorescence up-conversion in the UV*; O. Bräm, A. Ajdarzadeh Oskouei, A. Cannizzo, F. van Mourik, A. Tortschanoff, M. Chergui; SPS (Swiss Physical Society Conference), Zurich, Switzerland; Feb. 2007.

Poster presentations

1. *Excited state dynamics of tetraphenyl- and octaethyl-metalloporphyrins studied with time-resolved fluorescence*; O. Bräm, A. Cannizzo, M. Chergui, SCS (Swiss Chemical Society) Fall Meeting, Lausanne, Switzerland Sept. 2010.
2. *Electron injection into semiconductor thin films studied with time-resolved fluorescence*; O. Bräm, A. ElNahas, A. Cannizzo, M. Chergui, SCS (Swiss Chemical Society) Fall Meeting, Lausanne, Switzerland Sept. 2010.
3. *Electronic dephasing processes of non-polar solutes in both polar and non-polar solvents studied by UV 3-pulse photon echo measurements*; A. Ajdarzadeh. Oskouei, O. Bräm, A. Tortschanoff, F. van Mourik, A. Cannizzo and M. Chergui, SCS (Swiss Chemical Society) Fall Meeting, ETH Zurich, Switzerland; Sep. 2010.
4. *Femtosecond fluorescence up-conversion studies of electron injection in dye sensitized solar cells*; O. Bräm, A. Cannizzo, M. Chergui, 17th international conference on Ultrafast Phenomena, Snowmass Village, Colorado, United States, July 2010.

5. *Femtosecond UV Studies of Relaxation Processes in Cytochrome C*; A. Cannizzo, O. Bräm, C. Consani, F. van Mourik and M. Chergui, 17th international conference on Ultrafast Phenomena, Snowmass Village, Colorado, United States, July 2010.
6. *Electronic and vibrational relaxations of metalloporphyrins investigated by fs time-resolved fluorescence*; O. Bräm, A. Cannizzo and M. Chergui, 1st International Conference on Ultrafast Structural Dynamics; Lausanne, Switzerland, June 2010.
7. *Electronic dephasing processes of non-polar solutes in both polar and non-polar solvents studied by UV 3-pulse photon echo measurements*; A. Ajdarzadeh Oskouei, O. Bräm, A. Tortschanoff, F. van Mourik, A. Cannizzo and M. Chergui, 1st International Conference on Ultrafast Structural Dynamics; Lausanne, Switzerland, June 2010.
8. *Effect of the chirp on UV Photon Echo Peak Shift (PEPS) measurements*; A. Ajdarzadeh Oskouei, A. Cannizzo, O. Bräm, F. van Mourik, A. Tortschanoff and M. Chergui; Photonics day, EPFL, Switzerland; Nov. 2009.
9. *Femtosecond UV spectroscopic studies of cytochrome c dynamics*; O. Bräm, C. Consani, F. van Mourik, A. Cannizzo, M. Chergui; SCS (Swiss Chemical Society) Fall Meeting, EPFL, Switzerland; Sept. 2009.
10. *UV 3-pulse photon echo experiments on diphenylacetylene solution*; A. Ajdarzadeh Oskouei, A. Cannizzo, O. Bräm, F. van Mourik, A. Tortschanoff and M. Chergui; SCS (Swiss Chemical Society) Fall Meeting, EPFL, Switzerland; Sept. 2009.
11. *Femtosecond UV Fluorescence and Transient Absorption studies of Cytochrome c protein dynamics*; O. Bräm, C. Consani, F. van Mourik, A. Cannizzo, M. Chergui; XXIV International Conference on Photochemistry, Toledo, Spain, July 2009.
12. *UV 3-pulse photon echo experiments on diphenylacetylene solution*; A. Ajdarzadeh Oskouei, A. Cannizzo, O. Bräm, F. van Mourik, A. Tortschanoff and M. Chergui; XXIV International Conference on Photochemistry, Toledo, Spain, July 2009.
13. *Photon Echo spectroscopy in the UV*; A. Ajdarzadeh Oskouei, A. Cannizzo, O. Bräm, C. Consani, F. van Mourik, A. Tortschanoff and M. Chergui; Photonics day, EPFL, Switzerland; Oct. 2008.
14. *Photon Echo spectroscopy in the UV: Towards the investigation of protein dynamics*; A. Ajdarzadeh Oskouei, A. Cannizzo, O. Bräm, Cristina Consani, F. van Mourik, A. Tortschanoff and M. Chergui; The 4th International Conference on Coherent multidimensional Spectroscopy (CMDS2008), Kyoto, Japan, August 2008.
15. *Broadband femtosecond fluorescence up-conversion and Photon Echo experiments in the UV*; O. Bräm, A. Cannizzo, A. Ajdarzadeh Oskouei, F. van Mourik, A. Tortschanoff, M. Chergui; Ultrafast Phenomena conference 2008, Stresa, Italy, June 2008.
16. *Polychromatic femtosecond fluorescence up-conversion set-up in the UV: Towards tryptophan solvation dynamics*; O. Bräm, A. Cannizzo, A. Ajdarzadeh Oskouei, F. van Mourik, A. Tortschanoff, M. Chergui; European Science Foundation summer school of structural dynamics; Vilamoura; Portugal; June 2008.
17. *First UV Photon-Echo experiments on tryptophan. Towards investigation of protein dynamics*; A. Ajdarzadeh Oskouei, O. Bräm, A. Cannizzo, F. van Mourik A. Tortschanoff,

- M. Chergui; European Science Foundation summer school of structural dynamics; Vilamoura; Portugal; June 2008.
18. *Femtosecond dynamics of UV emitting dyes by broad band fluorescence upconversion*; O. Bräm, A. Cannizzo, A. Ajdarzadeh Oskouei, F. van Mourik, A. Tortschanoff, M. Chergui; SPS (Swiss Physical Society) Fall Meeting, University of Geneva (Uni MAIL), Switzerland; March 2008.
 19. *Ultrafast Ultraviolet Photon-Echo for the study of protein dynamics*; A. Ajdarzadeh Oskouei, O. Bräm, A. Cannizzo, F. van Mourik A. Tortschanoff, M. Chergui; Photonics day, EPFL, Switzerland; Oct. 2007.
 20. *Development of a broad-band femtosecond time-resolved fluorescence set-up in the UV: application to biological and chemical systems*; O. Bräm, A. Cannizzo, A. Ajdarzadeh Oskouei, F. van Mourik, A. Tortschanoff, M. Chergui; 10th Conference on Methods and Applications of Fluorescence: Spectroscopy, Imaging and Probes, Congress Center - Salzburg, Austria, Sept. 2007.
 21. *Ultraviolet Photon-Echo for the study of protein dynamics*; A. Ajdarzadeh Oskouei, O. Bräm, A. Cannizzo, F. van Mourik A. Tortschanoff, M. Chergui; SCS (Swiss Chemical Society) Fall Meeting, EPFL, Switzerland; Sept. 2007.
 22. *New broad-band femtosecond fluorescence up-conversion set-up in the UV for investigation of tryptophan solvation dynamics*; O. Bräm, A. Cannizzo, A. Ajdarzadeh Oskouei, F. van Mourik, A. Tortschanoff, M. Chergui; Femtochemistry and Femtobiology 8, Magdalen College, Oxford, England; July 2007.
 23. *UV Photon-Echo for the study of protein dynamics*; A. Ajdarzadeh Oskouei, O. Bräm, A. Cannizzo, F. van Mourik A. Tortschanoff, M. Chergui; Femtochemistry and Femtobiology 8, Magdalen College, Oxford, England; July 2007.
 24. *“Femtosecond tryptophan solvation dynamics by UV-Photon Echo”*; A. Ajdarzadeh Oskouei, O. Bräm, A. Cannizzo, F. van Mourik A. Tortschanoff, M. Chergui; OptETH Winter school, ETH, Zurich, Switzerland, Feb. 2007.
 25. *Towards femtosecond tryptophan solvation dynamics by polychromatic fluorescence upconversion in the UV*; A. Ajdarzadeh Oskouei, O. Bräm, A. Cannizzo, F. Van Mourik A. Tortschanoff, M. Chergui; Photonics day, EPFL, Switzerland, Nov. 2006.

Publications

1. “Ultrafast UV and Visible Studies of the Electronic Relaxation Processes in Cytochrome C”
Olivier Bräm, Cristina Consani, Andrea Cannizzo, Majed Chergui;
Submitted to Journal of Physical Chemistry B
2. “Energy transfer and relaxation mechanisms in Cytochrome C”
Cristina Consani, Olivier Bräm, Frank van Mourik, Andrea Cannizzo, Majed Chergui;
Submitted to Chemical Physics
3. “Polychromatic femtosecond fluorescence studies of metal-polypyridine complexes in solution and on semiconductor thin films”
Olivier Bräm, Fabrizio Messina, Ahmed El-Zohry, Andrea Cannizzo, Majed Chergui;
Work in progress
4. “Ultrafast Excited-State Dynamics of Rhenium(I) Photosensitizers [Re(Cl)(CO)₃(N,N)] and [Re(imidazole)(CO)₃(N,N)]⁺: Diimine Effects”
Amal El Nahhas, Cristina Consani, Ana María Blanco-Rodríguez, Kyle M. Lancaster, Olivier Bräm, Andrea Cannizzo, Michael Towrie, Ian P. Clark, Stanislav Zalis, Majed Chergui, and Antonín Vlcek, Jr.;
Inorganic Chemistry, **50**, 2932–2943 (2011)
5. “Relaxation Dynamics of Tryptophan in Water: A UV Fluorescence Up-Conversion and Molecular Dynamics Study”
Olivier Bräm, Ahmad Oskouei, Andreas Tortshanoff, Frank van Mourik, Marcos Madrid, Julian Echave, Andrea Cannizzo and Majed Chergui;
Journal of Physical Chemistry A, **114**, 9034–9042 (2010)
6. “Three pulse UV Photon Echo studies of molecules in solution: effect of the chirp”
Ahmad Ajdarzadeh Oskouei, Andreas Tortschanoff, Olivier Bräm, Frank van Mourik, Andrea Cannizzo, and Majed Chergui;
Journal of Chemical Physics, **133**, 064506 (2010)
7. “Coherent Ultrafast Torsional Motion and Isomerisation of a Biomimetic Dipolar Photoswitch”
Julien Briand, Olivier Bräm, Julien Réhault, Jérémie Léonard, Andrea Cannizzo, Majed Chergui, Vinicio Zanirato, Massimo Olivucci, Jan Helbing and Stefan Haacke;
Physical Chemistry Chemical Physics, **12**, 3178 (2010)

8. “First Photon Echo Peak Shift experiments in the UV: p-terphenyl in different solvents”
Ahmad Ajdarzadeh Oskouei, Olivier Bräm, Andrea Cannizzo, Frank van Mourik, Andreas Tortschanoff and M. Chergui;
Journal of Molecular Liquids, **141**, 118-123 (2008)
9. “Broadband femtosecond fluorescence up-conversion and Photon Echo experiments in the UV”
Olivier Bräm, Andrea Cannizzo, Ahmad Ajdarzadeh Oskouei, Andreas Tortschanoff, Frank van Mourik, and Majed Chergui;
Ultrafast Phenomena XVI, Proceedings of the 16th International Conference, Springer Series in Chemical Physics, **92**, 346 (2008)
10. “Ultrafast UV photon echo peak shift and fluorescence up conversion studies of non-polar solvation dynamics”
Ahmad Ajdarzadeh Oskouei, Olivier Bräm, Andrea Cannizzo, Frank van Mourik, Andreas Tortschanoff and Majed Chergui;
Chemical Physics, **350**, 104–110 (2008)
11. “A femtosecond fluorescence up-conversion set-up with broadband detection in the Ultraviolet”
Andrea Cannizzo, Olivier Bräm, Goran Zgrablic, Andreas Tortschanoff, Ahmad Ajdarzadeh Oskouei, Frank van Mourik and Majed Chergui;
Optics Letters, **32**, No. 24, 3555 (2007)

Remerciements

J'aimerais avant tout exprimer ma profonde gratitude à l'égard de celui qui m'a permis de commencer ce travail de doctorat, mon directeur de thèse, le professeur *Majed Chergui*. Son ouverture d'esprit, son altruisme et son soutien permanent ont été le gage d'une atmosphère de travail agréable et motivante. Les échanges que nous avons pu avoir m'ont énormément apporté tant au niveau scientifique qu'au niveau humain. Enfin merci Majed de m'avoir fait découvrir le monde passionnant de la femtochimie!

Je suis aussi profondément reconnaissant envers mon co-directeur de thèse, Dr *Andrea Cannizzo*, sans qui mon travail de recherche n'aurait pas eu la même profondeur. Certaines personnes sont particulièrement douées pour transmettre leur savoir, Andrea en fait partie sans aucun doute. Outre son éloquence et ses talents pédagogiques, sa bonne humeur et son caractère épicurien ont donné de la vie au groupe. Les discussions scientifiques (et souvent sans fin) que j'ai pu avoir avec toi Andrea m'ont permis de comprendre en profondeur beaucoup de concepts de la physique moléculaire. Merci encore à toi.

Je tiens à remercier les membres du jury de mon examen de thèse, les professeurs *Thomas Gustavsson*, *Jacques-Edouard Moser* et *Jean-Pierre Wolf*, qui ont porté un intérêt particulier aux travaux de ma thèse et ont accepté de l'évaluer. Merci à vous pour tous vos commentaires positifs et constructifs.

Je remercie beaucoup *Monique Bassin*, *Esther van Arx* et *Monique Grin Celka*, les secrétaires du laboratoire qui ont toujours été patientes et efficaces dans les tâches d'organisation et administratives liées à ma thèse.

J'aimerais remercier *Andreas Tortschanoff*, *Frank van Mourik* et *Gerald Auböck* pour leur importantes contributions dans mon projet à travers notamment des discussions scientifiques fructueuses et de nombreux conseils.

Je dois en particulier remercier deux collègues qui ont fait partie du même projet, et avec qui j'ai eu la chance de travailler en étroite collaboration. Merci tout d'abord à Dr *Ahmad Oskouei Ajdarzadeh*, pour tous nos échanges scientifiques, culturels et amicaux qui ont adoucis ces quatre années de labeur. Merci à *Cristina Consani* pour sa collaboration et sa vision alternative de la photophysique des systèmes que nous avons étudiés ensemble,

mais surtout pour sa gentillesse et ses commentaires pertinents qui ont rendu ces quatre années agréables et enthousiasmantes.

J'aimerais remercier tout particulièrement *Fabrizio Messina*, qui prend la relève du montage de conversion de fluorescence. J'ai pu travailler un an en étroite collaboration avec Fabrizio, qui m'a beaucoup apporté tant au niveau théorique et expérimental qu'au niveau humain. Merci Fabrizio pour ta constante bonne humeur qui m'a encouragé lors de la rédaction de ma thèse.

Je remercie encore deux collaborateurs externes, le professeur *Julian Echave* qui a effectué des calculs de simulation du tryptophane dans l'eau ainsi que le professeur *Antonin Vlcek*, pour ses précieux conseils et discussions.

Enfin je veux enfin remercier mes collaborateurs du LSU de Lausanne et du groupe de photochimie dynamique du professeur Moser, et en particulier *Amal El Nahhas*, *Renske Van der Veen*, *Thai Pham*, *Marco Reinhard*, *Frederico Alves Lima*, *Ahmed Maher Fahmy El-Zohry*, *Thomas James Penfold*, *Joël Teuscher*, *Jan Cornelius Brauer*, pour leur diverses collaborations. Sans oublier les membres du groupe travaillant ou ayant travaillé au LSU et avec qui j'ai pu passer de bons moments: *Ahmad Odeh*, *Erwin Portuondo*, *Christopher Milne*, *Pr. Christian Bressler*, *Pr. Fabrizio Carbone*, *Susanne Karlsson*, *Hannelore Rittmann-Frank*, *Roberto Monni*, *Mariateresa Scarongella*, et *Andre Al Haddad*. Merci aussi aux responsables des supports informatique *Michel Kessous* et *Pierre-André Perroud*, des ateliers mécanique, *Mr Moser* et électronique, *Mr Rittener*.

Ces quatre années de doctorat n'auraient pu aboutir sans le soutien et les encouragements de ma famille et de mes amis. En particulier mes parents n'ont cessé de me pousser à aller au-delà de mes limites, durant toutes mes études. De même je remercie ma sœur *Nathalie* et mon frère *Nicolas*, mais surtout ma femme *Sandrine* que j'ai eu la chance d'épouser lors de ma première année de thèse. Enfin, ma fille *Aïna*, qui a vu le jour au milieu de mon travail de doctorat et dont les sourires valent bien plus que n'importe quels encouragements.